

**Impacts of Urbanization on Extreme Precipitation in Coastal South
China and the Associated Weather Systems as Inferred from
Observation and Dynamical Downscaling Experiments**

HU, Chenxi

A Thesis Submitted in Partial Fulfillment
of the Requirements for the Degree of
Doctor of Philosophy
in
Earth and Atmospheric Sciences

The Chinese University of Hong Kong
August 2023

Thesis Assessment Committee

Professor LIU Lin (Chair)

Professor TAM Chi Yung Francis (Thesis Supervisor)

Professor TAI Pui Kuen Amos (Committee Member)

Professor YANG Zong Liang (External Examiner)

Abstract of thesis entitled

Impacts of Urbanization on Extreme Precipitation in Coastal South China and the Associated Weather Systems as Inferred from Observation and Dynamical Downscaling Experiments

Submitted by **HU, Chenxi**

for the degree of **Doctor of Philosophy in Earth and Atmospheric Sciences**

at The Chinese University of Hong Kong in **August 2023**

Abstract

The influence of urbanization on extreme precipitation is intricate, variable, and still inconclusive, and the impact remains context-dependent, with factors such as geographical location, synoptic systems, and urban heat island intensity (UHII) playing a crucial role. South China's coastal region (SC), located within the East Asia monsoon region, presents a particular case due to its diverse precipitation drivers, including frontal systems, the Asian summer monsoon, severe thunderstorm systems, and tropical cyclones (TC). Concurrently, this region has experienced rapid urbanization since the 1980s, particularly in the Greater Bay Area (GBA, located on the South China coast). While numerous studies have investigated the urban impact on extreme precipitation in GBA, the majority have focused on the summer monsoon season, leaving a knowledge gap regarding the effects of urbanization during other seasons and under different weather systems. To address this, our study examines the distinct influence of urbanization on extreme precipitation events in the GBA mega-city across various seasons and synoptic systems, offering a comprehensive and novel approach to the topic. We pose three key scientific questions to guide our investigation: (1) How does urbanization influence TC-induced extreme rainfall in the SC mega-city cluster? (2) Can urbanization continue to enhance extreme precipitation in the GBA mega-city during the winter season? (3) Does urbanization also amplify extreme rainfall in the GBA during the pre-monsoon period? If so, do these effects vary under

different synoptic systems? By addressing these questions, our research aims to contribute to the understanding of the intricate relationships between urbanization and extreme precipitation, providing valuable insights for urban planning and climate change adaptation strategies in the context of a rapidly urbanizing coastal monsoon region.

In the first part of this thesis, how urbanization affects TC rainfall is inferred from station observations over the GBA and numerical model experiments. Observations from 41 TCs indicate that surface wind is noticeably weaker in urban compared to rural stations during TC passages, while the UHI effect is considerably suppressed. Extreme (99th percentile of) hourly rainfall for these TC events from 2008 to 2017 is more intense over urban compared to rural stations. For eight selected TC cases, dynamical downscaling was carried out using the convection-resolving Weather Research and Forecasting (WRF) model, each with three parallel experiments: “Nourban” in which the urban area was replaced by cropland; “AH0” (“AH300”) in which the diurnal maximum anthropogenic heat (AH) was set to 0 (300W/m²) in city locations. Both AH0 and AH300 show a significant increase in urban hourly rainfall intensity and probability in all ranges (most obvious for heavy rainfall > 40mm/hr) over the GBA mega-city. Further diagnosis indicates increased moisture flux convergence in urban areas over a two-day period during the landfall, contributing to increased rainfall, likely induced by the surface roughness. The influence of AH, however, is found to be insignificant. The increase in accumulated rainfall due to urbanization is proportionate to the storm residence time over the city, implying greater rainfall exacerbation for slower or larger TCs. It is concluded that urbanization intensifies extreme TC rainfall over the coastal GBA mega-city mainly due to surface frictional convergence, with stronger intensification for those storms residing longer over the city.

In the second part, winter station observations from 2008 to 2017 show a strong urban dry island (UDI) effect in the GBA mega-city, while the 99th percentile hourly winter rainfall intensity is lower at urban stations than at surrounding rural stations. However, for the more intense extreme precipitation, GBA urban locations still have stronger annual maximum hourly rainfall (Rmax) and very extreme rainfall (99.99th percentile) than rural locations during winter, implying that urbanization may still have a positive effect on extreme winter precipitation. Case study based on 11 (12) strong (weak) UHI extreme events also indicated that the UHI effect can strongly enhance winter extreme rainfall intensity and probability in GBA mega-city. Moreover, two particular extreme cases (namely Case 2013 and Case 2015) were dynamically downscaled by WRF-UCM, for which four parallel experiments were designed: urban land use be replaced by cropland (Nourban), historical urban land use in 1999 (99LS), the near-future projection in 2030 urban land use (30LS), and urban land use in 2030 but with no AH (30LS-AH0). Numerical simulations show that for Case 2013 (Case 2015), 30LS has weaker (stronger) urban rainfall than Nourban. Synoptic analysis shows that cold air invasion associated with the approach of frontal systems highly suppressed the UHI effect in Case 2013, but does not affect the urban area in Case 2015. The remained UHI effect increases local convection and circulation between land and ocean, which leads to stronger moisture flux convergence that significantly enhances urban precipitation intensity and probability in Case 2015. On the other hand, the urban surface frictional effect has very little impact. Results as inferred from observations and modeling results suggest that urban impacts on extreme precipitation in GBA still exist in winter for some special cases when the UHI effect gets maintained.

The third part of this thesis investigates urbanization effects on pre-monsoon rainfall

using hourly station observations and WRF-UCM simulations. Observations show stronger extreme rainfall in GBA cities than in rural areas, with the UHI intensifying urban rainfall intensity and probability. Extreme cases were classified into frontal and shear-line + warm-sector types. Enhanced urban rainfall due to UHI was more pronounced under shear-line and warm-sector systems. Four frontal and four shear-line cases were dynamically downscaled using WRF-UCM, and four parallel experiments were conducted: "Nourban" (urban areas replaced by cropland), "AH0," "AH100," and "AH300" (normal land use, with diurnal maximum AH set to 0, 100, and 300 W/m² in UCM, respectively). In frontal cases, significantly reduced urban rainfall in AH0 was due to decreased (enhanced) surface evaporation (wind divergence) in urban areas compared to cropland. Strong northerly winds and cold air intrusion suppressed UHI in AH0 and AH100 during the rainfall process; enhanced urban rainfall occurred only in AH300. In contrast, for shear-line cases, urban friction and UHI promoted local convection and wind convergence, increasing urban rainfall significantly in all urban experiments compared to Nourban. Overall, urbanization's influence on extreme rainfall during the pre-monsoon period is highly sensitive to the type of synoptic systems, necessitating further investigation of urban rainfall in this season.

摘要

城市化對極端降水的影響是錯綜複雜的、多變的，而且仍然沒有定論，其影響仍然是取決於環境的，諸如地理位置、同步系統和城市熱島強度（UHII）等因素發揮着關鍵作用。華南沿海地區（SC）位於東亞季風區，由於其不同的降水驅動因素，包括鋒面系統、亞洲夏季季風、嚴重的雷暴系統和熱帶氣旋（TC），呈現出特殊的研究案例。同時，華南地區自 20 世紀 80 年代以來經歷了快速的城市化，特別是在大灣區（GBA，位於華南沿海）。雖然許多研究已經調查了城市對大灣區極端降水的影響，但大多數研究都集中在夏季季風季節，對於城市化在其他季節和不同天氣系統下的影響還存在知識空缺。為了解決這個問題，我們的研究考察了城市化對 GBA 特大城市不同季節和天氣系統的極端降水事件的獨特影響，為這個主題提供了一個全面和新穎的方法。我們提出了三個關鍵的科學問題：（1）城市化如何影響中國華南巨型城市群中颱風引起的極端降水？（2）城市化能否繼續增強 GBA 特大城市冬季的極端降水？（3）城市化是否也會放大 GBA 在季風前時期的極端降水？如果是的話，這些影響在不同的天氣系統下是否有所不同？通過解決這些問題，我們的研究旨在促進對城市化和極端降水之間錯綜複雜關係的理解，為快速城市化的沿海季風地區的城市規劃和氣候變化適應戰略提供寶貴的見解。

本論文的第一部分，通過對 GBA 的站點觀測和數值模型試驗，分析了城市化如何影響颱風降水。41 個颱風的觀測結果表明，與農村站點相比，城市站點在颱風過境期間地表風明顯減弱，而城市熱島效應則明顯被抑制。在 2008 至 2017 年的颱風事件中，城市站點的極端逐小時降水量（99% 百分位數）比農村站點更為強烈。對 8 個選定的颱風案例，採用允許對流解析精度的 Weather Research and Forecasting（WRF）模型進行了動力降尺度模擬，每個案例進行了三組敏感性試驗：「Nurban」（城市區域被農田取代）；「AHO」（在城市區域內，日最大人為熱量（AH）設為 0）；「AH300」（在城市區域內，日最大人為熱量（AH）

設為 300W/m^2 ）。AHO 和 AH300 試驗中，GBA 特大城市的城巿小時降水強度和概率在所有範圍內都有顯著增加（對於降水量 $>40\text{mm/hr}$ 的暴雨尤為明顯）。進一步診斷表明，在登陸過程的兩天內，城市地區的整層大氣水汽輻合通量增加，導致降水量增加，這是由於地表粗糙度引起的。然而，人為熱對颱風降水的影響被認為是不顯著的。此外，城市化對累積降水量增加的影響與風暴在城市上空的停留時間成正比，這意味着對於移動較慢或較大的颱風，降水量的加劇更為嚴重。因此，得出結論認為，城市化主要由於地表摩擦收斂作用，加劇了沿海 GBA 特大城市的極端颱風降水，對於在城市上空停留時間較長的風暴，強度加劇更為明顯。

在第二部分，2008 至 2017 年冬季站點觀測顯示，GBA 特大城市出現了明顯的城市干島 (UDI) 效應，99th 百分位數逐小時冬季降水強度在城市站點低於周圍農村站點。但對於非常極端的暴雨，GBA 城市群相對周圍農村站點來說依然擁有更高的年最大降水 (R_{\max}) 以及 99.99th 百分位數逐小時降水，意味著城市化對於冬季極端降水可能依然存在積極作用。基於 11(12) 個強（弱）熱島效應個例的案例分析同樣發現 UHI 可以強烈的增強 GBA 特大城市的冬季極端降水強度和頻率。此外，WRF-UCM 對兩個特殊的極端情況（即 Case 2013 和 Case 2015）進行了動態降尺度，為此設計了四個平行實驗：城市土地利用被耕地取代 (Nourban)，1999 年的歷史城市土地利用 (99LS)，2030 年城市土地利用的近未來預測 (30LS)，以及 2030 年的城市土地利用但沒有人為熱 (30LS-AHO)。數值模擬顯示，在 Case 2013 (Case 2015) 情況下，30LS 的城市降雨量比 Nourban 弱（強）。同步分析顯示，與鋒面系統接近相關的冷空氣入侵高度抑制了 Case 2013 中的 UHI 效應，但在 Case 2015 中並不影響城市地區。未被壓制的 UHI 效應增加了陸地和海洋之間的局部對流和環流，導致更強的水汽輻合通量，大大增強了 Case 2015 的城市降水強度和概率。另一方面，城市表面摩擦效應的影響非常小。從觀測和模擬結果推斷出的結果表明，在熱島效應得到維持的情況下，城市對 GBA 冬季極

端降水的影響仍然存在。

城市化對 GBA、SC 沿海地區季風前極端降雨的影響及其與不同天氣系統的關係仍然沒有得到充分研究。本論文的第三部分利用逐小時的站點觀測和 WRF-UCM 模擬研究了城市化對季風前時期極端降雨的影響。觀測結果顯示，GBA 城市的極端降雨比農村地區更強，同時 UHI 顯著加強了城市降雨強度和概率。極端情況被分為鋒面型和切變線+暖區型。在切變線和暖區系統下，UHI 導致的城市降雨量增強更為明顯。此外，我們使用 WRF-UCM 對四個鋒面和四個切變線案例進行了動態降尺度，並設計了四個平行實驗： "Nourban"（城市地區被耕地取代）、「AH0」、「AH100」和「AH300」（正常土地利用，UCM 中的日最大人為熱量（AH）分別為 0、100 和 300W/m^2 ）。在鋒面降水案例中，AH0 的城市降雨量明顯減少，是由於城市的表面蒸發（風輻合）比農田下墊面減少（增強）。強烈的北風和冷空氣入侵在降雨過程中抑制了 AH0 和 AH100 的 UHI；只有 AH300 的城市降雨量增強。相反，對於剪切線降水案例，城市的地表摩擦作用和 UHI 促進了當地的對流和風輻合，與 Nourban 相比，所有城市實驗中的城市降雨量都明顯增加。總的來說，城市化對季風前期極端降雨的影響對同步系統的類型非常敏感，因此有必要對這個季節的城市降雨進行進一步研究。

Acknowledgements

I would like to express my deepest gratitude to my supervisor, Prof. Tam Chi Yung Francis, for his invaluable guidance, unwavering support, and mentorship throughout my PhD journey. His expertise and wisdom have been instrumental in shaping me into an independent and qualified researcher, and I am grateful for the countless lessons imparted on research methodologies and critical thinking. I also extend my thanks to Prof. Tam for providing me with the resources and opportunities necessary for my academic and personal growth. Without his assistance, completing my doctorate degree and this thesis would not have been possible. I feel truly honored to have had the privilege of studying under his guidance and will forever be grateful for the chance to be a part of our atmosphere dynamics group.

I extend my heartfelt appreciation to the members of my thesis committee: Professor Liu Lin, Professor Tai Pui Kuen Amos, and Professor Yang Zong-Liang. Their constructive feedback, insightful suggestions, and commitment to my academic development have greatly contributed to the successful completion of this thesis.

To my loving parents, I express my deepest gratitude for their unwavering love, encouragement, and belief in my capabilities. Their constant support and sacrifices have fueled my determination to overcome challenges and achieve my goals.

Lastly, I dedicate this thesis to my late grandfather, whom I will always miss and cherish. The unfortunate circumstances of the epidemic prevented me from seeing him one last time during my doctorate studies, but his memory will forever inspire me to persevere and strive for excellence in all my endeavors.

Table of Contents

1. Introduction.....	1
1.1 Urban development in the Greater Bay Area (GBA).....	1
1.2 Urban climate.....	2
1.2.1 Urban morphology.....	2
1.2.2 Urban Heat Island (UHI) effect.....	4
1.2.3 Aerosols.....	6
1.3 Impact of urbanization on precipitation.....	8
1.3.1 Urban impacts on rainfall in inland cities.....	8
1.3.2 Urban impacts on rainfall in coastal cities.....	10
1.3.3 Studies focus on the GBA mega-city.....	11
1.4 Observation and reanalysis data.....	13
1.4.1 Rain gauge-based datasets.....	13
1.4.2 TRMM 3B42 product.....	14
1.4.3 Best Track datasets.....	15
1.4.4 ECMWF reanalysis datasets.....	15
1.5 Dynamical downscaling.....	16
1.6 Numerical model.....	17
1.6.1 The Weather Research and Forecasting (WRF) model.....	18
1.6.2 Urban Canopy Model.....	19
1.7 Motivation and objectives.....	20
1.8 Roadmap of thesis.....	22
2. How Does Urbanization Affect Tropical Cyclone Rainfall Extremes-Inferences from Observations and Convection-Permitting Model Experiments over the South China Greater Bay Area.....	24
2.1 Introduction.....	24
2.2 Methodology.....	26
2.2.1 TC case study based on observations.....	26
2.2.2 WRF model configuration and TC cases.....	27
2.2.3 Experimental design and UCM parameters.....	30
2.2.4 Model evaluation for TC tracks.....	33
2.3 Results.....	35
2.3.1 Results based on observations.....	35
2.3.1.1 TC rainfall distribution.....	35
2.3.1.2 Rainfall, temperature, and wind speed evaluation during TC passages.....	37
2.3.2 Results based on numerical modeling.....	40
2.3.2.1 Surface temperature and wind.....	40
2.3.2.2 TC rainfall extremes.....	42
2.3.2.3 Mechanism of enhanced accumulated rainfall.....	45

2.3.2.4 AH impacts on TC rainfall.....	48
2.3.2.5 The influence of TC movement.....	52
2.4 Brief Summary.....	54
Appendix: Definition of TC rainfall-affected area.....	56
3. Urban impact on winter extreme precipitation as inferred from observation and numerical simulation of two cases over the South China Greater Bay Area.....	58
3.1 Introduction.....	58
3.2 Methodology.....	60
3.2.1 Observations and winter case study.....	60
3.2.2 WRF model configuration and two winter cases.....	62
3.2.3 UCM, Model Experiments, and Local Climate Zone (LCZ) Data.....	64
3.2.4 Model evaluation.....	67
3.3 Results.....	73
3.3.1 Observation results.....	73
3.3.1.1 Winter temperature and precipitation.....	73
3.3.1.2 Case study for UHI effect on winter precipitation.....	77
3.3.2 Results based on numerical modeling.....	80
3.3.2.1 Synoptic background for two cases.....	80
3.3.2.2 Temperature results.....	83
3.3.2.3 Precipitation results.....	86
3.3.2.4 Mechanism of urban impact on winter precipitation.....	91
3.4 Brief Summary.....	99
4. Urbanization impacts on Greater Bay Area extreme rainfall - sensitivity to synoptic systems during pre-monsoon period.....	101
4.1 Introduction.....	101
4.2 Methodology.....	103
4.2.1 Pre-monsoon period and case selection.....	103
4.2.2 Synoptic cases.....	105
4.2.3 WRF model configuration and cases.....	106
4.2.4 Experiment design and UCM setup.....	108
4.3 Results.....	109
4.3.1 Observations.....	109
4.3.1.1 Pre-monsoon temperature and precipitation.....	109
4.3.1.2 Case study during pre-monsoon period.....	113
4.3.1.3 Synoptic case study.....	117
4.3.2 Numerical modeling results.....	121
4.3.2.1 Synoptic background for frontal and shear-line cases.....	121
4.3.2.2 Precipitation.....	124
4.3.2.3 Relationship between temperature (humidity) and precipitation differences.....	129

4.3.2.4 Mechanism for shear-line cases.....	134
4.3.2.5 Mechanism for frontal cases.....	139
4.3.2.6 Suppressed UHI effect during frontal cases.....	144
4.4 Brief Summary.....	151
5.Discussions and conclusions.....	154
5.1Major conclusions.....	154
5.1.1 Tropical cyclone rainfall.....	154
5.1.2 Winter precipitation.....	156
5.1.3 Pre-monsoon precipitation.....	158
5.2Uncertainties and limitations.....	160
5.3Innovation and significance.....	163
5.4Social-economic implications.....	165
5.5Research outlook.....	166
5.5.1 Urban impact on TC rainfall.....	166
5.5.2 Urban impact on winter extreme rainfall.....	166
5.5.3 Urban impact on pre-monsoon extreme rainfall.....	167
5.5.4 Diurnal and seasonal profile of AH.....	167
6.Reference.....	167

List of Figures

Figure 1.1 GBA urban area in (a) 1988, (b) 1999, and (c) 2010. Brown, yellow, and red shaded represent the Low-Density Residence, High-Density Residence, and Industrial and Commercial. (Source: You et al., 2019).....	2
Figure 1.2 Annual change of built-up area, population density, and urban ratio in GBA mega-city from 1980 to 2015. (Source: Wu et al., 2019).....	2
Figure 1.3 Diurnal variation of energy balance components in (a) urban, and (b) rural areas in Vancouver for 30 summer days in 1983 (Source: Cleugh and Oke, 1986).....	4
Figure 1.4 How UHI occurs. (Source: D.S. Lemmen and F.J. Warren, Climate Change Impacts and Adaptation).....	6
Figure 1.5 Summer total rainfall amounts averaged from 2008-2012 in Beijing under weak and strong UHI situations. (Source: Dou et al., 2015).....	10
Figure 1.6 (Left panel) August monthly average 2001-2008 rainfall difference between experiments in Tokyo. (Right panel) August monthly average 2001-2008 moist flux and difference (Source: Kusaka et al., 2014).....	11
Figure 1.7 Annual trend of precipitation intensity (mm), precipitation frequency (%), intense rainfall frequency (%), and extreme precipitation frequency (%) from 1981 to 2015 for (a) urban and (b) rural areas. (Source: Yan et al., 2020).....	12
Figure 1.8 Location of 86 observation stations over South China.....	14
Figure 1.9 Distributions of surface temperature (units: °C) in different seasons from 1981 to 2010 from (a-d) Observations, (e-h) R2 reanalysis, (i-l) RegCM4, and (m-p) WRF downscaling simulations. (Source: Gao, 2020).....	17
Figure 1.10 Direct interactions of parameterizations in WRF model.....	19
Figure 2.1 Location of observation stations over South China, with red (blue) dots representing 7 urban (rural) stations, other stations are shown in black dots. Green lines are the track of 41 TC cases.....	27
Figure 2.2 (a) Nested domains for the WRF simulations. (b) Land use categories in the innermost domain for AH0 and AH300 experiments, based on 2002 MODIS data with urban and build-up, cropland, forest and grassland showed areas in red, yellow, cyan and green.....	29
Figure 2.3 Diurnal profile of AH over urban grids of the innermost domain for experiments with peak AH = 300Wm ⁻² , the daily mean AH is about 166Wm ⁻²	32
Figure 2.4 Track of 8 TC cases (Victor, Utor, Dujuan, Mangkhut, Goni, Hal, Wanda, and York). Black line shows the historical track based on HKO best track data. Blue, purple, and red mean Nourban, AH0 and AH300 run. The GBA urban area is shown in green shaded area.....	34
Figure 2.5 (a) Extreme rainfall based 99th percentile of hourly rainfall during all TC cases in each station, with star means urban stations, and diamond means rural stations. (b) PDFs of hourly precipitation rates for rural (blue) and urban (red) stations, within the ranges of 1-10, 10-20, 20-30, 30-40, 40-50, 50-60, 60-70, 70-80, 80-90 mm/hr.....	36

- Figure 2.6** Scatter plot of distance between stations and ocean vs (a) 99th percentile of hourly rainfall, (b) accumulated rainfall during 41 TC cases in each station, with urban, rural and other stations shown in red, green and blue. The black box represents selected stations. Crosses represent the centroids of results in urban, rural, and other stations with the same color.....37
- Figure 2.7** (a) Time series of hourly 2m temperature (blue) and rainfall (red) difference between urban and rural stations averaged over all TC cases. Hourly rainfall differences exceeding the 95% significance level are denoted by red dots. (b) Same as (a) but for hourly 10m wind speed (blue) and rainfall (red), hourly wind difference exceeds the 95% significance level are denoted by red dots.....39
- Figure 2.8** Time series of hourly rainfall for rural (blue), and urban (red) area averaged over 41 TC cases based on TRMM reanalysis data, with smaller map representing the rural (blue) and urban (red) area.....40
- Figure 2.9** (a) Time series of hourly 2m temperature difference between AH0 and Nourban (blue), and that between AH300 and Nourban (red) averaged over 8 TC cases based on model simulation. (b) Same as (a) but for hourly 10m wind speed difference. Hourly wind difference between AH0 (AH300) and Nourban exceeds the 95% significance level are denoted by blue (red) dots.....42
- Figure 2.10** (a) Time series of hourly rainfall over urban locations within GBA area for Nourban (black), AH0 (blue), and AH300 (red) averaged over 8 TC cases based on model simulation. (b) PDFs of hourly precipitation rates over urban locations within GBA, within the ranges of 1-10, 10-20, 20-30, 30-40, 40-50, 50-60, 60-70, 70-80, and 80-90 mm/hr for the NO-URBAN (black), AH0 (blue), AH300 (red) experiments.....43
- Figure 2.11** Accumulated rainfall difference (units: mm/day) between (a) AH0 and Nourban, and (b) AH300 and Nourban. Rainfall is computed by averaging over entire integrations for 8 cases. Locations in which the difference exceeds the 95% significance level are denoted by black dots. Black contours represent the boundary of GBA mega-city.....45
- Figure 2.12** Three hours mean 10m-wind speed difference (AH0 vs Nourban) and wind vector at landfall hour for (a) Victor, and (b) Utor. Black contours represent the boundary of GBA mega-city.....46
- Figure 2.13** Time series of hourly rainfall for each case (Victor, Utor, Dujuan, Mangkhut, Goni, Hal, Wanda, and York). Black, blue, and red line mean Nourban, AH0, and AH300 experiments.....49
- Figure 2.14** Time series of CAPE over urban locations within GBA area for Nourban (black), AH0 (blue), and AH300 (red) for (a) Mangkhut and (b) Goni. (c), (d) Same as (a), (b) except for vertically integrated specific humidity. The specific humidity is computed by integrating over all model layers.....51
- Figure 2.15** Duration of TC residence time in each case, experiment, and ensemble members....52
- Figure 2.16** (a) A diagram example of how to define the TC residence time. TC tracks of Victor from Nourban, AH0, and AH300 are shown in black, blue, and red lines. Black circle means TC rainfall affected area, and the GBA mega-city is shown in green shaded. (b)

Scatter plot of relationship between duration of TC residence time and accumulated rainfall difference ratio between urban runs (AH0 and AH300) and Nourban runs in all cases and ensemble members.....	54
Figure 3.1 (a) Location of observation stations over South China, with red (blue) dots representing 7 urban (rural) stations. Monthly mean (b) temperature (units: °C), (c) accumulated rainfall (units: mm/hr), and (d) extreme rainfall (99 th percentile of hourly rainfall, units: mm/hr) in November, December, January, February, and March averaged from 2008 to 2017 for all urban and rural stations.....	62
Figure 3.2 (a) Nested domains for the WRF simulations. (b) Land use categories of 1999 in the innermost domain with “Low Intensity Residence”, “High Intensity Residence”, and “Commercial and Industrial” locations indicated by yellow, red, and purple shading. (c) Same as (b) but for projected 2030 urban land use.....	63
Figure 3.3 Land cover types from WUDAPT data, with LCZ 1 to 10 representing urban land use and LCZ A to G representing non-urban land use. (Source: Steward and Oke, 2012).....	65
Figure 3.4 (a) Surface temperature (units: °C), and U,V wind (units: m/s) averaged over Case 2013 from ERA5 reanalysis date, with shaded and vector representing temperature and wind. Black contours mean the coastline and boundary of province. (b) Same as (a) but for model outputs.....	69
Figure 3.5 (a) 925hPa temperature (units: °C), geopotential height (units: m), and U,V wind (units: m/s) averaged over Case 2013 from ERA5 reanalysis date, with shaded, blue contour, and vector representing temperature, geopotential height, and wind. Black contours mean the coastline and boundary of province. (b) Same as (a) but for model outputs.....	69
Figure 3.6 Same as Figure3.4 except for Case 2015.....	71
Figure 3.7 Same as Figure3.5 except for Case 2015.....	71
Figure 3.8 (a) Accumulated rainfall (units: mm) averaged over Case 2013 from model outputs. Black contours mean the GBA mega-city, coastline, and boundary of province. (b)(c) Similar to (a) but for ERA5 and station observations.....	73
Figure 3.9 Same as Figure3.8 except for Case 2015.....	73
Figure 3.10 (a) Surface temperature (units: °C) averaged over winter from 2008 to 2017, with star means urban stations, and diamond means rural stations. (b) Winter temperature (units: °C) derived from ERA5 reanalysis data. Black contours mean the coastline and boundary of province.....	74
Figure 3.11 (a) Extreme rainfall based 99th percentile of hourly rainfall (units: mm/hr) during winter in each stations, with star means urban stations, and diamond means rural stations. (b) PDFs of hourly precipitation rates during winter for rural (blue) and urban (red) stations, within the ranges of 1-4, 4-8, 8-12, 12-16, 16-20, 20-24, 24-28, 28-32, 32-36, and 36-40 mm/hr.....	76
Figure 3.12 Same as Figure 3.11a except for (a) Rmax (units: mm/hr), annual maximum value in winter averaged from 2008 to 2017 in each station, and (b) Extreme rainfall based 99.99th percentile of hourly rainfall (units: mm hr) during winter.....	77
Figure 3.13 (a) Time series of surface temperature (units: °C) averaged over urban and rural stations during all strong UHI cases, with red and blue line representing temperature in	

urban and rural stations. Time 0 refers to the peak rainfall hour averaged over the selected 14 stations. (b) Same as (a) except for surface temperature during weak UHI cases. (c) Time series of surface temperature difference (units: °C) between urban and rural stations for strong and weak UHI cases, red and blue line mean results in strong and weak UHI cases.....	78
Figure 3.14 (a) Temperature difference (units: K) between strong and weak UHI cases in each station.....	78
Figure 3.15 (a) Time series of hourly rainfall (units: mm/hr) averaged over urban and rural stations during all strong UHI cases, with red and blue line representing rainfall in urban and rural stations. Time 0 refers to the peak rainfall hour averaged over the selected 14 stations. (b) Same as (a) except for weak UHI cases. (c) PDFs of hourly precipitation rates in urban stations for weak UHI (blue) and strong UHI (red) cases, within the ranges of 1-3, 3-6, 6-9, 9-12, 12-15, 15-18, 18-21, 21-24, 24-27, and 27-30 mm/hr.....	80
Figure 3.16 Snapshot of 925hPa temperature (units: °C), geopotential height (units: m), and U,V wind (units: m/s) for Case 2013 from ERA5 reanalysis date at (a) 2013-12-15-00:00, (b) 2013-12-15-12:00, and 2013-12-16-00:00, with shaded, blue contour, and vector representing temperature, geopotential height, and wind. Black contours mean the coastline and boundary of province.....	82
Figure 3.17 Same as Figure3.16 except for Case 2015.....	83
Figure 3.18 2m temperature difference (units: °C) between (a) 30LS and Nourban and (b) 30LSAH0 and Nourban for Case 2013. Temperatures are computed by averaging over rainfall period. See text for details. The coastline is shown by black line. (c) (d) Same as (a) (b) except for Case 2015.....	86
Figure 3.19 Vertical profile of urban temperature difference (units: K) averaged over rainfall period for (a) Case 2013, and (b) Case 2015 from 1000hPa level to 500hPa level. Black, blue, and red line represent the temperature difference between 99LS and Nourban, 30LSAH0 and Nourban, and 30LS and Nourban.....	86
Figure 3.20 Daily accumulated rainfall (units: mm/day) difference between (a) 99LS and Nourban, (b) 30LS and Nourban, and (c) 30LS and 30LSAH0 for Case 2013. Black contours represent the boundary of 1999 and 2030 GBA mega-city. Locations in which the difference exceeds the 95% significance level are denoted by black dots.....	88
Figure 3.21 Same as Figure3.20 except for Case 2015.....	88
Figure 3.22 Snapshot of hourly rainfall (units: mm/hr) distribution at the rainfall peak hour for (a) 99LS, (b) 30LS, (c) Nourban, and (d) 30LSAH0. Black contours represent the boundary of 1999 and 2030 GBA mega-city.....	89
Figure 3.23 (a) Time series of hourly rainfall (units: mm/hr) over urban locations within GBA area for Nourban (black), 99LS (blue), 30LSAH0 (green), and 30LS (red) for Case 2013 based on model simulation. (b) PDFs of hourly precipitation rates over urban locations within GBA, within the ranges of 1-3, 3-6, 6-9, 9-12, 12-15, 15-18, 18-21, 21-24, 24-27, and 27-30 mm/hr for the Nourban (black), 99LS (blue), 30LSAH0 (green), and 30LS (red) experiments.....	90
Figure 3.24 Same as Figure 3.23 except for Case 2015.....	91

Figure 3.25 Surface evaporation difference (units: g/m ² /s) between 30LS and Nourban averaged over precipitation periods for Case 2013. Black contour represents the 2030 GBA mega-city.....	93
Figure 3.26 (a) South-to-North cross-section of difference of hourly vertical wind vector (units: m/s) and specific humidity (units: g/kg), averaged over the rainfall period of Case 2013, between 30LS and Nourban. Black line in the inset figure represents the location of cross-sectional plane. (b) Same as (a) except for East-to-West cross section.....	93
Figure 3.27 (a) Surface wind in 30LS, averaging over the rainfall period of Case 2015, black contour represents the 2030 GBA mega-city. (b) Surface wind speed difference and wind difference between 30LS and Nourban, averaging over rainfall period, with the wind speed difference and wind difference showing by shaded and vector. (c) Same as (b) except for difference between 30LS and 30LSAH0.....	95
Figure 3.28 Same as Figure 3.27 except for 850hPa wind.....	95
Figure 3.29 (a) South-to-North cross-section of difference of hourly vertical wind vector (units: m/s) and specific humidity (units: g/kg), averaged over the rainfall period of Case 2015, between 30LS and Nourban. Black line in the inset figure represents the location of the cross-sectional plane. (b) Same as (a) except for difference between 30LS and 30LSAH0.....	97
Figure 3.30 Same as Figure 3.29 except for West-to-East cross sectional plane.....	97
Figure 4.1 Flow chart of how to define the South China Sea monsoon onset day, and the monsoon onset day from 2008 to 2017.....	104
Figure 4.2 Examples of (a) frontal, (b) shear-line, and (c) Warm sector case, with shaded, and vector representing 850hPa temperature (units: °C), and wind ((units: m/s) derived from ERA5. Blue vectors mean the direction of the prevailing wind, black contours are the coastline and boundary of province.....	106
Figure 4.3 (a) Nested domains for the WRF simulations. (b) Land use categories in innermost domain for AH0, AH100 and AH300 experiments, based on 2002 MODIS data with urban and build-up, cropland, forest and grassland shown areas in red, yellow, cyan and green. (c) Land use categories for the Nourban experiment, in which urban and build-up areas are replaced by cropland.....	107
Figure 4.4 (a) Surface temperature (units: °C) averaged over pre-monsoon period from 2008 to 2017, with star means urban stations, and diamond means rural stations. (b) Pre-monsoon temperature (units: °C) derived from ERA5 reanalysis data. Black contours mean the coastline and boundary of province.....	110
Figure 4.5 (a) 95th and (b) 99th percentile of hourly rainfall (units: mm/hr) during the pre-monsoon period at each station. (c) PDFs of hourly precipitation rates for rural (blue) and urban (red) stations, within the bin ranges of 1-5, 5-10, 10-15, 15-20, 20-25, 25-30, 30-35, 35-40, 40-45, 45-50, 50-55, and 55-60 mm/hr.....	112
Figure 4.6 (a) Extreme rainfall based 99th percentile of hourly rainfall (units: mm/hr) during the pre-monsoon period from 1980 to 1993 based on Aphrodite data. (b) Same as (a) except for extreme rainfall from 1994 to 2007.....	113

- Figure 4.7** (a) Time series of pre-monsoon surface temperature (units: °C) averaged over urban and rural stations during all strong UHI cases, with red and blue line representing temperature in urban and rural stations. Time 0 refers to the peak rainfall hour averaged over the selected 14 stations. (b) Same as (a) except for surface temperature during weak UHI cases. (c) Time series of pre-monsoon surface temperature difference (units: °C) between urban and rural stations for strong and weak UHI cases, red and blue line mean results in strong and weak UHI cases.....115
- Figure 4.8** (a) Time series of pre-monsoon hourly rainfall (units: mm/hr) averaged over urban and rural stations during all strong UHI cases, with red and blue line representing rainfall in urban and rural stations. Time 0 refers to the peak rainfall hour averaged over the selected 14 stations. (b) Same as (a) except for weak UHI cases.....116
- Figure 4.9** (a) PDFs of hourly precipitation rates during all strong UHI cases for rural (blue) and urban (red) stations, within the ranges of 1-5, 5-10, 10-15, 15-20, 20-25, 25-30, 30-35, 35-40, 40-45, 45-50, 50-55, and 55-60 mm/hr. (b) Same as (a) except for hourly rainfall in urban stations during all strong UHI (red) and weak UHI (blue) cases.....117
- Figure 4.10** (a) Time series of surface temperature (units: °C) averaged over urban and rural stations during all strong UHI frontal cases, with red and blue line representing temperature in urban and rural stations. Time 0 refers to the peak rainfall hour averaged over the selected 14 stations. (b) Same as (a) except for surface temperature during strong UHI shear-line + warm sector cases.....118
- Figure 4.11** Time series of hourly rainfall (units: mm/hr) averaged over urban and rural stations during (a) strong UHI frontal UHI cases, (b) strong UHI shear+warm cases, (c) weak UHI frontal cases and (d) weak UHI shear+warm cases, with red (blue) line representing rainfall for urban (rural) stations. Time 0 refers to the peak hour of rainfall averaged over the selected 14 stations.....121
- Figure 4.12** (a) PDFs of hourly precipitation rates in urban stations during all frontal cases for weak UHI (blue) and strong UHI (red) cases, within the ranges of 1-5, 5-10, 10-15, 15-20, 20-25, 25-30, 30-35, 35-40, 40-45, 45-50, 50-55, and 55-60 mm hr. (b) Same as (a) except for all shear+warm cases.....121
- Figure 4.13** 850hPa temperature (shading; units: °C), geopotential height (blue contours; units: m), and U,V wind (vector; scale arrow in units of m/s) for frontal cases (a) 2010-05, (b) 2012-04, (c) 2013-04, and (d) 2016-05 from WRF model outputs. Blue arrows indicate the direction of wind in front and behind the front. (e,f,g,h) Same as (a,b,c,d) except for parameters in the same periods from ERA5.....123
- Figure 4.14** Same as Figure 4.13 except for shear-line cases (a) 2010-05, (b) 2014-05, (c) 2017-04, and (d) 2017-05.....124
- Figure 4.15** Daily accumulated rainfall (units: mm/day) difference between (a) AH0 and Nourban, (b) AH100 and Nourban, and (c) AH300 and Nourban for all shear-line cases. Black contours represent the boundary of the GBA mega-city. (d,e,f) Same as (a,b,c) except for all frontal cases. Locations in which the difference exceeds the 95% significance level are denoted by black dots.....128
- Figure 4.16** PDFs of hourly precipitation rates over urban locations within GBA for (a) Frontal, and (b) shear-line cases, within the ranges of 1-10, 10-20, 20-30, 30-40, 40-50, 50-60,

60-70, and 70-80 mm/hr for the Nourban (black), AH0 (blue), AH100 (green), and AH300 (red) experiments.....	128
Figure 4.17 Scatter plot of temperature (units: K) and daily rainfall difference (units: mm/d) during rainfall period of (a) Frontal cases, and (b) shear-line cases between AH0(black), AH100 (blue), AH300 (red) and Nourban over all urban grid points. Black, blue and red lines represent the best fit line of precipitation-temperature relationship. (c) (d) Same as (a)(b) except for specific humidity averaged from 950hPa to 300hPa (units: g/kg) and daily rainfall difference (units: mm/d).....	133
Figure 4.18 (a) Same as Figure 4.17b except for results in part of rural grid points. (b) Location of rural grids being used, see black rectangle. Black contours represent the GBA mega-city.....	133
Figure 4.19 Surface temperature (units: K) and wind (units: mm/s) difference between (a) AH0 and Nourban, (b) AH100 and Nourban, and (c) AH300 and Nourban averaged over 12 hours before rainfall peak hour of all shear-line cases. Shaded, vector, and black contours represent temperature, wind, and coastline and GBA mega-city.....	135
Figure 4.20 Vertical wind speed difference between (a) AH0 and Nourban, (b) AH100 and Nourban, and (c) AH300 and Nourban averaged from 950hPa to 300hPa level during rainfall period for all shear-line cases. Shaded, and black contours represent vertical wind speed, and coastline and GBA mega-city.....	136
Figure 4.21 Same as Figure 4.20 except for 10m wind divergence difference.....	138
Figure 4.22 Same as Figure 4.20 except for vertical wind shear difference, the VWS is defined as wind difference between 300hPa and 950hPa level.....	138
Figure 4.23 Same as Figure 4.20 except for specific humidity difference averaged from surface to 300hPa level.....	139
Figure 4.24 Surface temperature (units: K) and wind (units: mm/s) difference between (a) AH0 and Nourban, (b) AH100 and Nourban, and (c) AH300 and Nourban averaged over 12 hours before rainfall peak hour of all frontal cases. Shaded, vector, and black contours represent temperature, wind, and coastline and GBA mega-city.....	141
Figure 4.25 Vertical wind speed difference between (a) AH0 and Nourban, (b) AH100 and Nourban, and (c) AH300 and Nourban averaged from 950hPa to 300hPa level during rainfall period for all frontal cases. Shaded, and black contours represent vertical wind speed, and coastline and GBA mega-city.....	142
Figure 4.26 Same as Figure 4.25 except for 10m wind divergence difference.....	143
Figure 4.27 Same as Figure 4.25 except for specific humidity difference averaged from surface to 300hPa level.....	144
Figure 4.28 Vertical profile of urban temperature difference (units: K) averaged over rainfall period for all (a) frontal, and (b) shear-line cases from 1000hPa level to 500hPa level. Black, blue, and red line represent the temperature difference between AH0 and Nourban, AH100 and Nourban, and AH300 and Nourban.....	147
Figure 4.29 925hPa temperature difference (units: K) between (a) AH0 and Nourban, (b) AH100 and Nourban, and (c) AH300 and Nourban averaged over entire integrations for all frontal cases. Shaded, and black contours represent temperature difference, and coastline and	

GBA mega-city.....	147
Figure 4.30 925hPa temperature (shading; units: K) and wind (scale vector in units of mm/s) difference between (a) AH0 and Nourban, (b) AH100 and Nourban, and (c) AH300 and Nourban averaged over the rainfall period for all frontal cases. Black contours represent the coastline and boundary of the GBA mega-city.....	149
Figure 4.31 925hPa temperature advection (units: K/s) difference between (a) AH0 and Nourban, (b) AH100 and Nourban, and (c) AH300 and Nourban averaged over rainfall period of frontal case 2010-5. Shaded, and black contours represent temperature advection difference, and coastline and GBA mega-city.....	149
Figure 4.32 Time-longitude cross section of meridional gradient of the 925hPa equivalent potential temperature difference (units: K/100km) averaged between 22.8N to 24N between (a) AH0 and Nourban, (b) AH100 and Nourban, and (c) AH300 and Nourban for the frontal case 2016-5. Black dashed lines outline the location of the GBA mega-city. Blue (red) boxes indicate larger (weaker) EPT gradient, thus intensified (weakened) front intensity.....	152
Figure A1 (a) Azimuthal averaged hourly rainfall for TC Hal, with X and Y axis representing distance to TC center and time. (b) Curves of time mean rainfall with distance to TC center for TC Hal, with black, blue and red lines mean Nourban, AH0, and AH300 experiments.....	57
Figure A2 Radius of TC rainfall affected area in each case, experiment, and ensemble members.....	57

List of Tables

Table 1.1 Parameters included in SLUCM.....	20
Table 2.1 Name and time period for each TC case in WRF simulation.....	30
Table 2.2 Values of UCM parameters prescribed for the urban land use category.....	33
Table 2.3 Vertically integrated moisture flux divergence difference between AH0 (AH300) and Nourban for each case. Values are calculated by averaging over the GBA urban area and all ensemble members, with duv (dq) term representing the dynamic (thermal dynamic) term.....	48
Table 3.1 Values of UCM parameters prescribed for three types of urban categories.....	67
Table 3.2 Vertically integrated moisture flux divergence difference between 99LS and Nourban, 30LSAH0 and Nourban, and 30LS and Nourban for each case. Values are calculated by averaging over the GBA urban area and all ensemble members, with duv (dq) term representing the dynamic (thermal dynamic) term.....	99

1. Introduction

1.1 Urban development in the Greater Bay Area (GBA)

Over the past century, rapid urbanization has significantly altered the global demographic landscape, with the ratio of urban to rural populations increasing from 40% in 1950 to over 130% in 2020 (Our World in Data, 2020). Global urban areas expanded by approximately 80% between 1985 and 2015, at a rate of 9,687 km² per year (Liu et al., 2020). This swift urban expansion has induced substantial changes in local temperature, precipitation, and atmospheric circulation in cities (Mohajerani et al., 2017; Luo et al., 2017; Han et al., 2014; Li et al., 2016; Fan et al., 2018), drawing increased attention from researchers in recent decades. The GBA mega-city cluster, situated along the South China coast (covering 22-23.2°N, 112.6-114.3°E), receives high levels of precipitation due to the influence of the Asian summer monsoon, frontal systems, severe thunderstorms, and tropical cyclones (TC) (Ramage, 1952; Hallegatte et al., 2013; Luo et al., 2016). The rainy season typically extends from April to early October. Since the early 1980s, rapid urbanization has occurred in parts of South China, particularly in the GBA, which has evolved into one of the world's largest mega-city clusters. Figure 1.1 illustrates the expansion of urban areas in the GBA during 1988, 1999, and 2010 (You et al., 2019), with low-density residences, high-density residences, and industrial and commercial areas represented by brown, yellow, and red shading, respectively. The northwestern and eastern parts of the city have experienced especially rapid urban growth. Figure 1.2 provides a detailed overview of urban development in the GBA, revealing that built-up areas (urban ratio) increased from 500 km² (5%) to 6,000 km² (15%) between 1990 and 2015, accompanied by an approximately 80% rise in urban population density (Wu et al., 2019). Given this rapid urban development, it is crucial to examine its potential

impact on the local climate over the GBA.

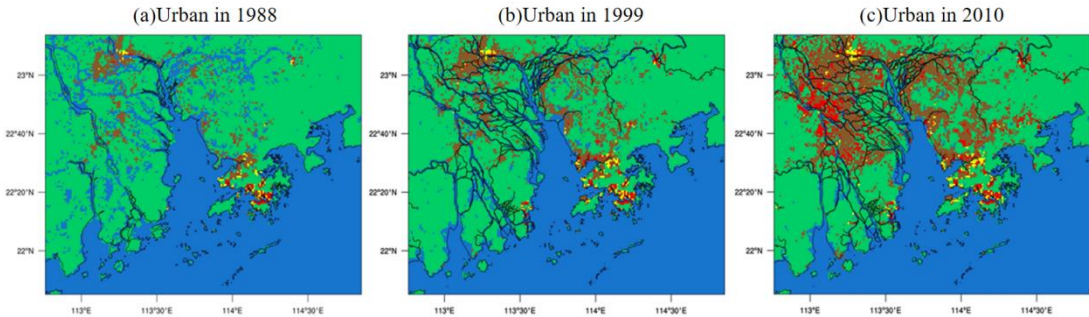


Figure 1.1 GBA urban area in (a) 1988, (b) 1999, and (c) 2010. Brown, yellow, and red shaded represent the Low-Density Residence, High-Density Residence, and Industrial and Commercial. (Source: You et al., 2019).

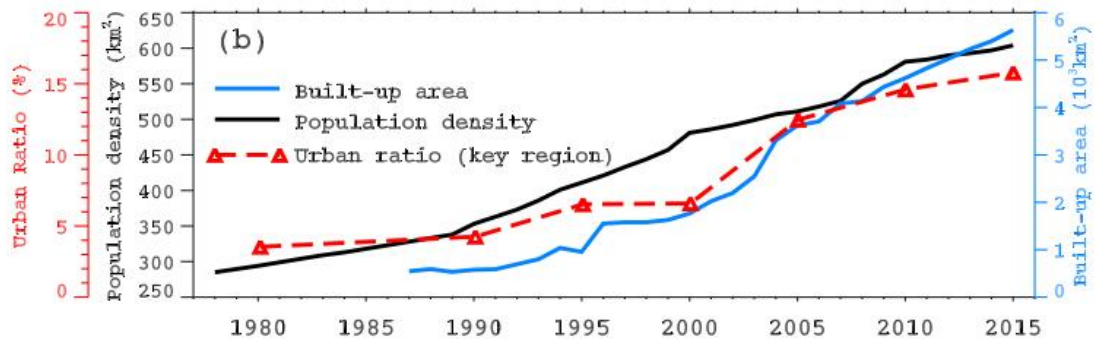


Figure 1.2 Annual change of built-up area, population density, and urban ratio in GBA mega-city from 1980 to 2015. (Source: Wu et al., 2019).

1.2 Urban climate

1.2.1 Urban morphology

Urbanization dramatically alters the local atmospheric environment through changes in land surface properties and anthropogenic emissions, particularly within the planetary boundary layer (PBL). Firstly, the conversion of natural surfaces to solid, impervious materials with distinct thermal properties results in higher surface temperatures and reduced evaporation (Bornstein, 1968; Oke, 1988). Urban land surfaces exhibit lower albedo compared to natural land

use (Ouyang et al., 2022), leading to decreased short-wave radiation reflectance and increased long-wave radiation absorption, ultimately enhancing surface temperatures (Jacobs and Delaney, 2015). Impervious urban surfaces elevate surface temperatures by increasing sensible heat flux (Kuang et al., 2017; Dai et al., 2019). Additionally, the complex building structures and materials in urban areas possess greater heat capacity and lower thermal conductivity (Osmond, 2016; Soltani and Sharifi, 2017), enabling heat storage and slow release, particularly at night during hot summers.

Secondly, the three-dimensional building structures in urban areas significantly alter wind flow, typically reducing wind speed and increasing frictional drag due to heightened surface roughness caused by variations in building heights and distances (Liu et al., 2018; Chen et al., 2020; Coceal and Belcher, 2004; Hou et al., 2013). The complex urban structure also generates greater turbulence, strongly impacting air ventilation and facilitating the exchange of hot, polluted surface and low-level air with cooler, cleaner air from higher altitudes (Ludwig and Dabberdt, 1973; Zhang et al., 1991; Ren et al., 2019).

Furthermore, urbanization substantially modifies local surface energy budget characteristics. Figure 1.3 demonstrates the diurnal variation of energy balance components in urban (a) and rural (b) areas in Vancouver during 30 summer days in 1983 (Cleugh and Oke, 1986). Urbanization reduces latent heat flux, which may lower convective available potential energy (CAPE) (Guo et al., 2006; Zhang et al., 2009), due to decreased natural water vapor release (evapotranspiration) from impervious urban surfaces (Mazrooei et al., 2021). This reduction results in weakened humidity in urban areas (Doan et al., 2016). Sensible heat flux is also markedly enhanced in urban areas compared to rural areas, with a slightly delayed peak.

Increased storage heat flux into building fabric occurs during the daytime in urban areas, with the stored heat released at night. Net heat flux increases during the day due to decreased short-wave radiation reflectance and increased long-wave radiation absorption (Jacobs and Delaney, 2015).

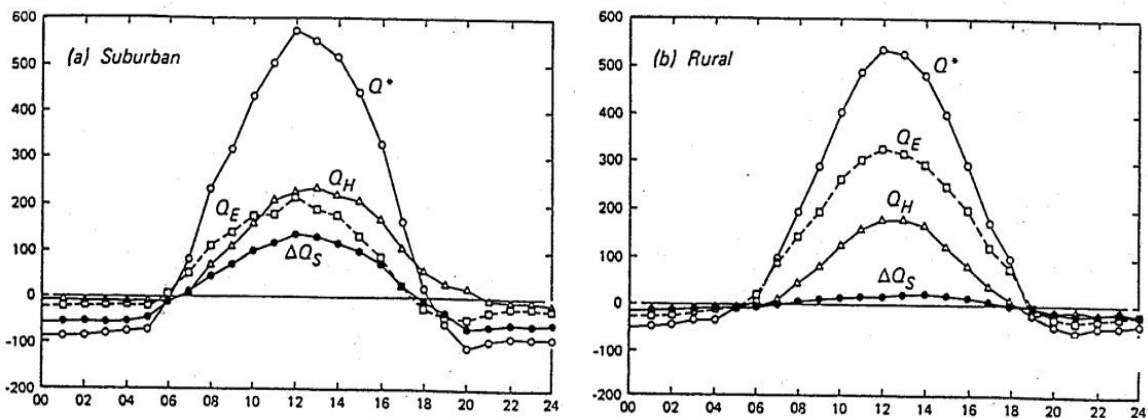


Figure 1.3 Diurnal variation of energy balance components in (a) urban, and (b) rural areas in Vancouver for 30 summer days in 1983 (Source: Cleugh and Oke, 1986).

Anthropogenic heat (AH), generated by human activities, transportation systems, industrial processes, and air conditioning, significantly influences local climate (Shahmohamadi et al., 2011; Wang et al., 2021). Numerous studies have demonstrated that AH can substantially enhance surface temperature, humidity, and precipitation in urban areas (Holst et al., 2017; Fung et al., 2021; Hu et al., 2021). Moreover, increased greenhouse gas emissions from anthropogenic activities exacerbate climate change, a major global concern in recent years (Raymond et al., 2016; Sheffield and Wood, 2007; Hsu et al., 2012).

1.2.2 Urban Heat Island (UHI) effect

Howard (1833) first observed a warming effect in London, which he attributed to urban density and development driven by population growth and combustion. Subsequent studies revealed an air temperature difference between urban and rural areas across various cities (Hann,

1885; Redway, 1919; Gordon, 1921). The UHI effect is now a well-known and widely studied phenomenon, with researchers identifying several key characteristics: (1) the UHI's magnitude varies with urban factors such as form and population density, (2) it is stronger under calm, stable, clear, and dry weather conditions, (3) it reduces the diurnal temperature range due to increased nighttime minimum air temperatures, and (4) a temperature gradient exists from the urban center to surrounding rural areas, with the highest temperatures in the city core (Kayane, 1960; Chandler, 1965; Oke et al., 1973; Oke et al., 2017; Stewart, 2011; Erell et al., 2011; Ramírez-Aguilar et al., 2019). The UHI effect is highly sensitive to weather conditions, with low wind speeds and cloud-free conditions leading to stronger nocturnal UHI intensities. The effect tends to be significantly higher under calm and stable synoptic backgrounds, such as anticyclonic weather (Arnds et al., 2017; Ivajnšič and Žiberna, 2019). Cloud cover and fog, on the other hand, result in lower UHI magnitudes (Bokwa et al., 2018). Figure 1.4 demonstrates an example of the UHI, showing a gradual decrease in temperature from downtown areas to residential, suburban, and rural areas. Factors contributing to this temperature difference include heat-retaining dark roads, rooftops, and asphalt surfaces, reduced shading and evapotranspiration due to less vegetation, and AH sources causing strong warming in urban areas. Furthermore, the UHI can also alter local climate conditions, with heat being advected by wind to downstream areas and warming downwind rural areas (Heaviside et al., 2015). Research has shown that the UHI effect can influence the development of clouds and fog (Sachweh and Koepke, 1995), change local atmospheric stability and the frequency of lightning strikes (Jin et al., 2015; Orville et al., 2001), and affect local convection and precipitation (Holst et al., 2017; Hu et al., 2021).

Urban Heat Island Effect

Urban cores retain heat for a variety of reasons, creating a heat island effect. Canadian researchers illustrated the differences between rural areas, leafy neighborhoods and downtown areas with the following summer example.

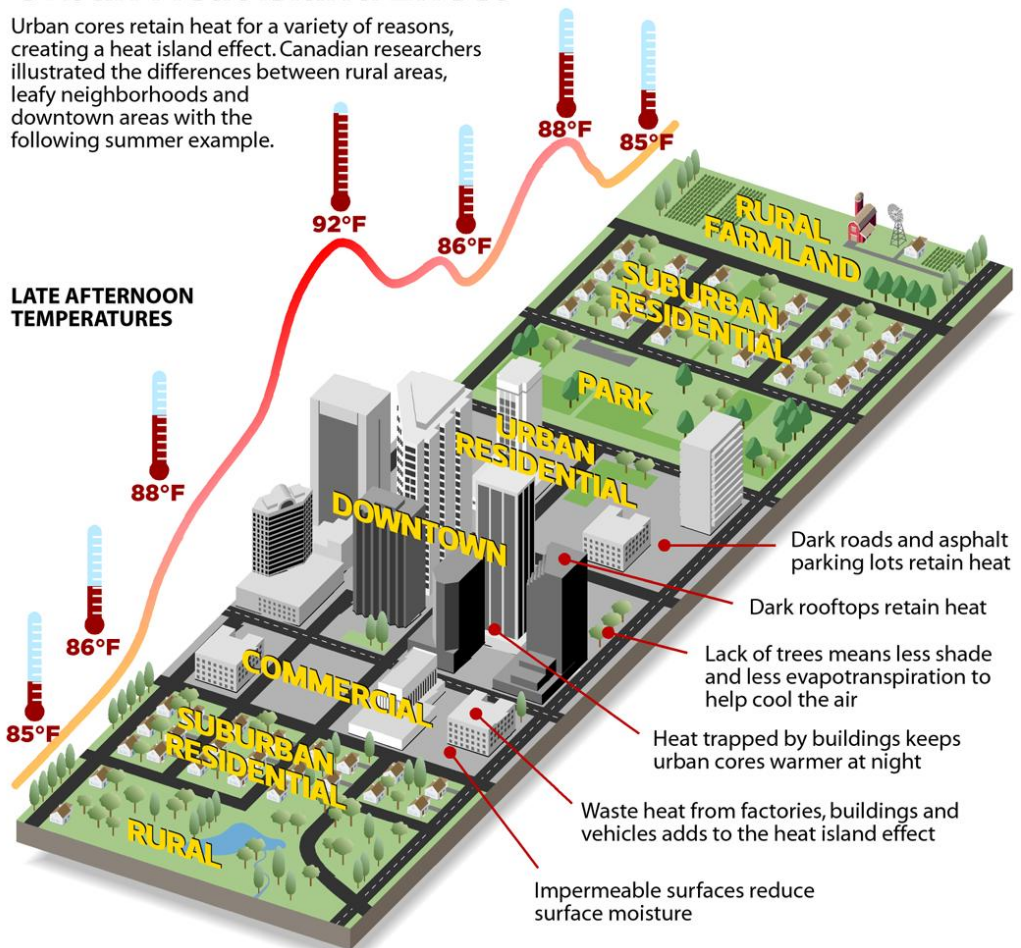


Figure 1.4 How UHI occurs. (Source: D.S. Lemmen and F.J. Warren, Climate Change Impacts and Adaptation).

1.2.3 Aerosols

Aerosols, particularly those of anthropogenic origin, have an intricate influence on local climate and precipitation patterns. Urban areas, with their significant pollution emissions and diverse human activities, release a substantial quantity of aerosol particles into the atmosphere (Lin et al., 2021; Miao et al., 2017). These aerosols serve as cloud condensation nuclei (CNN) and also ice nuclei (IN) in the process of cloud, influencing cloud microphysics by modulating the size and number of cloud droplets, and potentially intensifying rainfall (Andreae and Rosenfeld, 2008).

The impact of aerosols on cloud formation is contingent on the type of cloud. For warm clouds

which are composed entirely of water droplets at temperature above freezing, aerosols tend to result in more but smaller water droplets, thereby delay the coalescence of droplets and potentially suppress precipitation (Twomey, 1974; Albrecht, 1989). In contrast, for cold clouds consist of both ice particles and water, the aerosols can act as ice nuclei and augment precipitation (Rosenfeld and Woodley, 2000; Khain et al., 2005; Creamean et al., 2013; Fan et al., 2018).

Moreover, urban areas, owing to their dense populations and considerable industrial activities, are significant sources of anthropogenic aerosols, including sulfates, nitrates, organic aerosols, and black carbon (Lin et al., 2021; Miao et al., 2017). These anthropogenic aerosols interact differently with the local climate compared to natural aerosols such as sea salt and dust. For instance, sulfate (nitrate) aerosols generated from sulfur dioxide (nitrogen oxides) and fossil fuel combustion tend to generate smaller and more numerous cloud droplets, which can suppress precipitation (Rosenfeld et al., 2008; Seinfeld and Pandis, 2016). The impact of organic aerosols on precipitation is complex, with potential for both intensifying convection precipitation over South China and significantly decreasing rainfall intensity due to enhanced sinking motion and decreased atmospheric humidity (Change, 2014; Yang et al., 2023). Furthermore, black carbon (BC), produced from combustion of fossil fuels and biomass, can strongly absorb solar radiation and warm the atmosphere (Ming et al., 2010), decrease downward solar radiation (Ramanathan and Carmichael, 2008), and strongly suppress precipitation in short-term duration. Nevertheless, the decrease in rainfall can be mitigated over longer timescales by surface warming induced by BC (Sand et al., 2020).

While certain aerosols can exert a cooling effect and thus reduce urban surface temperatures (Wang et al., 2018), others can enhance the UHI effect. This intensification of UHI

can be primarily attributed to (1) aerosol absorption of both incoming solar radiation and outgoing long-wave radiation (Ramanathan et al., 2001); (2) Formation of haze and smog trap heat within urban areas (Jacobson, 2001); (3) low albedo aerosols, such as BC, which can increase local temperatures and thereby strengthen UHI intensity (Crutzen, 2004); (4) complex aerosol impacts on cloud microphysics, which can further influence UHI intensity. By exacerbating the UHI effect, aerosols can indirectly modify local precipitation patterns, particularly in urban environments. There is also evidence that the UHI effect intensifies sea breeze in coastal cities, which accelerates the transition from warm cloud to mixed-phase cloud, and the aerosol effect significantly enhances precipitation (Fan et al., 2020).

1.3 Impact of urbanization on precipitation

Urbanization's influence on precipitation has become a major concern and a hot research topic due to rapid urban development in recent decades. Pioneer work by Changnon (1968) reported intensified precipitation downwind of Chicago due to urban growth. The Metropolitan Meteorological Experiment (METROMEX) found that summertime extreme rainfall increased by about 30% to 100% downwind of St. Louis, indicating urbanization can enhance precipitation downstream of urban areas (Huff and Changnon, 1986). Shepherd and Burian (2003) also found the strongest annual mean precipitation downwind of Houston using Tropical Rainfall Measuring Mission (TRMM) data from January 1998 to May 2002. A summary provided by Lin and Niyogi (2019) about urban impact on rainfall, results from 85 studies in a quantitative meta-analysis assessment indicate that urbanization strongly enhances rainfall mainly in urban and downstream areas, with rainfall increasing by about 16% and 18%.

1.3.1 Urban impacts on rainfall in inland cities

As mentioned earlier, the influence of urbanization on precipitation is complex and highly sensitive to geographical location. In some inland cities, urbanization may decrease rainfall intensity in urban areas but enhance it in downstream areas (Hand and Shepherd, 2009; Mote et al., 2007; Schlünzen et al., 2010; Liu et al., 2021). Factors contributing to this effect include the urban dry island (UDI) effect, which results from reduced evaporation and water vapor due to impervious urban land surfaces, and a decrease in CAPE (Bornstein, 1968; Oke et al., 1988; Guo et al., 2006; Zhang et al., 2009; Hao et al., 2019; Du et al., 2019). However, other research has found increased precipitation over inland cities compared to surrounding rural areas (Schmid and Niyogi, 2013; Zhu et al., 2017). Research also indicates that precipitation variation is sensitive to the intensity of the urban heat island (UHI) effect. Numerical modeling outputs show that during weak UHI events, rainfall bifurcates and avoids the city center (Dou et al., 2015; Zhang et al., 2017), consistent with studies demonstrating the urban barrier effect, which divides rainstorms and causes them to move around the city (Bornstein and Lin, 2000; Yue et al., 2019), leading to lower rainfall in urban areas. Conversely, rainfall can increase directly in urban areas during strong UHI events for inland cities such as Beijing and Paris (Dou et al., 2015; Zhang et al., 2017; Steensen et al., 2022). Figure 1.5 presents examples of normalized total rainfall amounts averaged over the summer from 2008-2012 in Beijing under weak and strong UHI situations, with arrows representing the direction of 850 hPa winds and Beijing city outlined in red. It is evident that rainfall decreases in cities during weak UHI cases, which is consistent with observations in New York City (NYC) that moving thunderstorms were bifurcated by the city due to building barrier effect (Bornstein and Lin, 2000). But rainfall center directly occurs in Beijing urban areas during strong UHI cases.

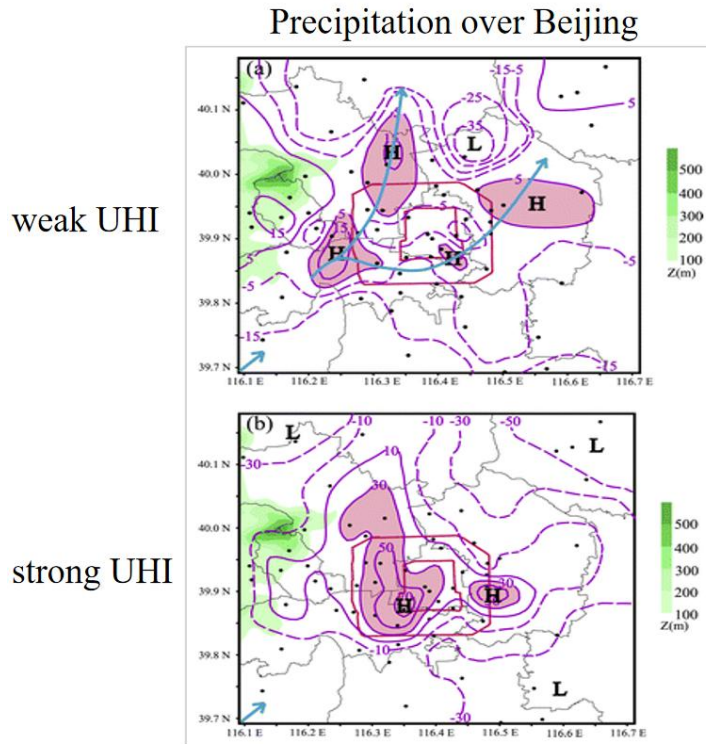


Figure 1.5 Summer total rainfall amounts averaged from 2008-2012 in Beijing under weak and strong UHI situations. (Source: Dou et al., 2015).

1.3.2 Urban impacts on rainfall in coastal cities

In contrast, urbanization's influence on precipitation in coastal cities exhibits distinct differences from inland regions. Numerous observational and numerical modeling studies have investigated the impact of urbanization on precipitation in coastal cities, employing reanalysis data and numerical models such as Weather Research and Forecasting (WRF) and uSINGV model. These studies have focused on diverse locations, including the Yangtze River Delta (East China), Pearl River Delta (South China), Houston (US), Osaka, Tokyo (Japan), Singapore, Chennai (India), the Michigan region, and idealized cities. The consensus among these studies is that urbanization strongly enhances extreme rainfall directly in urban areas, which can be attributed to reduced atmospheric stability, intensified convection induced by the UHI, and increased water vapor supply due to enhanced moisture flux convergence (Burian and Shepherd, 2005; Yan et al.,

2020; Kusaka, 2014; Shimadera et al., 2015; Pulipati et al., 2022; Yang et al., 2014; Zhang et al., 2018; Lu et al., 2019; Doan et al., 2020; Simón-Moral et al., 2021). Though surface water vapor content decreases, the ocean plays a crucial role in augmenting rainfall in coastal cities by providing an enhanced atmospheric water vapor source. A study focused on Tokyo, Japan (Kusaka et al., 2014), illustrated this point by examining the urban impacts on coastal rainfall, with precipitation in the metropolitan area increasing alongside urbanization levels, primarily due to the strongly enhanced moisture flux towards urban areas supplied by the ocean (Figure 1.6).

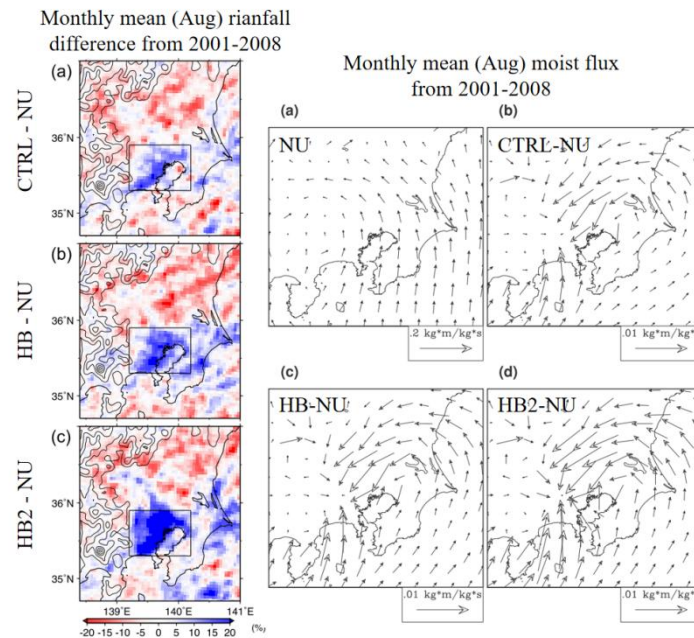


Figure 1.6 (Left panel) August monthly average 2001-2008 rainfall difference between experiments in Tokyo. (Right panel) August monthly average 2001-2008 moist flux and difference (Source: Kusaka et al., 2014).

1.3.3 Studies focus on the GBA mega-city

The GBA, which has experienced rapid urban development since the 1980s, has been the subject of numerous studies investigating the urban impacts on extreme rainfall. Observational and reanalysis data reveal a significant increase in extreme rainfall in the GBA from the 1970s to the present, with intensity increasing by more than 5% per decade (Meehl et al., 2007; Zhang et al.,

2009; Wong et al., 2011; Yang et al., 2019; Wu et al., 2019). Rapid urbanization is considered a primary driver of this trend (Meng et al., 2020; Yan et al., 2020; Wang et al., 2015; Wai et al., 2017; Zhang et al., 2017), particularly in major GBA cities such as Guangzhou (Liao et al., 2011; Wu and Huang, 2016; Chen et al., 2017). By examining the time series of precipitation amount, precipitation frequency, intense rainfall frequency, and extreme precipitation frequency from 1981 to 2015 derived from 15 (9) urban (rural) observational stations, Yan et al. (2020) found increasing trends in precipitation amount and intense rainfall frequency at urban stations, while rural areas experienced a decreasing trend in precipitation amount and a weaker increase in intense rainfall frequency (Figure 1.7). Observations also indicate that the UHI effect is the main factor leading to a significant enhancement of hourly extreme rainfall in GBA mega-cities (Sun et al., 2021). The positive effect of urbanization on rainfall is closely associated with abrupt and short-duration rainfall events (shorter than six hours), but relatively weaker for continuous and long-duration rainfall events (Wu et al., 2019).

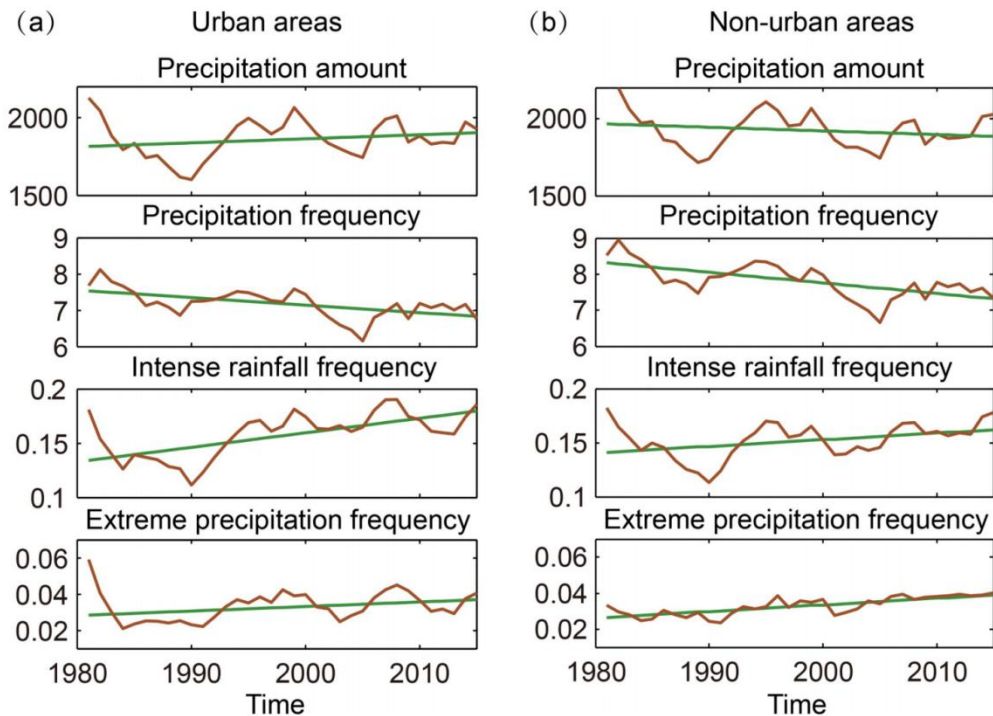


Figure 1.7 Annual trend of precipitation intensity (mm), precipitation frequency (%), intense rainfall frequency (%), and extreme precipitation frequency (%) from 1981 to 2015 for (a) urban and (b) rural areas. (Source: Yan et al., 2020).

Numerical modeling results corroborate that urbanization can significantly increase extreme rainfall in the GBA (Wang et al., 2014; Wu et al., 2016; Holst et al., 2016; Fung et al., 2021; Li et al., 2021; Hu et al., 2021; Hu et al., 2023). These models also suggest that the enhanced extreme rainfall in the GBA is highly sensitive to the AH magnitude and is primarily induced by the UHI (Wang et al., 2014; Holst et al., 2016; Fung et al., 2021; Sun et al., 2021; Zhang et al., 2019), with the ocean playing a critical role in supplying water vapor. Notably, the increased rainfall in GBA mega-cities is highly sensitive to the direction of prevailing winds (Hu et al., 2021). Hu et al. (2023) employed the WRF model to dynamically downscale 30 cases with 1999 GBA urban land use and predicted 2030 near-future urban land use, finding a 13.5% increase in accumulated rainfall due to urban development in GBA mega-cities. This increase is comparable to the rise in rainfall induced by near-future global warming effects. Additional studies have identified surface roughness effects and aerosol emissions as factors contributing to stronger rainfall in the GBA (Miao et al., 2011; Xiao et al., 2014; Lan et al., 2015). However, most of these studies focused on the summer monsoon period and local convective extreme rainfall (Li et al., 2021; Hu et al., 2021; Li et al., 2011; Cheng et al., 2012). Although some research has addressed single case studies for frontal rainfall (Wen et al., 2020), the impact and underlying mechanisms of urbanization on rainfall under different weather systems in the GBA remain unclear and present a significant challenge.

1.4 Observation and reanalysis data

1.4.1 Rain gauge-based datasets

This study utilizes in-situ observation datasets to investigate the urban impact on precipitation in the GBA and evaluate the WRF model's simulated rainfall in the SC region. The station-based observation data, developed by the National Meteorological Information Center of the Chinese Meteorological Administration (CMA), provides hourly parameters such as precipitation, surface temperature, surface relative humidity, surface pressure, surface wind, and evaporation. The dataset comprises 86 stations in the SC region with data from January 2008 to December 2017 (see Figure 1.8).

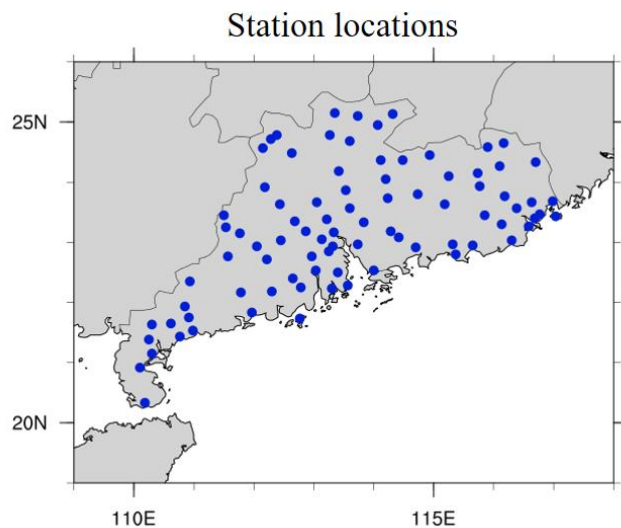


Figure 1.8 Location of 86 observation stations over South China.

1.4.2 TRMM 3B42 product

To examine urban impacts on TC precipitation and evaluate model performance, this study also employs the Tropical Rainfall Measuring Mission (TRMM) 3B42 dataset (Huffman et al., 2014), a joint satellite mission between the National Aeronautics and Space Administration (NASA) and the Japan Aerospace Exploration Agency (JAXA). TRMM 3B42 is a widely used product for researching spatial-temporal distribution and variability of tropical precipitation, combining satellite and rain gauge data. The dataset covers latitudes between 50°S and 50°N with a spatial grid spacing of $0.25^{\circ} \times 0.25^{\circ}$ (approximately 25 km x 25 km) and a temporal resolution of

3 hours from 1998 to 2018.

1.4.3 Best Track datasets

The Hong Kong Observatory's best track data is utilized to select historical TCs and evaluate the track and intensity of WRF-simulated TCs. This data is part of the International Best Track Archive for Climate Stewardship (IBTrACS), which is a comprehensive global collection of TCs with global TC data from many agencies (Knapp et al., 2010; Knapp et al., 2018). Developed by the World Meteorological Organization (WMO) Regional Specialized Meteorological Center and other organizations worldwide, IBTrACS provides maximum sustained wind speed, minimum central sea level pressure, and storm center of circulation. The dataset covers latitudes between 70S and 70N with a spatial grid spacing of $0.1^\circ \times 0.1^\circ$ (approximately 10 km x 10 km) and a temporal resolution of 3 hours (mostly reported at 6-hour intervals) from 1841 to the present.

1.4.4 ECMWF reanalysis datasets

For circulation variables like temperature and wind, this study uses two sets of global atmospheric reanalysis data from the European Center for Medium-Range Weather Forecasts (ECMWF) to analyze the synoptic background for extreme cases and provide initial boundary conditions for the WRF simulations. In part one of this research (see Chapter 2), the ERA-Interim reanalysis data (Dee et al., 2011) is employed as the initial boundary conditions for dynamical downscaling, which proposes to improve the performance of the previous ERA-40 reanalysis data in aspects such as the hydrological cycle (Berrisford et al., 2011). ERA-Interim covers global atmospheric observation parameters from January 1979 to August 2019 with a spatial resolution of $0.75^\circ \times 0.75^\circ$, 37 vertical levels, and a 6-hour temporal resolution. For synoptic analysis and model initial boundary conditions in parts two and three of this study (see Chapter 3 and Chapter

4), ERA5 reanalysis data (Herbsbach et al., 2020; Bell et al., 2021) is used. Produced by the Copernicus Climate Change Service (C3S) at ECMWF, ERA5 is the fifth-generation global climate and weather reanalysis. The reanalysis system uses ECMWF's atmospheric model Integrated Forecast System (IFS), which is coupled with other components such as ocean, sea ice, and land surface models. It covers hourly parameters of atmospheric, land, and oceanic climate variables from January 1940 to the present, with a 30 km spatial resolution, 137 pressure levels, and a 1-hour temporal resolution.

1.5 Dynamical downscaling

Dynamical downscaling is a method that utilizes high-resolution Regional Climate Models (RCMs) to derive detailed regional climate information by incorporating lower-resolution data, such as General Circulation Model (GCM) outputs and reanalysis data, as initial boundary conditions while adhering to physical principles (Giorgi et al., 2009; Fu et al., 2005; Xu et al., 2019; Gutowski, 2020). RCMs are adept at integrating climate information, including surface heterogeneities, land-sea contrasts, and complex topography, resulting in a more accurate regional circulation computation (Bao et al., 2015). It is commonly acknowledged that RCMs possess superiority compared to GCMs when it comes to temperature and precipitation simulations, due to their enhanced resolution and improved representation of crucial physical mechanisms (Nobre et al., 2001; Gao et al., 2006). Consequently, RCMs have become essential tools for simulating historical climate and predicting future changes (Fung et al., 2021; Wang et al., 2021; Hu et al., 2023). For instance, Figure 1.9 demonstrates the spatial distribution of seasonal mean precipitation in China using observations, R2 reanalysis data, RegCM4, and WRF downscaling simulations (Guo, 2020). Observations reveal a southeast-north temperature gradient for all

seasons, with a prominent warm center in central China during summer. In contrast, the coarse grid of reanalysis data inadequately captures both the distribution and intensity of temperature, particularly in the summer season. The application of dynamical downscaling using the WRF model yields a finer mesh for China, leading to a more distinct north-south temperature gradient with temperature values more closely aligned with observational data. Consequently, dynamical downscaling proves to be an invaluable technique for climate research, enhancing the reliability and accuracy of climate data analysis.

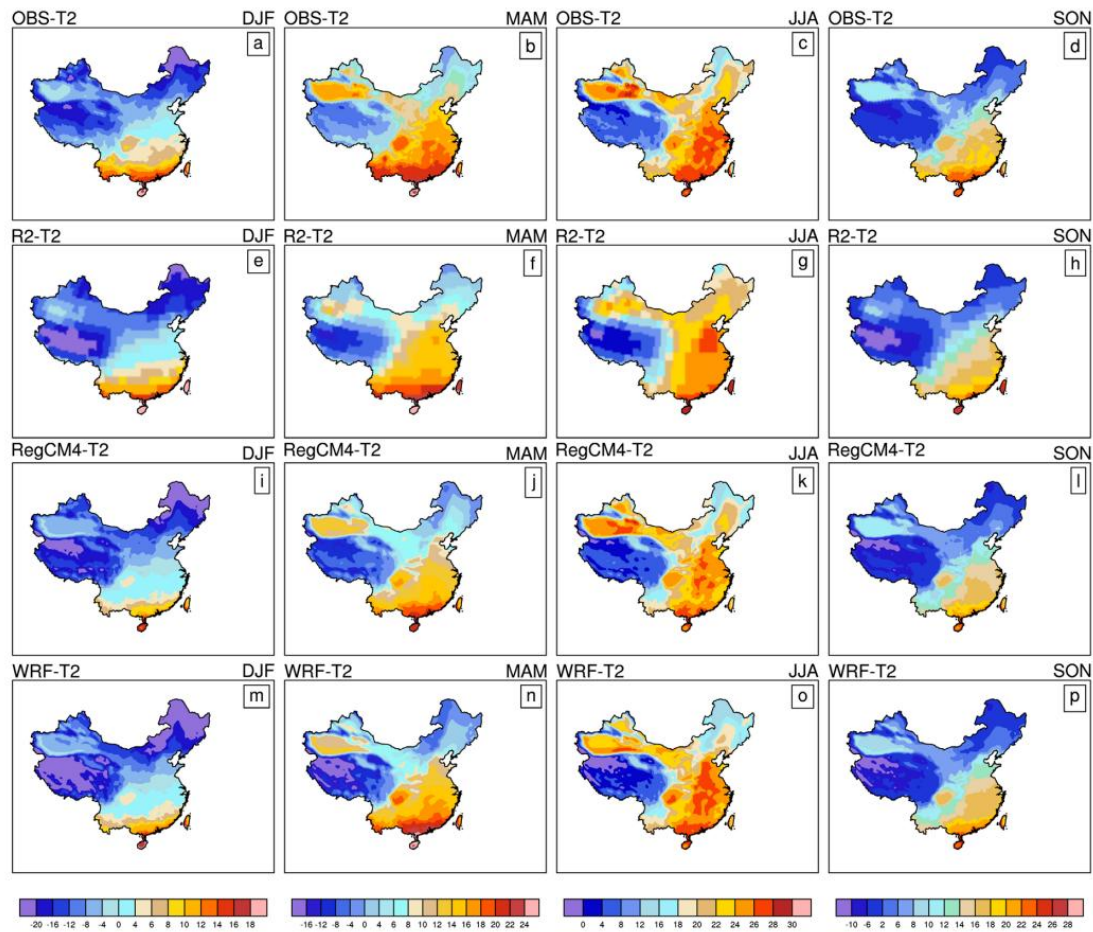


Figure 1.9 Distributions of surface temperature (units: $^{\circ}\text{C}$) in different seasons from 1981 to 2010 from (a-d) Observations, (e-h) R2 reanalysis, (i-l) RegCM4, and (m-p) WRF downscaling simulations. (Source: Gao, 2020).

1.6 Numerical model

1.6.1 The Weather Research and Forecasting (WRF) model

The WRF Model is a meso-scale numerical tool used for atmospheric research and forecasting, with a spatial grid spacing ranging from hundreds of meters to tens of kilometers. Developed collaboratively by the National Center for Atmospheric Research (NCAR), National Centers for Environmental Prediction (NCEP), Earth System Research Laboratory, U.S. Air Force, Naval Research Laboratory, University of Oklahoma, and Federal Aviation Administration (FAA), the WRF model has become a vital resource in the field of atmospheric science (Kusaka 2014; Shimadera et al., 2015; Zhang et al., 2017; Holst et al., 2017; Fung et al., 2021; Hu et al., 2023). The WRF model comprises two dynamical cores, a data assimilation system, and supports parallel computation and system extensibility. It is widely employed for dynamical downscaling of climate, utilizing initial boundary conditions derived from observations, reanalysis data, GCMs, or idealized conditions. The model's versatility allows it to generate numerical simulations of atmospheric conditions and offer flexible forecasting capabilities. The Advanced Research WRF (ARW) incorporates a diverse array of physical schemes to reproduce atmospheric conditions accurately. These schemes include microphysics, PBL physics, cumulus parameterization, longwave and short-wave radiation, land surface, surface layer, urban surface, and ocean model schemes, among others. Figure 1.10 presents a diagram illustrating the direct interactions of parameterizations within the WRF model framework.

Direct Interactions of Parameterizations

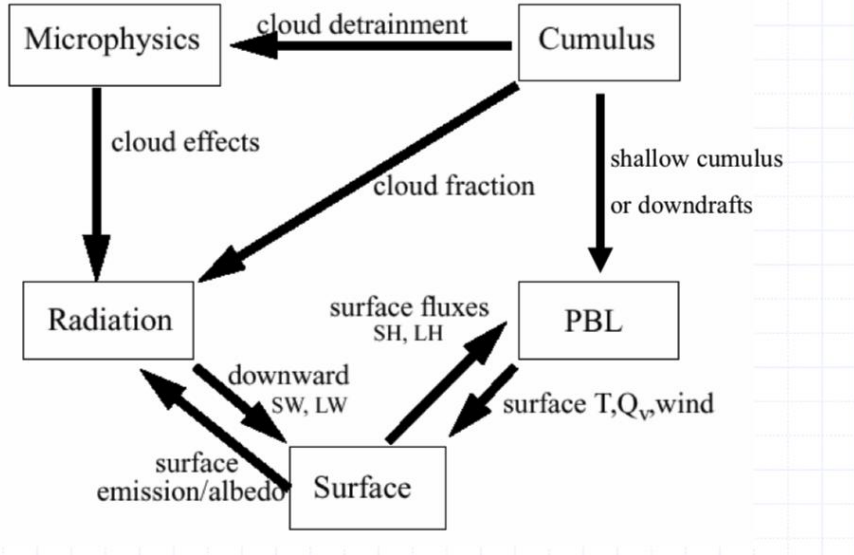


Figure 1.10 Direct interactions of parameterizations in WRF model.

1.6.2 Urban Canopy Model

The Single Layer Urban Canopy Model (SLUCM) is a single layer column model designed to parameterize urban heat and building effects, serving as a powerful tool for assessing the interactions between urban surfaces and the atmosphere (Kusaka et al., 2001; Kusaka and Kimura, 2004; Tewari et al., 2008). The UCM incorporates a three-dimensional radiation treatment that accounts for canyon orientation and the diurnal change of the azimuth angle. Capable of simulating energy and momentum exchanges between urban surfaces and the atmosphere, the UCM estimates the temperature of roofs, walls, and roads (Kusaka et al., 2001; Kusaka and Kimura 2004). It also captures the impacts of street canyons and parameterized urban geometry, effectively reproducing the diurnal cycle of urban temperature—typically hottest during daytime and coldest from nighttime to early morning. The UCM's straightforward parameterization enables its seamless integration into large-scale atmospheric simulations. Table 1.1 lists the parameters included in the Single Layer UCM, such as building height, standard

deviation of roof height, roof width, road width, AH, AH diurnal profile, urban fraction, heat capacity, thermal conductivity, and surface albedo, etc.

Parameter	Unit
Building height	m
Standard Deviation of roof height	m
Roof width	m
Road width	m
Anthropogenic heat	W m^{-2}
Anthropogenic heating diurnal profile	Fraction
Fraction of the urban	Fraction
Heat capacity of roof	$\text{J m}^{-3} \text{K}^{-1}$
Heat capacity of building wall	$\text{J m}^{-3} \text{K}^{-1}$
Heat capacity of road	$\text{J m}^{-3} \text{K}^{-1}$
Thermal conductivity of roof	$\text{J m}^{-1} \text{s}^{-1} \text{K}^{-1}$
Thermal conductivity of building wall	$\text{J m}^{-1} \text{s}^{-1} \text{K}^{-1}$
Thermal conductivity of road	$\text{J m}^{-1} \text{s}^{-1} \text{K}^{-1}$
Surface albedo of roof	Fraction
Surface albedo of building wall	Fraction
Surface albedo of road	Fraction
Surface emissivity of roof	-
Surface emissivity of building wall	-
Surface emissivity of road	-

Table 1.1 Parameters included in SLUCM.

1.7 Motivation and objectives

Rapid urban development has been observed worldwide, with significant impacts on local climate, temperature, circulation, and precipitation. These changes can further contribute to extreme weather events and related hazards, such as heatwaves, intense rainfall, and flooding disasters (Wang et al., 2021; Hu et al., 2021; Blum et al., 2020). In the GBA, public concern has grown regarding whether accelerated urban development may lead to increased precipitation. Previous studies have employed both observational data and numerical modeling to investigate this question, revealing that urbanization can indeed enhance precipitation in the GBA (Wang et al., 2015; Wu et al., 2018; Yan et al., 2020; Holst et al., 2016; Hu et al., 2021; Fung et al., 2021).

To our knowledge, the majority of research works have focused on the impact of urbanization on monsoon (summertime) precipitation in the GBA, excluding the influence of TC systems, such as local convection induced thunderstorms. However, as a coastal mega-city located within the East Asian monsoon region, the GBA experiences considerable rainfall due to TC storms, as well as elevated precipitation rates during winter and spring—seasons that extend beyond the summer monsoon. Additionally, the specific effects of urbanization on extreme rainfall induced by different weather systems and synoptic backgrounds remain unclear. Consequently, it is crucial to explore and comprehend how urbanization might affect extreme rainfall across various seasons and weather systems, thereby enhancing preparedness and disaster mitigation strategies in recent decades. To address these research gaps, this thesis employs long-term climate statistics, case studies, station observations, and a convection permitting WRF regional model.

The study aims to achieve the following objectives:

- Investigate the impact of urbanization on TC-induced extreme precipitation in the GBA mega-city, comparing the effects of UHI and urban surface land use on TC extreme rainfall.
- Examine the influence of urbanization on winter precipitation, assessing whether the UHI effect also contributes to extreme winter rainfall in the GBA mega-city.
- Analyze how urbanization affects GBA extreme rainfall during the pre-monsoon period and whether this impact varies under different synoptic backgrounds.

Several challenges arise when investigating these topics, including the performance of the WRF model on path and intensity of TC, synoptic background, and rainfall, which may affect

the reliability of results. Techniques such as the bogus method, spectral nudging, and ensemble approaches are employed in model simulations to reduce model bias and uncertainties. While initial results are derived from station observations, these data may be influenced by various factors, undermining their robustness. As a result, this thesis combines observational data with model-based sensitivity experiments, utilizing observations to guide further exploration of the effects and mechanisms identified in sensitivity tests. This integrative approach bolsters the credibility and persuasiveness of the findings, enabling a deeper understanding of the impact of urbanization on precipitation in the GBA under different weather systems.

1.8 Roadmap of thesis

This thesis investigates the impacts of urbanization, including urban land use and AH, on extreme rainfall in the GBA under different seasons and weather systems, using both observational data and the regional WRF-UCM. The thesis is organized into five chapters, with Chapters 2, 3, and 4 focusing on the influence of urbanization on tropical cyclone (TC) extreme rainfall, winter extreme rainfall, and pre-monsoon extreme rainfall, respectively. Each chapter comprises an introduction, methodology, results, and a brief summary of the corresponding study. Chapter 5 encompasses the main conclusions and research outlooks.

Chapter 2 examines the impact of urbanization on TC extreme precipitation in the GBA mega-city, utilizing station observations and WRF-UCM numerical modeling. A total of 41 TCs (occurring between June and October) were selected from the Hong Kong Observatory's best track data. Changes in temperature, wind speed, and rainfall characteristics during TC passage were identified for urban and rural locations based on station observations. Furthermore, 8 TCs were dynamically downscaled using WRF with different experiments, and the responses of rainfall

extremes to urban land use and AH were assessed. The moisture budget equation was employed to quantify the thermal-dynamical and dynamical terms of moisture flux convergence differences, revealing the sensitivity of rainfall intensity and probability to these two factors. Finally, the relationship between urban impacts on TC rainfall and storm duration time was explored.

Chapter 3 investigates the potential impacts of urbanization on extreme winter rainfall in the GBA mega-city. Winter extreme rainfall characteristics, such as intensity and frequency, were analyzed based on observational data, and case study was conducted to explore the UHI effect on winter extreme rainfall. Additionally, urban impacts on extreme rainfall in the GBA were estimated using parallel experiments with the WRF model. Two specific extreme rainfall events were dynamically downscaled, and the characteristics of rainfall, local convection, large-scale atmospheric circulation, and moisture flux divergence were examined to understand the contributions of urban land use and AH.

Chapter 4, similar to Chapter 3, focuses on extreme rainfall during the pre-monsoon period in the GBA. A 10-year climate dataset and case studies were used to reveal the urban influence on pre-monsoon extreme rainfall. Cases were further classified based on synoptic background, and the UHI effect on extreme rainfall characteristics was determined under different synoptic systems. Moreover, four frontal cases and four shear-line cases were numerically simulated in the GBA by WRF-UCM using four parallel experiments. The sensitivity of the corresponding rainfall extremes to urban land use and AH was investigated by analyzing local convection, circulation, convergence, and humidity variations.

Chapter 5 summarizes the main conclusions and presents research outlooks for future studies.

2. How Does Urbanization Affect Tropical Cyclone Rainfall Extremes-Inferences from Observations and Convection-Permitting Model Experiments over the South China Greater Bay Area

2.1 Introduction

TC is a powerful and well organized rotating system with strong winds and extreme rainfall, which is extremely dangerous and has become a major meteorological hazard in many subtropical coastal cities (Simpson and Starrett, 1955; Gray, 1986; Wang et al., 2013; Hon et al., 2022). It is well-known that the formation of TC is sensitive to environmental conditions like sea surface temperature (heat flux), vertical atmosphere motion, mid-level relative humidity (condensation), near surface vorticity (moisture convergence), vertical wind shear (ventilation), and Coriolis force (Ramsay, 2017). Moreover, the TC system is always related to extreme precipitation, which often results in inland flooding and causes huge life and economic losses (NOAA, 2020; Rappaport, 2014). The coastal SC area is one of the regions most frequently affected by TC, the annual mean number of storms passed through the SCS was 10.3 during 1969-1988 (Neumann, 1993), and such value decreased to only 9.2/year from 1981 to 2015 (Li et al., 2022). Moreover, the six highest records of 24h accumulated rainfall in SC are caused by TC (maximum reaches 1748.5mm; Chen et al., 2010; Chen et al., 2017), and the accumulated amount of TC rainfall is larger than 500mm/year, accounting for 20~40% of the total annual precipitation in SC (Ren et al., 2002; Ren et al., 2006). Results based on station observations reveal that urban area has stronger TC rainfall than surrounding rural area along the SC, and the trend of TC rainfall is keeping increasing since 1980 for both urban and rural locations (Yan et al., 2020). Considering the rapid urbanization process that the GBA has experienced in recent decades, it is a nice location

for investigating the relationship between urbanization and TC rainfall.

Studies revealed that the higher surface roughness could extend the time that rainfall system stays in urban, slow down surface wind speed which leads to low-level convergence, and enhance the local precipitation (Tan and Gu. 2015; Yue et al., 2019). On the other hand, there is already evidence that the surface roughness effect can enhance TC rainfall intensity. By using numerical simulation with land or water surface land use, results suggested that higher surface friction induces higher wind convergence at the lower troposphere, which enhances the convection and moisture flux convergence and thus results in higher TC rainfall intensity (Au-Yeung and Chan., 2010; Chan et al., 2019). Moreover, with the TC case being dynamically downscaled by the WRF model, results also indicated that urbanization can strongly enhance urban precipitation for TC Harvey and Lekima over Southeast US and East China, which can be attributed to the strongly enhanced local moisture flux convergence over the city (Zhang et al., 2018; Ao et al., 2022). By simulating three experiments in the WRF model, Zhang et al. (2018) found that urbanization increases both total storm rainfall and extreme flooding during TC Harvey in the period of 25-30 August 2017, with an increase in accumulated rainfall of more than 200mm/hr in the east of urban areas, which is attributed to the stronger wind convergence and convection due to urbanization. Numerical modeling results also indicated that urban development leads to higher flood risk related to TC over the SC area (Deng et al. 2022).

Moreover, as a mega-city cluster with substantial annual rainfall amounts, there is already a lot of research focusing on the urban influence on extreme rainfall over the GBA. Both observation and numerical modeling results indicated that the UHI effect can significantly enhance extreme precipitation not related to TC in GBA during summer (Wang et al., 2015; Wu et

al., 2019; Fung et al., 2021; Hu et al., 2021). However, results focusing on urban impacts on TC extreme rainfall is still lacking, more details and mechanism are waiting to be demonstrated in the GBA mega-city. In this work, we investigate: (1) how urbanization affects the TC extreme precipitation over the GBA mega-city, and (2) whether the effect of UHI and urban surface land use on TC extreme rainfall are comparable. This is done by (1) urban influence on SC precipitation during TCs based on station observations, and (2) dynamical downscaling of storms with a weather scale model at a convection-resolving resolution. Through various sensitivity experiments, we quantify changes in TC extreme rainfall due to the UHI effect and urban surface friction in the GBA. To our knowledge, this is the first study using a high-resolution convection-permitting model to examine the urban impact on GBA TC rainfall, specifically investigating the twin urban effect (UHI effect and urban surface frictional effect). Our findings, derived from both observations and model simulations, provide valuable insights into urban-atmosphere interactions and inform policymakers regarding urban TC-prevention planning and future public policies.

2.2 Methodology

2.2.1 TC case study based on observations

We used Hong Kong Observatory (HKO) best track data from 2007 to 2018 to identify storms that strongly influence the GBA (Knapp et al., 2010; Knapp et al., 2018). A total of 41 TCs were selected based on three criteria: (1) TC occurred in the extended summer season (June, July, August, September, and October, or JJASO); (2) the closest distance to the Guangdong province was within 500km; (3) TC affected period (the duration of TC staying within 500km of the coastline of Guangdong province) lasting at least 12 hours. Figure 2.1 shows the tracks of 41 TCs

affecting SC area. To investigate TC-related extreme rainfall, station observations taken from China Meteorology Administration (CMA) were utilized (86 stations over SC), which provide hourly precipitation, surface temperature, surface relative humidity, surface pressure, and surface U,V wind from January 2008 to December 2017. For GBA, seven urban and seven rural stations were further selected in the analysis. It is known that TC rainfall intensity is highly sensitive to the location, and typically stronger along the coast compared to inland areas. To minimize the error and uncertainties due to station location, rural stations near the SC coastline are considered. Locations of urban (red), rural (blue) and other stations (black) are given in Figure 2.1.

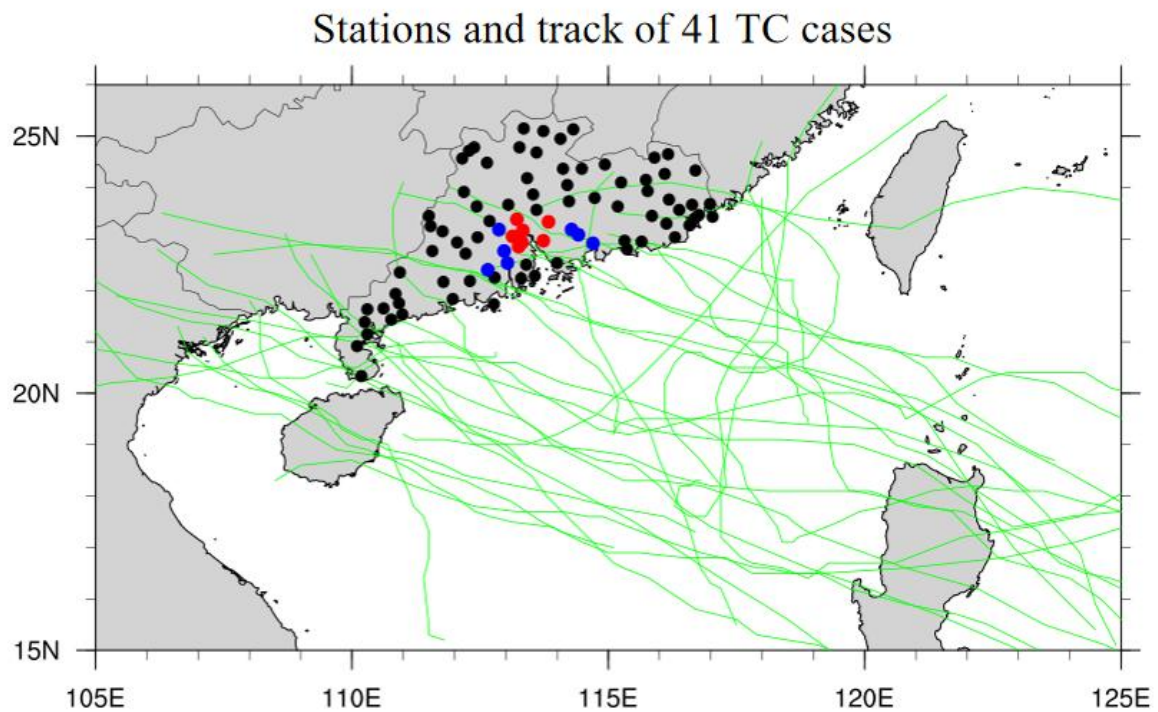


Figure 2.1 Location of observation stations over South China, with red (blue) dots representing 7 urban (rural) stations, other stations are shown in black dots. Green lines are the track of 41 TC cases.

2.2.2 WRF model configuration and TC cases

To further examine the sensitivity of TC precipitation to urbanization, the WRF model

with the ARW dynamical core version 3.8.1 (Skamarock et al., 2008) was used to dynamically downscale eight TC cases with boundary conditions from ERA-Interim (Berrisford et al. 2011). Nested domains of WRF (one-way nesting) are shown in Figure 2.2(a), with the outer domain ($9\text{km} \times 9\text{km}$ grid spacing) and the inner domain ($3\text{km} \times 3\text{km}$ grid spacing) encompassing the East Asia area (99-138E, 1-35N), and SC (106-125E, 13.8-26N), respectively. The model includes 39 vertical levels, reaching up to $\sim 23\text{km}$ in height. Physical parameterizations included the Rapid Radiative Transfer Model for General Circulation Model (RRTMG) for long-wave radiation (Iacono et al. 2008), the short wave radiation scheme by Dudhia (1989), the Eta (Ferrier) microphysics scheme (NOAA, 2001), the Revised MM5 scheme for the surface layer options (Jimenez et al. 2012), the NOAH land-surface model (LSM) (Niu et al., 2011; Yang et al., 2011), which supports the Single Layer Urban Canopy Model (SLUCM); (Kusaka et al., 2001; Chen and Dudhia, 2001; Tewari et al. 2008), the Yonsei University planetary boundary layer (PBL) scheme (Hong et al. 2006), and the grell 3D ensemble cumulus parameterization scheme used (Grell et al. 2002); (for the outermost domain only). To ensure that WRF can reproduce the same synoptic-scale circulation as in the driving data, spectral nudging was applied in the outermost domain for U, V wind above 500hPa, at the wavelength of about 1300km, which is commonly used in simulation (Gómez et al., 2017; Gómez et al., 2020). Moreover, TC bogus was used for initialization of adding an axisymmetric Rankine vortex in the observed location of the TC in the outermost domain (Ueno, 1995; Xiao et al., 2000; Xiao et al., 2006).

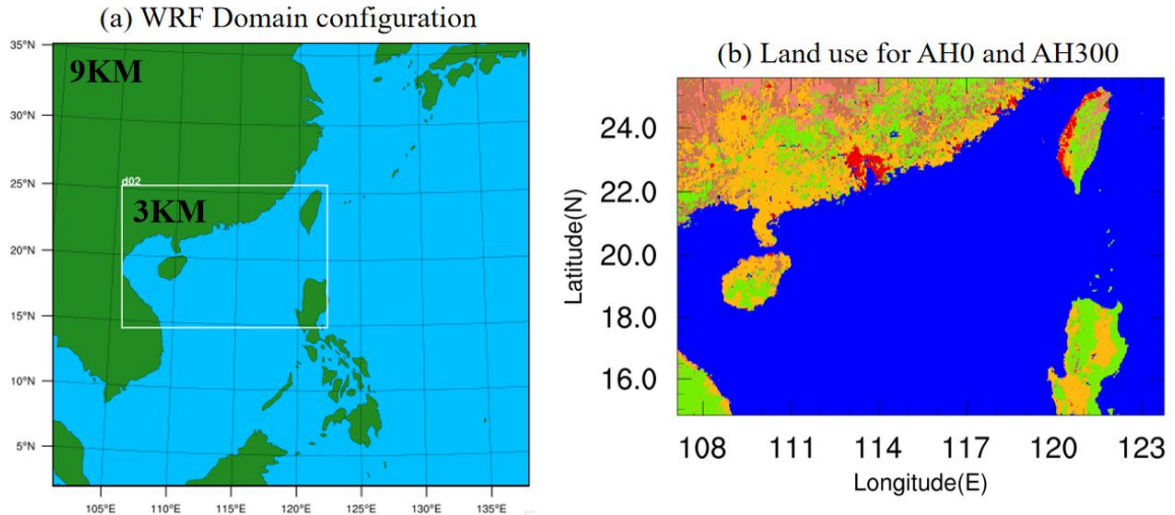


Figure 2.2 (a) Nested domains for the WRF simulations. (b) Land use categories in the innermost domain for AH0 and AH300 experiments, based on 2002 MODIS data with urban and build-up, cropland, forest and grassland showed areas in red, yellow, cyan and green.

Total eight storms, namely TC Victor (1997.7.31-1997.8.4), Utor (2001.7.3-2001.7.7), Dujuan (2003.8.30-2003.9.3), Mangkhut (2018.9.11-2018.9.17), Goni (2009.8.02-2009.8.07), Hal (1985.6.21-1985.6.26), Wanda (1962.8.28-1962.9.02), and York (1999.9.13-1999.9.17) were dynamically downscaled over the SC region to a grid spacing of $3\text{km} \times 3\text{km}$ and a 15-second timestep for the innermost domain (see table 2.1). These selected TCs met the following criteria: (1) TC landfall in the SC area, (2) substantial TC rainfall over the GBA mega-city, and (3) the simulation of TC track (determined by the location of minimum sea level pressure) in WRF is reasonable. For each storm, ensemble integration with three members was carried out, with different starting times at 6-hour intervals. And results were averaged across all members.

Name	Time	Name	Time
Victor	1997.7.31-1997.8.4	Wanda	1962.8.28-1962.9.02
Utor	2001.7.3-2001.7.7	Hal	1985.6.21-1985.6.26
Dujuan	2003.8.30-2003.9.3	York	1999.9.13-1999.9.17
Mangkhut	2018.9.11-2018.9.17	Goni	2009.8.02-2009.8.07

Table 2.1 Name and time period for each TC case in WRF simulation.

2.2.3 Experimental design and UCM parameters

For each TC case, three sets of parallel model experiments were carried out for examining the sensitivity of TC rainfall to urban surface land use as well as AH over the GBA. In Nourban experiment, urban areas were replaced by “cropland” in the land use categorization within the WRF model, reflecting the predominantly cropland surroundings of the GBA mega-city. For experiments AH0 and AH300, WRF coupled with a SLUCM (Kusaka and Kimura, 2004) was utilized, maintaining normal land use but incorporating different AH values in the urban area (0 and 300W/m² for diurnal maximum, respectively). Due to the lack of comprehensive datasets, the SLUCM is employed rather than Multi-Layer Urban Canopy Model (MLUCM). Land use categorization based on the Moderate resolution Imaging Spectro-radiometer (MODIS) data was adopted in SLUCM. Also shown in Figure 2.2b is the MODIS land use categories for AH0 and AH300 experiment within the SC region. SLUCM is capable of including three types of urban categories: “Low-Intensity Residence”, “High-Intensity Residence”, and “Commercial and Industrial” in WRF version 3.8.1. In particular, to simplify the experiment and unify the urban impact in the model, only one type of urban land use is used, all urban grid points were categorized as High-Intensity Residence with the same parameters in this study. Such a

homogeneous urban landscape provided a consistent and simplified framework but may overlook the diversity and complexity of urban environments in reality.

Table 2.2 presents the UCM parameters prescribed over urban grids based on MODIS data. The mean building height is set to be 30m (informed by data from the Hong Kong Lands Department). The standard deviation of building height is set at 4m, and the road width at 16m, adhering to the default values for High-Intensity Residence in the SLUCM. Satellite measurements indicated a 289Wm^{-2} diurnal peak value in AH in Hong Kong during summer (Wong et al., 2015), the high-resolution (100 m x 100 m) hourly gridded dataset also suggested a daily mean AH value exceeding 150Wm^{-2} in Los Angeles (Ko et al., 2022). Here a diurnal AH profile with a 300Wm^{-2} maximum was implemented in SLUCM for the entire GBA urban area in the AH300 experiment (see Holst et al., 2016, Hu et al., 2021), representing an extreme urbanization scenario equivalent to commercial and industrial land use at every urban location. Therefore, Urban effect = AH300 minus Nourban and surface roughness effect = AH0 minus Nourban. This approach serves to test how the UHI effect- and hence its impact on precipitation- might be modulated by the very strong TC wind as storm systems approach the GBA. The diurnal profile of AH in UCM is shown in Figure 2.3, which aligns with our previous studies (Fung et al., 2021; Hu et al., 2021). The diurnal profile is defined based on the UHI intensity and anthropogenic emission habits (such as the use of air conditioning at night) in GBA during summertime, with maximum AH released at mid-night and before sunrise. This AH then decreases gradually with the increase of solar radiation during the day. Nonetheless, the current AH diurnal profile has limitations when compared to the real-world scenario. Due to diverse sources and factors, direct observation and measurement of AH values in urban areas remain

challenging (Allen et al., 2011; Jin et al., 2019). In our further studies, a more comprehensive method will be used to define both AH intensity and diurnal profile. We will examine a diurnal profile of the temperature difference between urban and rural stations using observational data and perform similar computations for simulations without AH. The disparity between observation and model outputs will be deemed as the contribution of AH, further refining the diurnal profile of AH.

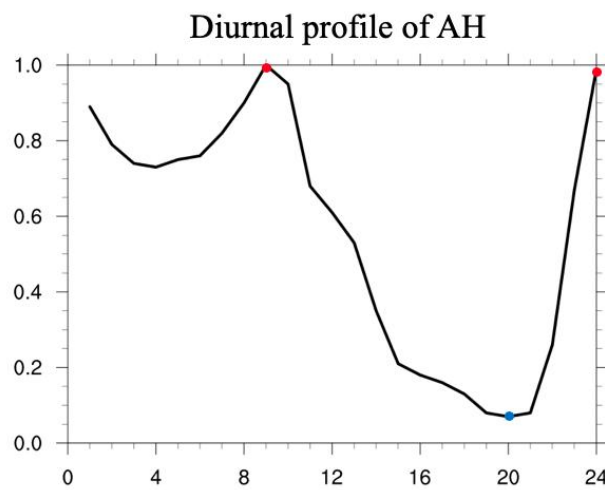


Figure 2.3 Diurnal profile of AH over urban grids of the innermost domain for experiments with peak AH = 300Wm⁻², the daily mean AH is about 166Wm⁻².

UCM parameter	High intensity residence
Anthropogenic heat(diurnal maximum) [W m ⁻²]	300.0
Building height [m]	30
Urban fraction	0.9
Standard Deviation of roof height [m]	4.0
Roof width [m]	9.4
Road width [m]	16.0
Surface albedo of road	0.2
Surface albedo of roof	0.2
Surface albedo of building wall	0.2

Table 2.2 Values of UCM parameters prescribed for the urban land use category.

2.2.4 Model evaluation for TC tracks

For TC simulation, to make sure the track of TC in each case, and experiment is reasonable, historical TC track derived from HKO best track data was used for model evaluation (see Figure 2.4). Black lines represent historical TC tracks, blue, purple, and red lines in Nourban, AH0, and AH300 experiments, respectively. The GBA mega-city is shown in green shading. The comparison reveals that model outputs yield similar tracks for all runs when juxtaposed with observations. Though some deviations occur in the ocean compared to observation (e.g., TCs Victor and Utor), the model produces reasonable tracks for most storms in the South China Sea. Moreover, model results yield identical landfall locations in SC for all storms as observed, which helps reduce the bias and uncertainties when assessing the urban impact on TC rainfall. Additionally, in all cases, ensemble integrations display nearly identical tracks across all experiments, leading to the conclusion that urban land cover and AH have negligible effects on TC tracks. The performance of TC maximum wind speed (Vmax) compared to HKO best tract data is

also assessed (Figure not shown), WRF outputs slightly overestimate Vmax for most TCs, but the trend is well captured by model. We emphasize that the accuracy of reproducing the TC as same as in best track data is not the main objective in this study, which is also challenging in simulation TCs using the WRF model (Clouthier-López, 2022; Chen et al., 2022). Sensitivity experiments with different urban levels were conducted to explore the effects of urbanization, specifically friction and AH, on TC precipitation in GBA mega-city. As such, we seek to reproduce the TC tracks as observed in the model environment, ensure that model TCs are realistic enough. And we still manage to capture storm tracks which are highly close to observations, particularly the landfall location. This is crucial as we want to investigate how GBA urban land use is affecting TC rainfall- hence the importance of reproducing the TC landfall. Also it appears that TC intensity in the model is reasonable. Hence, we consider the model's performance is reliable and reasonable, which does not introduce excessive uncertainties in this study.

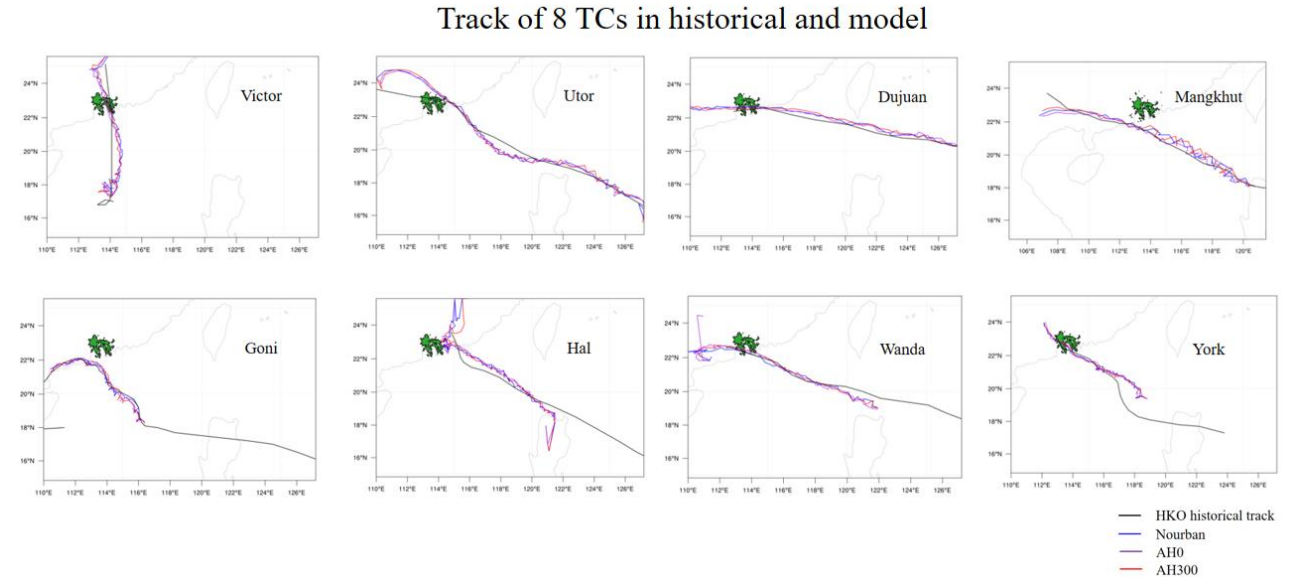


Figure 2.4 Track of 8 TC cases (Victor, Utor, Dujuan, Mangkhut, Goni, Hal, Wanda, and York). Black line shows the historical track based on HKO best track data. Blue, purple, and red mean Nourban, AH0 and AH300 run. The GBA urban area is shown in green shaded area.

2.3 Results

2.3.1 Results based on observations

2.3.1.1 TC rainfall distribution

Figure 2.5a presents the hourly TC extreme rainfall intensity (99th percentile of hourly rain rate based on 41 selected TCs) over SC derived from station observations. Seven urban and seven rural stations are indicated by stars and diamonds, other stations are depicted by dots. Generally, TC precipitation decreases gradually as one moves inland from the coast. Extreme hourly TC rainfall intensity exceeds 27mm/hr for stations in the coastline, particularly in the southern part of SC (Leizhou Peninsula), but only 13 to 15 mm/hour for inland stations located at 25°N. However, when comparing urban with surrounding rural locations, extreme hourly TC rainfall intensity reaches 23 to more than 27mm/hr for these seven urban stations, much stronger than in adjacent rural areas. Extreme rainfall intensity ranges from 19 to 25mm/hour in rural areas, despite rural stations being closer to the coast compared to urban stations. Additionally, the probability of TC hourly rain rate is considered by calculating its probability density functions (PDF) over urban and rural stations (see Figure 2.5b). It is noteworthy that urban stations exhibit more frequent rainfall heavier than 20mm/hr (except for rainfall in the range from 70 to 80mm/hr) than rural stations, particularly in the 30 to 60 mm/hr range. The frequency of heavy rainfall in urban stations increases by about 10% to 40% for the 20 to 50 mm/hr range, and more than five times for the 50 to 60 mm hr range compared to rural locations. However, it is noteworthy that the terrain also influences TC rainfall, while the GBA is located south of the mountain, windward positions receive higher amounts of rainfall than leeward positions. Quantifying the impacts of terrain on urban and rural locations based on observations is challenging.

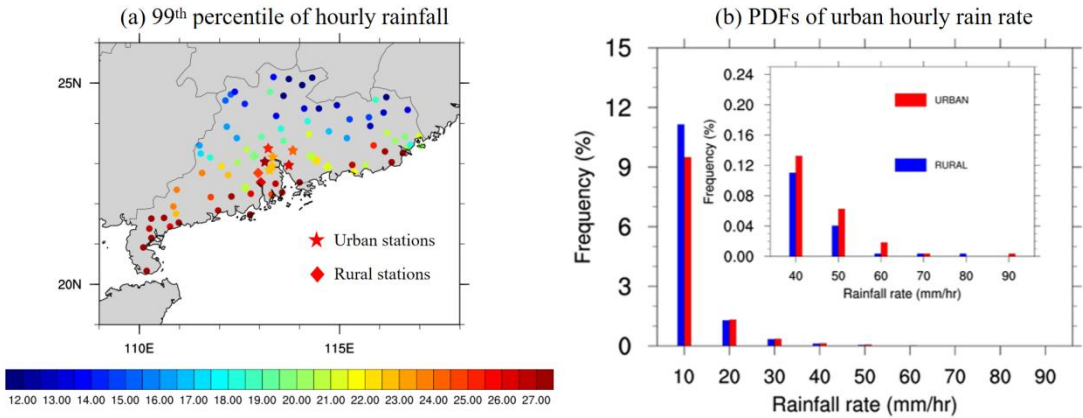


Figure 2.5 (a) Extreme rainfall based 99th percentile of hourly rainfall during all TC cases in each station, with star means urban stations, and diamond means rural stations. (b) PDFs of hourly precipitation rates for rural (blue) and urban (red) stations, within the ranges of 1-10, 10-20, 20-30, 30-40, 40-50, 50-60, 60-70, 70-80, 80-90 mm/hr⁻¹.

Figure 2.6 shows the scatter plot of the 99th percentile of TC hourly rainfall and accumulated TC rainfall as a function of distance of each central SC station (stations in the black box, see inset in Figure 2.6a) from the South China Sea coastline (here the Pearl River Estuary is not considered as part of the ocean), with red, green, and blue dots representing urban, rural, and other stations, respectively. Crosses indicate the centroid of results for urban, rural, and other stations with colors corresponding to the respective dots. Extreme rainfall intensity is seen to decrease as a function of the station-to-coast distance, with intensity decreasing from approximately 30 to 13mm/hr as the distance from the coastline increases from 10km to 200km. However, for urban locations, the increase is notably more pronounced than that expected from the best-fit relationship between extreme rainfall decrease and station-to-coast distance (see red cross). The difference between urban and rural deviations to the best-fit line exceeded the 99% significance level. Conversely, for accumulated rainfall, though the centroid of urban (rural) station results is slightly greater (smaller) than the best-fit line, the difference between urban and rural stations is much less significant. Overall, these findings are consistent with TC extreme

rainfall being stronger over urban than surrounding rural locations in the GBA.

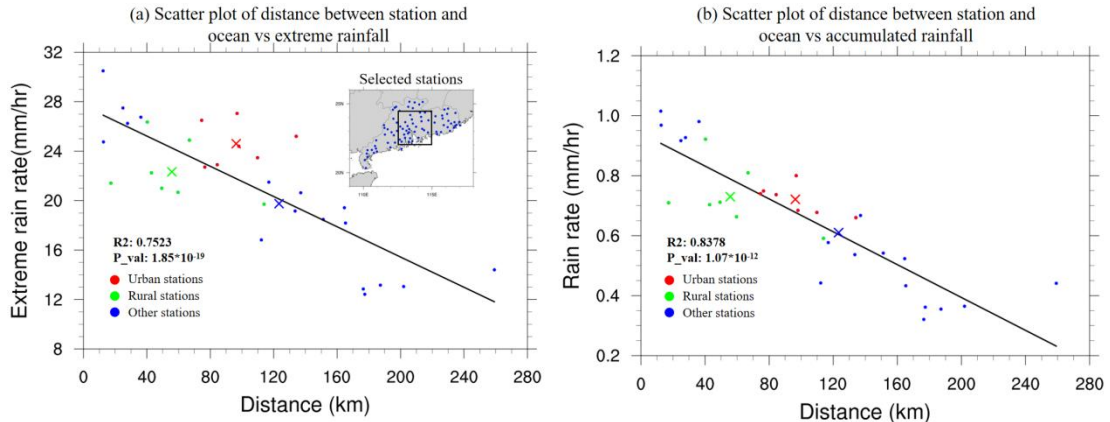


Figure 2.6 Scatter plot of distance between stations and ocean vs (a) 99th percentile of hourly rainfall, (b) accumulated rainfall during 41 TC cases in each station, with urban, rural and other stations shown in red, green and blue. The black box represents selected stations. Crosses represent the centroids of results in urban, rural, and other stations with the same color.

2.3.1.2 Rainfall, temperature, and wind speed evaluation during TC passages

To further investigate the urban impact on TCs, composite time series of rainfall, 2m temperature, and surface wind derived from station observations are computed, with $t=0$ referring to the hour of peak rainfall averaged over the selected 14 stations, and for all TC cases. Figure 2.7a shows the time series of temperature and rainfall differences between urban and rural stations, with the red (blue) line representing the rainfall (temperature) differences. Rainfall differences exceeding the 95% significance level are shown by red dots in Figure 2.7a. Averaging over all TC cases, there is stronger precipitation in urban compared to rural locations, especially at $t=0$. The rainfall differences between urban and rural locations are significant during $t=-10$ hours to $t=5$ hours. Moreover, the temperature difference (which can also be regarded as the UHI effect) initially increases, with the difference reaching more than 0.7K at $t=-20$ hours. This could be attributed to sinking motion related to TC circulation about ~ 1 day prior to the time of stronger storm impact, resulting in a more stable atmosphere condition in SC and a stronger UHI effect.

However, the UHI effect is then rapidly suppressed by approaching TCs at 20 hours prior to the rainfall peak hour; the temperature difference is reduced from 0.7K to being even negative, and reaches a minimum at t=0, likely due to the strong TC winds. The UHI effect gradually recovers at t=10 hours, but temperature differences remain insignificant throughout the time series. Also shown in Figure 2.7b is the time series of surface wind speed and rainfall difference between urban and rural stations averaged over all TCs, with the red (blue) line representing the rainfall (surface wind) difference. Red dots represent hourly wind difference exceeds the 95% significance level. Surface wind differences between urban and rural locations gradually decrease significantly from approximately -0.1m/s to lower than -0.6m/s, reaching the minimum at t=0. And such a difference returns to nearly 0 after t=15 hours, as the storm moves away. The suppressed surface wind can be attributed to higher surface roughness in urban compared to surrounding rural areas. Overall, based on observations, the UHI effect is highly suppressed by TCs, with the temperature initially difference increasing first one day prior to t=0, but subsequently decreasing to even negative at the hour of peak rainfall. Concurrently, the presence of urban land use can also significantly decrease surface wind during the TC passage in the city, and recovers after t=15 hours.

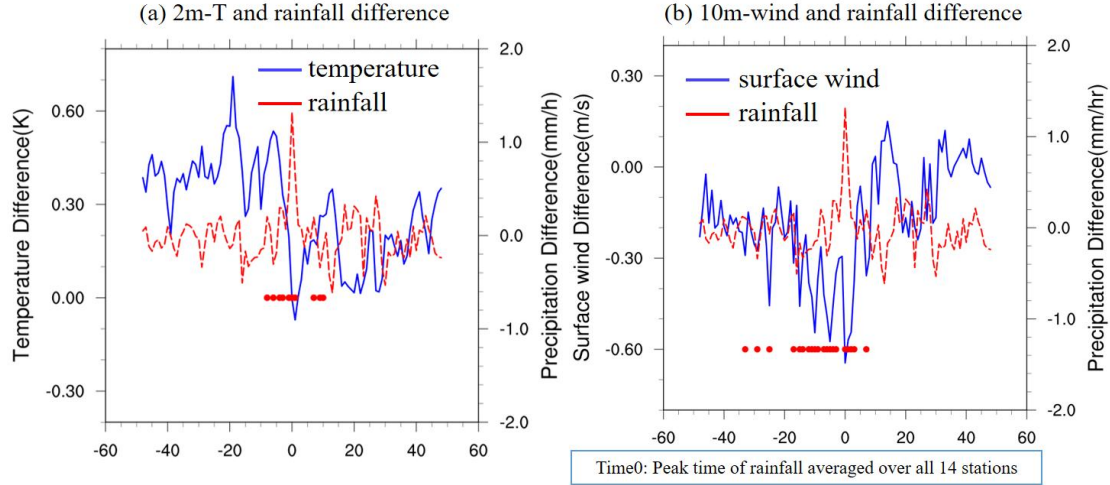


Figure 2.7 (a) Time series of hourly 2m temperature (blue) and rainfall (red) difference between urban and rural stations averaged over all TC cases. Hourly rainfall differences exceeding the 95% significance level are denoted by red dots. (b) Same as (a) but for hourly 10m wind speed (blue) and rainfall (red), hourly wind difference exceeds the 95% significance level are denoted by red dots.

Moreover, we also utilized the Tropical Rainfall Measure Mission (TRMM)-3B42 multi-satellite precipitation products (Huffman, 2014) to unveil the difference in TC rainfall between urban and rural areas. Figure 2.8 gives the composite time series of hourly rainfall averaged over the same 41 storms for urban and rural areas. 11 urban grid points and 11 rural grid points are selected, similar to the location of urban and rural stations (see inset in Figure 2.8), with $t=0$ referring to the hour of peak rainfall averaged over 22 grid points and all TCs. Stronger TC rainfall is observed in urban areas than rural stations, with urban rainfall intensity reaching 48mm/hr at $t=0$ hour, compared to only 42 mm/hr in rural locations. Results from TRMM reanalysis data are consistent with station observations shown above.

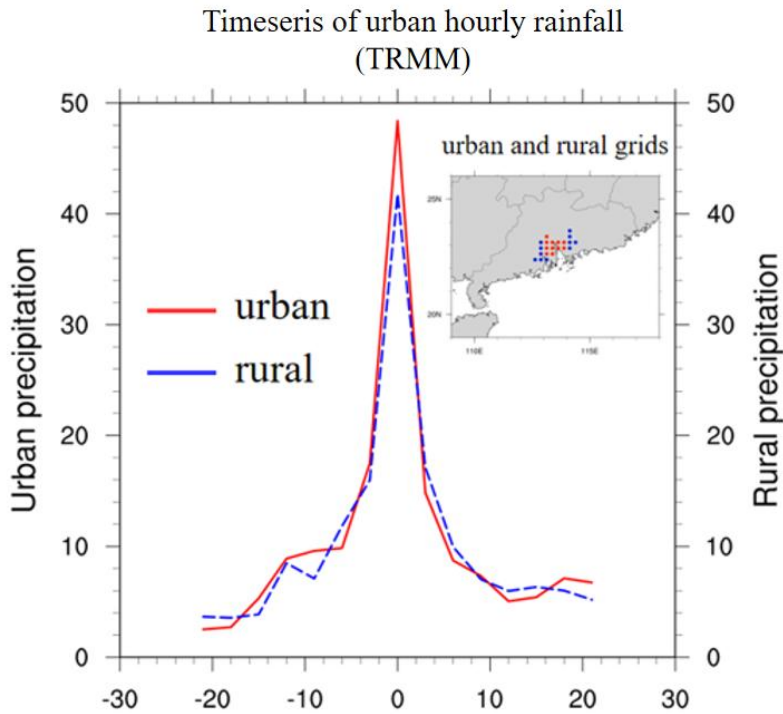


Figure 2.8 Time series of hourly rainfall for rural (blue), and urban (red) area averaged over 41 TC cases based on TRMM reanalysis data, with smaller map representing the rural (blue) and urban (red) area.

2.3.2 Results based on numerical modeling

2.3.2.1 Surface temperature and wind

To investigate the urban impacts on TC precipitation in the model environment, eight TC cases were dynamically downscaled by WRF with three parallel numerical experiments, accounting for different surface land use and AH. Figure 2.9a gives composite time series of the urban 2m temperature difference between AH0 and Nourban (blue), AH300 and Nourban (red) averaged across all TC cases, with $t=0$ corresponding to the hour of urban peak rainfall. Initially, the 2m temperature difference between both AH0 and AH300 compared to Nourban increases, with a maximum difference of 1.2K (2.5K) for AH0 (AH300) observed approximately 1day prior to $t=0$. This is consistent with observations that the sinking motion associated with TC circulation

can amplify the UHI effect in GBA (see Figure 2.7a). But the UHI effect then rapidly diminishes in both AH0 and AH300, reaching a minimum at t=0. Even with a 300W/m² diurnal maximum AH applied to GBA mega-city, the urban 2m temperature difference still declines to only 1.3K in AH300 compared to Nourban at t=0, and a mere 0.4K in the AH0 experiment compared to Nourban. These temperature differences are then quickly reestablished after t=0 for the AH300 scenario, due to its extreme urban warming. In contrast, the temperature difference between AH0 and Nourban remains weak at t=10 hours. And temperature differences are insignificant during the TC passage. Hence, model results suggest that the UHI effect is substantially suppressed during TC passages due to the strong TC wind.

Figure 2.9b gives the composite time series of urban 10m-wind speed difference between AH0 and Nourban (blue), AH300 and Nourban (red) averaged across all TCs. Hourly wind differences between AH0 (AH300) and Nourban that exceed the 95% significance level are denoted by blue (red) dots. Compared with Nourban, the urban 10m wind speed difference rapidly declines from -2m/s (-1.2m/s) to -6.8m/s (-6m/s) in AH0 (AH300) from t=-30 hours to t=0, and the wind difference reaches a maximum at t=0 with significant difference being found. The urban wind speed difference then gradually recovers after the rainfall peak in both AH0 and AH300 as storms move away. Model results are consistent with observations; this can be attributed to the higher surface roughness in urban areas compared to rural areas. Moreover, it is also found that AH300 exhibits stronger urban wind speed than AH0, despite using the same surface urban land use. This can be ascribed to the increased temperature induced by AH in the urbanized GBA, which intensifies the land-sea temperature gradient and strengthens the sea breeze in AH300 (Figures not shown). Thus higher surface wind speed can be observed over the urban area in

AH300 compared to AH0. Such a wind speed difference between AH0 and AH300 is most pronounced at $t=-30$ hours, but decreases gradually as the UHI effect is suppressed during the TC passage. Overall, the changes in 2m temperature and 10m wind speed due to urbanization is effectively simulated in the WRF model, with the UHI effect (surface wind speed) being highly suppressed as a result of strong TC winds (higher urban surface roughness) during TC passage.

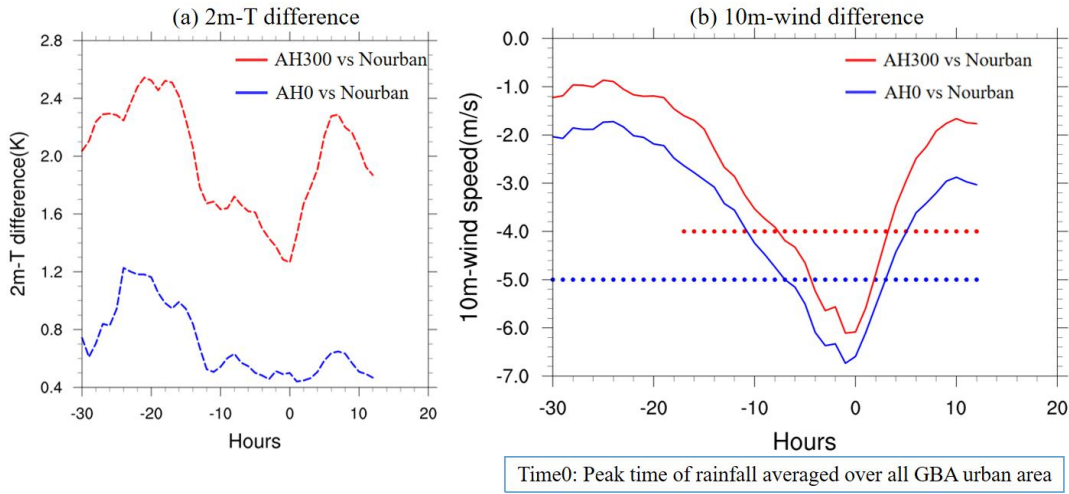


Figure 2.9 (a) Time series of hourly 2m temperature difference between AH0 and Nourban (blue), and that between AH300 and Nourban (red) averaged over 8 TC cases based on model simulation. (b) Same as (a) but for hourly 10m wind speed difference. Hourly wind difference between AH0 (AH300) and Nourban exceeds the 95% significance level are denoted by blue (red) dots.

2.3.2.2 TC rainfall extremes

For the characteristics of TC precipitation, Figure 2.10a presents the composite time series of urban hourly rainfall averaged over all TCs, with black, blue, and red lines representing Nourban, AH0, and AH300, respectively. Notably, both AH0 and AH300 exhibit stronger TC rainfall than Nourban experiment in the GBA mega-city, with the urban hourly rain rate peaking at approximately 12.5 mm/hr for AH0 and AH300, while such a value is only 10.5 mm/hr for Nourban at $t=0$. Interestingly, there is minimal difference in rainfall intensity between AH0 and AH300 during the TC passage, and the rainfall intensity in AH0 is even stronger from $t=-5$ to $t=3$

hours. It appears that urbanization enhances TC rainfall over the GBA mega-city, but the effect of adding AH is weak on TC rainfall.

The PDFs of urban hourly rain rate for all TCs are also shown in Figure 2.10b, with black, blue, and red bars representing Nourban, AH0, and AH300, respectively. Comparing urban experiments (AH0 and AH300) and Nourban, a strong increase in rainfall occurrence rate across all ranges is revealed, especially for heavy rainfall that heavier than 40mm/hr. For hourly rain rates in the range of 40-90mm/hr, the frequency increases drastically by about 20% to 50% in AH0 and AH300, compared to Nourban. The enhancement of hourly rain rate occurrence is relatively weak for light rainfall in the range of 1 to 20mm/hr, with the probability increasing by about 5% in AH0 and AH300 compared to Nourban. Furthermore, the probability of heavy rainfall in AH300 is similar to that in AH0, there is no significant difference between AH0 and AH300 in terms of heavy rainfall probability. Overall, urbanization considerably enhances the likelihood of rainfall in the GBA mega-city, particularly for heavy rainfall. But the impact of AH on urban hourly rain rate probability remains weak.

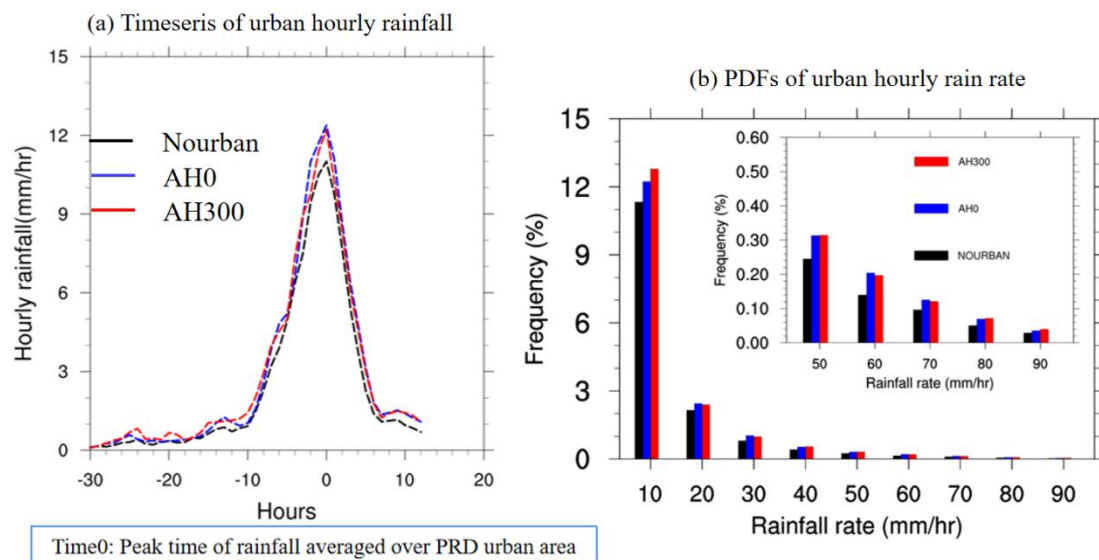


Figure 2.10 (a) Time series of hourly rainfall over urban locations within GBA area for Nourban (black), AH0 (blue), and AH300 (red) averaged over 8 TC cases based on model simulation. (b) PDFs of hourly precipitation rates over urban locations within GBA, within the ranges of 1-10, 10-20, 20-30, 30-40, 40-50, 50-60, 60-70, 70-80, and 80-90 mm/hr for the NO-URBAN (black), AH0 (blue), AH300 (red) experiments.

On the other hand, Figure 2.11 illustrates the accumulated precipitation differences between various experiments, computed by averaging over all selected TC cases, with black contours representing the boundary of GBA mega-city. Black dots indicate rainfall differences between the two experiments that pass the 95% significance level of the student t-test. Compared to Nourban, accumulated rainfall increases substantially across the whole urban area in AH0 (see Figure 2.11a), with daily mean rainfall enhancing by about 15 to 40 mm/d over the GBA mega-city. The differences are very small (no more than 5 mm/d) over most surrounding rural locations, and the difference is noisy and insignificant over the ocean. The aforementioned precipitation change due to land cover change alone (AH0 minus Nourban) is significant over the GBA mega-city, particularly in the central northwestern and eastern parts of the urban area that pass the 95% significance level of the t-test, but differences are insignificant over the southern part of the city. And changes in TC rainfall in the surrounding rural land areas and ocean are entirely insignificant. Meanwhile, the pattern of accumulated precipitation difference between AH300 and Nourban (see Figure 2.11b) is similar to Figure 2.11a, with significant enhancements of TC precipitation found primarily over the majority of the urban area. The magnitude of enhanced rainfall is comparable to the difference between AH0 and Nourban, with accumulated rainfall increasing by about 15 to 45 mm/d over the GBA mega-city. There is also slight enhancement of rainfall north of the city (downstream area). Changes in accumulated precipitation in surrounding rural areas and ocean due to both AH and urban land use remain insignificant. The above indicates that urbanization significantly enhances both TC rainfall intensity and frequency over the GBA

mega-city, especially for heavy rainfall exceeding 40mm/hr. This is mainly attributed to the urban frictional effect induced by the presence of urban surface land use, and such frictional impact is regional, with significant changes being found in GBA urban areas only. But the impact of AH is relatively weak on both TC rainfall intensity and frequency.

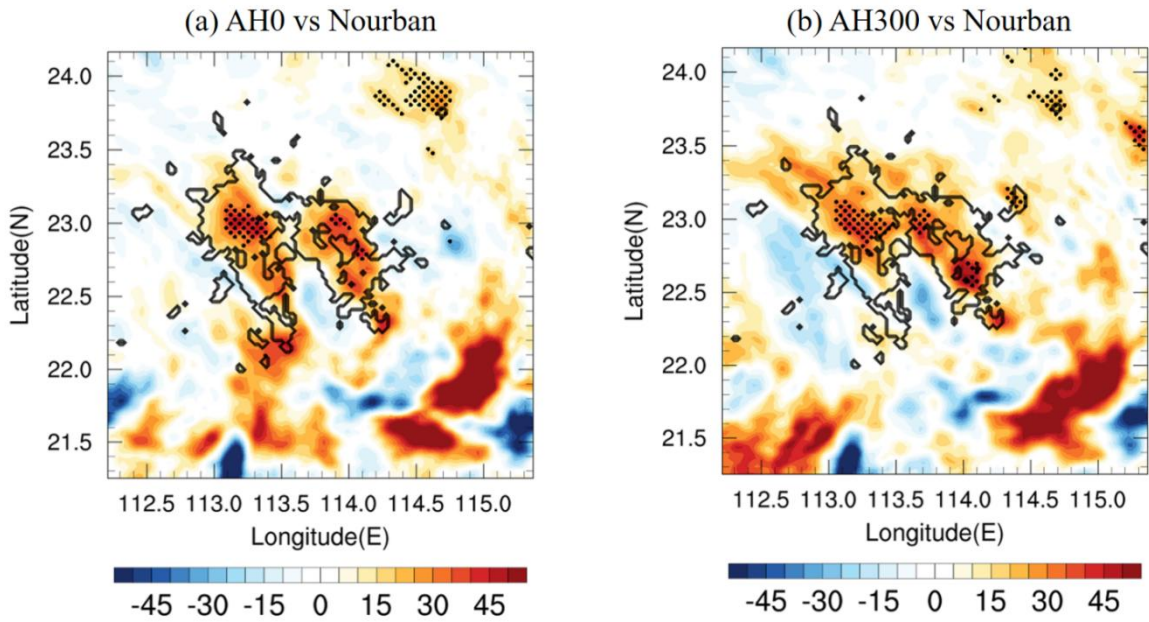


Figure 2.11 Accumulated rainfall difference (units: mm/day) between (a) AH0 and Nourban, and (b) AH300 and Nourban. Rainfall is computed by averaging over entire integrations for 8 cases. Locations in which the difference exceeds the 95% significance level are denoted by black dots. Black contours represent the boundary of GBA mega-city.

2.3.2.3 Mechanism of enhanced accumulated rainfall

Previous studies on non-TC rainfall (Samuel et al., 2021, Hu et al., 2021) have demonstrated that AH strongly influences non-TC precipitation extremes by providing a more unstable environment and enhancing moisture flux convergence in the coastal GBA mega-city. However, our results indicate that the impact of AH is relatively weak on TC rainfall, highlighting the importance of the frictional effect due to urban land use. Figure 2.12 shows the 3-hour mean

10-wind speed difference between AH0 and Nourban, as well as the 10m-wind vector from Nourban during the landfall of TCs (a) Victor and (b) Utor, with black contours outlining the boundary of the GBA mega-city. A strong cyclonic flow is observed over the urban areas, during landfall of these TCs. Comparisons between AH0 and Nourban reveal a substantial reduction in 10m-wind speed due to urban land use, with magnitudes decreasing by over 5m/s across most of the city and slightly increasing at the urban boundary. Differences in wind speed are negligible in surrounding rural areas and over the ocean. Under such a weather condition with more stagnant low-level wind over the urban area, the decreased surface wind speed induced by the urban frictional effect in turn enhances low-level convergence.

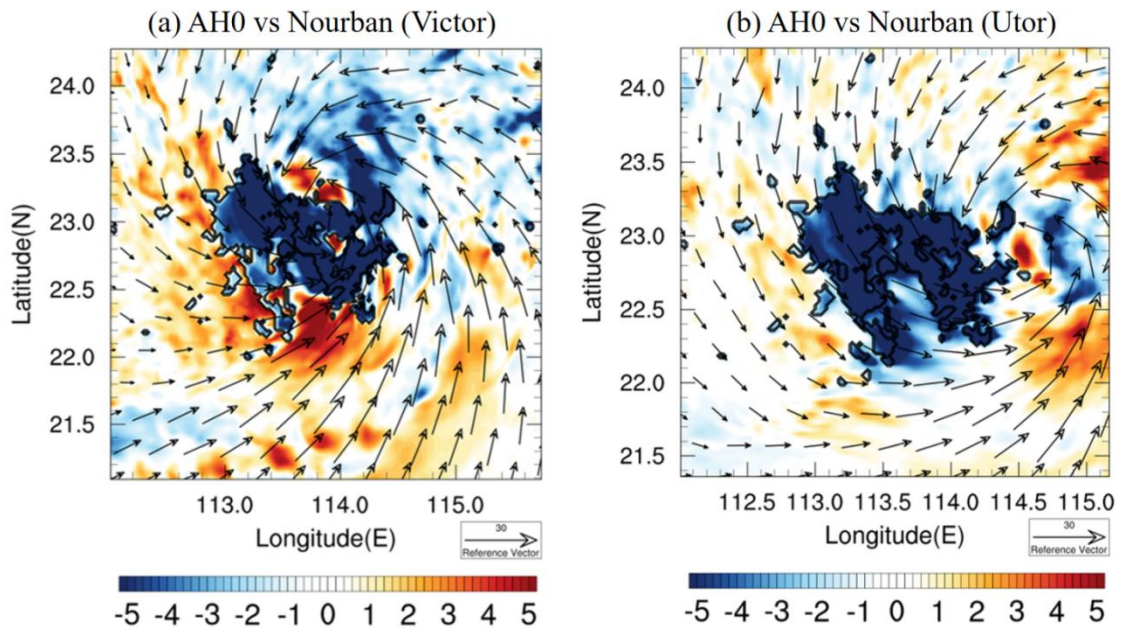


Figure 2.12 Three hours mean 10m-wind speed difference (AH0 vs Nourban) and wind vector at landfall hour for (a) Victor, and (b) Utor. Black contours represent the boundary of GBA mega-city.

We thus calculated the difference of vertically integrated urban moisture flux divergence averaged across all TCs (starting from (ending at) 24 hours before (after) the hour of urban peak

rainfall) between AH0 and Nourban, and also between AH300 and Nourban (see Table 2.3).

According to the moisture budget equation:

$$\bar{P} - \bar{E} = -\frac{1}{g} \nabla \cdot \int_{sfc}^{\text{top}} q \vec{V} dp$$

the accumulated rainfall (\bar{P}) equals the sum of surface evaporation (\bar{E}) and vertically integrated moisture flux convergence. Here q means specific humidity, \vec{V} represents horizontal wind vector, and p indicates the pressure. Moreover, the moisture flux divergence can be further divided into the dynamic term (duv):

$$-\frac{1}{g} \nabla \cdot \int_{sfc}^{\text{top}} (q_c \vec{V}) dp$$

and the thermal-dynamic term (dq):

$$-\frac{1}{g} \nabla \cdot \int_{sfc}^{\text{top}} (q' \vec{V}) dp$$

q' and \vec{V}' are the anomaly of specific humidity and horizontal wind. In comparison to Nourban, both AH0 and AH300 exhibit higher vertically integrated moisture flux convergence in all cases (see blue and red values in Table 2.3), with magnitude ranging from 0.04 to 0.33 g/m²/s. For most TC cases, the values of moisture flux divergence are similar in AH0 and AH300 (e.g., TC Utor, Dujuan, Wanda and York). On the other hand, stronger urban convergence is found in AH300 than AH0 in TC Mangkhut, and Goni. The difference in moisture flux convergence between AH300 and Nourban for Mangkhut and Goni reach 0.21 and 0.3 g/m²/s, respectively, but only 0.07 and 0.05 g/m²/s between AH0 and Nourban. The dynamic and thermodynamic terms of moisture flux divergence differences are also calculated (see purple and black values in Table 2.3).

The enhanced moisture flux convergence can be primarily attributed to the strongly intensified dynamic term (duv), with values of the dynamic term closely matching the changes in moisture flux divergence for all cases. Changes in the thermodynamic term are minimal for all TC cases. Consequently, such an increased moisture flux convergence is mainly due to the urban frictional effect. Overall, the above analysis paints a picture that the decreased surface wind speed induced by the urban surface friction leads to substantial enhancement of moisture flux convergence over the GBA mega-city, which results in increased water vapor content and supports the observed rise in urban TC precipitation. However, although the AH impact is generally weak for most TCs, it still plays a role in cases such as Mangkhut and Goni.

Moisture flux divergence	Victor (g/m²/s)	Utor (g/m²/s)	Dujuan (g/m²/s)	Mangkhut (g/m²/s)	Goni (g/m²/s)	Hal (g/m²/s)	Wanda (g/m²/s)	York (g/m²/s)
AH300-Nourban	-0.07	-0.12	-0.09	-0.21	-0.3	-0.33	-0.03	-0.05
AH300-Nourban (dq term)	0.01	0	0.01	-0.01	0	-0.05	0	0.01
AH300-Nourban (duv term)	-0.08	-0.13	-0.10	-0.20	-0.31	-0.3	-0.03	-0.07
AH0-Nourban	-0.26	-0.15	-0.09	-0.07	-0.05	-0.24	-0.04	-0.04
AH0-Nourban (dq term)	0.04	0.01	0.01	0.01	-0.02	-0.05	0	0
AH0-Nourban (duv term)	-0.29	-0.16	-0.10	-0.08	-0.03	-0.2	-0.03	-0.04

Table 2.3 Vertically integrated moisture flux divergence difference between AH0 (AH300) and Nourban for each case. Values are calculated by averaging over the GBA urban area and all ensemble members, with duv (dq) term representing the dynamic (thermal dynamic) term.

2.3.2.4 AH impacts on TC rainfall

Further study reveals that the impact of urbanization on TC rainfall in GBA urban areas varies across different cases, as evidenced by the time series of urban hourly rainfall for each case (see Figure 2.13). The black, blue, and red lines represent the hourly rainfall of Nourban, AH0, and AH300, respectively. For instance, TC Utor and Hal exhibit a marked increase in rainfall due

to urbanization, whereas the difference between urban and Nourban experiments is considerably smaller for TC Dujuan and York. Additionally, for TC Mangkhut, Goni, and Hal, strong urban TC rainfall is observed during the final 10 hours in AH300 when the TC has already moved away, creating a secondary or tertiary rainfall peak absent in AH0 and Nourban. The heightened urban TC rainfall in AH300 compared to AH0 for these three cases is further attributable to increased vertically integrated urban moisture flux convergence (see Table 2), while AH continues to enhance the urban TC rainfall for certain TCs after the TC passage. Two questions are further proposed: (1) How does AH influence TC precipitation in specific cases? (2) Is there any relationship between urban impact on TC rainfall under different TC movements over the urban area (e.g., slow or fast TC).

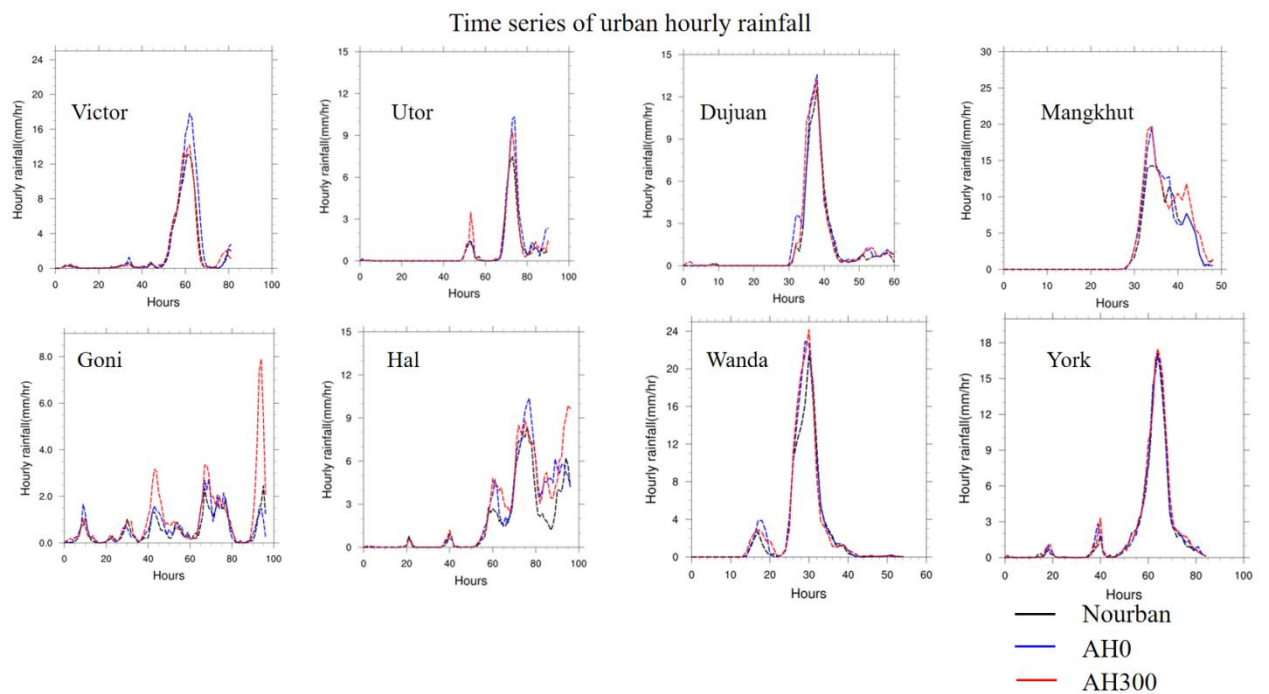


Figure 2.13 Time series of hourly rainfall for each case (Victor, Utor, Dujuan, Mangkhut, Goni, Hal, Wanda, and York). Black, blue, and red line mean Nourban, AH0, and AH300 experiments.

To understand why AH continues to augment urban TC rainfall during the last 10 hours in some TCs, Figure 2.14 shows the time series of convection available potential energy (CAPE)

averaged over the urban area for TC (a) Mangkhut, and (b) Goni, the black box highlights the period of second (third) rainfall peak time in AH300 of TC Mangkhut (Goni). It is seen that the CAPE is consumed strongly with the occur of TC rainfall in both Mangkhut and Goni, with minimal CAPE differences between AH300 and Nourban. However, CAPE is rebuilt really rapidly in AH300 after the 40th (85th) hour in Mangkhut (Goni), while the enhancement found in AH0 and Nourban is relatively much weaker. In the final 10 hours (see inset black box), the CAPE difference between AH300 and Nourban becomes pronounced, with the ratio of urban CAPE between AH300 and Nourban reaching ~1.3 to 2 (1.8 to 2.3) times in Mangkhut (Goni). Concurrently, the time series of vertically integrated specific humidity averaged over the GBA mega-city is also shown in Figure 2.14 for TC (c) Mangkhut, and (d) Goni. As the TC approaches, urban specific humidity also substantially increases with time for both TC Mangkhut and Goni, with specific humidity values rising from ~4g/kg (5g/kg) to 6g/kg (6.2g/kg) in TC Mangkhut (Goni). Plentiful water vapor is transported by TC to the GBA mega-city. During the last 10 hours in both TC Mangkhut and Goni (see black box), urban specific humidity remains elevated at approximately 5.8 to 6g/kg, supporting extreme rainfall induced by the rebuilt CAPE in the GBA mega-city after TC passage.

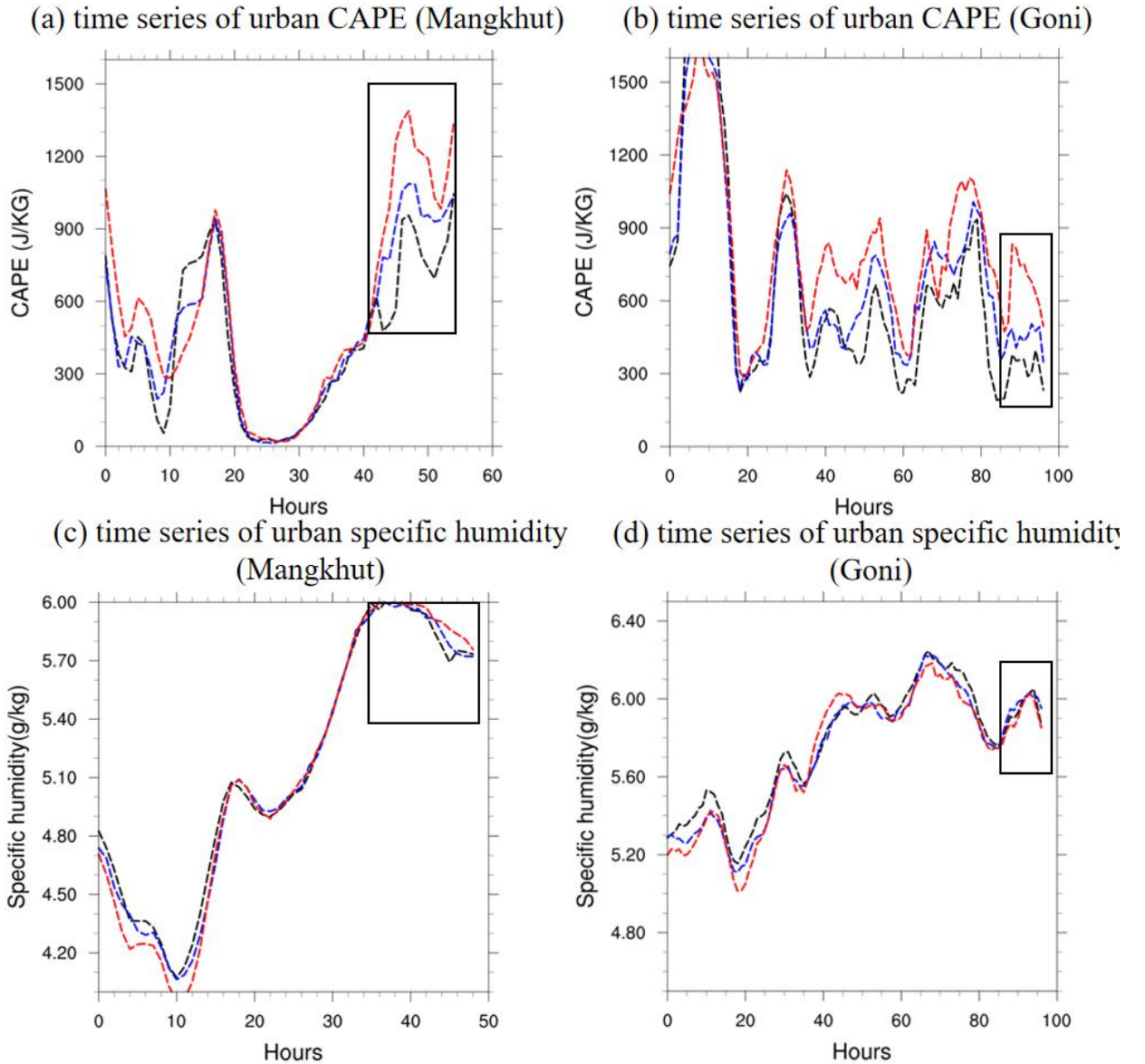


Figure 2.14 Time series of CAPE over urban locations within GBA area for Nourban (black), AH0 (blue), and AH300 (red) for (a) Mangkhut and (b) Goni. (c), (d) Same as (a), (b) except for vertically integrated specific humidity. The specific humidity is computed by integrating over all model layers.

Although TC Mangkhut and Goni did not make landfall in the GBA mega-city, their large sizes resulted in heavy rainfall over the urban area during their passage (Figure 2.4). Considering the extreme scenario of AH300, the UHI effect is not entirely suppressed by strong TC winds, allowing CAPE to be rebuilt in the urban area as the storms depart. Simultaneously, substantial water vapor is transported by the TC, both sufficient CAPE and water vapor in GBA mega-city support the second (third) rainfall peak in AH300 for TC Mangkhut (Goni); note that such rainfall

peaks are absent in AH0 and Nourban, as their urban CAPE is not as high as those in AH300.

Consequently, AH can still influence TC precipitation in specific cases after the TC passage under extreme scenario.

2.3.2.5 The influence of TC movement

It is also important to understand whether there is any relationship between urban impact on TC rainfall and TC characteristics, such as TC size, speed, and landfall angle. Based on the range of TC rainfall-affected area (see Appendix), the TC residence time is further defined for each case. Figure 2.16 illustrates the definition of TC residence time using TC Victor as an example, with black, blue, and red lines representing the TC tracks of Nourban, AH0, and AH300, respectively. The black circle denotes the TC rainfall-affected area, while the green shaded area represents the GBA mega-city. The period during when the city is covered by the TC rainfall-affected area is defined as the TC residence time. Based on such a definition, parameters like TC speed and size can be taken into account. The residence time of TC for all integrations are provided in Figure 2.15, and urban impact is found to have a negligible effect on the duration of TC residence time.

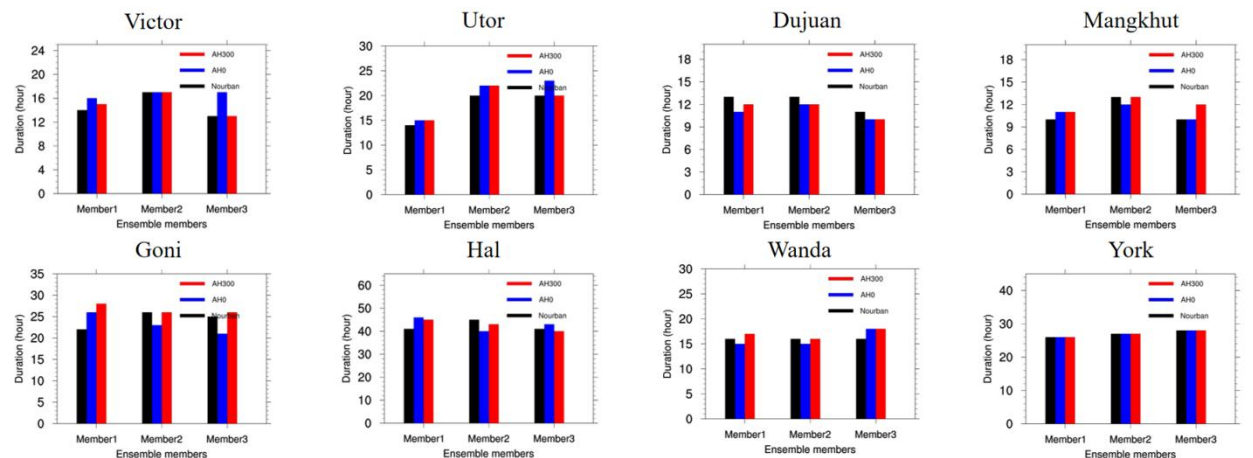


Figure 2.15 Duration of TC residence time in each case, experiment, and ensemble members.

Figure 2.16b shows a scatter plot illustrating the relationship between TC residence time and the urban accumulated rainfall difference ratio between urban (AH0 and AH300) and Nourban runs. The accumulated rainfall difference ratio is calculated as the urban accumulated rainfall difference between urban and Nourban experiments divided by Nourban accumulated rainfall averaged over the urban area. Red dots represent results from two comparisons (AH0 vs Nourban, and AH300 vs Nourban) across eight TC cases and three ensemble members, with the blue line indicating the best-fit line for all data points. For the comparison between urban and Nourban experiments, the fractional accumulated rainfall change in urban areas ranges from -3% to more than 80%, with the TC residence time varying from 10 to 46 hours. A positive relationship emerges between urban accumulated TC rainfall difference ratio and the TC residence time, indicating that experiments with longer duration tend to exhibit stronger fractional increases in TC rainfall over the GBA mega-city. This can be attributed to the urban frictional effect on enhanced TC precipitation. With longer TC residence time, frictional low-level moisture flux convergence results in increased accumulated moisture content, leading to more substantial TC accumulated rainfall. Overall, the urban impact (primarily the urban frictional effect) has a more significant impact on slower storms, suggesting that slower or longer-lasting TCs can cause more considerable economic and human losses in coastal cities.

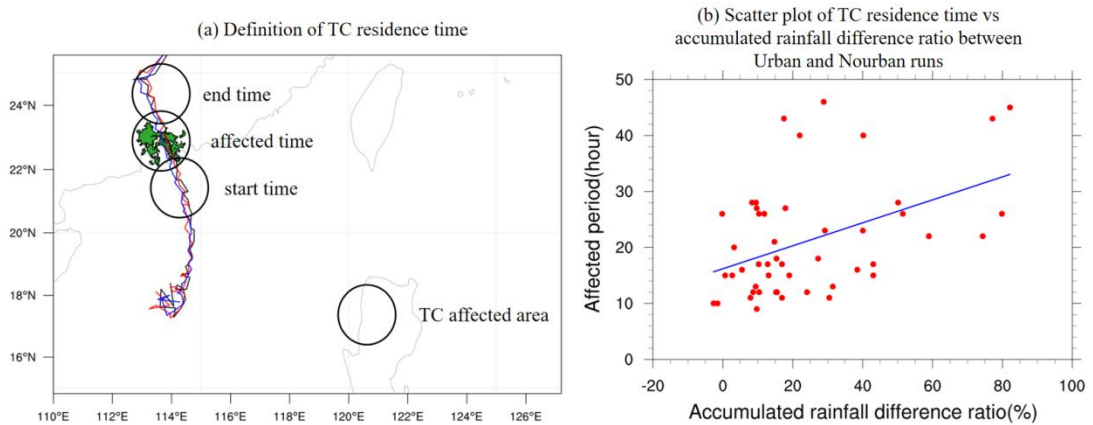


Figure 2.16 (a) A diagram example of how to define the TC residence time. TC tracks of Victor from Nourban, AH0, and AH300 are shown in black, blue, and red lines. Black circle means TC rainfall affected area, and the GBA mega-city is shown in green shaded. (b) Scatter plot of relationship between duration of TC residence time and accumulated rainfall difference ratio between urban runs (AH0 and AH300) and Nourban runs in all cases and ensemble members.

2.4 Brief Summary

By utilizing observations and WRF-SLUCM, the sensitivity of TC precipitation to the urban impact (AH and urban surface land use) over the GBA mega-city was assessed. Parallel experiments were designed in model simulations by varying the value of surface AH flux (0 or 300Wm^{-2} as the diurnal maximum) and land use types (urban or cropland), and eight TCs were dynamically downscaled in SC to a grid spacing of $3\text{km} \times 3\text{km}$. As a result, both observations and numerical modeling find that the surface wind is significantly decreased over the urban area during TC passage, attributable to the higher surface roughness in urban compared to rural areas. Concurrently, the UHI effect increases first at around one day prior to the TC rainfall peak hour, then it is greatly suppressed during the TC passage and reaches the minimum at the hour of peak rainfall due to strong TC winds. Observations reveal that urban locations in the GBA experience more intense TC extreme hourly rainfall (99th percentile of hourly rainfall) and more frequent heavy rainfall (30 to 60 mm/hr range) than surrounding rural areas. Furthermore, numerical model

results indicate that both intensity and occurrence rate of TC rainfall in AH0 and AH300 experiments are significantly increased over the GBA meta-city compared to Nourban. The accumulated rainfall increases by about 15 to 40 mm/day regionally, which is only significant over the urban area. The probability for TC rainfall is enhanced by about 20% to 50% across all ranges (1 to 90mm/hr) over the GBA mega-city in both AH0 and AH300, compared to Nourban, especially for heavy rainfall exceeding 40mm/hr. However, the comparison between AH0 and AH300 reveals that the AH impact on TC precipitation intensity and frequency over the GBA mega-city appears to be weak. The enhanced TC precipitation can primarily be attributed to the strongly suppressed surface wind speed induced by the higher urban surface roughness, which intensifies low-level moisture flux convergence and supports increased TC rainfall over urban areas. Moreover, case study of special cases, such as TC Mangkhut and Goni, whose tracks did not directly pass through the city, reveal that AH can still increase TC precipitation in GBA urban areas after TC has moved away. New rainfall peak is observed only in AH300 when rainfall increases strongly during the last 10 hours, while no such an enhancement is found in AH0 and Nourban. This can be attributed to the rapid rebuilding of urban CAPE in AH300 after the TC passage, and also the abundant water vapor brought by TC in the city. Finally, model results also indicate that urban impact on rainfall increase is proportional to the “storm residence time” over the city, revealing a positive relationship between urban impact on urban TC accumulated rainfall and the duration of the TC residence time. Urbanization tends to enhance more precipitation in urban areas for TC with longer residence time to the city, this implies that slower or larger TCs may result in more considerable economic and human losses in coastal cities amid rapid urban development.

Appendix: Definition of TC rainfall-affected area

The TC rainfall-affected area was defined as follows: First, the azimuthally averaged TC rainfall is calculated for each case and experiment. Fig. A1a gives an example for TC Hal. It can be seen that rainfall is very weak in the eye, but reaches its maximum at around 75km from the TC center. Second, we define the TC rainfall period as one over which the storm rainfall, averaged within a 200 km radius, is greater than 5 mm/hr. Third, a TC rainfall profile, as a function of distance from the storm center, is computed by taking the mean of the azimuthally averaged rainfall over the TC rainfall period. Figure A1 shows the results for TC Hal, with black, blue, and red line representing Nourban, AH0, and AH300, respectively. Finally, the radius of the disk-shaped TC rainfall-affected area is defined as the threshold location beyond which rainfall is less than 5mm/hr (Kim et al. 2018). For TC Hal the radius is about 155 to 160km from 3 experiments (see Fig. A1b). More details for all cases and experiments are shown in Figure A2. For each TC case, the radius from the experiments are almost the same, with less than 5% difference between urban and Nourban. In other words, there is almost no urban impacts on the TC rainfall-affected size.

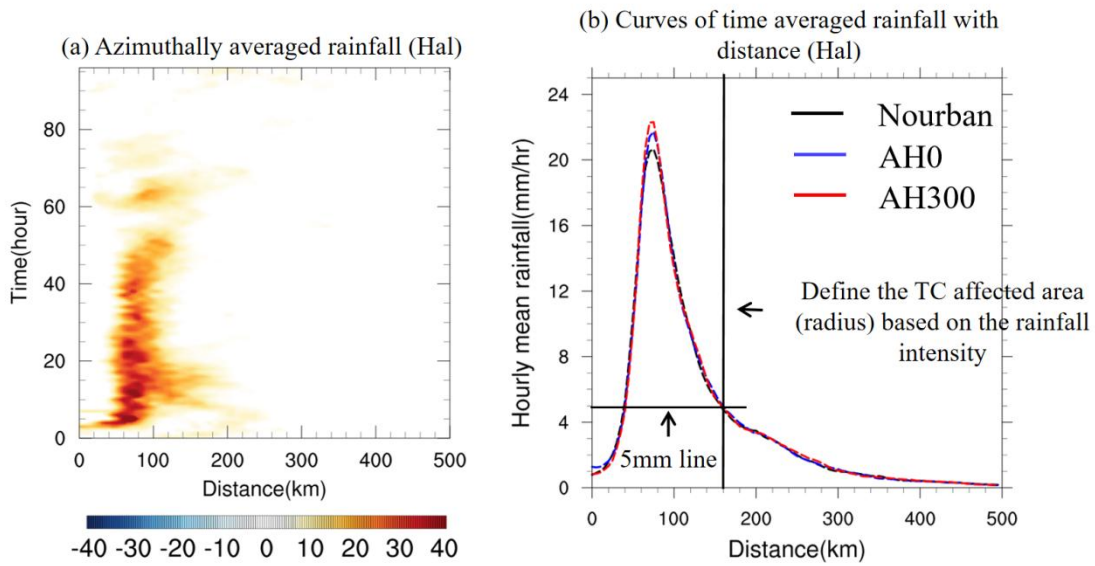


Figure A1 (a) Azimuthal averaged hourly rainfall for TC Hal, with X and Y axis representing distance to TC center and time. (b) Curves of time mean rainfall with distance to TC center for TC Hal, with black, blue and red lines mean Nourban, AH0, and AH300 experiments.

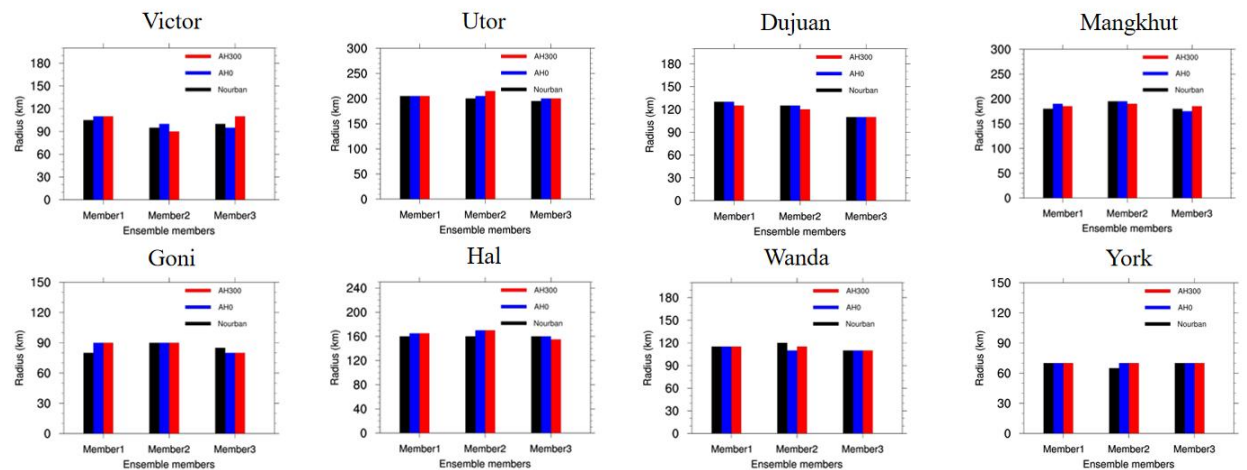


Figure A2 Radius of TC rainfall affected area in each case, experiment, and ensemble members.

3. Urban impact on winter extreme precipitation as inferred from observation and numerical simulation of two cases over the South China Greater Bay Area

3.1 Introduction

During the winter season, numerous studies have focused on the UHI effect in the GBA mega-city. Based on Landsat ETM thermal radiation data, it is demonstrated that the UHI-induced winter warming in Guangzhou metropolitan area significantly exceeds that due to global warming, primarily attributing it to industrial and transportation activities (Xiong et al., 2012). Observations indicate that the urban-rural temperature difference in winter is comparable to that in summer, and can reach 0.4 to 1.8K in major GBA mega-cities from 2000 to 2017, due to the vast city size and population, maintaining a rapid increasing trend (Hou et al., 2020). Remote sensing maps indicate an even stronger UHI intensity index in winter than in summer for Guangzhou metropolitan (Wang et al., 2007). Furthermore, Feng et al. (2012) found that AH has a greater influence on surface air temperature in winter than on urban land surface, with the opposite being true in summer. Notably, the diurnal profile is likely to differ between winter and summer in the GBA, as air conditioning systems lead to higher AH at summer night, while industry and traffic are the main contributors to AH in winter. Numerical simulation results also unveil that urbanization results in stronger upward surface sensible heat flux, increasing the temperature in GBA mega-cities by approximately 0.5 to 2K, particularly in the northwestern highly urbanized areas. (Luo et al., 2017). Overall, it is evident that the GBA mega-city experiences a high level of UHI during winter, which may still influence the local climate.

Additionally, due to the influence of the East Asian winter monsoon, extreme winter precipitation still occurs in coastal South China (SC), causing significant impacts on local

agriculture, transportation, human life, and the economy (Wang et al., 2018). Accumulated winter precipitation contributes to over 10% of the annual rainfall in SC, with heavy rainfall still occurring despite less favorable weather conditions compared to summer (Wang et al., 2011; Ge et al., 2016). Numerous studies have investigated the relationship between SC winter rainfall and factors such as the sea surface temperature (SST) in SCS, El Niño-Southern Oscillation (ENSO) and winter monsoon (Wang et al., 2000; Jia et al., 2017; Wang et al., 2022). The SC winter precipitation is sensitive to synoptic conditions such as large scale circulation over the western North Pacific as well as sea surface temperature in SCS (Wu et al., 2010; Chung et al., 2011; Ma et al., 2022). However, the local impact of rapid urban development in GBA on winter rainfall in SC remains uncertain. Generally, the atmosphere is drier in winter compared to summer, and coastal cities tend to exhibit a stronger urban drying island (UDI) effect during winter, with an increasing trend observed in recent decades (Liu et al., 2007; Luo et al., 2021). This may decrease local precipitation by reducing local moisture content in urban areas (Hand and Shepherd, 2009; Mote et al., 2007; Schlünzen et al., 2010; Liu et al., 2021; Hao et al., 2019; Du et al., 2019). For instance, Wang et al. (2009) found that precipitation decreased by about 19% in downtown and southern Beijing during the 1981-2000 fast-urbanization period compared to the 1961-1980 slow-urbanization period, which can be attributed to reduced water vapor content due to urban expansion. Similar results were found in GBA, with Cheng and Chan (2012) discovering that the urban land surface tends to reduce accumulated winter precipitation in GBA cities due to drier northerly winds and enhanced atmospheric stability. Luo et al. (2017) found that winter rainfall strongly decreased in the eastern part of GBA mega-city due to reduced latent heat in a numerical simulation focusing on a case from January 2 to 3, 2010.

Despite these findings, most studies have focused solely on long-term climatic accumulated winter precipitation, leaving the urban impacts on extreme winter rainfall characteristics under different weather conditions unexplored. In this work, we investigate: (1) how urbanization (the UHI effect and urban land use) affects winter rainfall characteristics in GBA mega-cities, and (2) whether urban impacts on winter heavy rainfall vary with different synoptic backgrounds. They are achieved by (1) examining the climatology of winter precipitation in GBA and UHI impact on extreme winter rainfall based on station observations, and (2) using WRF-UCM to dynamically downscale two specific winter extreme events with different weather conditions. Through various model experiments, we investigate the impacts of urban surface land use and the UHI effect on winter rainfall in GBA mega-cities. Specifically, we explore whether the UHI effect can also enhance winter extreme rainfall. These findings can fill gaps in winter extreme precipitation studies and urban climate in GBA, providing a scientific basis for policy makers regarding planning and public policy making for agriculture and transportation in the future.

3.2 Methodology

3.2.1 Observations and winter case study

In this study, we aimed to investigate the urban influence on winter precipitation using observational data from CMA (see Chapter 2.2.1). The locations of urban (red), rural (blue) stations are given in Figure 3.1(a), seven urban stations and seven rural stations in the GBA were further selected for analysis. To define the extended winter period for this study, we considered both temperature and precipitation. Figure 3.1 also presents the monthly mean temperature (b),

precipitation (c), and extreme precipitation (d) (99th percentile of hourly precipitation) for the 14 selected stations from 2008 to 2017. We standardized the parameters by recalculating surface temperatures at each station to sea-level values, using a temperature lapse rate of 0.6 K/100 m. The 10-year average temperature exhibits a decrease from November to January, reaching the lowest monthly average of approximately 14.5°C in January, and increasing to around 18°C in March. Meanwhile, the monthly mean accumulated rainfall (extreme rainfall) intensity from November to March ranged from 0.095 mm/hour (2.5 mm/hour) to 0.2 mm/hour (5 mm/hour). Similar intensities are observed for accumulated and extreme rainfall from November to February, with values not exceeding 0.1 mm/hr and 3 mm/hr. However, in March, these values reached 0.2 mm/hr and 5 mm/hr, showing a distinct difference from the other months. Based on these findings, we defined the extended winter season as November through February (NDJF).

Moreover, 27 extreme rainfall events were identified by applying the threshold of the 99th percentile of hourly extreme rainfall, averaged over the 14 stations. To further examine the impact of UHI effect on winter extreme rainfall, these events were further categorized into strong UHI cases and weak UHI cases. This classification was based on the temperature difference between seven urban and rural stations, averaged from one day prior to the hour of rainfall peak until the peak hour. 11 strong UHI cases (urban-rural temperature difference > 0.8°C) and 12 weak UHI cases (urban-rural temperature difference < 0.5°C) were selected.

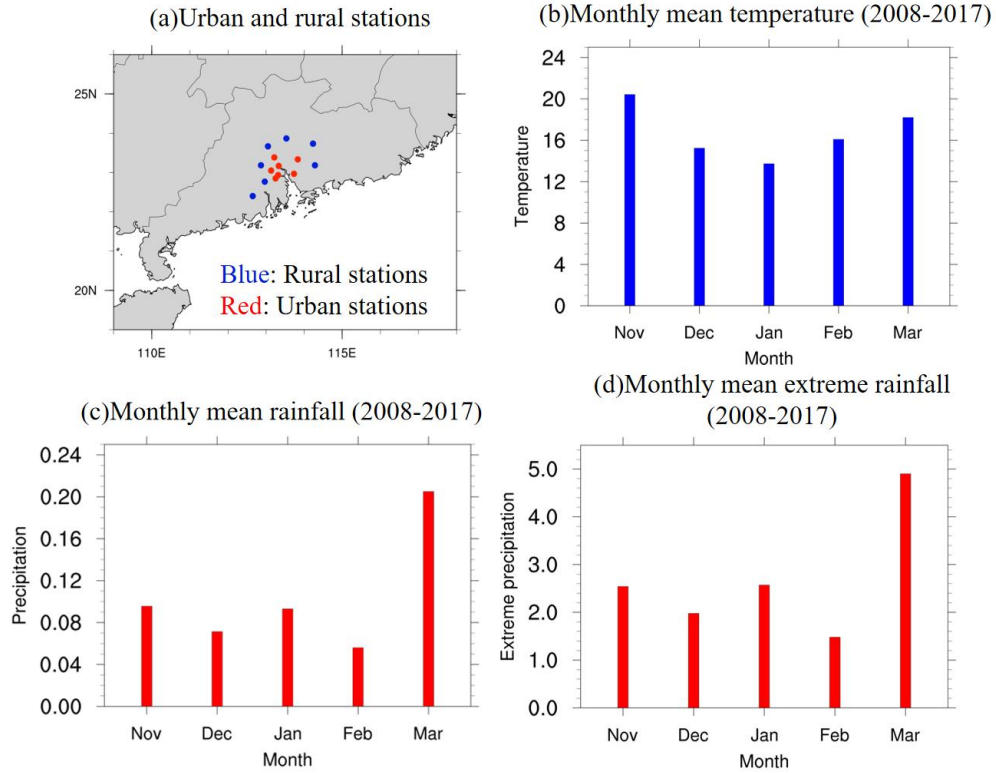


Figure 3.1 (a) Location of observation stations over South China, with red (blue) dots representing 7 urban (rural) stations. Monthly mean (b) temperature (units: $^{\circ}\text{C}$), (c) accumulated rainfall (units: mm/hr), and (d) extreme rainfall (99th percentile of hourly rainfall, units: mm hr) in November, December, January, February, and March averaged from 2008 to 2017 for all urban and rural stations.

3.2.2 WRF model configuration and two winter cases

In order to investigate the sensitivity of extreme winter precipitation to urbanization, the WRF model with the Advanced Research WRF (ARW) dynamical core version 3.8.1 was used to dynamically downscale two winter extreme rainfall cases using boundary conditions from ERA5 (Heshbach et al. 2020). Figure 2a shows the nested domains for the downscaling experiments, encompassing East Asia/western north Pacific ($2.23\text{-}43.82^{\circ}\text{N}$, $70.81\text{-}147.05^{\circ}\text{E}$, at $50\text{km} \times 50\text{km}$ grid spacing), South China ($19.94\text{-}27.09^{\circ}\text{N}$, $110.68\text{-}117.60^{\circ}\text{E}$, at $10\text{km} \times 10\text{km}$ grid spacing) and GBA ($21.5\text{-}23.83^{\circ}\text{N}$, $112.51\text{-}115.04^{\circ}\text{E}$, at $2\text{km} \times 2\text{km}$ grid spacing), with one-way nesting utilized. There are extending up to a height of approximately 10 hPa. The physical parameterizations in the

WRF include the use of the NOAH Land Surface Model (LSM) (for supporting SLUCM in the model environment (Chen et al., 2001; Tewari et al., 2008), the Rapid Radiative Transfer Model for General Circulation Model (RRTMG) for long-wave radiation (Iacono et al., 2008), the short wave radiation scheme by Dudhia (Dudhia 1989), the WRF single-moment 6-class microphysics scheme (Hong et al., 2006), Eta similarity theory for surface layer options (Janjic, 2002), the Bougeault-Lacarrere planetary boundary layer scheme (Bougeault and Lacarrere, 1989), and the simplified Arakawa-Schubert (SAS) GFS cumulus parameterization (Han and Pan, 2011; for the outermost domain only). To ensure that WRF can reproduce the same synoptic-scale circulation as in the driving data, spectral nudging was applied in the outermost domain for U, V wind above 500hPa, at the wavelength of about 1300km, which is commonly used in simulation (Gómez et al., 2017; Gómez et al., 2020).

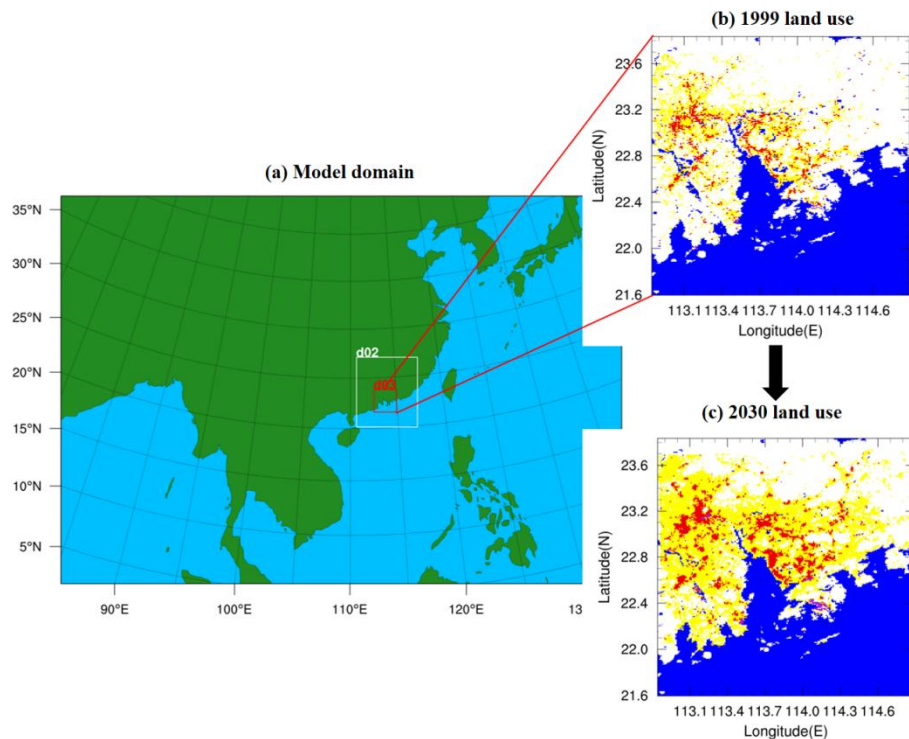


Figure 3.2 (a) Nested domains for the WRF simulations. (b) Land use categories of 1999 in the innermost domain with “Low Intensity Residence”, “High Intensity Residence”, and “Commercial and Industrial” locations indicated by yellow, red, and purple shading. (c) Same as (b) but for

projected 2030 urban land use.

In addition, dynamic downscaling was conducted for two winter extreme precipitation cases, namely Case 2013 (2013-12-13 to 2013-12-17) and Case 2015 (2015-12-05 to 2015-12-11), with a grid spacing of 2 km × 2 km. For each case, we executed ensemble integration with nine members at 1-hour intervals for the starting simulation time and averaged the results across all ensemble members.

3.2.3 UCM, Model Experiments, and Local Climate Zone (LCZ) Data

To assess the urban impact on winter extreme rainfall, four sets of experiments were designed utilizing the WRF model with varying land use configurations in the innermost domain. In the Nourban experiment, the urban land use was replaced by cropland; in the 99LS and 30LS experiments, urban land use information from 1999 and projected for 2030 in the GBA area was incorporated into the SLUCM; and in the 30LS-AH0 experiment, 2030 land use data with zero AH in the urban area was employed for dynamical downscaling. For the highly urbanized GBA region, we developed detailed land use/land cover change (LULCC) data for 1999 and a near-future projection for 2030 based on the World Urban Database and Access Portal Tools (WUDAPT) protocol (Ching and Mills, 2018; Wang et al., 2019). These datasets had a spatial grid spacing of 1 km × 1 km and were classified according to the local climate zone (LCZ) scheme (Stewart and Oke, 2012). The LCZ classification encompasses ten urban land use types (see Figure 3.3) including Compact High-Rise, Compact Mid-Rise, Compact Low-Rise, Open High-Rise, Open Mid-Rise, Open Low-Rise, Lightweight Low-Rise, Large Low-Rise, Sparsely Built, and Heavy Industry, as well as seven natural land use types: Dense Trees, Scattered Trees, Bush and Scrub, Low Plants, Bare Rock or Paved, Bare Soil or Sand, and Water (Steward

and Oke, 2012). Each LCZ type is associated with a unique set of UCM parameters and attributes (Stewart and Oke, 2014), such as surface albedo, building height, and sky view factor. These parameters were specifically tailored for the GBA mega-city. We prescribed urban land use information for the GBA in 1999 (the historical era) and 2030 (the projected near-future era) differently in the model (Wang et al., 2019).

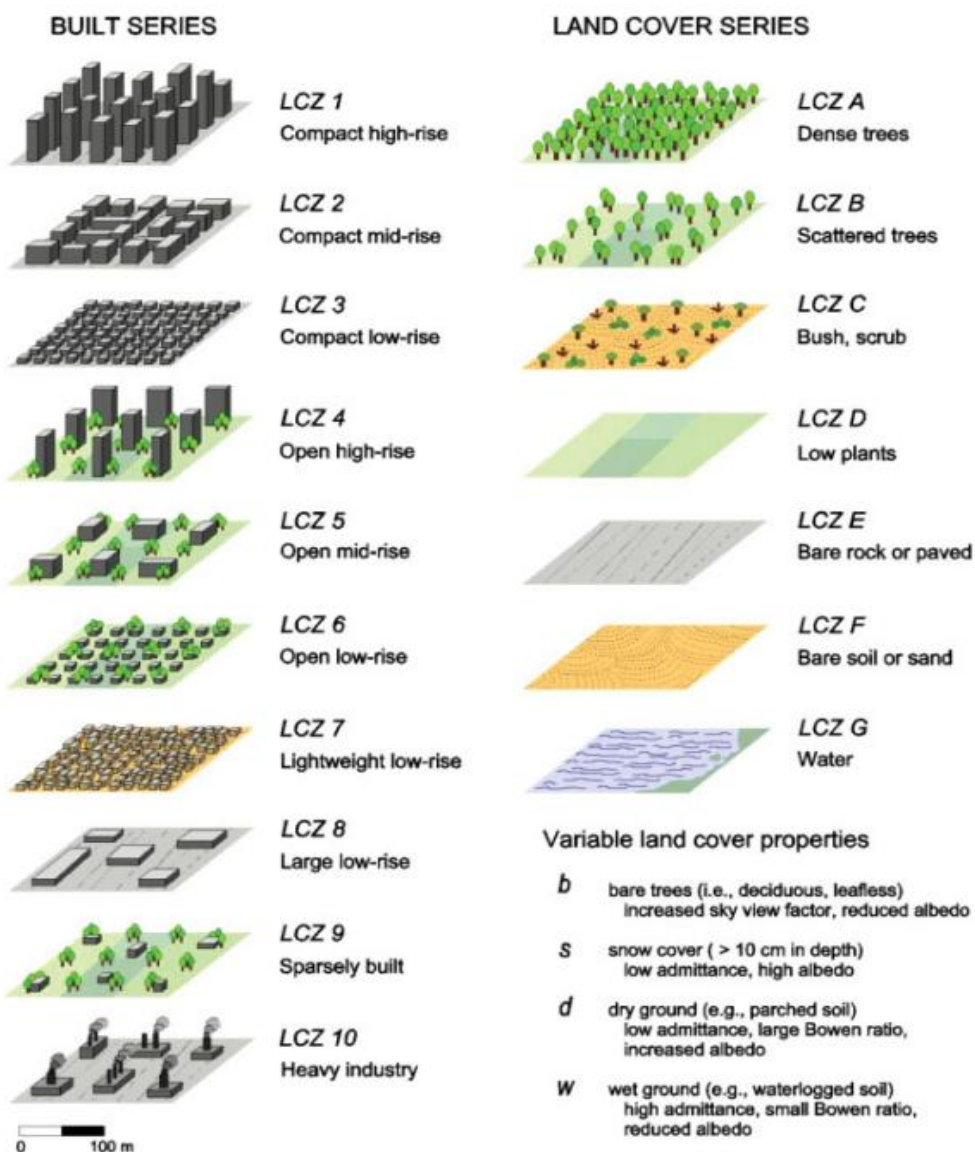


Figure 3.3 Land cover types from WUDAPT data, with LCZ 1 to 10 representing urban land use and LCZ A to G representing non-urban land use. (Source: Steward and Oke, 2012)

To project urban land use in the GBA for 2030, we employed the near-future LCZ maps developed by Huang et al. (2021). These projections utilized the Geographical Simulation and Optimization System (GeoSOS) - Future Land Use Simulation (FLUS) model (Liu et al., 2017; Chen et al., 2014) based on historical LCZ maps and the interactions between different land uses.

The process involved three main steps:

1. An Artificial Neural Network (ANN) was applied to learn the occurrence probability of each land use from historical LCZ maps, taking into account geographical factors such as slope, aspect, elevation, and distances to city centers, roads, and highways, as derived from current LCZ maps.
2. Future demands for urban land use and land cover changes were predicted based on demographic and socioeconomic development trajectories.
3. A Cellular Automata (CA) model was employed to simulate land use conversions using the current LCZ maps (2014 LCZ maps), with occurrence and neighborhood influence probabilities iterated until future demands were met. The CA model then generated the projected near-future maps.

To reduce complexity and prediction uncertainties, the ten urban LCZ types were consolidated into three categories: “Low Intensity Residence” (type 1) comprises Open Mid Rise, Open Low Rise, Sparsely Built, Open High Rise, Lightweight Low Rise, Large Low Rise; “High Intensity Residence” (type 2) comprise Compact Mid Rise; Compact Low Rise, and finally, “Commercial and Industrial” (type 3) includes both Compact High Rise and Heavy Industry. This regrouping was based on the AH values of each urban LCZ, with higher AH values corresponding

to more intensive land use types, e.g., Compact High Rise and Heavy Industry have the highest AH, which exceed 150W/m^2 , are regrouped as “Commercial and Industrial”. Urban LCZs with AH lower than 25W/m^2 are regrouped as “Low Intensity Residence” (see Wang et al., 2021; Hu et al., 2023). Table 3.1 presents the UCM parameters prescribed for these three land use types, with values derived from the WUDAPT project for GBA-based parameters and recalculated based on the new classification. Also shown in Figure 3.2 are the 1999 and 2030 urban land use distributions (after regrouping) in the innermost model domain, with yellow, red, and purple indicating type 1, type 2 and types 3 urban land use, respectively.

UCM parameter	Type1	Type2	Type3
Anthropogenic heat [W m^{-2}]	15.0	50.0	200.0
Building height [m]	13.31	14.01	53.92
Urban fraction	0.4	0.9	0.7
Standard Deviation of roof height [m]	10.42	5.64	33.18
Roof width [m]	38.01	14.28	35.5
Road width [m]	22.98	13.91	29.6
Surface albedo of road	0.2	0.17	0.18
Surface albedo of roof	0.142	0.165	0.115
Surface albedo of building wall	0.208	0.2	0.22

Table 3.1 Values of UCM parameters prescribed for three types of urban categories.

3.2.4 Model evaluation

To evaluate the performance of the WRF model, weather parameters from the model outputs were compared with station observations and ERA5 reanalysis data. Figure 3.4 displays

the surface temperature and U, V wind components derived from (a) ERA5 and (b) model output, averaged over Case 2013. In ERA5, a pronounced temperature gradient is observed from the north of the SC region to the ocean, with surface temperatures increasing from 2°C to over 20°C. Cold air is situated north of SC, while higher temperatures are evident in the GBA mega-city, reaching 13°C — significantly warmer than the surrounding rural areas, where temperatures range from 10-12°C. This enhanced temperature can be attributed to the UHI effect in the GBA mega-city. Simultaneously, prevailing northerly winds dominate the SC land area, leading to the intrusion of cold air into the region. Along the coast and over the ocean, these winds become northeasterly. The model's simulated surface temperature and wind patterns (Figure 3.4b) reasonably align with ERA5 data, capturing the temperature gradient and cold air distribution in the north of SC. However, the northerly wind north of GBA is slightly shifted to the west compared to ERA5. In addition, Figure 3.5 illustrates the low-level temperature and wind at 925 hPa, averaged over Case 2013, for (a) ERA5 and (b) model outputs. Similar to surface temperature, the reanalysis data exhibits a strong temperature gradient from north to south, with cold air located in the northern part of SC, ranging from 1-5°C. The UHI effect is notably weaker at the 925 hPa, with temperatures in the GBA urban area comparable to those in surrounding areas. The northerly winds in the north of SC transition to northeasterly winds in the SC and ocean regions. The model outputs exhibit accurate temperature and wind simulations for the SC area, demonstrating the model's reliability.

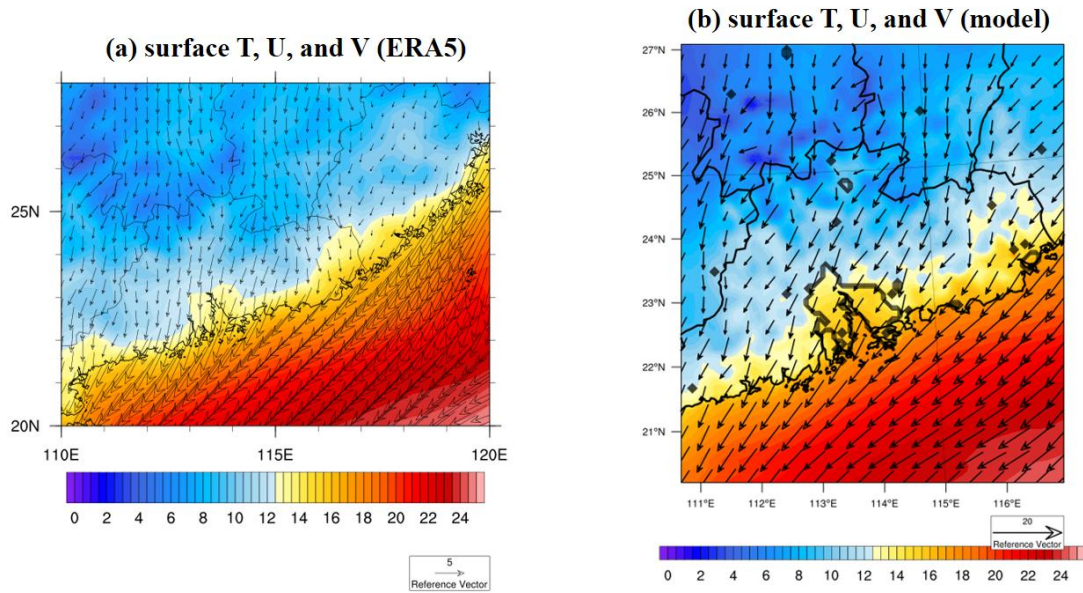


Figure 3.4 (a) Surface temperature (units: $^{\circ}\text{C}$), and U,V wind (units: m/s) averaged over Case 2013 from ERA5 reanalysis date, with shaded and vector representing temperature and wind. Black contours mean the coastline and boundary of province. (b) Same as (a) but for model outputs.

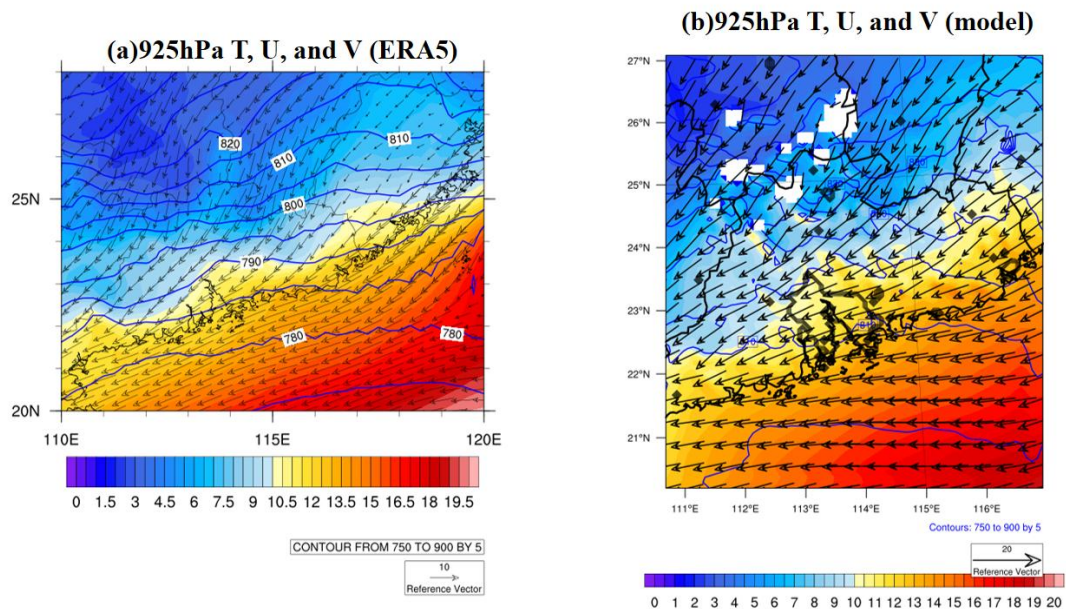


Figure 3.5 (a) 925hPa temperature (units: $^{\circ}\text{C}$), geopotential height (units: m), and U,V wind (units: m/s) averaged over Case 2013 from ERA5 reanalysis date, with shaded, blue contour, and vector representing temperature, geopotential height, and wind. Black contours mean the coastline and boundary of province. (b) Same as (a) but for model outputs.

Similar to Case 2013, Figure 3.6 and Figure 3.7 shows the temperature and wind at the surface and 925 hPa for ERA5 and model outputs, averaged over Case 2015. With regard to surface temperature and wind, the meteorological conditions in Case 2015 closely resemble those in Case 2013. For ERA5 data, prevailing northerly winds govern the entire SC region, and cold air is situated north of SC, with temperatures ranging from 5-8°C. However, during Case 2015, temperatures in GBA are higher than in Case 2013, reaching approximately 15-18°C in the GBA mega-city (see Figure 3.6). The model accurately reproduces the background surface winds in the SC area, demonstrating satisfactory performance in simulating the speed and direction of the northerly winds. Although the model slightly underestimates the temperature in the southern portion of SC compared to ERA5, the surface temperature performance in the GBA mega-city and the ocean remains reasonable. For the weather parameters at 925hPa, ERA5 data reveal that a cold center dominates north of SC, with temperatures between 2-5°C. The background winds are also similar to those in Case 2013, with northerly winds present north of SC and northwesterly winds found in the SC and GBA regions. The model's output of 925 hPa temperature in SC closely aligns with ERA5 data (see Figure 3.7), capturing the cold air center in the north of SC and the warmer temperatures along the coast. Furthermore, the wind direction and speed in the SC and oceanic regions simulated by the model are reasonable. In summary, the model's performance in reproducing surface and low-altitude weather parameters is deemed acceptable and reasonable for both cases. These results underscore the WRF model's ability to capture key meteorological features of the regional climate, providing a solid foundation for further analysis of urbanization impacts on winter extreme precipitation.

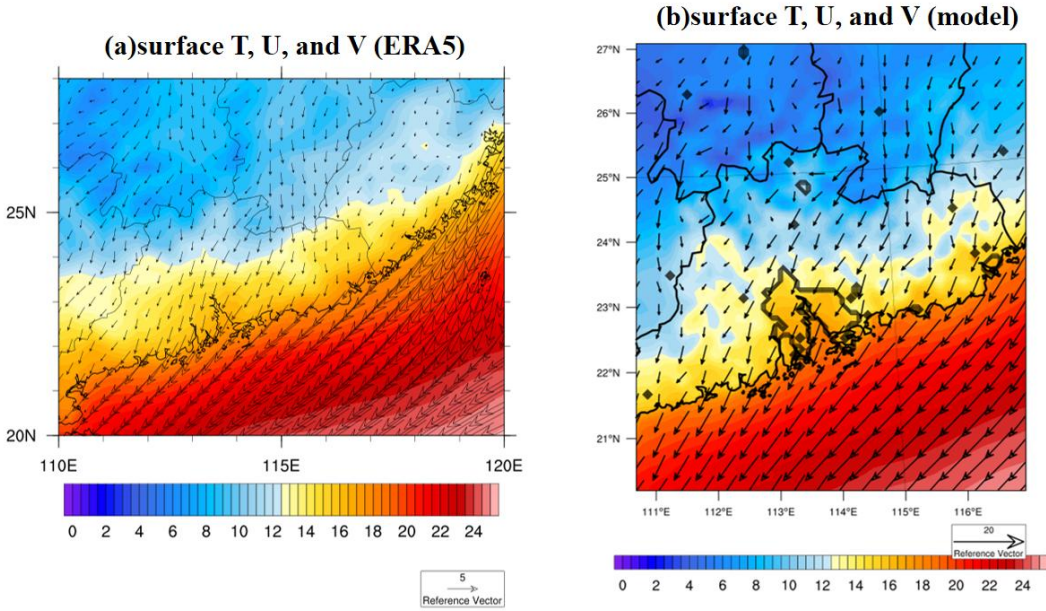


Figure 3.6 Same as Figure 3.4 except for Case 2015.

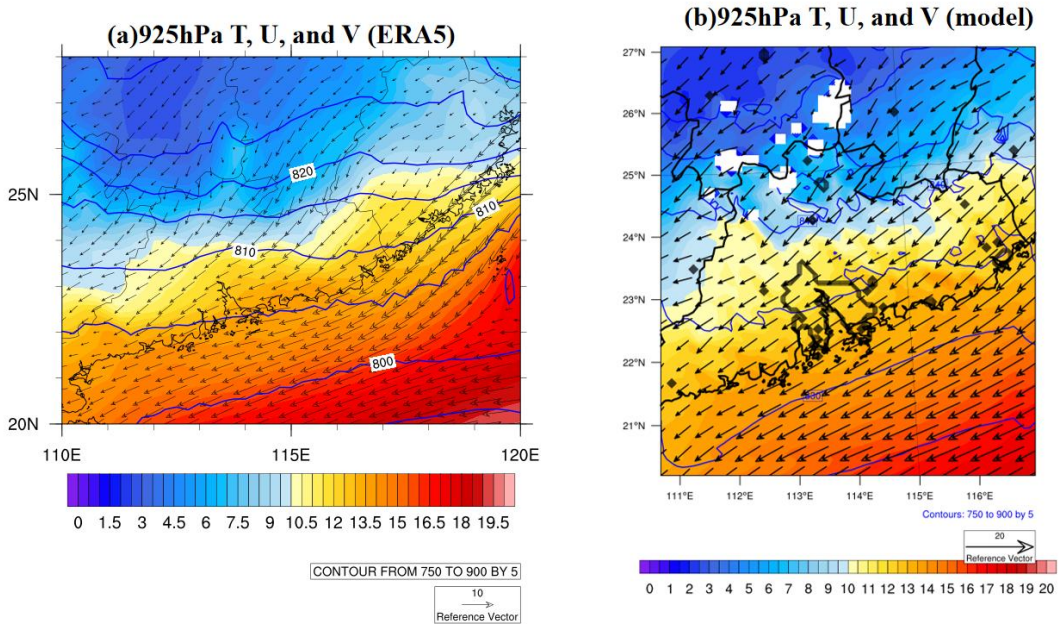


Figure 3.7 Same as Figure 3.5 except for Case 2015.

Moreover, an evaluation of the model's performance in simulating precipitation in the SC area has been conducted. Figure 3.8 presents the accumulated rainfall for Case 2013, derived from (a) model output, (b) ERA5, and (c) station observations. According to station observations, the most intense rain bands are situated in the northwestern and southwestern portions of the SC area,

reaching intensities of approximately 200 to 230 mm. Heavy rainfall is observed across the northern part of SC, with intensities between 100 and 150 mm in the GBA mega-city. Accumulated rainfall in the eastern part of SC is lower, with intensities ranging from 10 to 100 mm. The distribution and intensity of accumulated rainfall in the model output align with the observations. Strong rainfall is observed in the northern and northwestern parts of SC, and the model's performance is generally satisfactory throughout the SC area, particularly in the northern and eastern regions. However, the model significantly underestimates rainfall in the southwestern part of SC, which is likely due to the area's proximity to the model domain boundary. On the other hand, the simulated rainfall intensity over the GBA urban area closely matches the observations, only slightly underestimating the intensity over the southeastern and coastal areas of GBA.

For Case 2015, Figure 3.9 displays the accumulated precipitation in (a) model output, (b) ERA5, and (c) station observations. Based on station observations, heavy precipitation occurred in the eastern part of SC, with intensities between 140 and 180 mm. The most intense rain bands are located from central to northwestern SC. In the model outputs, the rain band shifts slightly towards the coastal area and extends across the entire coastal region of SC. The model results also overestimate the intensity in GBA and southwestern SC, with model cumulative rainfall reaching 150 mm in the GBA mega-city, while observed values range from 100 to 120 mm. However, the presence of strong rainfall over the GBA is deemed acceptable to support the study. In conclusion, the weather parameters of temperature, wind, and precipitation are well-simulated in the model for the two winter extreme events in the SC region. The model results are reasonable and comparable to station observations.

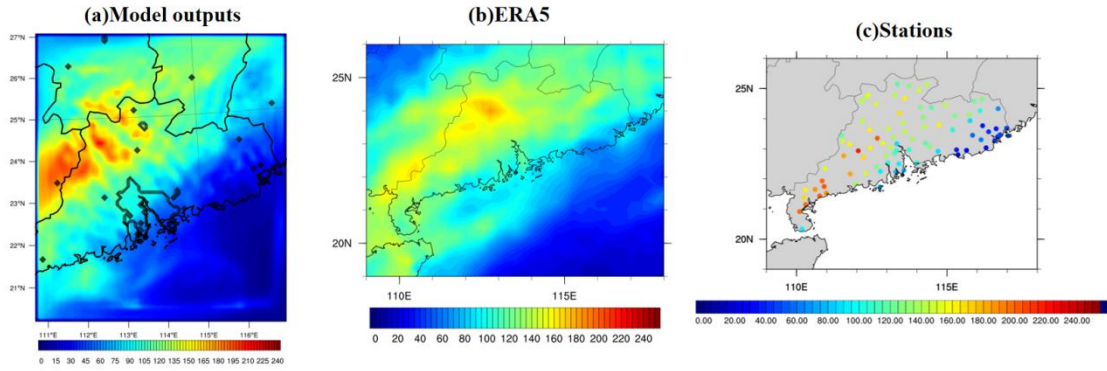


Figure 3.8 (a) Accumulated rainfall (units: mm) averaged over Case 2013 from model outputs. Black contours mean the GBA mega-city, coastline, and boundary of province. (b)(c) Similar to (a) but for ERA5 and station observations.

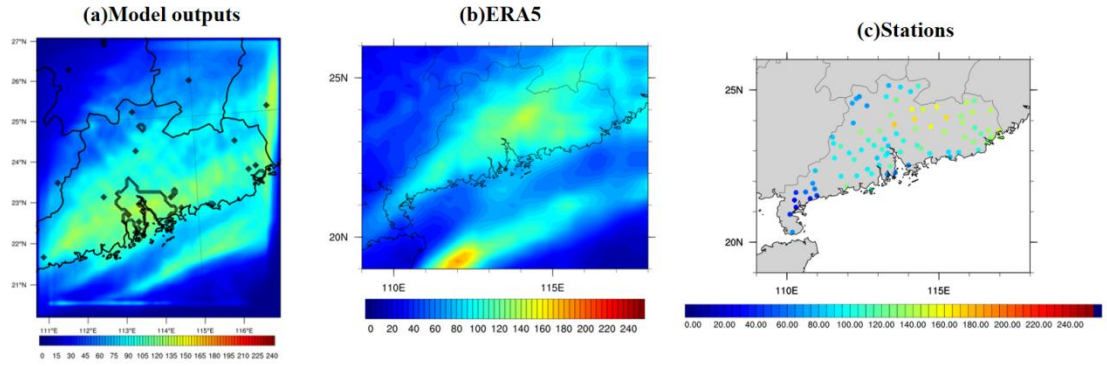


Figure 3.9 Same as Figure 3.8 except for Case 2015.

3.3 Results

3.3.1 Observation results

3.3.1.1 Winter temperature and precipitation

Figure 3.10 shows the winter temperatures from 2008 to 2017, including results from (a) observations and (b) ERA5. For observations, urban, rural, and other stations are shown in stars, diamonds, and dots, respectively. Winter temperatures exhibit a gradual decline from south to north, with maximum temperatures exceeding 18°C in the southern part of SC (Leizhou Peninsula)

and only reaching 12-13°C at inland stations located at 25°N. Coastal areas also exhibit warmer temperatures than their inland counterparts when comparing urban and surrounding rural stations, winter temperatures at urban stations range from 16.5 to 17.5°C, while rural stations exhibit temperatures only between 15.6 and 17°C. From 2008 to 2017, the temperature difference between all urban and rural stations was 1.02°C on average. Results from ERA5 are consistent with observations, revealing higher temperatures in the SCS area compared to the land area during winter, with temperatures exceeding 20°C. Land temperatures in the SC area gradually decrease from 19°C to below 10°C at 25°N. Moreover, the GBA exhibits higher temperatures than surrounding rural areas, with temperatures in the GBA mega-city ranging from 17 to 18.5°C, while temperatures in adjacent areas vary between 15 and 17.5°C. Given that urban areas consistently display higher temperatures than surrounding rural regions, a strong UHI is evident during winter in the GBA.

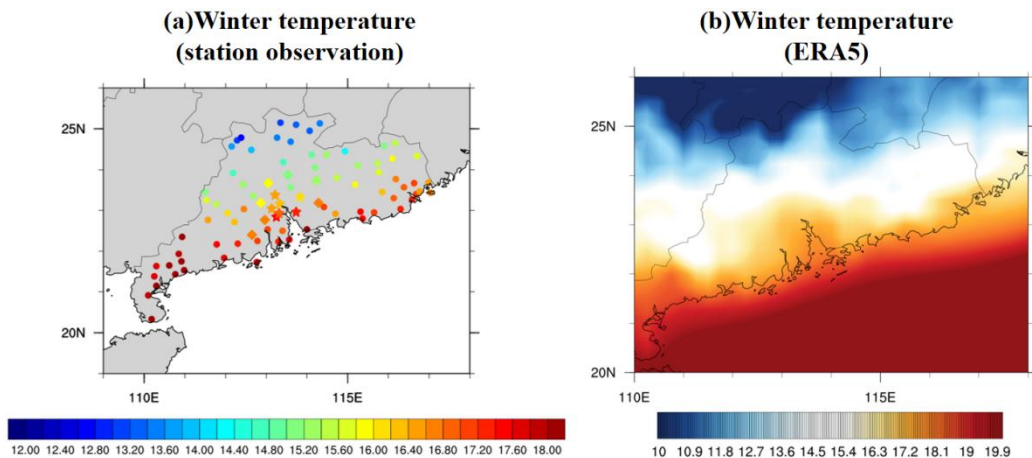


Figure 3.10 (a) Surface temperature (units: °C) averaged over winter from 2008 to 2017, with star means urban stations, and diamond means rural stations. (b) Winter temperature (units: °C) derived from ERA5 reanalysis data. Black contours mean the coastline and boundary of province.

Analysis of precipitation in SC reveals distinct patterns in extreme rainfall intensity during winter. Figure 3.11a shows the hourly winter extreme rainfall intensity, based on the 99th

percentile of hourly rainfall for the entire winter over the 10-year period (2008-2017) in SC derived from station observations, with seven urban and seven rural stations represented by stars and diamonds, and the other stations represented by dots. Extreme rainfall intensities during winter are highly variable, with only the southern part of SC experiencing intensities above 10 mm/hr. In contrast, urban areas exhibit lower extreme rainfall intensities, ranging from 6.5 to 7.75 mm/hr, compared to surrounding rural areas with intensities of 8.5 mm/hr or more. Also shown are the PDFs of hourly rainfall for urban and rural stations (Figure 3.11b). Rainfall probability in winter is generally lower than in other seasons, with frequencies of 1-10 mm/hr rainfall occurring less than 3% for both urban and rural locations. Notably, light rain (<16 mm/hr) is more probable in rural areas, with a decrease of about 30% to 5% in the 1-16 mm hr range compared to urban areas. However, heavy rainfall (>16 mm hr) is more likely in urban locations, with a 10% to 30% increase in the 16-28 mm hr range compared to rural areas. These observations suggest that the UDI effect induced by lower urban evaporation and humidity may contribute to the lower intensity and probability of rainfall in GBA mega-city relative to surrounding rural areas. Nevertheless, more frequent intense rainfall events exceeding 16 mm hr still occur in urban regions.

To further investigate the urban impact on very extreme winter precipitation, Figure 3.12 shows the (a) mean value of Rmax (annual maximum precipitation) from 2008 to 2017, and (b) the 99.99th percentile of hourly rainfall in SC derived from station observations. The distribution of Rmax and 99.99th percentile of hourly rainfall aligns with extreme rainfall (see Figure 3.11a) patterns, with the southern part of SC receiving the highest rainfall. Notably, urban stations, particularly Guangzhou, Foshan, and Dongguan, exhibit stronger Rmax intensities than their rural counterparts, reaching over 20 mm hr, while those in rural stations are only about 10-17 mm hr.

Similarly, the 99.99th percentile of hourly precipitation is more intense in urban areas, ranging from 18 to over 30 mm/hr, compared to 14-25 mm/hr in rural locations. Consequently, while the 99th percentile of hourly rainfall is suppressed in urban areas during winter, very extreme rainfall events like Rmax and the 99.99th percentile of hourly rainfall remain notably stronger in urban areas compared to rural areas, indicating a positive urban impact on winter extreme rainfall in GBA mega-city.

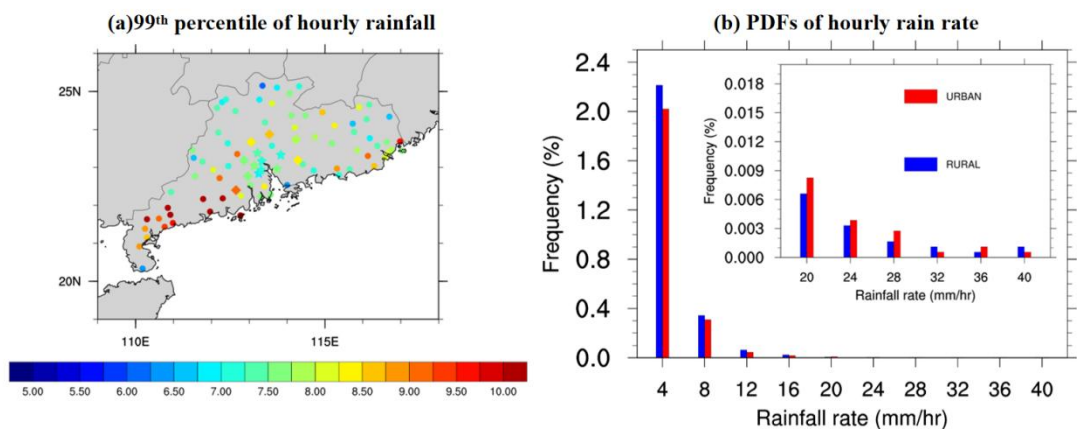


Figure 3.11 (a) Extreme rainfall based 99th percentile of hourly rainfall (units: mm/hr) during winter in each stations, with star means urban stations, and diamond means rural stations. (b) PDFs of hourly precipitation rates during winter for rural (blue) and urban (red) stations, within the ranges of 1-4, 4-8, 8-12, 12-16, 16-20, 20-24, 24-28, 28-32, 32-36, and 36-40 mm/hr.

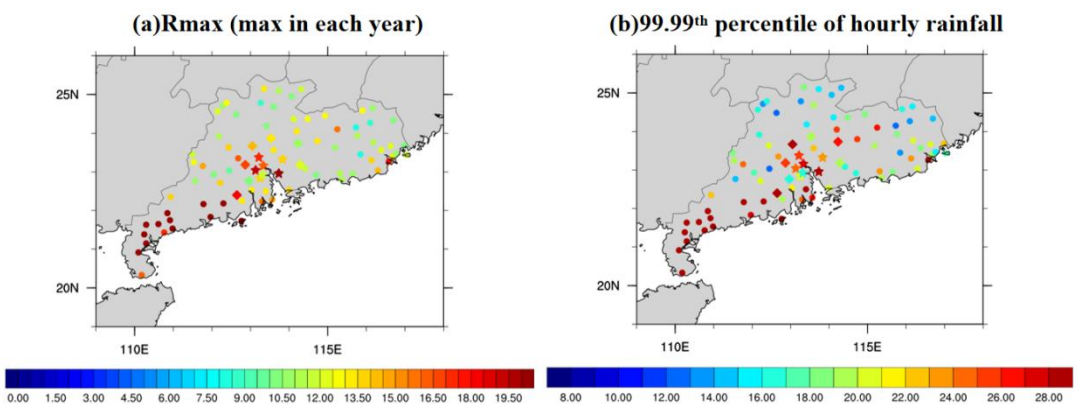


Figure 3.12 Same as Figure 3.11a except for (a) Rmax (units: mm/hr), annual maximum value in winter averaged from 2008 to 2017 in each station, and (b) Extreme rainfall based 99.99th percentile of hourly rainfall (units: mm hr) during winter.

3.3.1.2 Case study for UHI effect on winter precipitation

A total of 27 cases were selected based on the 99th percentile of winter extreme rainfall for urban and rural stations, with 11 (12) Strong (weak) UHI cases further classified. Figure 3.13 shows the composite time series of (a) temperature in urban and rural locations for strong UHI cases, (b) temperature in urban and rural locations for weak UHI cases, and (c) temperature difference between urban and rural locations for strong (red) and weak (blue) UHI cases. Time t=0 denotes the hour of peak rainfall averaged over the selected 14 stations. Both strong and weak UHI cases exhibit a gradual decrease in GBA temperatures during rainfall events, which is typically associated with cold air intrusion during winter rainfall. In strong UHI cases, urban (rural) temperatures decrease from 20.6°C (19.5°C) to 17.1°C (16.6°C) from t=-24 hours to t=20 hours. For weak UHI cases, urban (rural) temperatures decrease from 19.6°C (19°C) to 15.1°C (14.7°C) from t=-24hr to t=10hr. Before t=0, the urban-rural temperature difference is 0.8 to 1.1 K for strong UHI cases and 0.3 to 0.5 K for weak UHI cases. The onset of extreme rainfall suppresses the UHI effect in both cases, reducing the urban-rural temperature difference to 0.4 to 0.7 K for strong UHI cases and 0.2 to 0.5 K for weak UHI cases after t=0 hour. On the other hand, the distribution of temperature differences between strong and weak UHI cases is shown in Figure 3.14. Generally, the south-to-north temperature gradient is larger in SC for strong UHI cases compared to weak UHI cases, with higher temperatures in the southern part and lower temperatures in the northern part of SC. Notably, the GBA mega-city exhibits a more substantial temperature increase of 0.2 to over 0.5 K in urban locations, while the surrounding rural areas

show a negligible or even negative temperature difference. These results highlight the pronounced UHI differences between the two groups of cases.

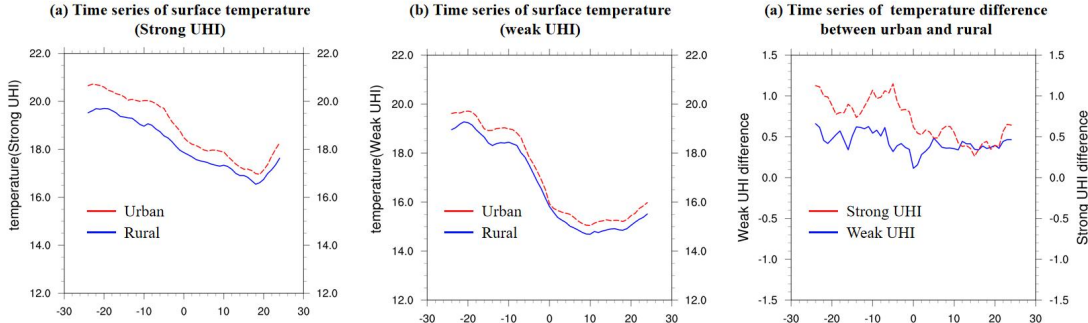


Figure 3.13 (a) Time series of surface temperature (units: $^{\circ}\text{C}$) averaged over urban and rural stations during all strong UHI cases, with red and blue line representing temperature in urban and rural stations. Time 0 refers to the peak rainfall hour averaged over the selected 14 stations. (b) Same as (a) except for surface temperature during weak UHI cases. (c) Time series of surface temperature difference (units: $^{\circ}\text{C}$) between urban and rural stations for strong and weak UHI cases, red and blue line mean results in strong and weak UHI cases.

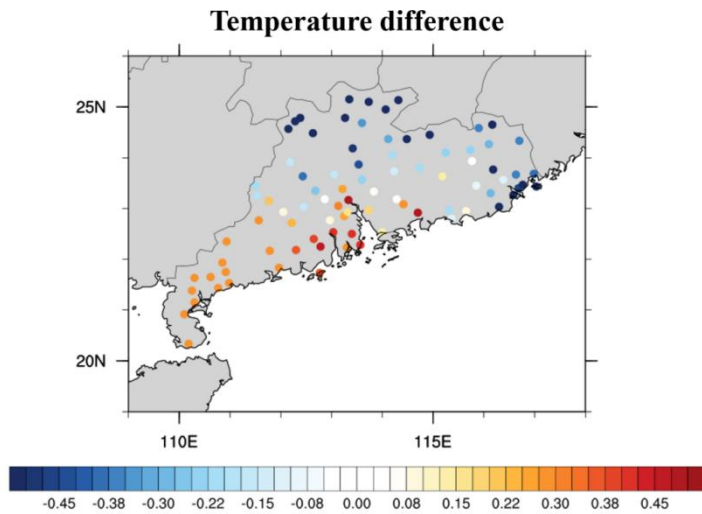


Figure 3.14 (a) Temperature difference (units: K) between strong and weak UHI cases in each station.

Based on an analysis of 11 strong and 12 weak UHI cases, this study investigates the impact of UHI on extreme winter precipitation across urban and rural locations in the GBA. The composite time series of hourly rainfall is presented in Figure 3.15 for (a) strong UHI cases, and

(b) weak UHI cases, with $t=0$ hour denoting the time of peak rainfall averaged over the 14 selected stations for all cases. and for all selected cases. For strong UHI cases, a higher precipitation intensity is observed in rural areas from $t=12$ h to $t=5$ h compared to urban areas, which could be attributed to the placement of some rural stations to the north of the city. These rural locations experience more precipitation before the peak hour due to the prevalence of frontal-related winter precipitation from the north. However, at $t=0$ hour, the rainfall intensity in urban locations reaches 5.5 mm/h, while it amounts to only about 3.2 mm/h in rural areas. Urban areas exhibit stronger precipitation from $t=2$ h to $t=7$ h in comparison to rural areas. For weak UHI cases, similar patterns emerge, with higher rainfall in rural areas preceding the peak hour. Yet, the rainfall difference between urban and rural locations remains marginal at $t=0$ hour, with urban and rural areas experiencing 4 mm/h and 3.6 mm/h, respectively. This difference rapidly diminishes to negative values after $t=2$ hours. These findings indicate that precipitation differences between urban and rural areas are more pronounced in strong UHI events than in weak ones, implying that the UHI effect can influence extreme winter precipitation intensities in the GBA mega-city.

The PDFs of hourly rainfall over urban stations for strong and weak UHI cases are depicted in Figure 3.15c. Although the probability of very light rainfall (1-3 mm/h) decreases by more than 20% in strong UHI cases compared to weak ones, the hourly urban rainfall probability across nearly all ranges (except 24-27 mm/h) is higher in the strong UHI case. For rainfall intensities between 3 mm/h and 24 mm/h, the probability increases by approximately 5% to over 200%, particularly for hourly rainfall exceeding 15 mm/h, which is considered extremely heavy rainfall during winter. Overall, the observations indicate that the UHI effect may still enhance the intensity and likelihood of extreme rainfall events in the GBA urban area, even though urban areas

generally receive less winter precipitation than rural areas due to the lower evaporation and humidity of urban land surface.

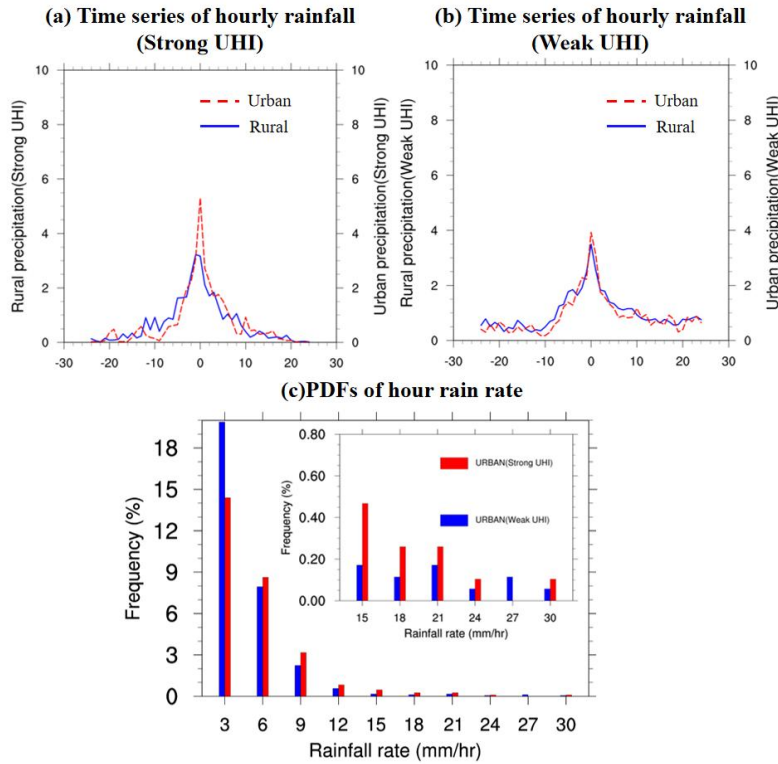


Figure 3.15 (a) Time series of hourly rainfall (units: mm/hr) averaged over urban and rural stations during all strong UHI cases, with red and blue line representing rainfall in urban and rural stations. Time 0 refers to the peak rainfall hour averaged over the selected 14 stations. (b) Same as (a) except for weak UHI cases. (c) PDFs of hourly precipitation rates in urban stations for weak UHI (blue) and strong UHI (red) cases, within the ranges of 1-3, 3-6, 6-9, 9-12, 12-15, 15-18, 18-21, 21-24, 24-27, and 27-30 mm/hr.

3.3.2 Results based on numerical modeling

3.3.2.1 Synoptic background for two cases

Based on the 99.9th percentile of hourly rainfall in GBA, two extreme winter rainfall events were selected and dynamically downscaled within the SC region and GBA. Figure 3.16 shows the snapshots of ERA5-derived low-level (925hPa) temperatures, U and V winds, and geopotential heights during days of peak rainfall for Case 2013 and Case 2015 (refer to the time in the figure title). For Case 2013, it is evident that the prevailing low-level winds north of SC are

northerly before the rainfall, while SC experiences easterly winds. A significant temperature gradient exists from north to south, with temperatures ranging from 3°C to 13°C, and ocean temperatures lying between 12°C and 20°C. The geopotential height gradient is relatively relaxed over SC. However, during the rainfall event, cold air infiltrates SC, leading to an increased temperature gradient and negative temperatures in the northern part of SC. The temperature over the GBA urban area is only about 6-8°C. On December 16th, a stronger northerly wind appears over the entire SC landmass, replacing the prevailing easterly wind. This northerly wind, associated with the advancement of cold air towards the SC coastline, forces the easterly winds to retreat to the ocean, resulting in a strong cold front over SC. Notably, the geopotential height gradient becomes much denser in the SC area during rainfall events, corresponding to the rapid movement of cold air. The invasion of cold air and the approach of cold fronts primarily contribute to the extreme winter precipitation in the western part of SC for Case 2013.

Similar to Case 2013, Figure 3.17 displays snapshots of low-level (925 hPa) temperature, U and V winds, and geopotential height derived from ERA5 during the day of peak rainfall for Case 2015. At 12:00 p.m. on December 8th, the prevailing wind direction across the SC region is from the east, with strong northeasterly winds over the ocean. A cold center with temperatures around 0-2°C is present north of SC, accompanied by weak northerly winds. During the extreme rainfall event, the cold air does not move south to SC, although the northerly winds strengthen over time. Temperatures in the GBA mega-city range from 12°C to 14°C, while the cold air center remains north of SC. Nonetheless, strong northerly winds persist east of SC during the rainfall. These winds flow into powerful easterly winds over the ocean, creating a convergence zone and surface front along the SC coastline. This front coincides with the location of extreme rainfall in

the eastern part of SC. It is also worth noting that the geopotential height gradient remains loose on December 9th, associated with a weaker temperature gradient in SC.

In summary, surface fronts induced by northerly winds from land and easterly winds from the ocean cause extreme rainfall in GBA cities for both Case 2013 and Case 2015. However, the synoptic backgrounds of the two events differ, and in Case 2015, cold air does not dominate the cities, resulting in varying temperatures within the GBA. Consequently, further research will investigate (1) the potential role of urban impact on winter extreme rainfall, and (2) whether this influence varies under different synoptic backgrounds.

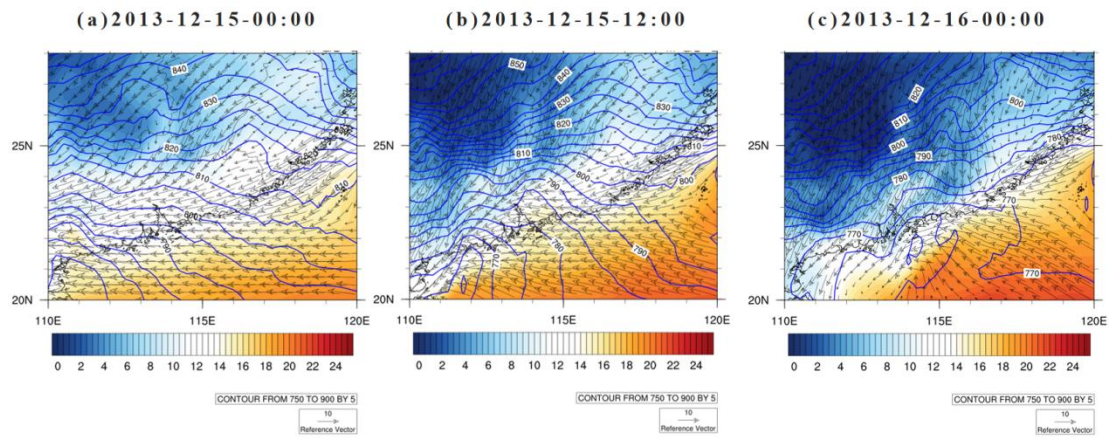


Figure 3.16 Snapshot of 925hPa temperature (units: $^{\circ}\text{C}$), geopotential height (units: m), and U,V wind (units: m/s) for Case 2013 from ERA5 reanalysis date at (a) 2013-12-15-00:00, (b) 2013-12-15-12:00, and 2013-12-16-00:00, with shaded, blue contour, and vector representing temperature, geopotential height, and wind. Black contours mean the coastline and boundary of province.

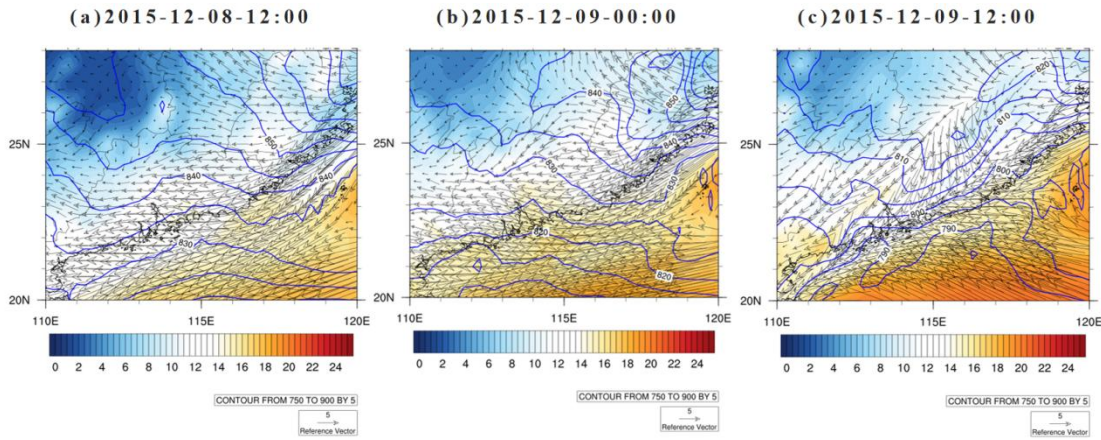


Figure 3.17 Same as Figure 3.16 except for Case 2015.

3.3.2.2 Temperature results

Figure 3.18 shows the 2m temperature differences between (a)30LS and Nourban, (b)30LSAH0 and Nourban for Case 2013, averaged over the rainfall period. The black contours delineate the boundary of the 2030 GBA mega-city. In Case 2013, urbanization results in surface warming of approximately 0.5 to 1K in the GBA urban area, primarily in the northeastern and southwestern regions where major cities such as Guangzhou (113.29E, 23.13N), Shenzhen (114E, 22.32N), and Hong Kong (114.17E, 22.3N) are situated. However, the warming induced by urbanization is minimal in the northern part of the city, particularly at the northern boundary of the GBA mega-cities, with temperature differences around 0-0.3K. Intriguingly, certain areas exhibit significant temperature decreases due to urbanization, which can be attributed to the replacement of water bodies in Nourban with low-intensity residential areas in 30LS, leading to reduced surface thermal capacity. Urbanization-induced temperature differences are also minimal in rural and marine areas, with a mere 0.2 to 0.3K of AH-induced warming in the Greater Bay, downstream of the region associated with prevailing surface northerly winds. Additionally, the temperature changes caused solely by urban land use are shown in Figure 3.18b, revealing

minimal temperature differences across the entire GBA mega-city.

In contrast, Figure 3.18 also presents 2m temperature differences for Case 2015 between (c)30LS and Nourban, and (d)30LSAH0 and Nourban. A temperature increase of over 1K is observed across nearly the entire GBA urban area, with a warming of 0.3-0.5K in the downstream ocean area due to urbanization. Nonetheless, the temperature difference remains weak at the city's northern boundary, and the temperature increase at the northern and eastern boundaries does not exceed 0.5K. Warming in the surrounding rural and marine areas due to urbanization is also minimal. In Case 2015, urban land use substantially increases surface temperatures in the northwestern part of the urban area, as shown in Figure 3.18d. Major GBA cities, such as Guangzhou and Foshan, experience temperature increases of about 0.4 to 0.8K, while most urban areas exhibit a temperature increase of approximately 0.3K due to urban land use alone.

To further examine temperature changes resulting from urbanization, Figure 3.19 presents vertical profiles of urban temperature differences for (a) Case 2013 and (b) Case 2015, averaged over the rainfall period. The black, blue, and red lines represent the temperature differences between 99LS and Nourban, 30LSAH0 and Nourban, and 30LS and Nourban, respectively. The largest urban temperature differences occur at the 1000 hPa level, with differences between 99LS, 30LSAH0, 30LS, and Nourban reaching 0.03K (0.43K), 0.28K (0.75K), and 0.4K (0.85K) for Case 2013 (Case 2015). In Case 2013, all temperature differences decrease rapidly with height from the 1000 hPa to 925 hPa layer, with negative values above the 950 hPa level for all urban experiments. The UHI is highly suppressed even in 30LS, exhibiting a decrease of about 0.12K at 925 hPa compared to Nourban. The UHI then gradually increases to 0 above the 850hPa level. Conversely, although the UHI also decreases with height in Case 2015,

the temperature differences remain positive between the 1000 hPa and 800 hPa levels for all urban experiments compared to Nourban, and the UHI is nearly suppressed to 0 above the 800 hPa level.

In summary, while urbanization leads to increased urban surface temperatures in both Case 2013 and Case 2015, the warming is more pronounced in Case 2015. In contrast, the temperature difference resulting solely from urban land use is minimal in Case 2013. Additionally, the UHI effect is substantially suppressed in Case 2013, which is associated with strong northerly winds and cold air intrusion. This suggests that temperature changes due to urbanization are highly sensitive to the synoptic background during winter, which varies under different synoptic conditions.

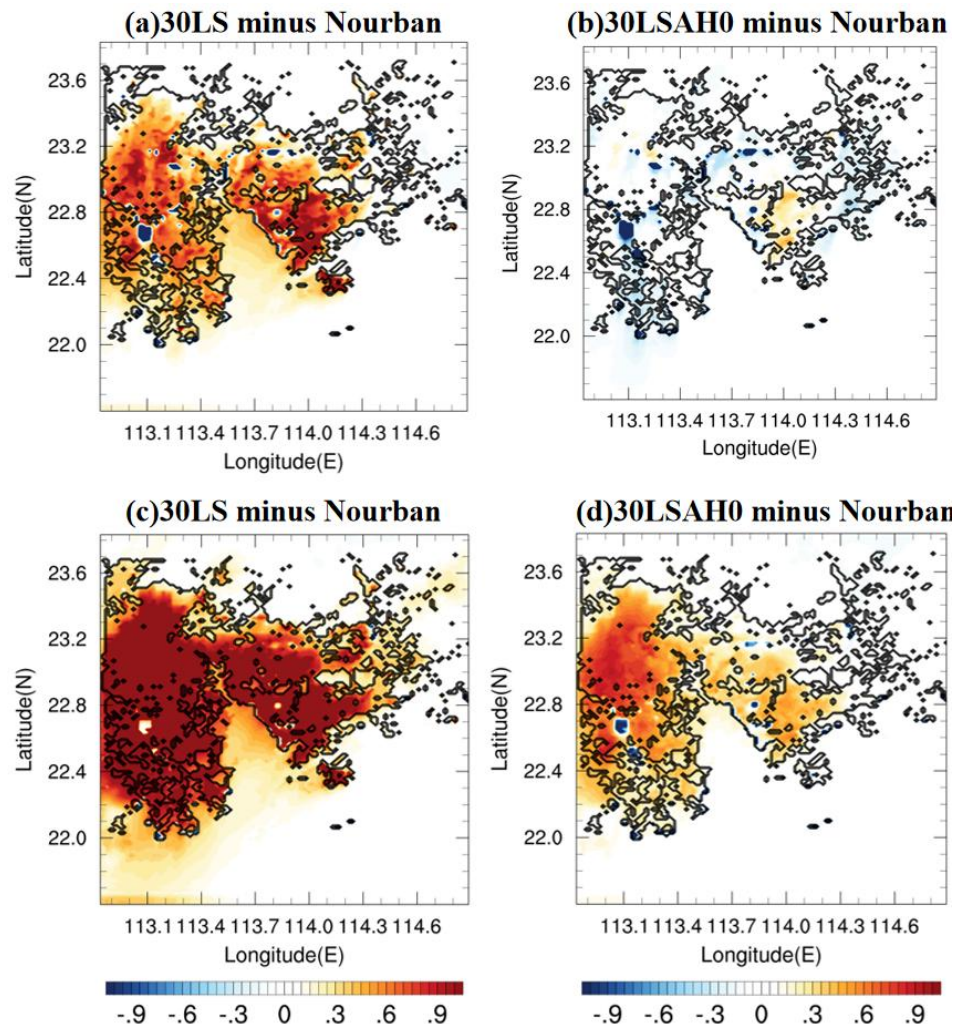


Figure 3.18 2m temperature difference (units: $^{\circ}\text{C}$) between (a) 30LS and Nourban and (b) 30LSAH0 and Nourban for Case 2013. Temperatures are computed by averaging over rainfall period. See text for details. The coastline is shown by black line. (c) (d) Same as (a) (b) except for Case 2015.

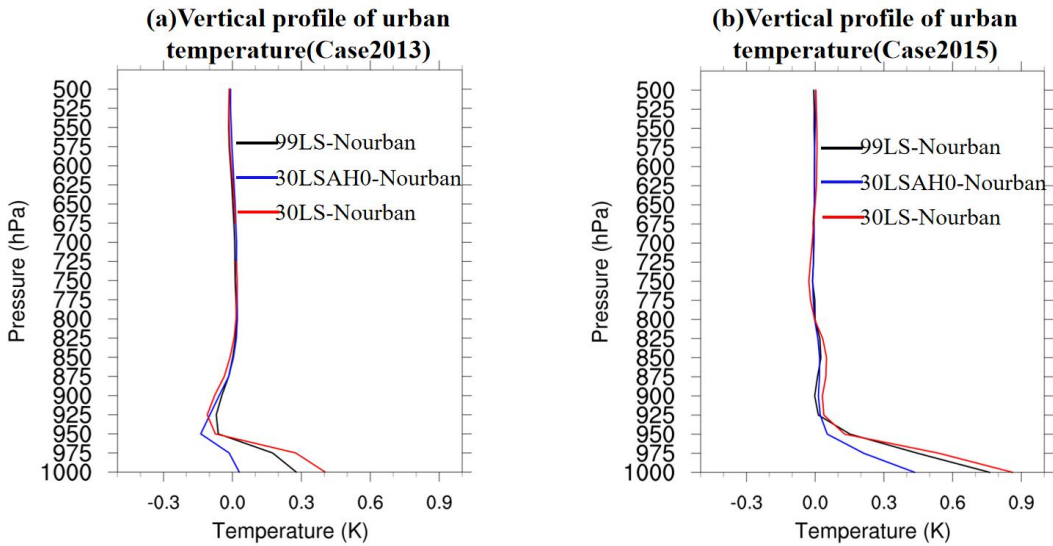


Figure 3.19 Vertical profile of urban temperature difference (units: K) averaged over rainfall period for (a) Case 2013, and (b) Case 2015 from 1000hPa level to 500hPa level. Black, blue, and red line represent the temperature difference between 99LS and Nourban, 30LSAH0 and Nourban, and 30LS and Nourban.

3.3.2.3 Precipitation results

Figure 3.20 shows the accumulated rainfall difference between (a) 99LS and Nourban, (b) 30LS and Nourban, and (c) 30LS and 30LSAH0 for Case 2013, with black contours delineating the 2009 and 2030 GBA mega-city boundaries. Statistically significant differences (95% confidence level) are indicated by black dots. In urban areas, both 99LS and 30LS exhibit substantially lower precipitation intensities than Nourban, with the western and central parts of the city experiencing significantly reduced accumulated precipitation, exceeding -2 mm/day. Precipitation variability in surrounding rural and oceanic regions is highly irregular, but 30LS still displays enhanced precipitation in the eastern part of the city and the downwind

area. AH does not augment precipitation in urban areas, and its influence on precipitation changes is weak, with most urban areas experiencing less than 0.5 mm/day differences. Precipitation is enhanced only in specific oceanic areas downwind of the city, with differences reaching 1.5 mm/day.

Figure 3.21 illustrates the accumulated rainfall differences for Case 2015 between (a) 99LS and Nourban, (b) 30LS and Nourban, and (c) 30LS and 30LSAH0. In contrast, urbanization markedly intensifies precipitation in the central, eastern, and southern GBA mega-city. For 30LS, precipitation enhancement ranges from 1.5 to 2.5 mm/day in the southern and eastern urban areas compared to Nourban, with most enhanced precipitation areas passing the 95% significance threshold. However, rainfall changes are minimal in the northwestern part of the city. Notably, decreased rainfall is observed in the oceanic downstream areas. Furthermore, AH enhances precipitation across the entire urban region, with increases varying from 1 to 2.5 mm/day. Despite this, signals over most areas do not pass the 95% significance level, and significant precipitation enhancement is only observed in the city's southwestern portion. In contrast, AH has a negligible effect on precipitation in the surrounding rural and marine areas. To better understand precipitation enhancement, Figure 3.22 showcases snapshots of hourly precipitation for (a) 99LS, (b) 30LS, (c) Nourban, and (d) 30LSAH0 during the hour of peak urban rainfall. In Nourban, precipitation spans the entire land area and part of the ocean within the innermost domain, with intensities ranging from approximately 4 to 12 mm/hr. Heavy rainfall occurs in the southern GBA land area and the Greater Bay. Hourly peak rainfall intensity ranges from 4 to 8 mm hr in the northern and central GBA. Conversely, 99LS and 30LS exhibit significantly enhanced rainfall across the entire GBA mega-city, with the central and eastern regions receiving increased rainfall from 4-8 mm hr

in Nourban to 6-14 mm/hr in 30LS. Relative to Nourban, 30LSAH0 features stronger precipitation in the city's central region, but rainfall intensity diminishes in the southern portion and the ocean. AH also boosts rainfall in most urban areas at the hour of peak rainfall.

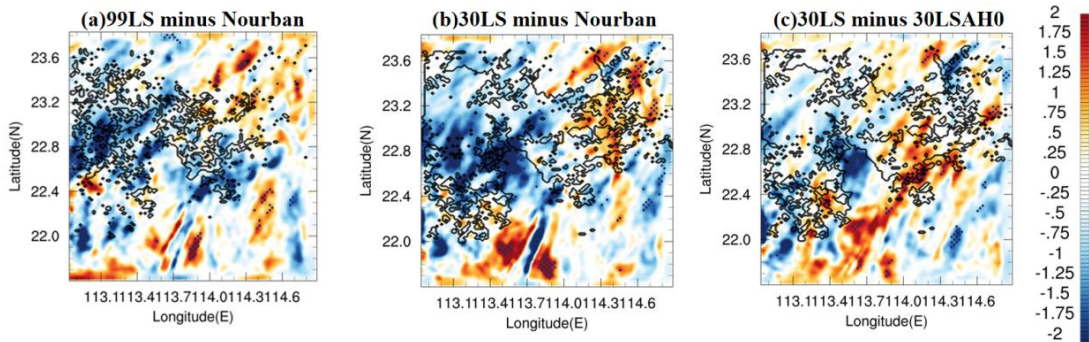


Figure 3.20 Daily accumulated rainfall (units: mm/day) difference between (a) 99LS and Nourban, (b) 30LS and Nourban, and (c) 30LS and 30LSAH0 for Case 2013. Black contours represent the boundary of 1999 and 2030 GBA mega-city. Locations in which the difference exceeds the 95% significance level are denoted by black dots.

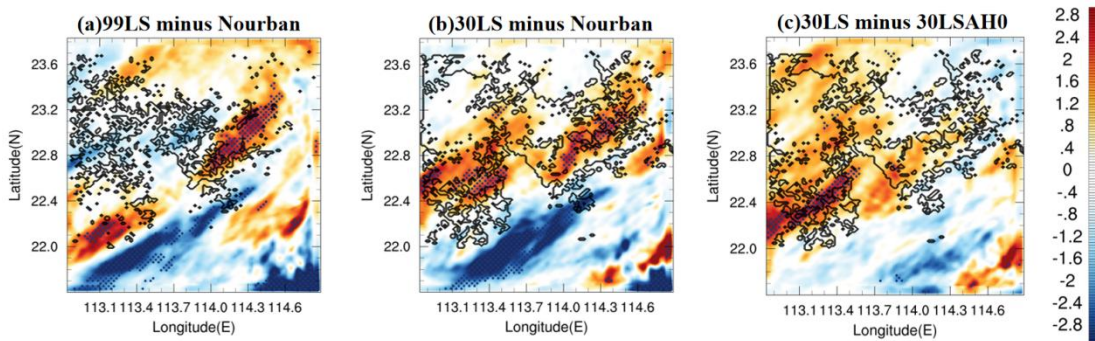


Figure 3.21 Same as Figure 3.20 except for Case 2015.

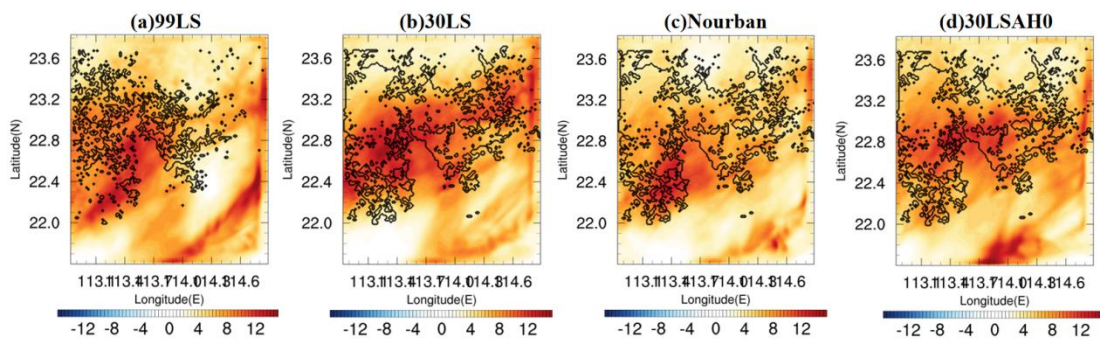


Figure 3.22 Snapshot of hourly rainfall (units: mm/hr) distribution at the rainfall peak hour for (a) 99LS, (b) 30LS, (c) Nourban, and (d) 30LSAH0. Black contours represent the boundary of 1999

and 2030 GBA mega-city.

Figure 3.23 examines the influence of urbanization on precipitation characteristics during Case 2013 by displaying (a) time series of urban rainfall and (b) PDFs of urban hourly rain rates for each experiment. Nourban, 99LS, 30LSAH0, and 30LS are represented by black, blue, green, and red lines (bars), respectively. The observed differences in urban hourly rainfall across experiments are minimal, with disparities not exceeding 0.1 mm/h during the initial peak rainfall period from $t=45$ to $t=60$ hours. The hourly rainfall difference between 30LS and 30LSAH0 is also negligible, suggesting that AH exerts a weak impact on urban hourly rainfall during Case 2013. PDFs of urban hourly rain rates reveal a mild urban effect on very light rainfall, while Nourban experiences more frequent rainfall than urban experiments (99LS, 30LSAH0, and 30LS) for rates between 3 and 15 mm/h. However, the decrease in rainfall probability due to urbanization is also modest, ranging from 5% to 30% less. In contrast, urban experiments exhibit higher probabilities of rainfall exceeding 20 mm/h, particularly 99LS, though the results are not robust due to the small absolute rainfall probabilities. Consequently, the urban influence on winter precipitation during Case 2013 is weak and potentially negative for the GBA mega-city.

For Case 2015, Figure 3.24 presents analogous plots for (a) time series of urban rainfall and (b) PDFs of urban hourly rain rates. Urban rainfall commences at $t=70$ hours, peaking at $t=93$ hours. Peak precipitation intensities for Nourban, 99LS, 30LSAH0, and 30LS are 7 mm/hr, 8 mm/hr, 8 mm/hr, and 8.7 mm/hr, respectively, with the difference between 30LS and Nourban at peak hours being significant at the 95% confidence level according to the Student's t-test. Nevertheless, urban precipitation enhancement is robust only from $t=90$ to $t=95$ hours. The

PDFs of urban hourly rain rates indicate that urbanization increases rainfall frequency over the GBA mega-city. Comparing urban experiments (99LS, 30LSAH0, and 30LS) to Nourban, rainfall occurrence rates rise for hourly rainfall across all ranges (except 3-6 mm/hr), particularly for rates exceeding 12 mm/hr. For hourly rain rates between 10 and 25 mm/hr, frequency increases markedly by 30% to 80% in 30LS compared to Nourban. Moreover, without AH in urban areas, 30LSAH0 exhibits decreased hourly rainfall probabilities across most ranges relative to 30LS, though it still outperforms Nourban in terms of rainfall frequency. Hence, urbanization enhances both rainfall intensity and probability over the GBA mega-city during Case 2015. In summary, despite employing identical model configurations, the impact of urbanization on winter precipitation varies between cases. Results demonstrate that during Case 2013, urbanization exerts a weak influence on precipitation intensity and probability in cities, even producing a negative effect on hourly precipitation probability within the 3-20 mm/hr range. In contrast, during Case 2015, urbanization significantly intensifies both rainfall metrics, with the UHI effect primarily driving this enhancement.

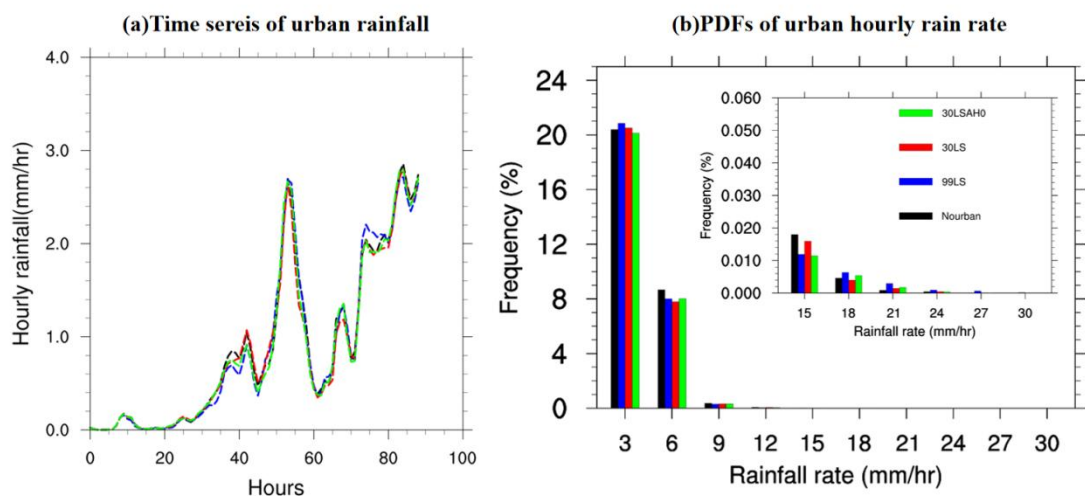


Figure 3.23 (a) Time series of hourly rainfall (units: mm/hr) over urban locations within GBA area for Nourban (black), 99LS (blue), 30LSAH0 (green), and 30LS (red) for Case 2013 based on

model simulation. (b) PDFs of hourly precipitation rates over urban locations within GBA, within the ranges of 1-3, 3-6, 6-9, 9-12, 12-15, 15-18, 18-21, 21-24, 24-27, and 27-30 mm/hr for the Nourban (black), 99LS (blue), 30LSAH0 (green), and 30LS (red) experiments.

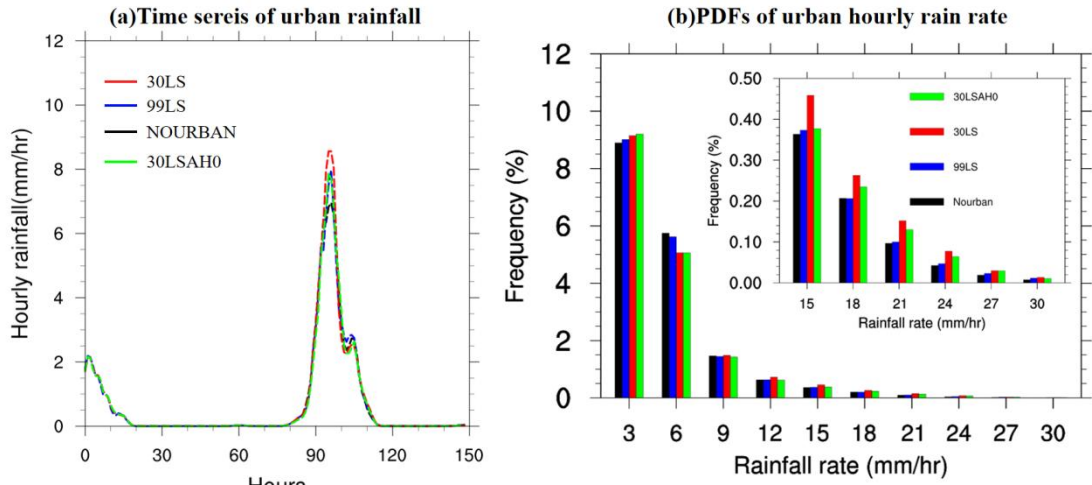


Figure 3.24 Same as Figure 3.23 except for Case 2015.

3.3.2.4 Mechanism of urban impact on winter precipitation

To elucidate the varying urban precipitation changes under different synoptic backgrounds due to urbanization, we further investigated the mechanisms underlying urban influence on winter precipitation. Figure 3.25 shows the difference in average surface evaporation during precipitation periods between 30LS and Nourban in Case 2013. The findings reveal that surface evaporation driven by urban land use is lower across the GBA mega-city than that associated with natural land use. This reduction can be attributed to impermeable surfaces in urban areas, with decreased surface evaporation occurring solely in these regions. Consequently, a decline in water vapor is observed at the surface and in the lower atmospheric layers of urban areas.

Moreover, Figure 3.26 presents the (a) south-to-north and (b) west-to-east cross-sections of vertical specific humidity and wind vector differences between 30LS and Nourban for Case

2013, with the black line in the inset figure denoting the cross-sectional plane. It is evident that specific humidity decreases markedly at the surface and lower layers due to urbanization, with reductions ranging from 0.04 to 0.08 g/kg in both directions. Conversely, enhanced southerly winds are observed above 2 km over the southwestern portion of the GBA, resulting in a slight increase in specific humidity. However, this enhancement is limited to the southwestern and eastern areas of the GBA and remains weak overall. The substantial reduction in water vapor content within the lower layers of the urban atmosphere, stemming from weakened surface evaporation, primarily accounts for the decreased precipitation in the GBA mega-city during Case 2013. Concurrently, urban temperatures are considerably suppressed throughout Case 2013 as cold air dominates the entire synoptic condition, leading to a weakened UHI (see Figure 3.18a,b). Although the UHI effect still contributes to slightly enhanced southerly winds and humidity above 2 km altitude in the southern part of the GBA mega-city, its impact is not comparable to the drying of the lower atmosphere induced by the UDI effect and is insufficient to support urban precipitation.

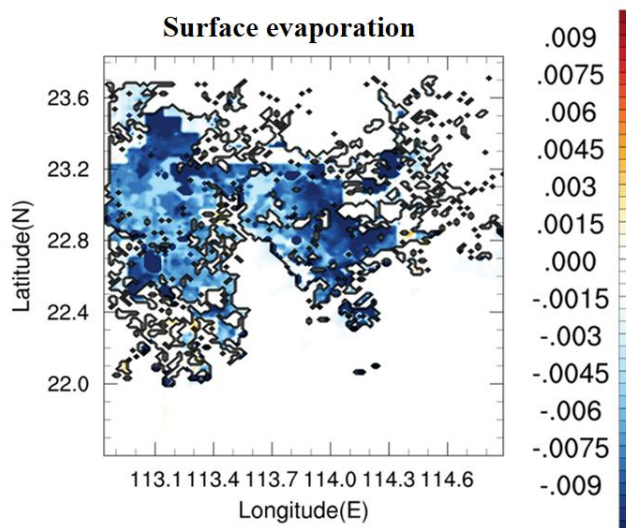


Figure 3.25 Surface evaporation difference (units: $\text{g/m}^2/\text{s}$) between 30LS and Nourban averaged

over precipitation periods for Case 2013. Black contour represents the 2030 GBA mega-city.

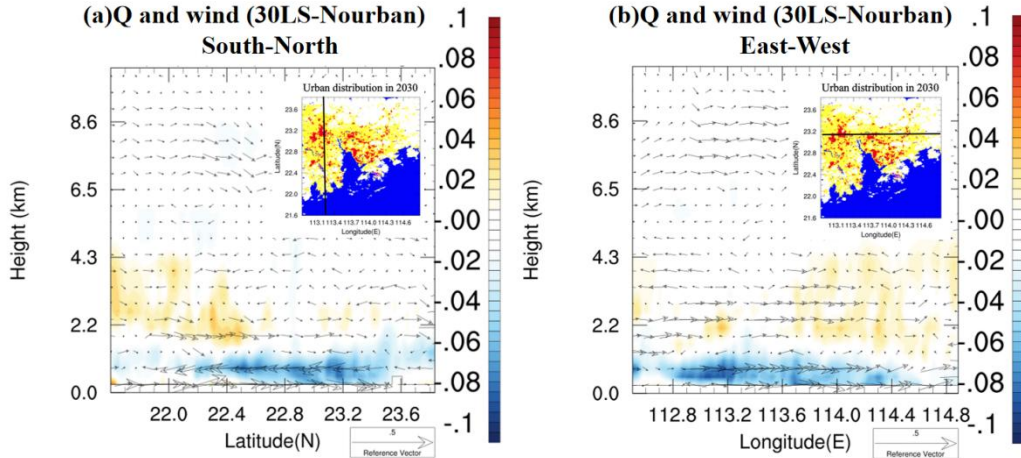


Figure 3.26 (a) South-to-North cross-section of difference of hourly vertical wind vector (units: m/s) and specific humidity (units: g/kg), averaged over the rainfall period of Case 2013, between 30LS and Nourban. Black line in the inset figure represents the location of cross-sectional plane. (b) Same as (a) except for East-to-West cross section.

However, in Case 2015, the UHI persists, as shown in Figure 3.18 and Figure 3.19. Figure 3.27a gives the surface wind in 30LS, averaged over the rainfall period. During this period, prevailing northerly winds dominate the entire GBA, with wind speeds reaching 3-4 m/s on land and 5-6 m/s over the ocean. Figure 3.27 also presents the wind speed and wind vector differences between (b) 30LS and Nourban, and (c) 30LS and 30LSAH0 for Case 2015, with shaded areas representing wind speeds and vectors indicating wind direction. Compared to Nourban, 30LS exhibits stronger northerly (northwesterly) winds in the northeastern (northwestern) part of the GBA mega-city, with wind speeds intensifying by approximately 0.3 to 0.5 m/s. Northerly winds are significantly weakened to the south of the city, and stronger southerly winds are observed over the ocean compared to Nourban. The influence of AH on surface wind is depicted in Figure 3.27c (30LS minus 30LSAH0), which demonstrates a considerable

enhancement of northwesterly winds over the entire urban area and stronger southerly winds over the ocean. We propose that both the UHI effect and urban surface contribute to surface wind changes, with the former yielding a larger (smaller) temperature gradient between urban and northern rural areas (ocean areas), thereby accelerating (decelerating) the prevailing surface northerly winds over the northern part of the urban area (southern part of the urban area and ocean area). The latter results in reduced wind speeds in urban areas due to increased urban surface roughness. By altering circulation, urban influence also promotes greater water vapor convergence and convection in urban areas, ultimately enhancing precipitation.

Regarding low-level wind, Figure 3.28 displays the 850 hPa wind speed and wind vector in 30LS, averaged over the rainfall period. In contrast to surface winds, the 850 hPa winds shift from northerly to southeasterly and southerly over the GBA. The differences in wind speed and wind vector between (b) 30LS and Nourban, and (c) 30LS and 30LSAH0 for Case 2015 are also depicted. Urbanization is shown to lead to significantly stronger southeasterly winds over the ocean and the southeastern portion of the GBA mega-city, which can further increase water vapor supply from the ocean to urban areas. Conversely, when considering only the impact of AH (30LS minus 30LSAH0), enhanced southeasterly winds are observed over the ocean and nearly the entire GBA mega-city compared to Nourban, which can also result in a more humid atmosphere and support rainfall.

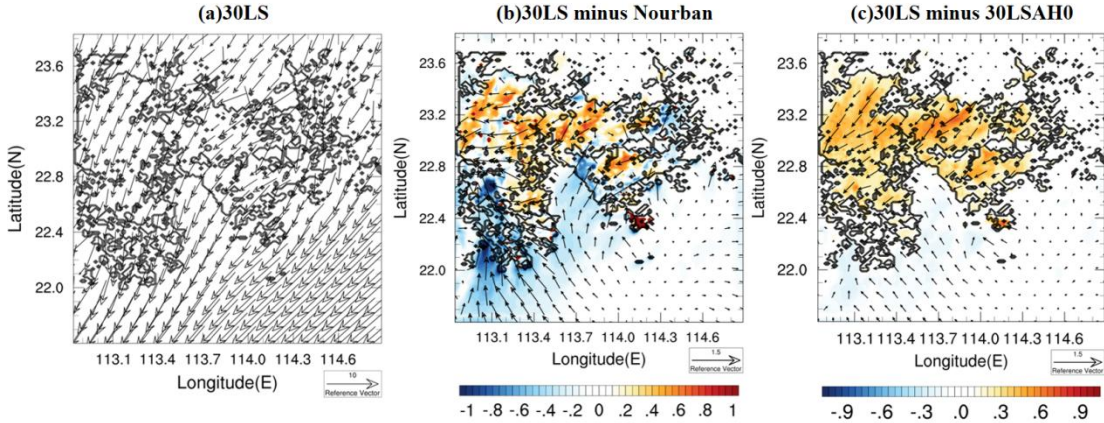


Figure 3.27 (a) Surface wind in 30LS, averaging over the rainfall period of Case 2015, black contour represents the 2030 GBA mega-city. (b) Surface wind speed difference and wind difference between 30LS and Nourban, averaging over rainfall period, with the wind speed difference and wind difference showing by shaded and vector. (c) Same as (b) except for difference between 30LS and 30LSAH0.

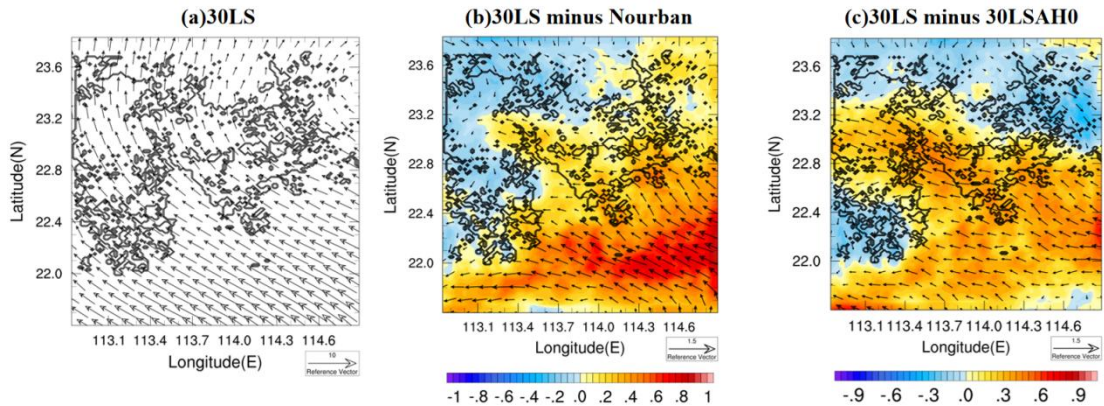


Figure 3.28 Same as Figure 3.27 except for 850hPa wind.

In order to further explore the urban impacts on local circulation and humidity during Case 2015, Figure 3.29 presents the south-to-north cross-section of vertical specific humidity and wind vector differences averaged over the rainfall period between (a) 30LS and Nourban, and (b) 30LS and 30LSAH0. The black line in the inset figure represents the cross-section plane. It is noteworthy that for 30LS, specific humidity below 1.5 km height decreases due to the lower urban surface evaporation and the strengthening of synoptic northerly winds. However, increased humidity is observed at near-surface levels from 22N to 22.6N,

attributable to the strengthening of southerly winds south of the GBA mega-city caused by the UHI effect. Furthermore, elevated water vapor content is found above 1.5 km throughout the urban area, particularly from 22.8 to 24N, with a specific humidity increase of approximately 0.04 to over 0.1 g/kg compared to Nourban. This enhanced humidity is associated with intensified low-level southerlies supplying water vapor to urban areas from the ocean. If only AH impact is considered (see Figure 3.29b), the enhancement of specific humidity at near-surface levels and above 1.5 km becomes more pronounced than in Figure 3.29a, while the drier airflow caused by stronger northerly winds between 500 m and 1.5 km altitude weakens.

Cross-sections of specific humidity and wind in other directions are also examined. Figure 3.30 illustrates the west-to-east cross-section of vertical specific humidity and wind vector differences averaged over the rainfall period between (a) 30LS and Nourban, and (b) 30LS and 30LSAH0. Compared to Nourban, the specific humidity slightly decreases at low levels in 30LS, but a significant enhancement of water vapor content is observed above the height of 2 km, with an increase of approximately 0.4 to 1 g/kg spanning almost the entire area. Concurrently, stronger easterly winds are detected at altitudes of 2 to 4.5 km in 30LS compared to Nourban, aligning with the enhanced southeasterly winds over the urban area. When comparing 30LS and 30LSAH0, the AH impact results in a dramatic increase in specific humidity and intensified easterly winds in the western part of the GBA mega-city. Additionally, a slight enhancement of specific humidity near the surface in 30LS compared to 30LSAH0 can be attributed to increased wind convergence due to AH.

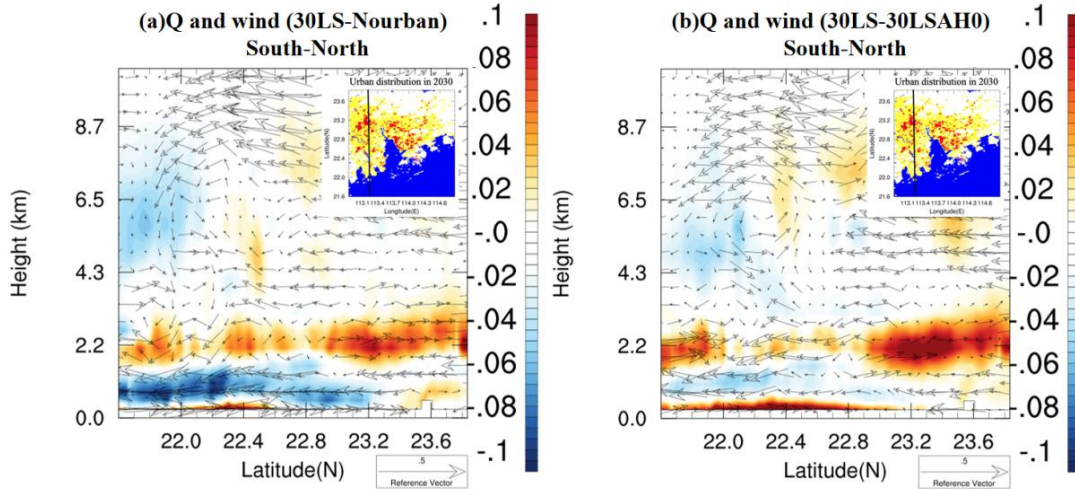


Figure 3.29 (a) South-to-North cross-section of difference of hourly vertical wind vector (units: m/s) and specific humidity (units: g/kg), averaged over the rainfall period of Case 2015, between 30LS and Nourban. Black line in the inset figure represents the location of the cross-sectional plane. (b) Same as (a) except for difference between 30LS and 30LSAH0.

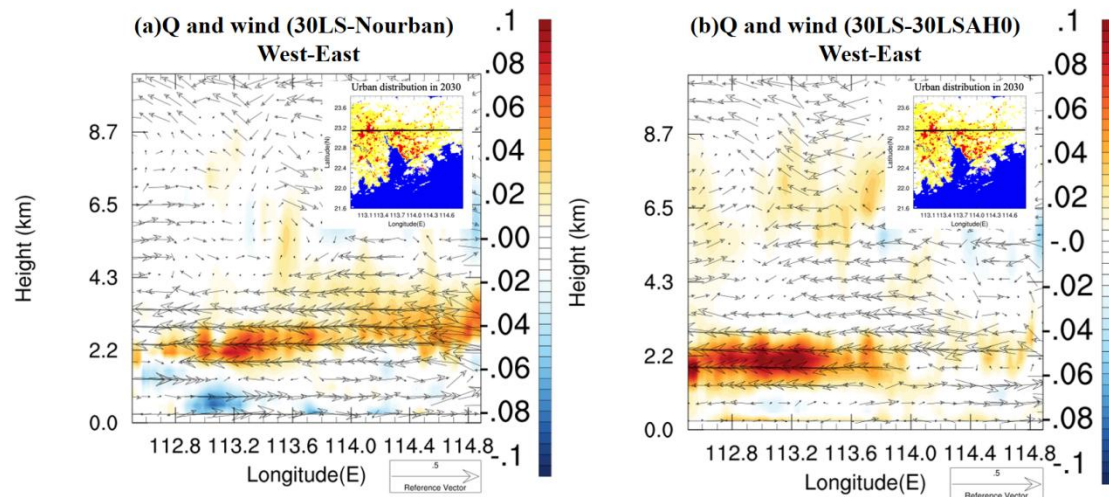


Figure 3.30 Same as Figure 3.29 except for West-to-East cross sectional plane.

Table 3.2 shows the urban moisture flux convergence integrated over all layers for Case 2013 and Case 2015, averaged over the rainfall period. Differences between 30LS and Nourban, 99LS and Nourban, and 30LSAH0 and Nourban are displayed, with results divided into thermodynamic (dq) and dynamic (duv) terms (see Chapter 2.3.2.3). Comparing 30LS and

Nourban, urban moisture flux convergence is found to be higher in 30LS for both Case 2013 and Case 2015. However, the difference in moisture flux convergence is much larger in Case 2015, reaching $-0.01525 \text{ g/m}^2/\text{s}$ compared to only $-0.000389 \text{ g/m}^2/\text{s}$ in Case 2013. This change in moisture flux convergence is primarily induced by the dynamic term. The difference in moisture flux convergence between 99LS and Nourban is similar to that between 30LS and Nourban, with higher convergence observed in 99LS compared to Nourban. This enhancement is significantly stronger during Case 2015 than during Case 2013. Furthermore, considering the impact of urban land use, results indicate that there is an even larger urban moisture flux divergence in 30LSAH0 compared to Nourban for both Case 2013 and Case 2015, which can be attributed to both thermodynamic (dq) and dynamic (duv) terms. Consequently, we propose that urbanization substantially enhances moisture flux convergence in urban areas during Case 2015, which can be primarily attributed to the UHI effect. However, this effect is considerably weaker during Case 2013. The presence of urban land use even results in stronger moisture flux divergence in the GBA mega-city during the rainfall period.

Moisture flux convergence	Case2013 (g/m²/s)	Case2015 (g/m²/s)
30LS-Nourban	-0.0003892	-0.01525656
30LS-Nourban (dq term)	-0.0014431	-0.00220539
30LS-Nourban (duv term)	0.00106824	-0.01276407
99LS-Nourban	-0.0007035	-0.00837247
99LS-Nourban (dq term)	0.00019069	-0.00149234
99LS-Nourban (duv term)	-0.0008912	-0.00696497
30LSAH0-Nourban	0.04116	0.02187916
30LSAH0-Nourban(dq term)	0.01753	0.01529839
30LSAH0-Nourban(duv term)	0.02326	0.006581262

Table 3.2 Vertically integrated moisture flux divergence difference between 99LS and Nourban, 30LSAH0 and Nourban, and 30LS and Nourban for each case. Values are calculated by averaging over the GBA urban area and all ensemble members, with duv (dq) term representing the dynamic (thermal dynamic) term.

3.4 Brief Summary

In this study, we investigated the effects of urbanization on winter extreme precipitation in the GBA mega-city using observations and the WRF-SLUCM model. Parallel experiments were designed in model simulations by varying the land use types (urban land use in 1999 and projected 2030, and cropland), and the value of surface AH flux. Observation results reveal that UHI remains pronounced during winter, with temperature differences exceeding 1 K between urban and rural areas. We observed weaker precipitation and reduced 99th percentile hourly rainfall in urban locations compared to rural areas, which we attributed to the UDI effect induced by lower evaporation and humidity of urban land surface. However, for very extreme

rainfall such as annual maximum and 99.99th percentile hourly rainfall, urban areas experienced higher intensities than rural locations. Our case study analysis, comparing 11 strong and 12 weak UHI cases, indicates that the UHI effect can significantly enhance winter extreme rainfall intensity and probability, particularly for rainfall exceeding 10 mm/hr. We further examined two specific extreme events, Case 2013 and Case 2015, by dynamically downscaling them over the GBA. Numerical modeling results demonstrate that urban impacts on winter extreme rainfall are highly sensitive to synoptic background conditions. In Case 2013, the influence of urbanization on precipitation was minimal and even led to a significant decrease in accumulated rainfall over the GBA mega-city, which can be attributed to the UDI effect and the suppression of the UHI by northerlies and cold air. In contrast, during Case 2015, the persistent UHI effect led to a significant enhancement of precipitation intensity and probability over the GBA mega-city, primarily due to the AH effect. Urbanization-induced changes in circulation led to increased low-level water vapor over urban areas, along with enhanced urban moisture flux convergence compared to Nourban scenarios. This supported increased precipitation in the city during Case 2015. Overall, although the UDI effect induced by lower surface urban evaporation can reduce urban precipitation during winter, in some instances where the UHI effect persists, urbanization can still lead to more intense and frequent extreme rainfall events in the GBA mega-city. This is mainly due to enhanced circulation and convection, which transports additional water vapor from the ocean to the urban areas located along the coast.

4. Urbanization impacts on Greater Bay Area extreme rainfall - sensitivity to synoptic systems during pre-monsoon period

4.1 Introduction

The rainy season in SC also includes the pre-monsoon period from April to May. Precipitation from April to mid-June (pre-summer period) typically accounts for half of the annual rainfall in SC (Qiang et al., 2008; Luo et al., 2017). In contrast to monsoon period precipitation in SC, which is mainly driven by short-term local convection or tropical cyclone systems, pre-monsoon precipitation is closely associated with synoptic and intermediate-scale environmental factors, such as land-sea breeze contrasts (Chen et al., 2017; Wu et al., 2019), surface fronts, shear-lines (Huang et al., 1986), topographic lifting and terrain effects (Jiang et al., 2017; Tu et al., 2014), mesoscale cold pools (Wu and Luo, 2016), and mesoscale convection systems. Li et al. (2020) classified extreme rainfall events in the pre-monsoon period into four types based on synoptic background in SC: (1) surface front, (2) low-level shear-line, (3) low-level vortex, and (4) warm-sector (or weak gradient) (Li et al., 2019; Luo et al., 2020). The first three types are induced by strong synoptic forcing and cold air invasion from the north of SC, while the latter accounts for 43% of total extreme hourly rainfall during the pre-monsoon period and is unrelated to cold air intrusion (Huang, 1986; Luo et al., 2020).

The influence of urbanization on precipitation remains a subject of debate. Numerical models suggest that urban development can have varying effects on extreme rainfall across the continental US and mainland China, either enhancing or decreasing it (Georgescu et al., 2021; Huang et al., 2022). Some studies reveal a decrease in rainfall intensity in certain inland urban areas due to reduced atmospheric water vapor and a decline in CAPE (Hand and Shepherd, 2009;

Mote et al., 2007; Schlünzen et al., 2010; Liu et al., 2021; Hao et al., 2019; Du et al., 2019). But the variation of urban precipitation is sensitive to the intensity of UHI (Dou et al., 2015; Zhang et al., 2017). Furthermore, numerous studies report enhanced rainfall intensity downstream of cities due to urbanization (Changnon, 1968; Shepherd and Burian, 2003; Lin et al., 2008). Lin and Niyogi (2019) reviewed urban influences on rainfall based on meta-analysis, revealing increases in precipitation intensity of approximately 11% (14%) to 21% (22%) over urban (downstream) areas, while effects on other regions are weaker. Modeling results also highlight the role of AH in intensifying extreme rainfall over coastal urban areas by strengthening local convection, land-sea circulation, and local moisture flux convergence (Kusaka, 2014; Shimadera et al., 2015; Xiao et al., 2020; Holst et al., 2016; Fung et al., 2021; Hu et al., 2021). Nonetheless, most of these studies focus on summertime non-TC precipitation. Although the pre-monsoon period in SC features high rainfall intensity and probability without the influence of the summer monsoon, limited studies have investigated the anthropogenic impact on extreme rainfall during this period, such as urban development. Station observations in SC from 2008 to 2017 suggest that the UHI can enhance convection, increase CAPE, and strengthen sea breezes in the GBA, resulting in intensified pre-summer precipitation in the city and downstream areas (Shou et al., 2019). Furthermore, observations from 1979 to 2015 also reveal that GBA urban locations exhibited a more significant increasing trend in pre-summer precipitation than rural areas, and the rate of increase in the number of extremely intense pre-summer rainfall days was much stronger in urban locations compared to non-urban areas (Su et al., 2019).

This study seeks to elucidate the mechanisms and details of urban impacts on the pre-monsoon period and quantify the contributions of factors such as urban surface and UHI.

Additionally, how such urban impacts depend on synoptic background has not been examined before. To address these research gaps, we investigate: (1) the impacts of urbanization (urban land surface and AH) on pre-monsoon extreme rainfall characteristics in SC; and (2) whether the urban impact on pre-monsoon rainfall varies under different synoptic systems, such as surface fronts and shear-lines, and if so, the differences and reasons behind them. We accomplish this by (1) conducting climatology analysis and case studies based on station observations during the pre-monsoon period from 2008 to 2017; and (2) using WRF-UCM to dynamically downscale frontal and shear-line cases in the GBA. To our knowledge, this is the first study to employ both observations and numerical modeling to investigate the urban impact on the pre-monsoon period under different weather systems in the GBA. This approach will help us better understand whether the urbanization effect on pre-monsoon rainfall is sensitive to the synoptic background and may serve as a new scientific basis for researchers exploring urban climate details in SC during different periods.

4.2 Methodology

4.2.1 Pre-monsoon period and case selection

To investigate the urban impacts on pre-monsoon extreme rainfall, the same station observations as in winter study are used, with seven urban stations and seven rural stations being identified (see Chapter 3.2.1). In this study, the period from April 1st to the monsoon onset day in SCS each year is defined as the pre-monsoon period. To identify the monsoon onset day in the SCS annually, we employed wind parameters derived from ERA5 reanalysis data (Hersbach et al., 2020), with three conditions that must be satisfied: (1) the regional mean 850 hPa U wind over the SCS area ($5\text{-}20^{\circ}\text{N}$, $110\text{-}120^{\circ}\text{E}$) exceeds 0; (2) to ensure that the source of warm and

humid westerly winds in the SCS is the Bay of Bengal (rather than the Indo-Burma trough), the latitude of the maximum zonal average 850 hPa westerly winds over 80-95°E should be below 15°N during the monsoon period; (3) both conditions must persist for more than five days, with the number of consecutive interruption days thereafter not exceeding three times the number of monsoon days preceding them. Figure 4.1a shows a flow chart of the definition of the monsoon onset day in SCS, and monsoon onset day in each year (see Figure 4.1b). Notably, employing a strict methodology focusing on the entire SCS region (5-20°N) led to very early monsoon onset days in some years (e.g., April 14th, 2009). However, such extreme cases provided valuable insights into urban impacts on pre-monsoon extreme rainfall in the GBA.

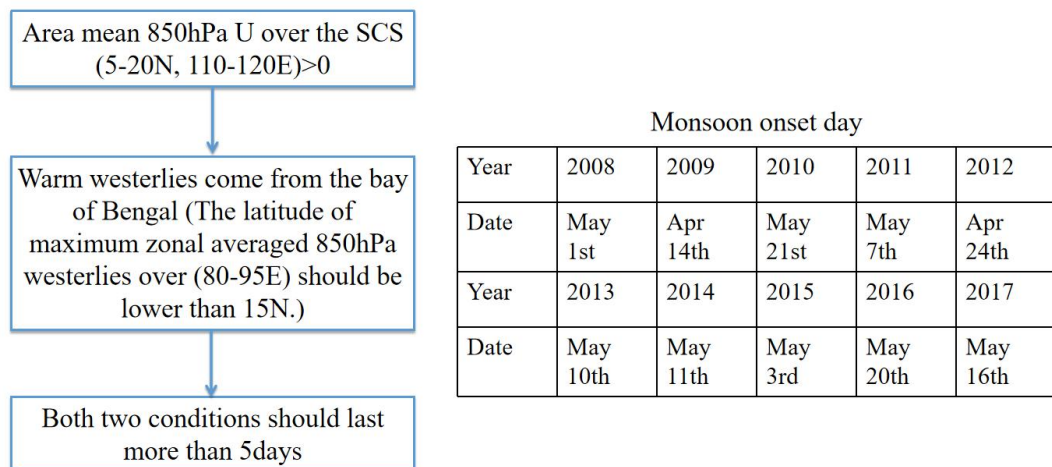


Figure 4.1 Flow chart of how to define the South China Sea monsoon onset day, and the monsoon onset day from 2008 to 2017.

After determining the SCS pre-monsoon period from 2008 to 2017, we calculated the mean hourly rainfall for 14 stations (seven urban and seven rural) during this period. Extreme rainfall events were defined as rain events exceeding the 99th percentile of wet hourly rainfall (hourly rain rate > 0.1 mm/hr), selecting a total of 45 extreme rainfall cases. To examine the UHI effect on pre-monsoon extreme rainfall, we categorized these extreme cases into strong

UHI and weak UHI cases. Strong (weak) UHI cases required the 24-hour average surface temperature difference between urban and rural sites prior to the peak hour of rainfall (14 stations) to be greater than 0.8°C (less than 0.3°C or even a negative value). This classification yielded 18 strong UHI cases and 16 weak UHI cases for further analysis.

4.2.2 Synoptic cases

In order to understand the urban impacts on pre-monsoon extreme rainfall under different synoptic backgrounds, extreme rainfall events were categorized as "frontal," "shear-line," and "warm-sector" based on hourly temperatures and winds derived from the ERA5 reanalysis data. Figure 4.2 provides examples of 850 hPa temperatures and winds in the SC area for (a) frontal, (b) shear-line, and (c) warm-sector cases, with blue arrows denoting the direction of the prevailing wind. In frontal and shear-line cases, a prominent, dense temperature gradient from north to south is associated with cold air intrusion, dominating the northern part of the SC region. For frontal cases, strong northerly winds from the north coupled with southerly or westerly winds in the SC region constitute a large-scale frontal system, leading to extreme precipitation in the SC region. In contrast, for shear-line cases, prevailing northeasterly winds and opposing southwesterly winds result in a shear-line system, with extreme precipitation typically occurring between the two opposing winds. During warm-sector cases, the temperature background is relatively warm and stable, with prevailing southerly or westerly winds governing the SC area. Based on the background weather system for each case, 18 strong UHI and 16 weak UHI extreme events were further classified into two groups: "Frontal" and "Shear+warm". Upon classification, six frontal strong UHI, eight frontal weak UHI, eight shear-line + warm-sector strong UHI, and seven shear-line + warm-sector weak UHI cases were identified.

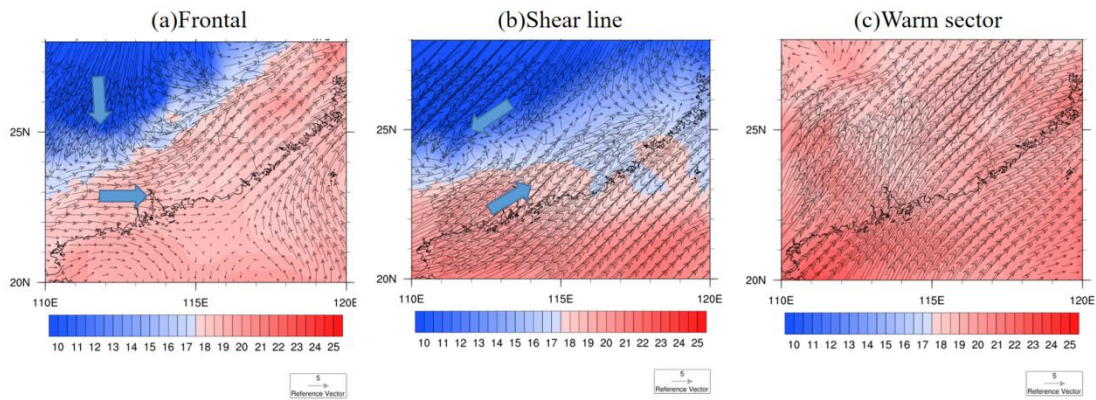


Figure 4.2 Examples of (a) frontal, (b) shear-line, and (c) Warm sector case, with shaded, and vector representing 850hPa temperature (units: °C), and wind ((units: m/s) derived from ERA5. Blue vectors mean the direction of the prevailing wind, black contours are the coastline and boundary of province.

4.2.3 WRF model configuration and cases

In this part, the Weather Research and Forecasting (WRF) model with the Advanced Research WRF (ARW) dynamical core version 4.3.3 was used to dynamically downscale pre-monsoon extreme rainfall cases with boundary conditions from ERA5 (Heshbach et al. 2020). Figure 4.3 shows the nested domains for the downscaling experiments, which cover East Asia/western North Pacific (50km × 50km grid spacing), expanded South China (10km × 10km grid spacing) and GBA (2km × 2km grid spacing). Other model configurations and physical schemes in WRF are as same as part 2 (see Chapter 3.2.2).

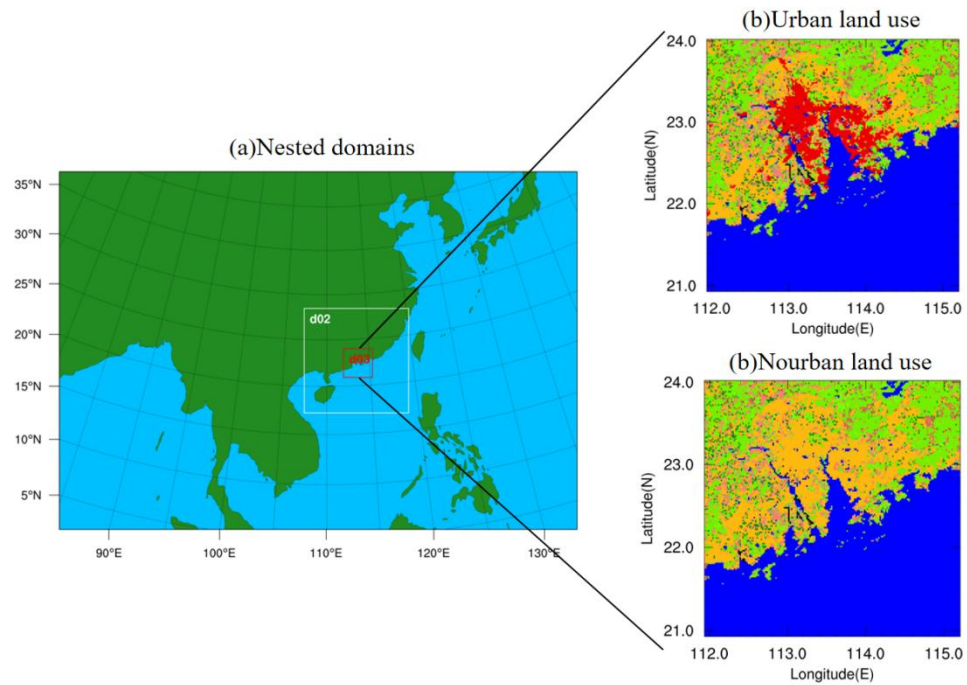


Figure 4.3 (a) Nested domains for the WRF simulations. (b) Land use categories in innermost domain for AH0, AH100 and AH300 experiments, based on 2002 MODIS data with urban and build-up, cropland, forest and grassland shown areas in red, yellow, cyan and green. (c) Land use categories for the Nourban experiment, in which urban and build-up areas are replaced by cropland.

Moreover, extreme rainfall cases for dynamic downscaling were also identified from observations. 10 frontal and 8 shear-line extreme rainfall cases were selected from synoptic cases and subsequently dynamically downscaled using WRF-UCM. Downscaling results were evaluated, with only cases producing strong precipitation over the GBA being considered. Due to the WRF model's limitations in simulating spring cases in coastal areas, the model performed poorly in most cases, and in some events, it produced even no precipitation in the GBA. After identification, four frontal cases (specifically, 2010-05, 2012-04, 2013-04, and 2016-05) and four shear-line cases (namely, 2010-05, 2014-05, 2017-04, and 2017-05) were chosen and further dynamically downscaled over the GBA to a grid spacing of 2 km × 2 km. Additionally, for each case,

ensemble integration with three members was conducted, with starting times at 6-hour intervals, and all results were averaged across the entire ensemble.

4.2.4 Experiment design and UCM setup

After case selection, four distinct sets of parallel numerical experiments were conducted to investigate the impacts of urbanization (urban land use and AH) on pre-monsoon extreme rainfall under various weather systems in GBA. In Experiment 1 (referred to as Nourban), the urban area of GBA was replaced by "cropland" in the land use categorization for WRF, reflecting the predominant land use in surrounding regions. Experiments 2, 3, and 4 (labeled AH0, AH100, and AH300, respectively) employed WRF coupled with the SLUCM and incorporated different values of AH (0 W/m^2 , 100 W/m^2 , and 300 W/m^2 for diurnal maximum, the diurnal profile is shown in Figure 2.3). The 2002 MODIS land use data was utilized in the WRF-SLUCM (see Chapter 2.2.2); Figure 4.3 also illustrated the MODIS land use distribution for (b) urban and (c) Nourban experiment. UCM parameters prescribed over urban grids based on MODIS data are presented in Table 2.2. The mean building height was set at 30 m, based on data from the Hong Kong Lands Department (HKLD). The standard deviation of building height is 4 m, and the road width is 16 m, in accordance with default values for commercial land use in the SLUCM (Fung et al., 2021; Hu et al., 2021). For the AH100 experiment, the 100 W/m^2 diurnal peak value in AH is derived from the WUDAPT land use data for high-intensity residences in the GBA mega-city (Hu et al., 2023). Consequently, the AH100 represents a highly urbanized scenario, with the entire GBA mega-city comprised of commercial and industry. In contrast, for the AH300 experiment, satellite measurements indicated a 289 W/m^2 diurnal peak value in AH in Hong Kong during summer (Wong et al., 2015). A diurnal AH profile with a 300 W/m^2 maximum was

established in the SLUCM over the entire GBA urban area in the AH300 experiment (Holst et al., 2016; Holst et al., 2017; Fung et al., 2021; Hu et al., 2021). This experiment is akin to having commercial and industrial land use as Hong Kong at every urban location within the GBA, representing an extreme future urbanized scenario. These two urban scenarios contribute to a deeper understanding of the sensitivity of pre-monsoon extreme rainfall to varying AH levels.

4.3 Results

4.3.1 Observations

4.3.1.1 Pre-monsoon temperature and precipitation

Based on hourly observations, the average surface temperature during the pre-monsoon period from 2008 to 2017 in the SC area is shown in Figure 4.4a. The surface temperature is recomputed to values at a height of 0 m (sea level) using a temperature lapse rate of 0.6 K/100 m. The highest (lowest) temperatures are found in the southwestern (northern) SC region. A south-to-north temperature gradient is present, albeit weaker than during winter (see Figure 3.10). As the latitude increases from 20°N to 25°N, the surface temperature decreases from above 25°C to 21.2°C. On the other hand, urban areas experience significantly higher temperatures than rural areas. The surface temperature in the GBA mega-city ranges between 23.2°C and 24.5°C, while temperatures in surrounding rural areas fall between 22°C and 23.5°C. The pre-monsoon period surface temperature derived from ERA5 reanalysis data in the SC area is also shown in Figure 4.4b, averaged over the same period as observations. Similarly, reanalysis data also reveal a gradual decrease in temperature from south to north. Temperatures can exceed 27°C in the South China Sea, but only reach 18°C to 20°C in the northern SC region. Notably, a distinct

high-temperature center emerges in the GBA mega-city, with temperatures exceeding 24.5°C in most urban areas. Both observations and reanalysis data indicate a pronounced UHI over the GBA mega-city during the pre-monsoon period.

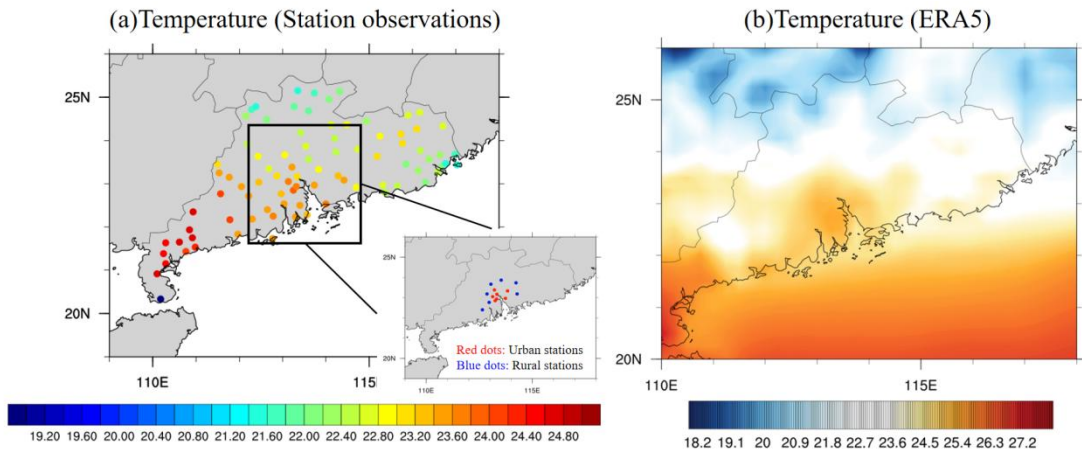


Figure 4.4 (a) Surface temperature (units: °C) averaged over pre-monsoon period from 2008 to 2017, with star means urban stations, and diamond means rural stations. (b) Pre-monsoon temperature (units: °C) derived from ERA5 reanalysis data. Black contours mean the coastline and boundary of province.

Figure 4.5 depicts the pre-monsoon extreme rainfall at the (a) 95th percentile and (b) 99th percentile of the wet hourly rainfall threshold derived from observations in the SC area. Wet hourly rainfall is defined as an hourly rain rate > 0.1 mm/hr. For the 95th percentile of wet hourly rainfall, observations show a decrease in rainfall intensity from coastal to inland areas, with extreme rainfall above 20 mm/hr observed in the southwestern part of SC and only 7 to 9 mm/hr at 25°N. Notably, the 95th percentile of wet hourly rainfall in the GBA mega-city ranges from 15 to 19 mm/hr, significantly stronger than in surrounding rural areas. Results for very extreme rainfall (defined as the 99th percentile of wet hourly rainfall) exhibit a similar situation over the SC area (see Figure 4.5b). The intensity of very extreme rainfall is below 30 mm/hr in most of the SC region, particularly in the northern and western parts. Even in coastal areas, the 99th percentile of wet hourly rainfall intensity is only around 25 to 35 mm hr. However, in the urban areas of

GBA, it ranges from 33 to 40 mm/hr, which is much higher than the surrounding rural areas with rainfall intensities of 23 to 30 mm/hr.

Also shown in Figure 4.5c are the Probability Density Functions (PDFs) of hourly rain rates in urban and rural locations during the pre-monsoon period. Blue (red) bars represent PDFs of hourly rain rates in rural (urban) locations for rates between 1 to 60 mm/hr. Although urban areas receive less light rainfall (less than 10 mm/hr) than rural areas, the probability of heavy rainfall is much higher in urban areas, especially in the range of 30 to 40 mm/hr and 55 to 60 mm/hr. The probability of rainfall < 25 mm/hr is slightly higher in rural locations, and the probability of hourly rainfall decreases by about 5-20% in urban locations. However, the probability of rainfall > 30 mm/hr increases by about 30% to even 300% in urban locations compared to rural areas, except for rainfall in the range of 45 to 50 mm/hr. Overall, observations reveal that GBA urban locations experience stronger and more frequent extreme rainfall than rural locations during the pre-monsoon period, which is more evident for very extreme rainfall, such as the 99th percentile of wet hourly rainfall and hourly rain rates exceeding 35 mm/hr.

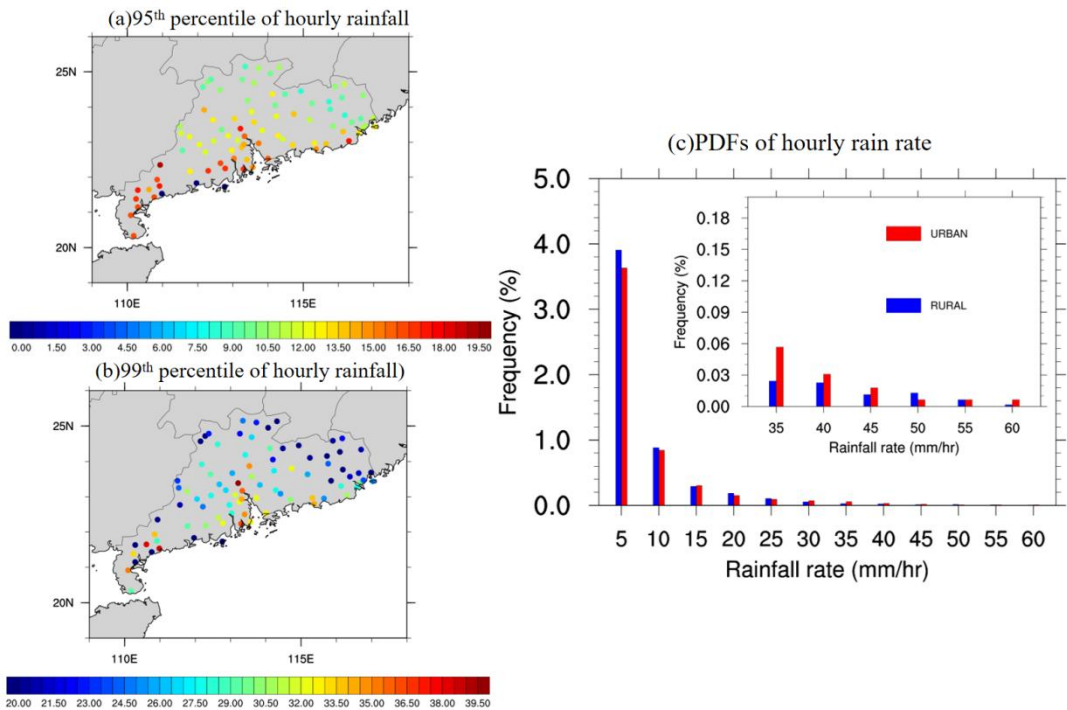


Figure 4.5 (a) 95th and (b) 99th percentile of hourly rainfall (units: mm/hr) during the pre-monsoon period at each station. (c) PDFs of hourly precipitation rates for rural (blue) and urban (red) stations, within the bin ranges of 1-5, 5-10, 10-15, 15-20, 20-25, 25-30, 30-35, 35-40, 40-45, 45-50, 50-55, and 55-60 mm/hr.

Furthermore, pre-monsoon extreme rainfall (99th percentile of wet hourly rainfall) derived from APHRODITE (Asian Precipitation Highly Resolved Observational Data Integration Toward Evaluation) land precipitation data (Yotagai et al., 2012) was also examined. Figure 4.6 displays the extreme rainfall in (a) the pre-urbanization period (1980-1993) and (b) the urbanization period (1994-2007), with black dots representing the locations of seven urban stations. The results indicate a substantial enhancement of pre-monsoon extreme rainfall in GBA urban locations, with the centroid of SC extreme rainfall shifting from the east of the GBA mega-city to urban areas from the pre-urbanization period to the urbanization period.

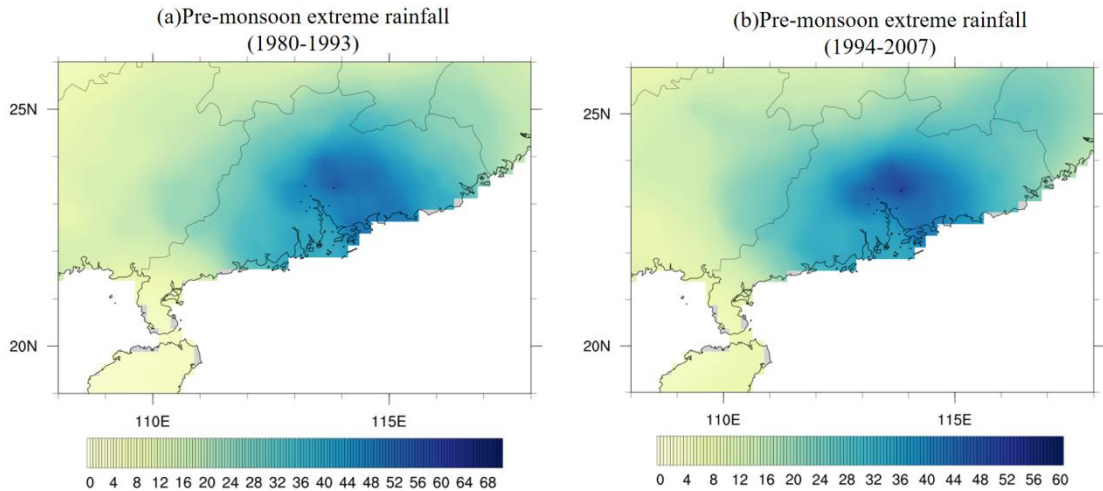


Figure 4.6 (a) Extreme rainfall based 99th percentile of hourly rainfall (units: mm/hr) during the pre-monsoon period from 1980 to 1993 based on Aphrodite data. (b) Same as (a) except for extreme rainfall from 1994 to 2007.

4.3.1.2 Case study during pre-monsoon period

Based on the temperature difference between urban and rural locations, 18 strong UHI and 16 weak UHI cases were selected from pre-monsoon extreme rainfall events that exceed the 99th percentile of wet hourly rain rate for all urban and rural stations. Figure 4.7 illustrates the composite time series of surface temperature averaged over urban (red) and rural (blue) stations during (a) strong UHI, and (b) weak UHI cases, with t=0 representing the hour of peak rainfall averaged over the selected 14 stations. For strong UHI cases, hourly temperature results reveal a difference of 0.8 to 1.1 K between urban and rural temperatures from t= -20 hours to t= -5 hours. Surface temperature gradually decreases from 26.5 (25.8)°C at t= -24 hours to 25.1 (24.3)°C at t= -10 hours and then slightly increases before the rain peak hour, which can be attributed to the latent heat release of water vapor. Surface temperature rapidly drops to only 22.4°C for all stations at t=0. After the rainfall peak hour, temperature changes in urban and rural locations are minimal, recovering after t=20 hours. The time series of surface temperature in weak UHI cases is similar to that in strong UHI cases, but with a much smaller temperature difference between urban

and rural locations. The reduced surface temperature is likely related to cold air from the north, which dominates the SC area and is the primary cause of extreme rainfall during the pre-monsoon period. Figure 4.7c displays the time series of temperature differences between urban and rural locations, with red (blue) lines representing results for strong (weak) UHI cases. The temperature difference between urban and rural areas in the strong UHI case is about 0.8 to 1.1 K before the peak of rainfall, while it is only around 0.3K in the weak UHI case. In both strong and weak UHI cases, the temperature difference between urban and rural stations reaches its maximum at t=-2 hours and rapidly decreases, becoming negative at t=0. The UHI effect is temporarily suppressed by extreme rainfall. However, the UHI effect re-establishes quickly during strong UHI cases, with temperature difference increasing from -0.1 K at t=0 to 0.75 K at t=20 hours. In contrast, in weak UHI cases, the enhancement of the UHI effect is slower, and the temperature difference only increases from -0.2 K at t=2 hours to 0.25 K at t=20 hours.

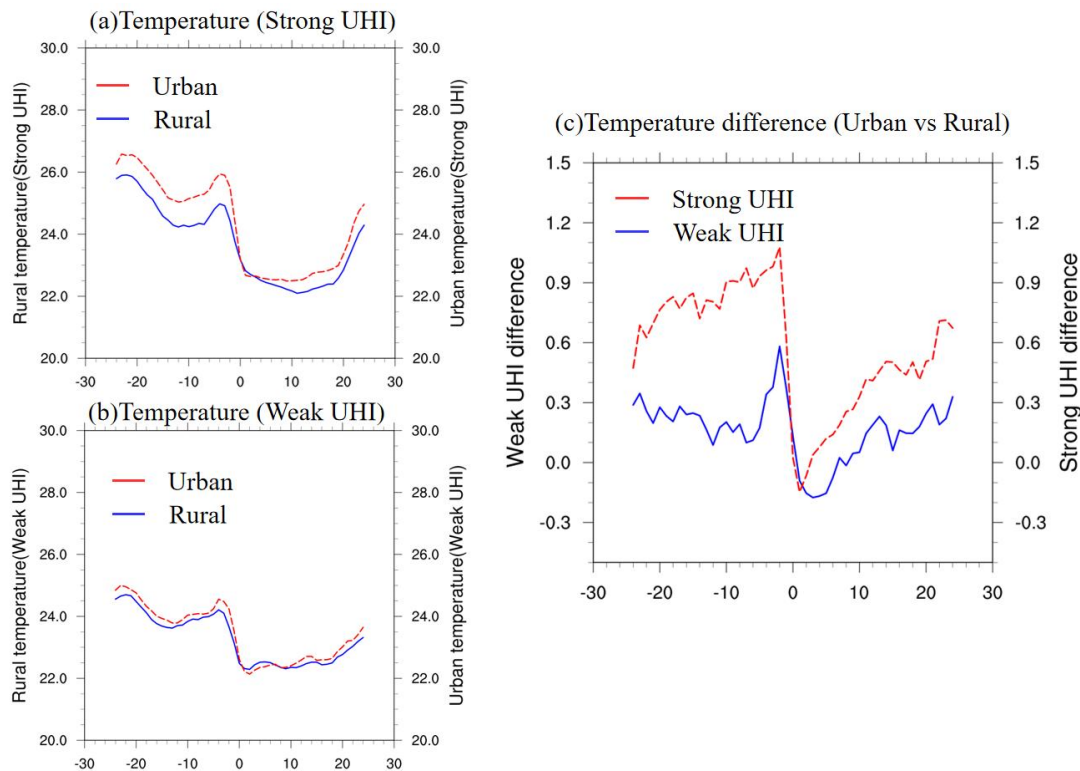


Figure 4.7 (a) Time series of pre-monsoon surface temperature (units: °C) averaged over urban and rural stations during all strong UHI cases, with red and blue line representing temperature in urban and rural stations. Time 0 refers to the peak rainfall hour averaged over the selected 14 stations. (b) Same as (a) except for surface temperature during weak UHI cases. (c) Time series of pre-monsoon surface temperature difference (units: °C) between urban and rural stations for strong and weak UHI cases, red and blue line mean results in strong and weak UHI cases.

Figure 4.8 illustrates the composite time series of hourly rainfall for (a) strong UHI and (b) weak UHI cases, averaged over all selected cases. Blue (red) lines represent rainfall in rural (urban) locations, with t=0 corresponding to the time of peak rainfall averaged across the 14 selected stations. In strong UHI extreme rainfall events, hourly rainfall remains subdued before t=-8 hours, with intensities not exceeding 1 mm/hr. Rainfall begins to escalate at t= -10 hours, reaching a maximum at t=0 for both urban and rural locations. Notably, the intensity of peak rainfall reaches approximately 13 mm/hr in urban stations, compared to only 5 mm/hour in rural stations. Significant precipitation disparities between urban and rural areas emerge during t= -2 hours to t= 4 hours. Conversely, weak UHI cases reveal lower rainfall intensities in urban locations from t= -6 hours to t= -2 hours. Hourly rainfall peaks at t=0, with urban (rural) locations registering approximately 11 (7.9) mm/hr (see Figure 4.8b). Although urban locations still demonstrate stronger peak rainfall in weak UHI cases, the discrepancy between urban and rural sites is considerably diminished compared to strong UHI cases. This difference further narrows as the rainfall intensity rapidly declines to no more than 1 mm/hr after t=0.

To further compare the characteristics of extreme rainfall, the PDFs of hourly rain rates were examined. Figure 4.9a shows the PDFs of rainfall for strong UHI cases, with red (blue) bars representing urban (rural) locations, respectively. Contrasted with rural stations, urban areas exhibit less frequent light rainfall (1 to 5 mm/hr) but a considerably higher probability of rainfall exceeding 30 mm hr during strong UHI cases, except in the 45 to 50 mm hr range. This is

consistent with the PDFs of rainfall throughout the pre-monsoon period (see Figure 4.5c). The probability of heavy rainfall (>30 mm/hr) is approximately 60% or even 500% higher in urban areas than in rural areas, with no rural rainfall exceeding 55 mm/hr. Additionally, we compared the PDFs of rainfall in urban locations during strong and weak UHI cases (see Figure 4.9b). Results indicate that weak UHI events exhibit more frequent light rainfall (<10 mm/hr), with probabilities increasing by approximately 22% (15%) in the ranges of 1 to 5 (5 to 10) mm/hr compared to strong UHI cases. However, strong UHI cases demonstrate higher probability for rainfall >10 mm/hr, particularly for heavy rainfall exceeding 30 mm/hr, with likelihood enhancing by about 15% to more than 300%. Our findings suggest that urban areas experience more frequent heavy rainfall than rural locations under strong UHI conditions, while UHI significantly amplifies the probability of heavy rainfall over the GBA urban locations. In summary, case study observations reveal that the UHI contributes to a substantial increase in both the intensity and likelihood of extreme rainfall in the GBA mega-city during the pre-monsoon period. The influence of the UHI effect on pre-monsoon and summer precipitation is consistent in GBA, with the latter having already been extensively studied (Wang et al., 2015; Wu et al., 2019; Li et al., 2021).

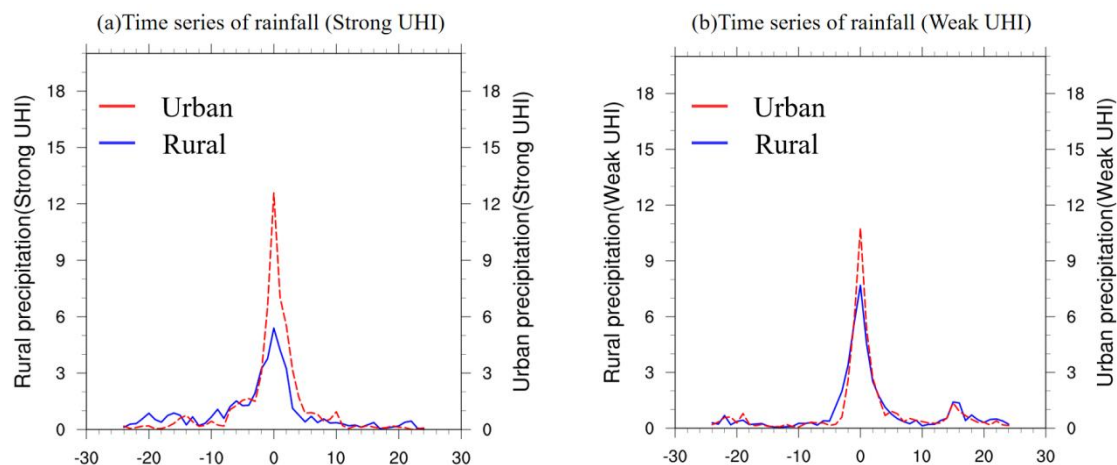


Figure 4.8 (a) Time series of pre-monsoon hourly rainfall (units: mm/hr) averaged over urban and

rural stations during all strong UHI cases, with red and blue line representing rainfall in urban and rural stations. Time 0 refers to the peak rainfall hour averaged over the selected 14 stations. (b) Same as (a) except for weak UHI cases.

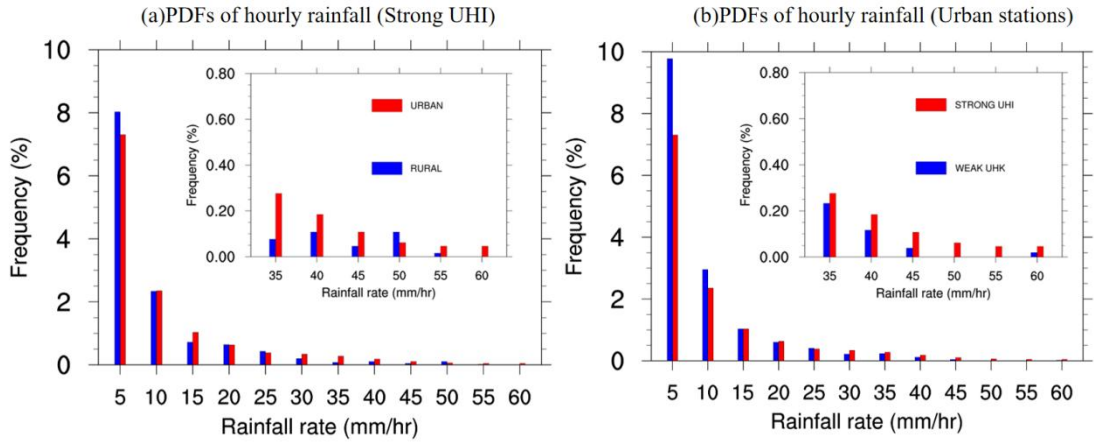


Figure 4.9 (a) PDFs of hourly precipitation rates during all strong UHI cases for rural (blue) and urban (red) stations, within the ranges of 1-5, 5-10, 10-15, 15-20, 20-25, 25-30, 30-35, 35-40, 40-45, 45-50, 50-55, and 55-60 mm/hr. (b) Same as (a) except for hourly rainfall in urban stations during all strong UHI (red) and weak UHI (blue) cases.

4.3.1.3 Synoptic case study

Previous observational findings suggest that UHI can exacerbate extreme rainfall during the pre-monsoon period. However, the specific impacts of urbanization on extreme rainfall under different synoptic systems remain unclear. Here, we further classified strong and weak UHI extreme events into two categories based on the synoptic system: six frontal strong UHI, eight frontal weak UHI, eight shear-line + warm-sector strong UHI, and seven shear-line + warm-sector weak UHI cases. Figure 4.10 shows the composite time series of surface temperature in (a) frontal strong UHI cases, and (b) shear+warm strong UHI cases, with red and blue lines representing urban and rural stations, and t=0 referring to the time of peak rainfall averaged over the selected 14 stations. For frontal cases, the temperature begins to decrease rapidly at t=-20 hours, with urban (rural) temperatures dropping from 28.3°C (27.4°C) to 25°C (24°C) at t=-8 hours. Following a short-term warming from t=-7 hours to t=-3 hours due to latent heat release, temperatures at

urban and rural stations strongly and rapidly decrease at $t=0$, coinciding with the occurrence of extreme rainfall peaks. However, temperatures continue to decrease after the peak rainfall hour, with urban (rural) temperatures reaching a minimum of approximately 20.8°C (20.2°C) at $t=17$ hours and then rapidly increasing after $t=20$ hours. In contrast, temperature changes during shear+warm cases are relatively weaker from $t=-24$ hours to $t=-8$ hours and even slightly enhanced in urban stations. The temperature also decreases rapidly from $t=-4$ hours to the peak rain hour. After $t=5$ hours, urban and rural temperatures gradually recover to 24.5°C and 23.8°C at $t=24$ hours. Overall, the results indicate that temperature changes differ between frontal and shear+warm events. During frontal cases, urban and rural temperatures decrease gradually over time and reach a minimum even after the time of peak rainfall of 14 stations, which is associated with the strong large-scale frontal system from the north controlling the SC area during frontal extreme events. In contrast, for shear+warm cases, cooling occurs only around the time of peak rainfall, and temperatures recover quickly after the extreme rainfall.

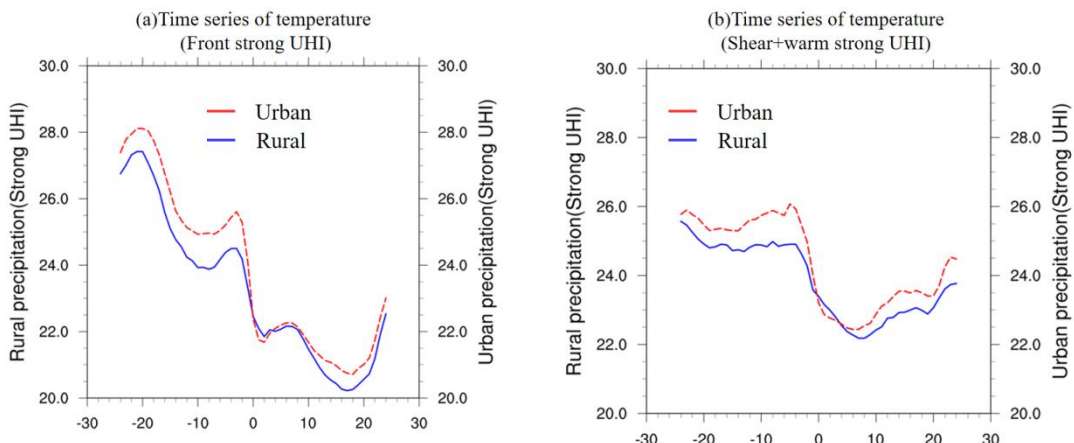


Figure 4.10 (a) Time series of surface temperature (units: $^{\circ}\text{C}$) averaged over urban and rural stations during all strong UHI frontal cases, with red and blue line representing temperature in urban and rural stations. Time 0 refers to the peak rainfall hour averaged over the selected 14 stations. (b) Same as (a) except for surface temperature during strong UHI shear-line + warm sector cases.

Figure 4.11 presents the time series of urban and rural precipitation during (a) frontal strong UHI, (b) shear-line + warm-sector strong UHI, (c) frontal weak UHI, and (d) shear-line + warm-sector weak UHI events. Red (blue) lines represent rainfall in urban (rural) stations, with t=0 referring to the hour of peak rainfall averaged over the selected 14 stations. For frontal cases, urban precipitation consistently surpasses rural precipitation, particularly during the peak hour of rain for both strong and weak UHI cases. The maximum rainfall in urban and rural locations can reach 12.8 and 7.3mm/hr (10.9 and 8.3mm/hr), respectively, in frontal strong (weak) UHI cases. This indicates that the UHI effect amplifies frontal system-related precipitation over the GBA mega-city. In contrast, for shear-line + warm-sector cases, the maximum rainfall intensity during strong UHI cases reaches 15.3mm/hr in urban locations, compared to a maximum of 3mm/hr in rural areas. During weak UHI cases, only a slight enhancement of urban precipitation around the peak hour of rainfall is found. Case study reveals a more pronounced UHI on urban rainfall during shear-line + warm-sector cases than frontal cases, with much larger differences observed between urban and rural locations. We propose that the nature of synoptic systems plays a role in these differences: frontal system-related extreme rainfall manifests as large-scale heavy rainfall across the study area, and the GBA mega-city is influenced by a vast, cold system with cold air intrusion, the impact of UHI may be suppressed and become insignificant. However, in shear-line and warm-sector cases, where the synoptic scale is smaller or not associated with sustained cooling, the UHI tends to result in more potent localized rainfall in the GBA mega-city.

Furthermore, Figure 4.12 displays the PDFs of hourly rainfall in urban locations during frontal and shear-line + warm-sector cases, with red (blue) bars representing results in strong

(weak) UHI cases. UHI enhances urban rainfall probability for nearly all ranges (except 15 to 20mm/hr) during frontal events, with increases in rainfall probability ranging from 5% to 20%, even for heavy rainfall exceeding 30mm/hr. In contrast, for shear-line + warm-sector cases, although there is less frequent urban rainfall in the 1 to 15mm/hr range in strong UHI cases compared to weak UHI cases, UHI still increases the probability of rainfall greater than 15mm/hr, with the probability of heavy rainfall (>30mm/hr) being significantly increased by a factor of 3 to 5 with the presence of UHI, a much more substantial effect than on frontal rainfall. In conclusion, observations demonstrate that UHI results in stronger and more frequent rainfall in the GBA mega-city during both frontal and shear-line + warm-sector cases. However, this impact is much more pronounced in shear-line + warm-sector cases during the pre-monsoon period.

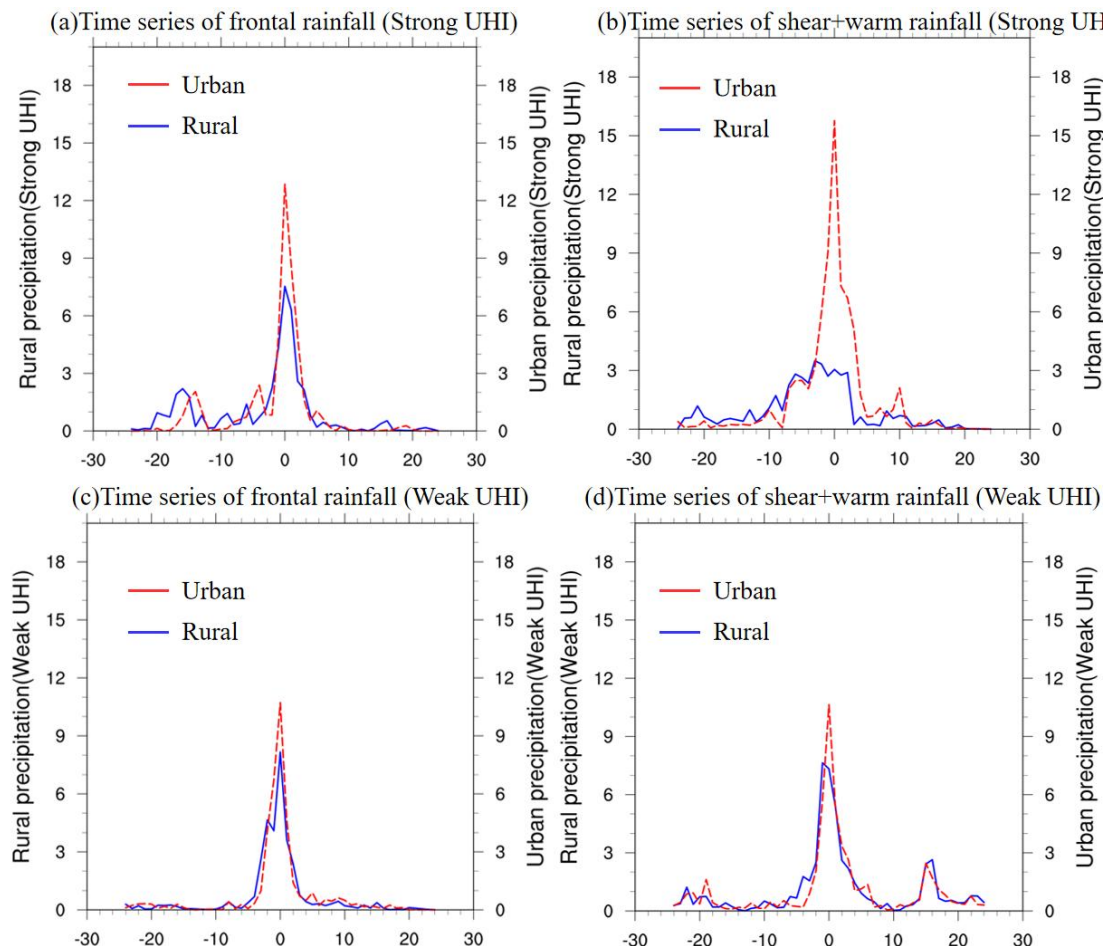


Figure 4.11 Time series of hourly rainfall (units: mm/hr) averaged over urban and rural stations during (a) strong UHI frontal UHI cases, (b) strong UHI shear+warm cases, (c) weak UHI frontal cases and (d) weak UHI shear+warm cases, with red (blue) line representing rainfall for urban (rural) stations. Time 0 refers to the peak hour of rainfall averaged over the selected 14 stations.

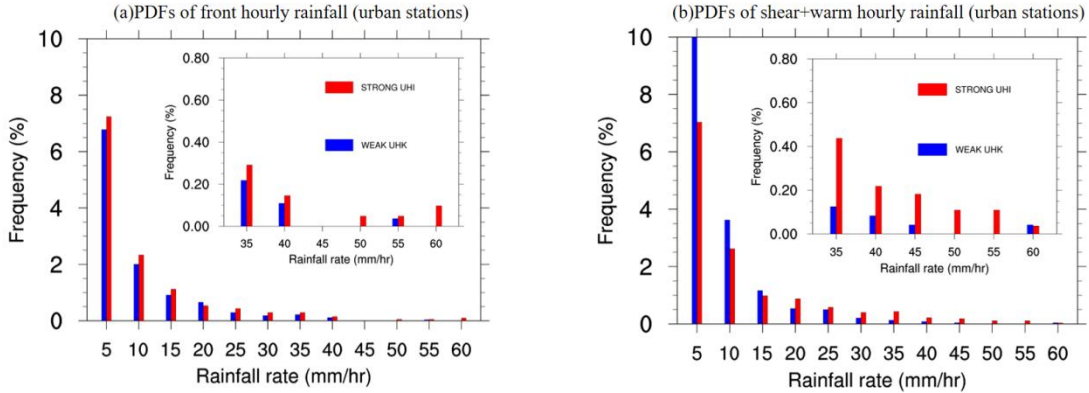


Figure 4.12 (a) PDFs of hourly precipitation rates in urban stations during all frontal cases for weak UHI (blue) and strong UHI (red) cases, within the ranges of 1-5, 5-10, 10-15, 15-20, 20-25, 25-30, 30-35, 35-40, 40-45, 45-50, 50-55, and 55-60 mm/hr. (b) Same as (a) except for all shear+warm cases.

4.3.2 Numerical modeling results

4.3.2.1 Synoptic background for frontal and shear-line cases

To further elucidate the influence of urbanization on pre-monsoon extreme precipitation under various weather systems, we conducted dynamical downscaling for four frontal cases and four shear-line cases in the SC area using the WRF-UCM. Figure 4.13 presents snapshots of the 850 hPa temperature, wind, and geopotential height from WRF model outputs for the four frontal cases ((a) 2010-05, (b) 2012-04, (c) 2013-04, and (d) 2016-05) captured prior to the peak rainfall hour. Model outputs reveal that all frontal cases are characterized by cold air intrusion and northerly winds, which dominate the northern SC region and serve as the primary drivers of extreme rainfall in the GBA. In each case, a sharp temperature gradient decreases rapidly from south to north, accompanied by a dense geopotential gradient associated with the

fronts. Strong southwesterly winds are present in the SC area, but southerly winds recede into the ocean due to frontal advancement during the rainfall process. Extreme rainfall events in the GBA can be primarily attributed to cold fronts. Also shown in Figures 4.13 (e), (f), (g), (h) is the 850hPa temperature and wind for frontal cases from ERA5 reanalysis data during the same period as model outputs, with blue arrows indicating the wind direction in front and behind the front. In comparison to ERA5 reanalysis data, the WRF model slightly underestimates (overestimates) the temperature north of SC area (ocean) for all cases. Nevertheless, the WRF model accurately captures the temperature magnitude in the GBA mega-city, and the wind direction and speed performance in SC is reasonable. The model is capable of reproducing the low-level synoptic circulation and temperature in the SC area during all frontal cases.

Figure 4.14 illustrates analogous plots for the shear-line cases, specifically (a) 2010-05, (b) 2014-05, (c) 2017-04, and (d) 2017-05. In these cases, the blue arrows signify wind direction on both sides of the shear-line, with northeasterly (southwesterly) winds governing the north of SC (SC area). The shear-line cases also exhibit a connection to cold air intrusion; however, during extreme rainfall events, the GBA remains under the influence of southwesterly winds, which are primarily driven by the wind shear-line. Moreover, prevailing southwesterly wind dominates the GBA mega-city during shear-line events, with opposite direction northeasterly winds located on north of SC. Similarly, Figures 4.14 (e), (f), (g), (h) shows the 850hPa temperature and wind for shear-line cases from ERA5 reanalysis data during the same period as model outputs. The WRF model also slightly underestimates the temperature gradient, with simulated temperatures being slightly higher (lower) north of the SC (ocean) compared to ERA5 reanalysis data.

In this study, the primary objective of our study is to conduct a sensitivity

experiment with a focus on exploring the effects of urbanization, specifically friction and AH, on frontal and shear-line extreme rainfall in the GBA mega-city. The accuracy of reproducing extreme events is not the main objective here. However, the WRF model provides satisfactory and reasonable representation of low-level circulation and temperature when compared to ERA5 reanalysis data for all frontal and shear-line events. This is important as we want to investigate the sensitivity of urban impact on extreme rainfall under different synoptic systems- hence the importance of reproducing the frontal and shear-line systems. As it is crucial to acknowledge that the synoptic backgrounds of the two sets of cases differ during the rainfall period.

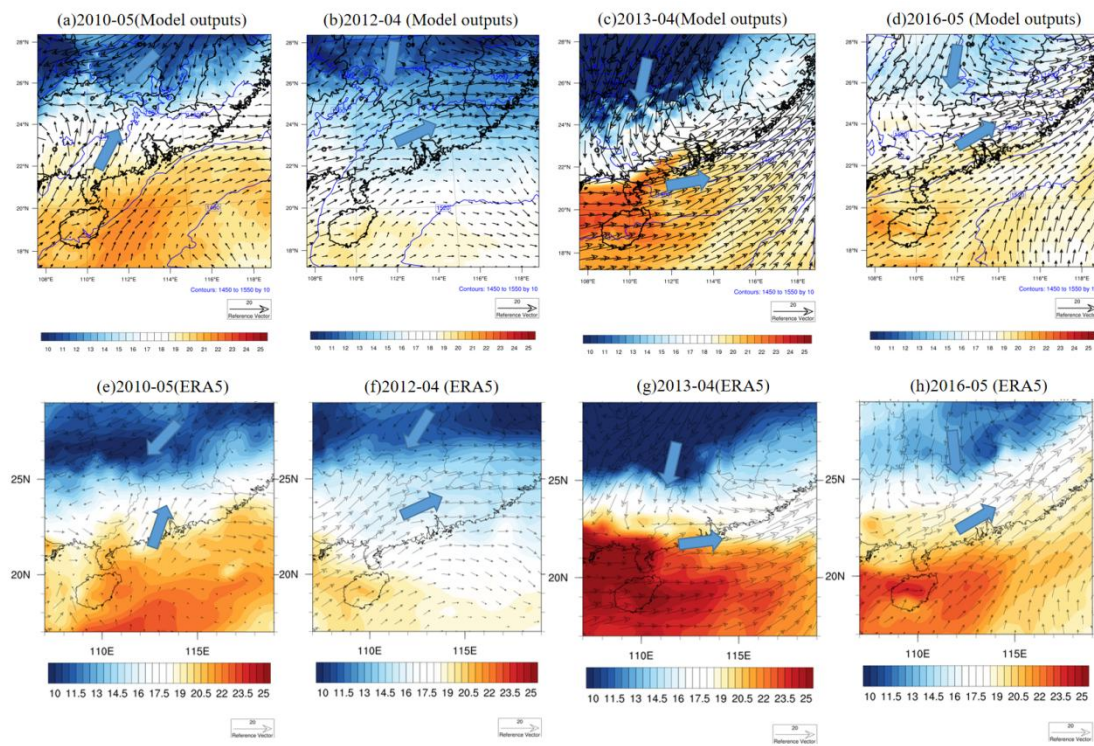


Figure 4.13 850hPa temperature (shading; units: $^{\circ}\text{C}$), geopotential height (blue contours; units: m), and U,V wind (vector; scale arrow in units of m/s) for frontal cases (a) 2010-05, (b) 2012-04, (c) 2013-04, and (d) 2016-05 from WRF model outputs. Blue arrows indicate the direction of wind in front and behind the front. (e,f,g,h) Same as (a,b,c,d) except for parameters in the same periods from ERA5.

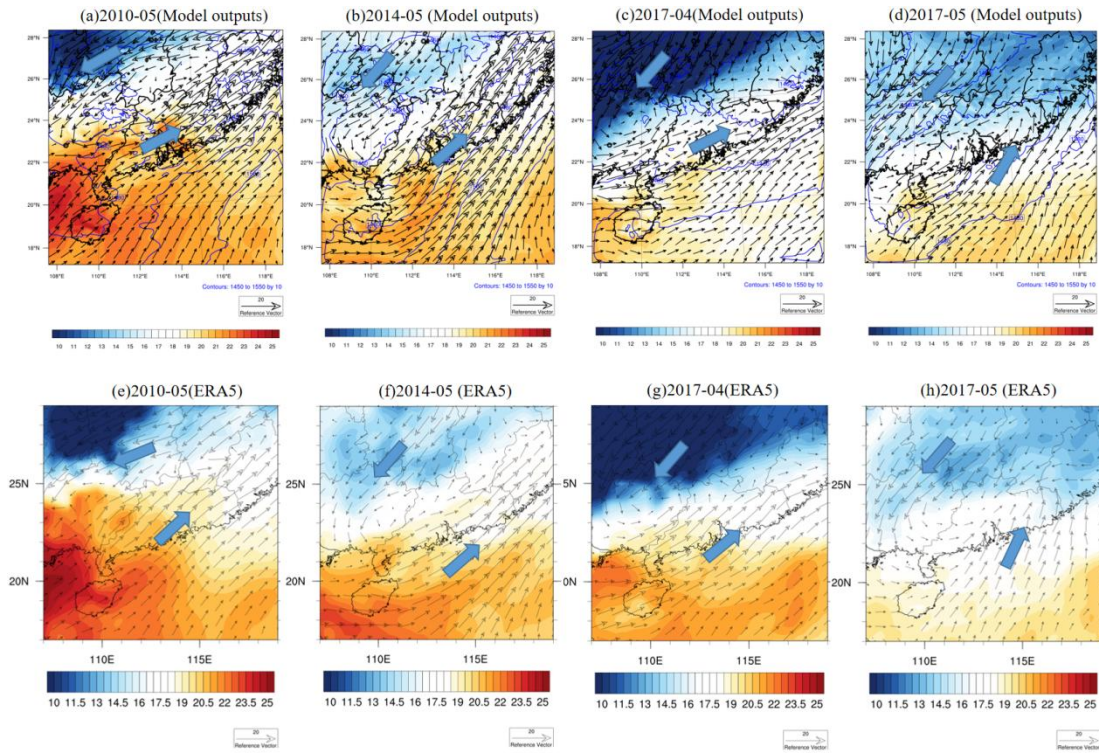


Figure 4.14 Same as Figure 4.13 except for shear-line cases (a) 2010-05, (b) 2014-05, (c) 2017-04, and (d) 2017-05

4.3.2.2 Precipitation

The accumulated rainfall differences for all shear-line cases were examined by averaging across all members of four experiments: (a) AH0 and Nourban, (b) AH100 and Nourban, and (c) AH300 and Nourban (Figure 4.15). The GBA mega-city boundary is delineated by a black contour, with significant rainfall differences ($p < 0.05$, Student's t-test) marked by black dots. When only urban land use is considered (AH0 experiment), precipitation increases in most urban areas compared to Nourban, with a significant enhancement of about 3-7 mm/day. This enhancement is more pronounced in the northern part of the GBA mega-city, particularly in highly urbanized cities such as Guangzhou (113.29°E, 23.13°N), Foshan (113.15°E, 22.51°N), and Dongguan (113.44°E, 22.58°N). However, the rainfall difference between AH0 and Nourban is negligible in most rural and marine areas, not exceeding 3 mm/day. Comparing AH100 and Nourban, AH further

enhances urban precipitation in shear-line cases. The increase reaches 6-10 mm/hour in the northern GBA mega-city, with significant differences throughout the city. Notably, AH also enhances precipitation by approximately 3-6 mm/day in the rural area northeast of the city, which is downstream due to the prevailing southwesterly winds. Most rural and oceanic areas, however, exhibit weak and insignificant urbanization impacts. In the AH300 scenario, precipitation significantly increases across the northern and eastern GBA mega-city and parts of the downstream rural area, with increases exceeding 10 mm/day in most areas.

For frontal cases (Figure 4.15 e, d, f), the comparison of AH0 and Nourban reveals that urbanization leads to reduced precipitation in the northern GBA mega-city and parts of the rural area located northeast of the city. Eastern regions of GBA mega-city experience significant precipitation decreases due to urban land use, with reductions of 5-8 mm/day in urban and 3-6 mm/day in surrounding rural areas. Such a decline due to urban land surface is similar but much stronger than that in summertime (Hu et al., 2021). A slight but insignificant increase in rainfall occurs in the southern city regions. In the AH100 scenario, AH enhances accumulated rainfall intensity over urban areas and parts of the rural area northeast of the city. However, it is seen that the Urban Dry Island (UDI) induced by lower evaporation of urban land surface might counterbalance these enhancements, resulting in a slight reduction of 0-2 mm/day in accumulated rainfall compared to Nourban, which is commonly observed in some inland cities (Doan et al., 2016; Guo et al., 2006; Zhang et al., 2009; Hao et al., 2019; Du et al., 2019). No significant signal was found, and oceanic rainfall differences remain negligible and insignificant. When the diurnal maximum AH input increases to 300 W/m² (AH300 scenario), extreme AH enhances rainfall intensity over the northern and eastern urban areas by 6-10 mm/day, with significant enhancement

observed in the eastern GBA mega-city. However, precipitation changes remain insignificant in other urban areas, particularly in the southwestern city regions. Additionally, AH leads to a strong but insignificant enhancement of 3-8 mm/day in precipitation in the rural areas northeast of the city compared to Nourban.

To better understand the characteristics of urbanization-induced rainfall variability, Figure 4.16 show the PDFs of hourly rain rate over all urban grid points for all (a) frontal, and (b) shear-line cases, with black, blue, green, and red bars representing probability of hourly rainfall in Nourban, AH0, AH100, and AH300 experiment, respectively. For frontal cases, urban land use markedly reduces rainfall probability across all ranges in the urban area, with a 15-70% decrease for AH0 compared to Nourban. Conversely, AH100 increases rainfall probability at all ranges, particularly for heavy rainfall exceeding 40 mm/hr, where the probability increases 2-3 times compared to AH0. However, the rainfall probability in AH100 remains lower than Nourban across all ranges, suggesting that the enhancement due to a diurnal maximum of 100 W/m² of AH was counterbalanced by the negative UDI effect (Cheng and Chan, 2012). In AH300, AH further increases the probability of rainfall in all ranges, with heavy rainfall probability (>40 mm/hr) being 60 to 120% higher than in Nourban. Nevertheless, the enhancement of light rainfall probability are only 10-25% due to such extreme AH. In contrast, for shear-line cases, all three urban experiments (AH0, AH100, and AH300) exhibit more frequent rainfall probabilities than Nourban across all ranges. Comparing AH0 and Nourban, rainfall frequency increases markedly in all ranges due to urban land use alone, with an enhanced probability of 15 to even 100%. However, the difference in rainfall frequency between AH100 and AH0 is relatively weak for rainfall rates below 50 mm/hr. A strong enhancement of rainfall

probability due to AH is observed for very heavy rainfall > 50 mm/hr, with a 30 to 120% increase in AH100 compared to AH0. Extreme AH further improves rainfall probability in all ranges, with AH300 exhibiting the highest probability among all four scenarios.

In summary, the impact of urbanization on precipitation varies significantly between frontal and shear-line events. For frontal cases, urban land use considerably reduces rainfall intensity and probability in the urban area, while AH enhances both. However, significantly enhanced rainfall is only observed in AH300 compared to Nourban, with AH100 still exhibiting a slight reduction in urban precipitation relative to Nourban. In contrast, both urban land use and AH substantially increase the intensity and probability of rainfall for shear-line cases in the GBA mega-city, displaying a more pronounced effect than observed during frontal events. This highlights the importance of considering different meteorological conditions while examining the impact of urbanization on regional precipitation dynamics.

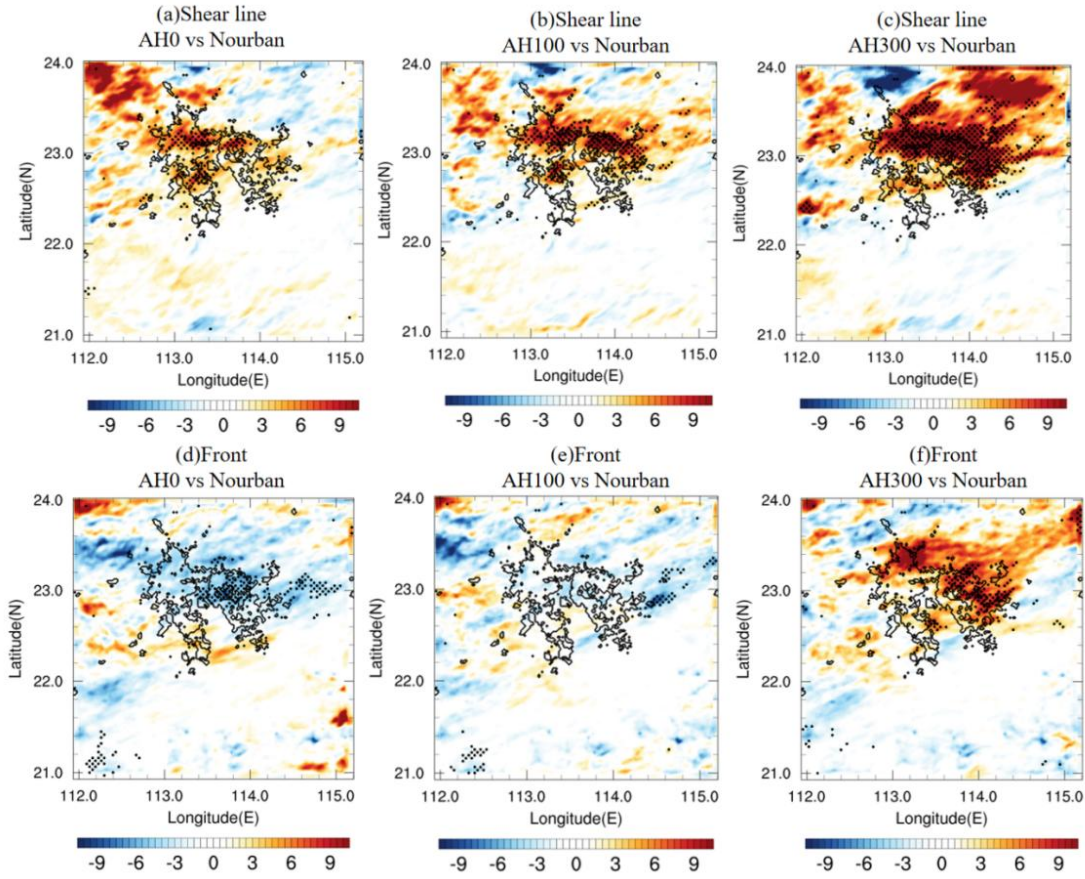


Figure 4.15 Daily accumulated rainfall (units: mm/day) difference between (a) AH0 and Nourban, (b) AH100 and Nourban, and (c) AH300 and Nourban for all shear-line cases. Black contours represent the boundary of the GBA mega-city. (d,e,f) Same as (a,b,c) except for all frontal cases. Locations in which the difference exceeds the 95% significance level are denoted by black dots.

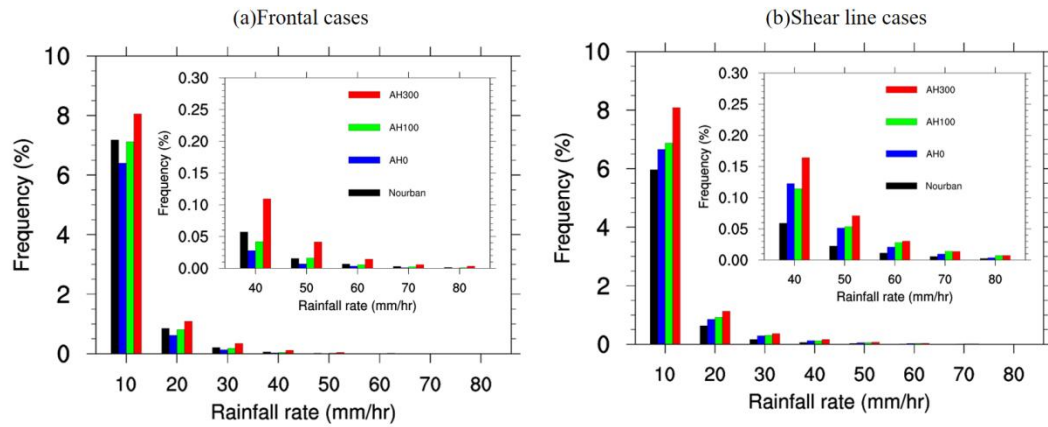


Figure 4.16 PDFs of hourly precipitation rates over urban locations within GBA for (a) Frontal, and (b) shear-line cases, within the ranges of 1-10, 10-20, 20-30, 30-40, 40-50, 50-60, 60-70, and 70-80 mm/hr for the Nourban (black), AH0 (blue), AH100 (green), and AH300 (red) experiments.

4.3.2.3 Relationship between temperature (humidity) and precipitation differences

The relationship between temperature and precipitation in the urban area is further investigated, focusing on the differences in 2m temperature and rainfall during frontal and shear-line cases. Figure 4.17 shows scatter plots of 2m temperature and rainfall differences (averaged during rainfall period) across all urban grid points for (a) frontal, and (b) shear-line, with black, blue, and red dots (lines) representing the differences (regression line) between AH0 and Nourban, AH100 and Nourban, and AH300 and Nourban, respectively. For frontal cases, a negative correlation is observed between temperature and rainfall differences between AH0 and Nourban. However, this does not imply that higher temperatures lead to reduced rainfall; rather, it can be attributed to a more pronounced UHI in the northern part of the city, which also experiences a significant decrease in rainfall potentially due to the drier atmosphere induced by urban land surfaces (Doan et al., 2016; Hu et al., 2021). Conversely, as the AH increases, both urban precipitation and surface temperature rise. The slope of the precipitation-temperature relationship also shifted from a negative value in AH0 to a positive value in AH300, suggesting a positive correlation between UHI and rainfall enhancement in urban areas during frontal cases, especially in AH300. Although this relationship is suppressed by the drier atmosphere in AH0 and AH100 experiments.

In contrast, during shear-line cases, the increase in rainfall is highly proportional to the intensity of UHI, which is markedly stronger in all urban experiments compared to frontal events (see Figure 4.17b). The temperature difference between urban and Nourban experiments is positive in all urban grid points, with the maximum temperature difference reaching over 4.5 K for

shear-line cases, but only around 3K for frontal cases (see Figure 4.17a). Urban rainfall intensity increases with 2m temperature in all urban scenarios (AH0, AH100, and AH300) compared to Nourban. Regression lines reveal that the slope of the precipitation-temperature relationship rises with the input AH value, indicating that UHI on urban precipitation is stronger for higher AH values in urban areas. Thus, UHI enhances urban rainfall in both frontal and shear-line cases, with a stronger impact on precipitation as the base temperature in urban areas increases (as in AH300). However, this correlation is relatively weaker in frontal cases than in shear-line events and is often strongly suppressed by the drier atmosphere induced by urban land surface in AH0 and AH100.

To gain further insight into the relationship between local humidity and precipitation in urban areas. Figure 4.17 also shows scatter plots of specific humidity and rainfall differences (averaged during rainfall period) across all urban grid points for (c) frontal, and (d) shear-line. Specific humidity is vertically averaged from 950hPa to 300hPa level. For frontal events, lower atmospheric specific humidity is observed during the rainfall period in the AH0 urban area compared to Nourban, with a decrease of more than 0.05 g/kg in almost all urban grids. This can be attributed to the reduced evaporation from urban surfaces compared to natural land use. A strong correlation between specific humidity and rainfall differences is also noted, with the significant decrease in frontal precipitation in the northern part of the city of AH0 primarily due to the lower atmosphere humidity, which explains the negative correlation between temperature and rainfall difference between AH0 and Nourban (see Figure 4.17a). In the AH100 scenario, most urban areas still exhibit slightly reduced specific humidity compared to Nourban, with differences ranging from 0.02 g/kg to -0.07 g/kg in most grids, leading to marginally reduced urban rainfall. Only AH300 has substantially stronger atmosphere specific humidity during rainfall period than

Nourban in urban areas, resulting in higher precipitation in urban grids with increased water vapor compared to Nourban.

Conversely, for shear-line cases (see Figure 4.17d), higher specific humidity is observed in most urban grids of the AH0 experiment compared to Nourban. However, no correlation is found between urban humidity and rainfall differences, as indicated by the near-zero slope of the regression line. The drier atmosphere caused by reduced evaporation from urban land use is counterbalanced by other urban factors during shear-line cases, which has a positive relationship with precipitation and results in significantly enhanced precipitation in the northern part of the GBA mega-city (Figure 4.15a). Furthermore, almost all grid points in the AH100 and AH300 experiments exhibit higher specific humidity than Nourban, with humidity differences ranging from 0.02 to over 0.2 g/kg in most urban areas. Urban grid points with higher specific humidity generally experience greater precipitation during shear-line cases in the AH100 and AH300 experiments compared to Nourban, with rainfall intensity increasing by more than 20 mm/day in some areas where humidity is enhanced by approximately 0.18 to 0.25 g/kg. Consequently, the significantly enhanced urban rainfall is strongly supported by increased humidity in urban areas during shear-line cases in AH100 and AH300. According to previous studies, this can primarily be attributed to the enhanced moisture flux convergence and convection induced by the UHI (Hu et al., 2021; Hu et al., 2023). The analysis of the mechanism will be shown in chapter 4.3.2.4 and 4.3.2.5.

Additionally, the distribution of precipitation differences between AH300 and Nourban in shear-line cases (Figure 4.15c) reveals that the AH impact on precipitation is not limited to urban areas, with significant precipitation enhancement also evident in some downstream areas.

To understand the correlation between UHI and rural precipitation, Figure 4.18a displays scatter plots of 2m temperature and rainfall differences at selected surrounding rural grid points for shear-line cases, with black, blue, and red dots (lines) representing the differences (regression lines) between AH0 and Nourban, AH100 and Nourban, and AH300 and Nourban, respectively. Results are averaged over the entire rainfall period for each case. The selected areas are shown in Figure 4.18b. No relationship was found between UHI and rural rainfall differences when comparing AH0 and Nourban, with surface temperature variations in most surrounding rural areas only around 0-0.2 K and the slope of the precipitation-temperature relationship being almost zero. However, AH further increases precipitation over some downstream rural areas, displaying a positive relationship between temperature and precipitation differences for both AH100 (AH300) and Nourban. Although temperature and rainfall changes over most surrounding rural areas remain weak for AH100 and AH300 compared to Nourban, temperature enhancement reaches about 0.5-1.5 K (1-2.2 K) for AH100 (AH300) in some rural areas. UHI enhances precipitation in downstream rural areas, particularly to the northeast of the city, with the slope of the relationship increasing with AH. In general, we posit that AH is associated with enhanced precipitation in downstream rural areas during shear-line cases, and UHI on precipitation enhancement tends to be stronger with higher urban temperatures.

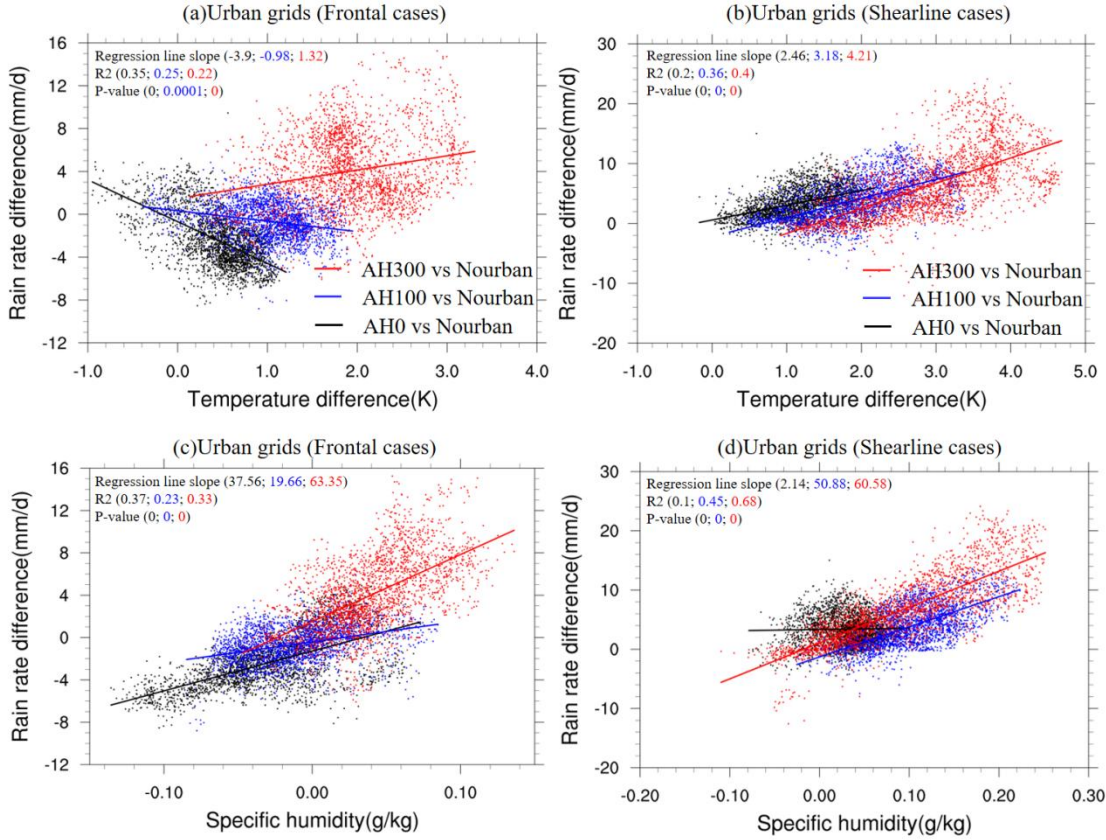


Figure 4.17 Scatter plot of temperature (units: K) and daily rainfall difference (units: mm/d) during rainfall period of (a) Frontal cases, and (b) shear-line cases between AH0(black), AH100 (blue), AH300 (red) and Nourban over all urban grid points. Black, blue and red lines represent the best fit line of precipitation-temperature relationship. (c) (d) Same as (a)(b) except for specific humidity averaged from 950hPa to 300hPa (units: g/kg) and daily rainfall difference (units: mm/d).

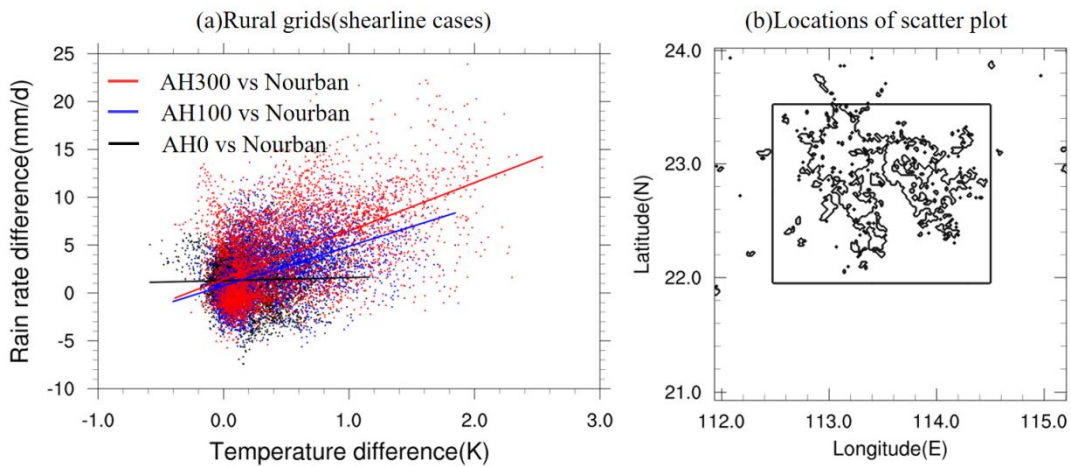


Figure 4.18 (a) Same as Figure 4.17b except for results in part of rural grid points. (b) Location of rural grids being used, see black rectangle. Black contours represent the GBA mega-city.

4.3.2.4 Mechanism for shear-line cases

Numerical modeling results demonstrate that both urban land use and AH significantly enhance local atmosphere humidity, rainfall intensity and probability in urban areas during shear-line events. To understand the mechanism through which urbanization affects extreme shear-line rainfall, Figure 4.19 displays the 2m temperature and surface wind differences averaged over 12 hours before the rain peak hour for various experiments during shear-line events, with temperature and wind difference shown as shaded area and vector arrow. The GBA mega-city and coastline boundaries are outlined in black contours, and blue arrows highlight the direction of wind difference. Results reveal that the presence of urban land use leads to higher temperatures in urban areas in the AH0 compared to the Nourban, with the most pronounced warming in the northwestern part of the city (approximately 1-1.5 K), and the temperature difference in other urban areas ranges from 0.5 to 1 K. AH further elevates surface temperatures over urban areas, with AH100 and AH300 increasing temperatures by 2-3.5 K and 3.5-5 K, respectively, compared to Nourban. The substantially enhanced temperatures before the rain peak hour further modulate local circulation. The presence of urban land use and the UHI intensify southwest (northeast) winds over the southwest (northeast) of the city, respectively, in all urban experiments, particularly in AH300 compared to Nourban. This leads to higher wind convergence over urban areas, which is associated with the prevailing southwesterly winds over the GBA mega-city during the shear-line rainfall period. The UHI widens the urban-rural and urban-ocean temperature gradient, accelerating prevailing southwesterly winds over the southwest of urban areas while decelerating winds over downstream areas. Additionally, the higher roughness in urban areas due to the friction effect hinders wind speed in urban and downstream areas.

Figure 4.20 presents the 950 hPa to 300 hPa vertical wind speed differences averaged over the entire rainfall period of shear-line cases between (a) AH0 and Nourban, (b) AH100 and Nourban, and (c) AH300 and Nourban, respectively, with vertical wind speed difference. The boundary of GBA mega-city is shown in black contours. Results indicate that even in the absence of AH, the presence of urban land surface contributes to a stronger vertical motion in AH0 compared to Nourban, particularly in the northwestern part of urban areas. Furthermore, AH can intensify vertical wind speeds within the urban region. In AH100, vertical wind speeds increase by more than 0.04 m/s across most of the northern section of the GBA mega-city, while vertical motion is also enhanced in a small rural area to the northeast of the city. With a diurnal maximum of 300 W/m² in AH, vertical wind speeds exhibit a more pronounced increase across almost the entire GBA mega-city and some downstream rural areas. Conversely, the effects of urban land use and AH on vertical motion in most rural and ocean regions are minimal and inconsistent. Thus, we conclude that both urban land use and AH contribute to stronger convection in urban areas during shear-line cases, leading to the occurrence and intensification of precipitation.

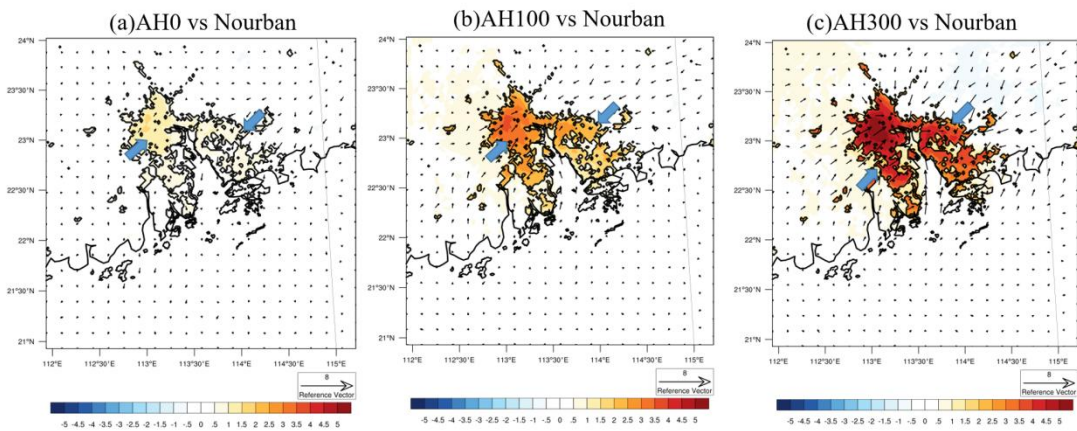


Figure 4.19 Surface temperature (units: K) and wind (units: mm/s) difference between (a) AH0 and Nourban, (b) AH100 and Nourban, and (c) AH300 and Nourban averaged over 12 hours

before rainfall peak hour of all shear-line cases. Shaded, vector, and black contours represent temperature, wind, and coastline and GBA mega-city.

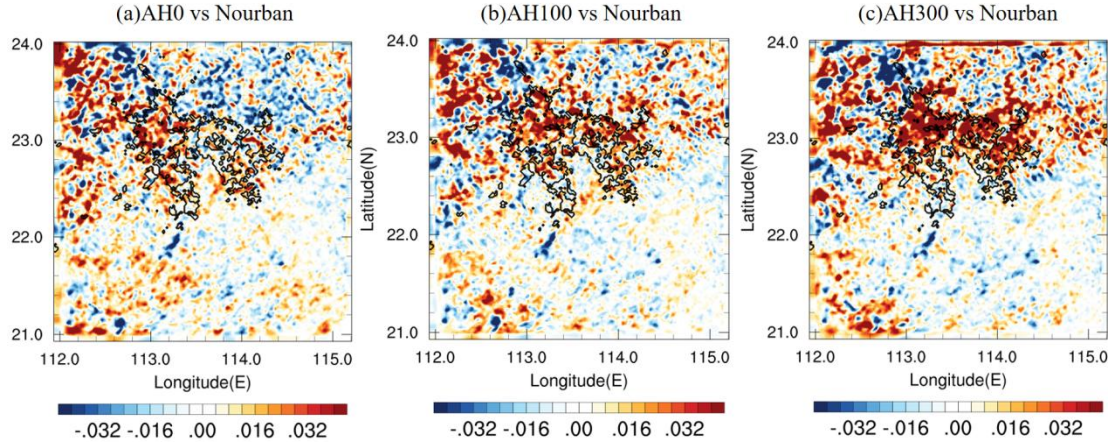


Figure 4.20 Vertical wind speed difference between (a) AH0 and Nourban, (b) AH100 and Nourban, and (c) AH300 and Nourban averaged from 950hPa to 300hPa level during rainfall period for all shear-line cases. Shaded, and black contours represent vertical wind speed, and coastline and GBA mega-city.

As circulation and convection strengthen, local wind convergence patterns shift accordingly. Figure 4.21 displays the 10m wind divergence differences, averaged over the entire rainfall period for shear-line cases, between (a) AH0 and Nourban, (b) AH100 and Nourban, and (c) AH300 and Nourban. For AH0, variations in surface wind circulation and enhanced convection result in higher convergence in northwestern urban areas compared to Nourban, with an increase of approximately -0.00005 s^{-1} . However, this difference remains relatively weak in most urban regions. Furthermore, AH can amplify wind convergence in urban areas, particularly in the northern GBA mega-city. Wind divergence values, averaged over urban areas and adjusted for Nourban, are -0.000028 s^{-1} , -0.00011 s^{-1} , and -0.00018 s^{-1} for AH0, AH100, and AH300, respectively. Enhanced wind divergence is also observed along the southwestern boundary of the urban area due to AH, which is linked to the modulated surface wind. The increased temperature

gradient induced by AH between urban and rural areas to the southwest of the city significantly accelerates the prevailing southwesterly winds, resulting in even higher wind divergence along the southwestern city boundary. Additionally, wind divergence variations in rural and marine areas are relatively weak and negligible when compared to Nourban across all urban experiments.

Moreover, Figure 4.22 illustrates the vertical wind shear (VWS) differences, averaged over the entire rainfall period for shear-line cases, between (a) AH0 and Nourban, (b) AH100 and Nourban, and (c) AH300 and Nourban. VWS is defined as the wind difference between the 300hPa and 950hPa levels. For the AH0 experiment, results reveal that VWS is significantly enhanced in urban areas compared to Nourban, creating an environment with increased instability and potentially heightened convection. This can be attributed to the suppression of surface and low-level wind speeds by the urban surface, while mid- and upper-level wind speeds remain relatively stable, leading to a higher VWS. Furthermore, the VWS values for AH100 and AH300 are markedly reduced in the southwest and southwestern parts of the city relative to Nourban. However, VWS is stronger in the northeast of the city (downstream rural areas). This can also be ascribed to the modulated wind circulation, as the UHI effect accelerates the prevailing southwesterly winds in the southwest urban region, but decelerates them in the downstream area. The substantially enhanced VWS over the downstream rural area is consistent with stronger convection and can further contribute to increased precipitation in the downstream rural area during AH100 and AH300 shear-line events.

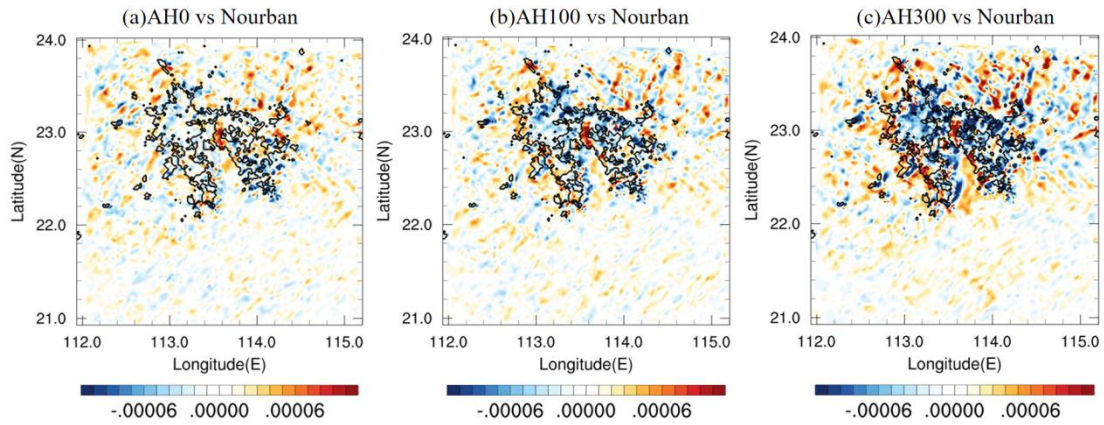


Figure 4.21 Same as Figure 4.20 except for 10m wind divergence difference.

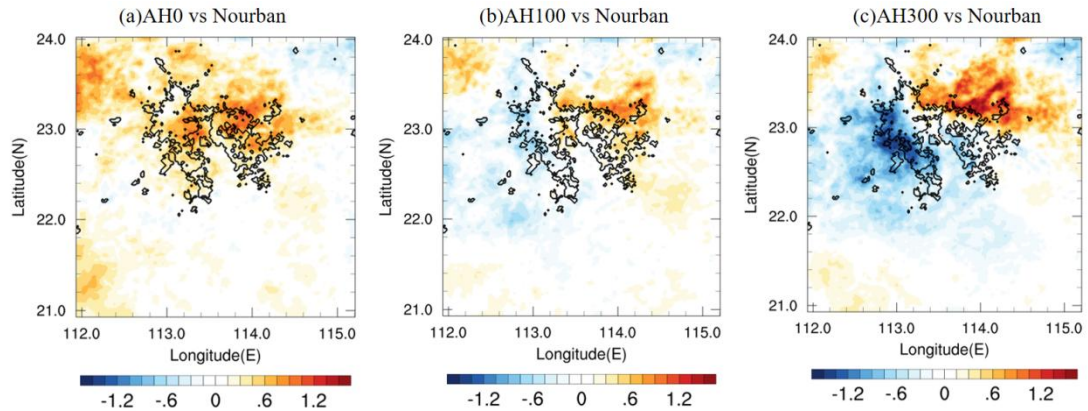


Figure 4.22 Same as Figure 4.20 except for vertical wind shear difference, the VWS is defined as wind difference between 300hPa and 950hPa level.

Finally, changes in specific humidity are examined. Figure 4.23 displays the specific humidity differences, averaged over the entire rainfall period for shear-line cases, between (a) AH0 and Nourban, (b) AH100 and Nourban, and (c) AH300 and Nourban. Humidity is averaged from the 950hPa up to the 300hPa level. AH0 slightly increases specific humidity compared to Nourban, with an increase of approximately 0.05 to 0.012 g/kg in most urban regions. Moreover, AH significantly raises the water vapor content over urban areas and the northeast of the city (downstream rural area) in AH100 and AH300, particularly in the northern part of the GBA mega-city. This change aligns closely with the observed alterations in precipitation and local

convection. Moreover, a slightly lower humidity is also observed over the southwest urban area and the ocean region in AH300 compared to Nourban, especially in the upstream rural area. The decrease in water vapor can be attributed to the increased wind divergence in the southwest urban region and parts of the ocean area, as well as to reduced convection due to the stronger sinking motion caused by increased convection within the city.

In summary, during shear-line cases, the results indicate that the presence of urban land surfaces and AH can significantly enhance the intensity and likelihood of precipitation in urban areas. This enhancement can be ascribed to the substantial increase in local convection and wind convergence. Furthermore, it is important to note that the augmented water vapor and convection resulting from AH can lead to increased precipitation over the downstream rural area of the GBA mega-city.

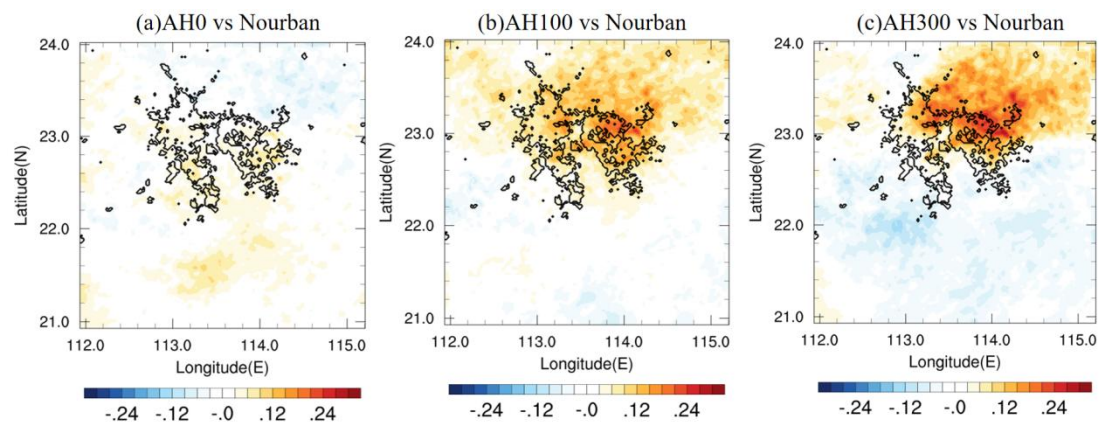


Figure 4.23 Same as Figure 4.20 except for specific humidity difference averaged from surface to 300hPa level.

4.3.2.5 Mechanism for frontal cases

In contrast to shear-line cases, the frontal cases reveal that urban land use can significantly decrease rainfall in urban areas of GBA, while the AH impact tends to increase it. To

understand the differing roles of urban impacts on frontal and shear-line rainfall, Figure 4.24 also illustrates the 2m temperature and surface wind differences, averaged over 12 hours before the rain peak hour, during frontal events for three comparisons: (d) AH0 and Nourban, (e) AH100 and Nourban, and (f) AH300 and Nourban. During frontal rainfall periods, the prevailing surface wind over the north (south) of the GBA mega-city is northeasterly (southerly). It is observed that even for AH0, the 2m temperature in urban areas is higher than in rural areas, with an increase of approximately 0.5 to 1 K, particularly in the northern part of the GBA mega-city. The AH further enhances the temperature difference between urban and Nourban experiments. However, UHI induced by both urban land use and AH is weaker during frontal rainfall periods compared to shear-line rainfall periods (see Figure 4.19) and the previous work focusing on summer (Hu et al., 2021). Additionally, urban land surface results in stronger south (north) winds in the northern (southern) part of the GBA mega-city due to frictional effects that decelerate wind speed on both sides. But this wind-regulating circulation increases local wind divergence in urban areas. Additionally, AH100 exhibits stronger southwest winds in the northern part of the city compared to Nourban, with slightly enhanced southerly winds observed in the southern part of the urban area. This can be attributed to the larger temperature gradient between urban areas and the ocean. Considering a diurnal maximum of 300 W/m^2 AH, the western (eastern) part of the GBA city experiences stronger westerly and southerly (easterly) winds due to the influence of the extreme AH, resulting in increased wind convergence over the city and promoting rainfall enhancement.

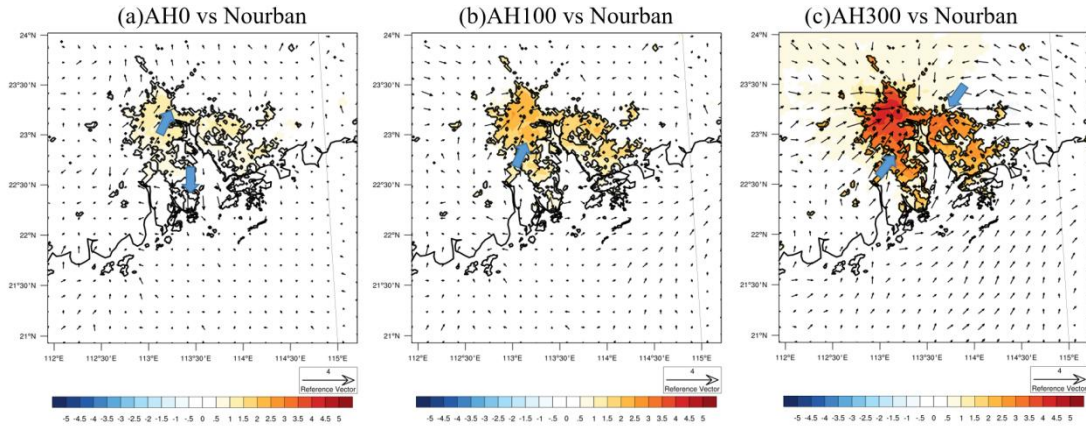


Figure 4.24 Surface temperature (units: K) and wind (units: mm/s) difference between (a) AH0 and Nourban, (b) AH100 and Nourban, and (c) AH300 and Nourban averaged over 12 hours before rainfall peak hour of all frontal cases. Shaded, vector, and black contours represent temperature, wind, and coastline and GBA mega-city.

Analogous analyses for vertical motion and surface wind divergence during frontal cases were conducted. Figure 4.25 displays the 950 hPa to 300 hPa vertical wind speed differences averaged over the rainfall period for all frontal cases between (a) AH0 and Nourban, (b) AH100 and Nourban, and (c) AH300 and Nourban. For AH0, a more robust downward motion is evident in the majority of the northern parts of the GBA mega-city, especially in the eastern urban region. Even for AH100, convection remains weaker in most urban areas compared to Nourban, consistent with precipitation variability (see Figure 4.15). Only AH300 exhibits stronger convection relative to Nourban, with vertical motion increasing by 0.03 m/s over the eastern and northeastern parts of the city, aligning closely with the locations of AH-induced frontal precipitation enhancement.

Additionally, Figure 4.26 presents the 10m wind divergence difference averaged over the rainfall period during frontal events. Enhanced wind divergence is observed in most urban areas for AH0 compared to Nourban, corresponding to the stronger southerly (northerly) wind in the northern (southern) part of the GBA mega-city induced by urban land use. For AH100, slightly

enhanced wind convergence is seen in the northern part of the city, while enhanced divergence is still apparent in most urban areas. Strongly enhanced wind convergence is only observed in AH300 in the majority of the northern city area due to extreme AH impacts. The wind divergence differences after subtracting Nourban for AH0, AH100, and AH300 are 0.00004/s, -0.00004/s, and -0.00018/s, respectively, averaged over the entire urban area. Thus, unlike shear-line cases, urban land use appears to negatively impact both local convection and wind divergence during the rainfall period of frontal cases, potentially leading to a more stable and drier atmosphere that reduces rainfall. Moreover, the enhanced convection and convergence due to AH in the GBA mega-city are weaker during frontal cases than in shear-line cases.

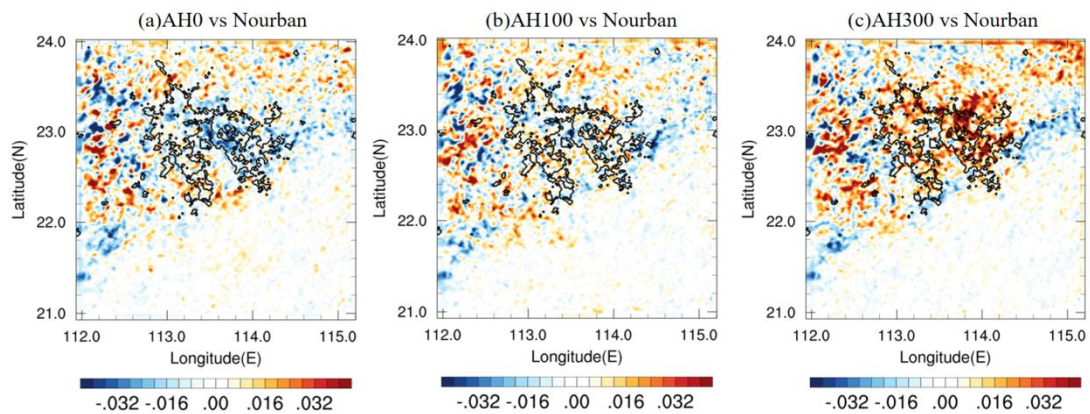


Figure 4.25 Vertical wind speed difference between (a) AH0 and Nourban, (b) AH100 and Nourban, and (c) AH300 and Nourban averaged from 950hPa to 300hPa level during rainfall period for all frontal cases. Shaded, and black contours represent vertical wind speed, and coastline and GBA mega-city.

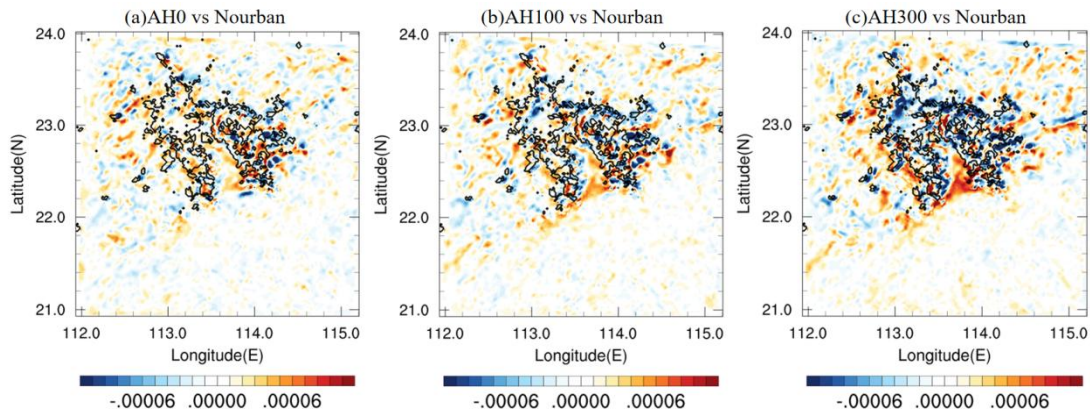


Figure 4.26 Same as Figure 4.25 except for 10m wind divergence difference.

Figure 4.27 presents the specific humidity difference averaged over the rainfall period for all frontal cases between (a) AH0 and Nourban, (b) AH100 and Nourban, and (c) AH300 and Nourban, with humidity averaged from the 950 hPa to the 300 hPa level. The results reveal that specific humidity is lower in urban areas for AH0 compared to Nourban, primarily due to reduced surface evaporation and increased wind divergence caused by urban land use. While AH can further increase specific humidity through enhanced wind convergence in the city, a slight decrease in humidity is still observed in urban areas for AH100 compared to Nourban. Higher specific humidity is only noted in AH300 relative to Nourban, with enhanced humidity observed in the eastern part of the GBA mega-city and rural areas to the northeast of the urban region. Here, specific humidity increases by approximately 0.1 to 0.15 g/kg, consistent with the locations of significantly enhanced precipitation in AH300 compared to Nourban.

In summary, the influence of urban factors (urban land surface and AH) on frontal precipitation extremes in urban areas differs from their impact on shear-line events. The lower evaporation and increased wind divergence induced by urban land surfaces are the main drivers for the significant decrease in precipitation in urban areas in AH0 compared to Nourban.

Furthermore, slightly reduced convection, and specific humidity in the GBA mega-city are observed in AH100 compared to Nourban, resulting in a minor decrease in precipitation. However, extreme AH contributes to enhanced wind convergence and stronger vertical motion in urban areas in AH300, which in turn leads to a significant increase in urban rainfall during frontal cases. Overall, urban land surfaces and AH have opposing effects on precipitation in frontal cases. Further investigation is needed to understand why the effect of AH on precipitation variability in urban areas is much weaker in frontal cases compared to shear-line cases.

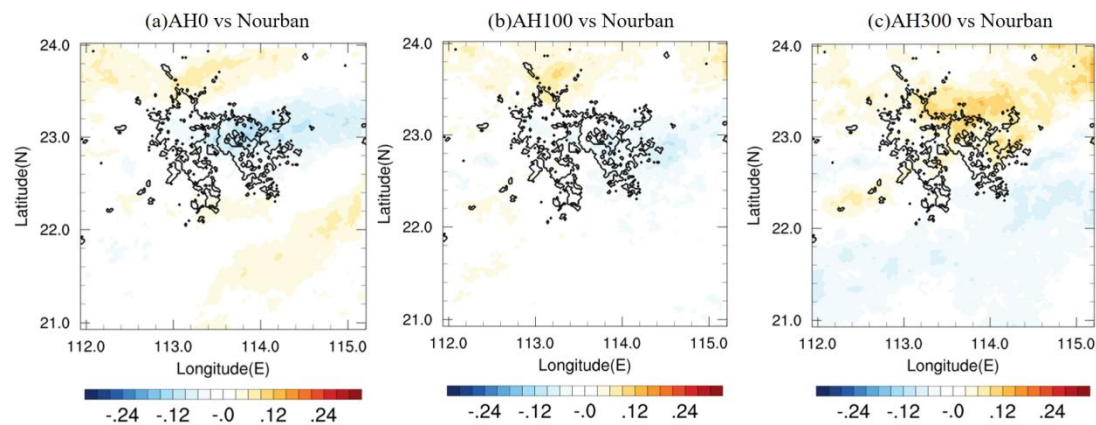


Figure 4.27 Same as Figure 4.25 except for specific humidity difference averaged from surface to 300hPa level.

4.3.2.6 Suppressed UHI effect during frontal cases

In order to understand the diminished impact of AH in frontal cases compared to shear-line cases, Figure 4.28 presents vertical profiles of urban temperature differences for (a) frontal cases and (b) shear-line cases. These profiles are averaged over the rainfall period, with black, blue, and red lines illustrating urban temperature differences between AH0 and Nourban, AH100 and Nourban, and AH300 and Nourban, respectively. At the 1000 hPa level, the urban

temperatures for all three urban experiments are higher than Nourban. However, these temperature differences rapidly decline with increasing altitude, registering -0.2, -0.16, and 0.2 K at 925 hPa for AH0, AH100, and AH300, respectively, relative to Nourban. The temperature differences between AH0 (AH100) and Nourban gradually approach zero, while that between AH300 and Nourban decreases to zero above the 800 hPa level. Consequently, the UHI in the three urban experiments is subdued at low levels during the rainfall period of frontal cases, particularly for AH0 and AH100, which exhibit even lower temperatures than Nourban at low levels. In contrast, results from shear-line cases reveal that only the temperature difference between AH0 and Nourban becomes negative between 950 hPa and 850 hPa level. Both AH100 and AH300 still exhibit higher urban temperatures at low levels compared to Nourban, with the temperature differences between AH100 (AH300) and Nourban gradually decreasing from 1.3 K (1.95 K) at the 1000 hPa level to nearly 0 K (0.1 K) at 850 hPa. Furthermore, the lapse rate of temperature difference is substantially lower in shear-line cases than that in frontal cases. Above 800 hPa, there is negligible temperature difference between all urban experiments and Nourban. Overall, the UHI is substantially suppressed at low levels during the rainfall period of frontal cases, whereas AH100 and AH300 maintain higher urban temperatures than Nourban at levels around 925 hPa during the rainfall period of shear-line events, indicating a persisting UHI.

Moreover, Figure 4.29 presents the 925 hPa temperature difference throughout the entire model time period for all frontal cases between (a) AH0 and Nourban, (b) AH100 and Nourban, and (c) AH300 and Nourban. Notably, in AH0 compared to Nourban. Notably, in AH0 compared to Nourban, higher rural temperatures are observed north of the GBA mega-city, with an increase of approximately 0.1-0.25 K in the northern rural areas. However, temperature decreases

in most urban areas of AH0, particularly in the northern and eastern parts of the city. Similar results are observed for AH100 compared to Nourban, with higher temperatures in the northern urban area and rural areas north of the city, exhibiting warming of about 0.2 K to 0.4 K. Lower temperatures are also found in the southern urban areas of AH100 compared to Nourban. In AH300, both the city and surrounding rural areas exhibit significantly higher temperatures than in Nourban, particularly in the northern city and rural areas north of the urban region, where warming exceeds 0.5 K. Given that the prevailing winds at 925 hPa are predominantly southerly during most simulation periods (before and after the frontal system reaches the GBA), we attribute the warming in the rural areas north of the city to a warmer flow from the urban areas to the northern rural areas, driven by stronger southerly winds. Furthermore, the regional average 925 hPa urban temperature difference between the urban and Nourban experiments is only -0.16 K (0.2 K) for AH100 (AH300) compared to Nourban during the rainfall period (see Figure 4.28). However, the temperature difference is much higher throughout the entire simulation time period. Indicating a suppressed UHI during the rainfall period.

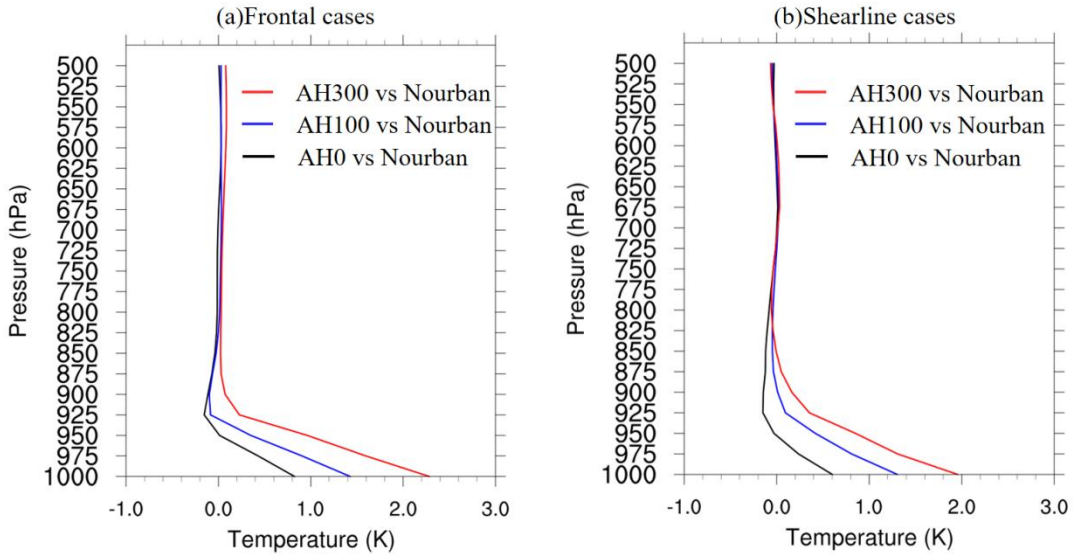


Figure 4.28 Vertical profile of urban temperature difference (units: K) averaged over rainfall period for all (a) frontal, and (b) shear-line cases from 1000hPa level to 500hPa level. Black, blue, and red line represent the temperature difference between AH0 and Nourban, AH100 and Nourban, and AH300 and Nourban.

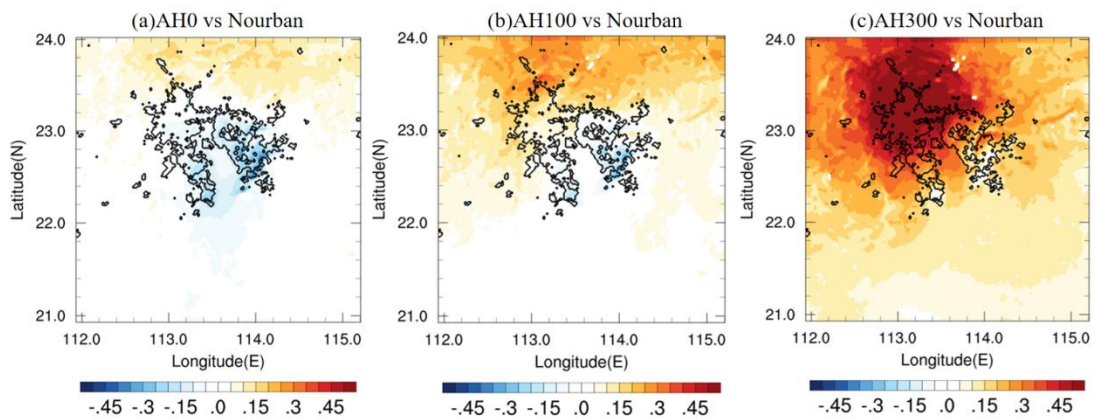


Figure 4.29 925hPa temperature difference (units: K) between (a) AH0 and Nourban, (b) AH100 and Nourban, and (c) AH300 and Nourban averaged over entire integrations for all frontal cases. Shaded, and black contours represent temperature difference, and coastline and GBA mega-city.

Figure 4.30 shows temperature and wind differences at 925 hPa, averaged over the rainfall period between (a) AH0 and Nourban, (b) AH100 and Nourban, and (c) AH300 and Nourban during frontal events. Temperature and wind differences are represented by shading and

vectors, respectively. AH0 and AH100 exhibit a slight decrease in urban area temperatures relative to Nourban, with temperature difference decreasing by approximately 0-0.8K in the northern part of GBA mega-city. AH300 maintains higher temperatures over northeastern urban areas and parts of surrounding rural areas compared to Nourban, with an increase of approximately 0.2 to 1 K, attributable to the extreme AH transported from the surface. Simultaneously, stronger northeasterly winds are observed north of urban areas and within urban regions for all three urban experiments compared to Nourban, particularly for AH300. This can be ascribed to the intensified temperature gradient induced by AH, which accelerates the prevailing northeast wind over the northern part of the study area. Therefore, it is suggested that UHI in the three urban experiments is significantly suppressed by the stronger northerly winds during the rainfall period of frontal cases. To further investigate this, Figure 4.31 presents the temperature advection difference at the 925 hPa level, averaged over the rainfall period of the frontal case 2010-5. Stronger cold advection is observed in the eastern part of the urban area for AH0 compared to Nourban, with even greater cold advection in AH100 and AH300, especially in AH300. Additionally, stronger cold advection is evident over rural areas north of the city in AH100 and AH300, consistent with the enhanced northeasterly winds in the same locations relative to Nourban.

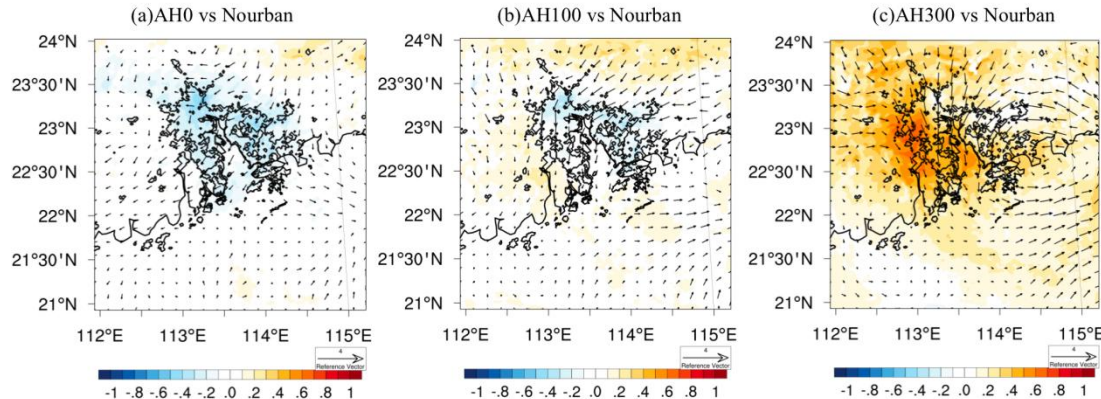


Figure 4.30 925hPa temperature (shading; units: K) and wind (scale vector in units of mm/s) difference between (a) AH0 and Nourban, (b) AH100 and Nourban, and (c) AH300 and Nourban averaged over the rainfall period for all frontal cases. Black contours represent the coastline and boundary of the GBA mega-city.

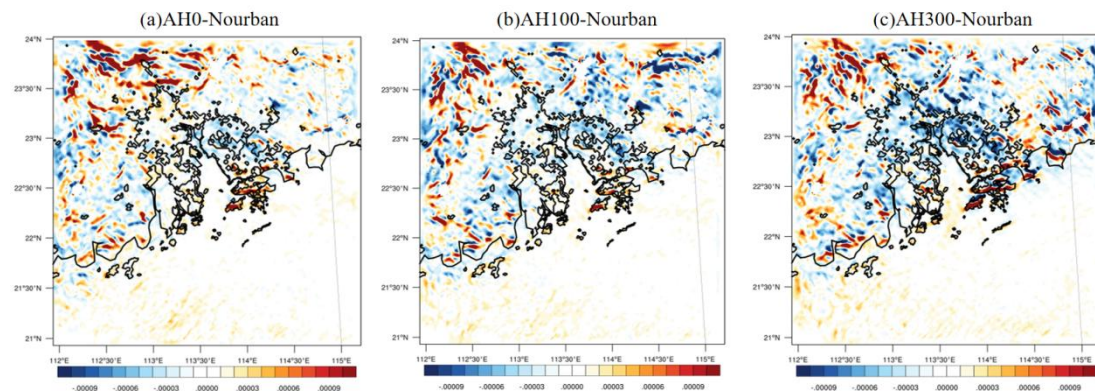


Figure 4.31 925hPa temperature advection (units: K/s) difference between (a) AH0 and Nourban, (b) AH100 and Nourban, and (c) AH300 and Nourban averaged over rainfall period of frontal case 2010-5. Shaded, and black contours represent temperature advection difference, and coastline and GBA mega-city.

Finally, the time-longitude cross sections of 925hPa equivalent potential temperature (EPT) meridional gradient difference, averaged between 22.8N to 24N, between (a) AH0 and Nourban, (b) AH100 and Nourban, and (c) AH300 and Nourban for frontal case Case 2016-5 are given in Figure 4.32. Time 0 on Y axis refer to the hour of urban rainfall peak. Black dashed lines outline the location of the GBA mega-city. Blue (red) box indicate larger (weaker) EPT gradient,

thus intensified (weakened) front intensity. The EPT gradient is a key variable that characterizes the intensity of the frontal system, with larger negative values indicating a stronger gradient and thus a more intense system. It is seen that for AH0, AH100, and AH300, the EPT gradient is larger in urban areas at 20 hours before the hour of peak rainfall compared to Nourban, with an expansion of approximately 3 to 6K/100km (see blue boxes). This enhancement results in the strengthening of the frontal system and the acceleration of northerly winds, consistent with the stronger cold advection in urban areas during the rainfall period (see Figure 4.31). However, results indicate that the enhanced EPT gradient transitions to a decaying gradient from $t = -12$ hours to $t = 2$ hours in AH0 and AH100 (see red boxes). We attribute this decay to the suppression of urban temperatures resulting from the stronger northerly winds and frontal systems, which cause the EPT gradient to decrease. In contrast, the weakening of the gradient in AH300 is short-lived, and due to the strong warming, AH300 maintains a robust larger EPT gradient after $t = -7$ hours than Nourban (blue box), indicating intensified front intensity during the rainfall process. This finding aligns with the results in Figure 4.30, which show that only AH300 still has higher urban temperatures during the rainfall period compared to Nourban.

Overall, UHI in urban experiments initially contributes to a larger EPT gradient that intensifies the frontal system. This intensification subsequently results in stronger northerly winds and colder advection at low levels, leading to the suppression of temperatures in the GBA mega-city during the rainfall period in frontal cases. Ultimately, this dynamic manifests as a weaker impact of AH on urban precipitation during frontal cases as opposed to shear-line cases.

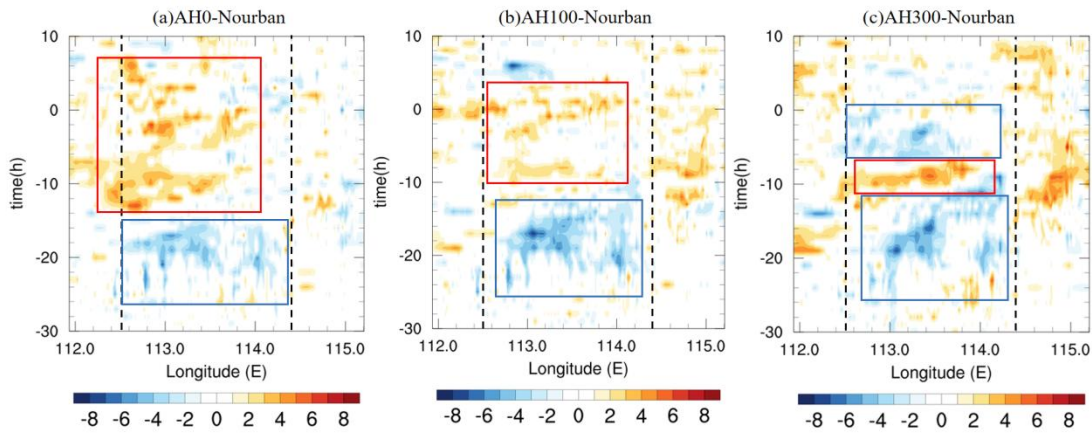


Figure 4.32 Time-longitude cross section of meridional gradient of the 925hPa equivalent potential temperature difference (units: K/100km) averaged between 22.8N to 24N between (a) AH0 and Nourban, (b) AH100 and Nourban, and (c) AH300 and Nourban for the frontal case 2016-5. Black dashed lines outline the location of the GBA mega-city. Blue (red) boxes indicate larger (weaker) EPT gradient, thus intensified (weakened) front intensity.

4.4 Brief Summary

In this study, the impacts of urbanization (urban land use and AH) on pre-monsoon extreme rainfall were investigated by using station observations and parallel experiments in WRF-SLUCM. Observations indicate that urban locations had much stronger extreme pre-monsoon rainfall (both 95th and 99th percentile of hourly rain rate) than surrounding rural areas, as well as the probability of pre-monsoon rainfall, especially for heavy rainfall in the range of 30 to 60 mm/hr, with hourly rain rate probability increasing by about 30% to even 300% in urban locations compared to rural. Furthermore, 18 strong UHI and 16 weak UHI cases were selected from pre-monsoon extreme rainfall events exceeding the threshold of the 99th percentile of wet hourly rain rate for all urban and rural stations. Case studies demonstrated that UHI significantly increased the intensity and probability of extreme rainfall in the GBA mega-city during the pre-monsoon period. At the rain peak hour of 14 stations, the rainfall difference between urban and rural stations reached 8mm/hr during strong UHI events, but only 4mm/hr in

weak UHI cases. There is also more frequent heavy rainfall in GBA mega-city during strong UHI cases than weak UHI cases, with probability enhancing of about 15% to 300% for rainfall heavier than 30mm/hr. On the other hand, based on synoptic background, pre-monsoon extreme rainfall events were further classified into two groups: frontal cases, shear-line + warm-sector cases. Observations unveil that the enhanced precipitation intensity and probability due to UHI were much stronger in shear-line and warm-sector cases than frontal, suggesting that urban impacts on rainfall are sensitive to synoptic systems during the pre-monsoon period.

To further explore the urban impacts on pre-monsoon extreme precipitation under different weather systems, four frontal cases and four shear-line cases were dynamically downscaled by WRF in the SC area, with four sets of parallel numerical experiments being carried out. In the Nourban experiment, the GBA urban area was replaced with "cropland" in WRF simulations. The other three experiments (AH0, AH100, and AH300) were performed using WRF coupled with SLUCM at different AH values in urban areas (0 W/m^2 , 100 W/m^2 , and 300 W/m^2 for diurnal maximum). For frontal cases, the presence of urban land use significantly decreased rainfall intensity and probability in GBA mega-city, while the AH enhanced both metrics, but significantly enhanced rainfall can only be observed in AH300 compared to Nourban. There was still a slight reduction in urban precipitation in AH100 compared to Nourban. Conversely, both urban land use and AH can significantly enhance the intensity and probability of rainfall for shear-line cases in urban areas. A positive correlation was also found between temperature and precipitation difference for shear-line cases in urban and downstream areas, with the slope of correlation increasing with higher AH values, which means UHI on precipitation is proportional to basic urban temperature. Moreover, further analysis found the enhanced precipitation during

shear-line cases was mainly due to the modified circulation and convection induced by UHI, leading to increased wind convergence and water vapor content in urban and some downstream areas. The presence of urban land surface also leads to larger VWS and convection in urban areas, resulting in significantly enhanced precipitation. But for frontal cases, the urban land use decreased (increased) local water vapor content (wind divergence), resulting in significantly decreased frontal rainfall in urban areas. UHI still led to increased water vapor content, convection, and wind convergence, but the low-level urban temperature in AH100 was strongly suppressed due to intensified fronts and cold advection from the north. Consequently, only AH300 exhibited significantly enhanced precipitation intensity and probability compared to Nourban.

5. Discussions and conclusions

5.1 Major conclusions

By using station observations and numerical simulation outputs of WRF-UCM, the impacts of urbanization on extreme precipitation in GBA mega-city. Our analysis focused on different seasons and weather systems, including TC, winter rainfall, and pre-monsoon extreme rainfall. We aimed to quantify the individual impacts of urban land surface and AH on extreme precipitation and assess the sensitivity of these phenomena to synoptic background conditions.

5.1.1 Tropical cyclone rainfall

Using data from 41 historical storms in the SC region, we observed a significant reduction in surface wind speeds over the GBA mega-city compared to surrounding rural areas during TC events, with decreases ranging from 0.15 to 0.6 m/s. Coinciding with these changes was an increase in the UHI approximately one day prior to the hour of peak TC rainfall, followed by a rapid suppression during the TC passage. Interestingly, the temperature difference between urban and rural areas was found to be as low as -0.08 K at the hour of rainfall peak. In addition to these changes in wind speed and temperature, stronger TC extreme hourly rainfall intensity (99th percentile of hourly rainfall) was observed in GBA urban locations, reaching 23 to 28 mm/hr compared to 17 to 24 mm/hr in rural areas. Additionally, more frequent precipitation was recorded in the GBA mega-city, with rainfall probabilities increasing by 10% to 40% for 20 to 50 mm/hr intensities and over five times for 50 to 60 mm/hr intensities. Moreover, extreme TC rainfall intensity was found to decrease with increasing station-to-coast distance, but the rainfall intensity is evidently stronger than that expected based on the best-fit relationship for urban stations than rural stations.

We conducted three parallel numerical experiments using the WRF model, simulating eight TC cases under different surface land use and AH conditions: Nourban, where urban areas were replaced by cropland; AH0, with a diurnal maximum AH of 0 W/m² in urban areas; and AH300, with a diurnal maximum AH of 300 W/m² in urban areas. Model outputs have satisfactory and reasonable performance in TC track and intensity, and the changes of wind speed and temperature due to urbanization were successfully reproduced as observed, with surface winds significantly reduced and the UHI effect initially increasing before being strongly suppressed during TC passage. Accumulated rainfall increased by approximately 15 to 40 mm/day regionally, with significant enhancements observed only over urban areas. The probability of TC rainfall increased by 20% to 50% across all ranges (1 to 90 mm/hr) within the GBA mega-city, particularly for heavy rainfall events exceeding 40 mm/hr when comparing both AH0 and AH300 to Nourban. Our analysis revealed that the intensified TC rainfall was primarily due to the urban surface roughness effect, which increased low-level moisture flux convergence and supported enhanced TC rainfall over urban areas. The impact of AH on GBA TC rainfall was generally weak in most storms, likely due to the suppression of the UHI effect by extreme winds. However, in specific cases such as storms Mangkhut and Goni, characterized by large TC sizes and tracks that did not directly pass through the GBA mega-city, AH still contributed to increased urban TC precipitation following the storm's departure. This was attributed to the rapid rebuilding of urban CAPE in the AH300 and the influx of water vapor brought by the TC. Notably, our results indicate that the fractional increase in accumulated rainfall due to urbanization is proportional to the storm residence time over the city, suggesting that slower or larger TCs lead to greater exacerbation of rainfall in the GBA mega-city.

5.1.2 Winter precipitation

In the second part of this study, the winter season is identified as November through February (NDJF), based on temperature, monthly mean rainfall, and the 99th percentile of hourly rainfall from 2008 to 2017 at 14 stations in GBA, while similar rainfall amounts were observed during these four months, but abnormally higher value was detected in March. Observations and ERA5 reanalysis data revealed that the temperature difference between GBA urban areas and their surrounding rural counterparts could exceed 1K on average, indicating that the UHI remains strong during the winter season in the GBA. This finding is consistent with previous literature (Wang et al., 2007; Xiong et al., 2012; Hou et al., 2020; Feng et al., 2012). Urban areas in GBA experience lower extreme rainfall (99th percentile of hourly rainfall) during the winter compared to rural locations, attributable to reduced evaporation and water vapor content due to urban land surfaces. However, the probability of heavy rainfall remains higher in urban areas, with an increase of approximately 10% to 30% for rainfall rates ranging from 16 to 28 mm/hour compared to rural regions. For very extreme winter precipitation, urban areas also tend to exhibit stronger annual maximum precipitation (R_{max}) and 99.99th percentile of hourly rainfall than rural locations. By classifying strong and weak UHI extreme rainfall cases based on temperature differences between urban and rural stations, case study results demonstrated that the UHI effect can still intensify both the intensity and probability of extreme winter rainfall in urban areas. The probability of rainfall increased by approximately 5% to over 200% for rates between 3 and 24 mm/hr, particularly for hourly rainfall exceeding 15 mm/hr.

Moreover, two extreme winter rainfall events were selected and dynamically downscaled within the GBA by WRF-UCM, namely Case 2013 and Case 2015. Four sets of experiments were

designed to investigate the urban impact on extreme winter rainfall. In the Nourban experiment, urban land use in the innermost domain was replaced by cropland; the 99LS and 30LS experiments incorporated urban land use information from 2009 and projected for 2030 over the GBA; and the 30LS-AH0 experiment utilized 2030 land use data with 0 AH in the urban area.

During Case 2013, both surface temperature and low-level temperature were substantially decreased due to the intrusion of cold air from the north. The temperature difference caused by urbanization was only 0.5 to 1°C in the GBA urban area, with warming occurring primarily in the northeastern and southwestern parts of the city. The warming attributed to urban land use was almost negligible. Both rainfall intensity and probability were lower in urban experiments than in Nourban runs, particularly in 30LSAH0, which could be attributed to the substantial decrease in surface and low-level specific humidity resulting from lower evaporation in urban areas. Only 99LS still exhibited slightly higher rainfall probability for rates heavier than 15 mm/hr. In contrast, for Case 2015, both urban land surface and AH substantially enhanced urban temperatures, with an increase of more than 1K in 30LS compared to Nourban across nearly the entire urban area.

Vertical temperature difference profiles revealed that all three urban experiments exhibited higher urban temperatures than Nourban below the 925 hPa level, with the difference returning to zero above the 800 hPa level. Additionally, significantly enhanced rainfall was observed in the southern and eastern parts of the GBA urban area in 30LS compared to Nourban, with an increase exceeding 2 mm/day, primarily due to the impact of AH. Rainfall probability increased for hourly rainfall rates in all ranges (except 3-6 mm/hr) in 99LS and 30LS compared to Nourban, particularly for rates heavier than 12 mm/hr. The frequency increased dramatically by approximately 30% to 80% for rainfall heavier than 10 mm/hr in 30LS compared to Nourban.

However, with no AH added to urban areas, the hourly rainfall probability of 30LSAH0 decreased in almost all ranges compared to 30LS, but still remained higher than Nourban. Such enhanced rainfall intensity and probability were mainly driven by modified circulation patterns, with stronger southeasterly winds observed at the 850 hPa level due to AH. This led to an increase in specific humidity of around 0.4 to 1 g/kg across almost the entire GBA urban area in 30LS compared to Nourban at low levels. Moisture flux convergence was also strongly amplified due to the UHI in the urban area, with a difference reaching -0.01525g/m²/s between 30LS and Nourban, but the presence of urban land use even led to stronger moisture flux divergence in GBA mega-city during rainfall period. Overall, the urban impact on winter precipitation in the GBA urban area varied significantly between Case 2013 and Case 2015. This difference could be attributed to the sensitivity of the urban impact to the synoptic background. While the presence of urban land use tended to result in lower urban precipitation, the UHI effect could still enhance intense winter rainfall if the UHI intensity remained constant.

5.1.3 Pre-monsoon precipitation

The final section of this study investigated the impact of urbanization on extreme pre-monsoon rainfall in the GBA mega-city. A rigorous approach was employed to identify the SCS monsoon onset day annually from 2008 to 2017, using ERA5 reanalysis data. The pre-monsoon period is further defined as Apr 1st to SCS monsoon onset day. Station observations revealed that urban areas experienced significantly stronger extreme pre-monsoon rainfall (both 95th and 99th percentiles of hourly rain rate) compared to surrounding rural regions. The probability of pre-monsoon rainfall, particularly heavy rainfall of 30-60 mm/hr, increased by approximately 30% to 300% in urban areas compared to rural ones. These findings are consistent

with previous literature (Shou et al., 2019; Su et al., 2019). Further analysis of 18 strong and 16 weak UHI cases, selected from pre-monsoon extreme rainfall events exceeding the 99th percentile of wet hourly rain rate, demonstrated that the UHI effect significantly enhanced the intensity and likelihood of extreme rainfall in the GBA mega-city during the pre-monsoon period. During strong UHI events, the rainfall difference between urban and rural stations reached 8 mm/hr at the hour of peak rainfall, while weak UHI cases exhibited differences of only 4 mm/hr. Moreover, heavy rainfall occurred more frequently in the GBA mega-city during strong UHI cases than weak ones, with the probability of rainfall exceeding 30 mm/hr increasing by 15% to 300%. On the other hand, by examining the synoptic background, pre-monsoon extreme rainfall events were categorized into two groups: frontal cases and shear-line + warm-sector cases. Observations revealed that the enhanced precipitation intensity and probability due to the UHI effect were more pronounced in shear-line and warm-sector cases than in frontal ones. This finding suggests that urban impacts on rainfall are sensitive to synoptic systems during the pre-monsoon period.

To further explore the urban influence on pre-monsoon extreme precipitation under different weather systems, four frontal and four shear-line cases were dynamically downscaled in the GBA using the WRF model. Four sets of parallel numerical experiments were conducted: Nourban, in which GBA urban areas were replaced by "cropland" in the land-use categorization; AH0, AH100, and AH300, normal urban land use were utilized in SLUCM with various values of AH at 0W/m², 100W/m², and 300W/m² for diurnal maximum. WRF model outputs indicated that, for frontal cases, urban land use significantly reduced rainfall intensity and probability in the GBA mega-city, whereas AH enhanced both. However, significant enhancement of rainfall was only observed in the AH300 experiment compared to Nourban. There was still a slight reduction

in urban precipitation in AH100 compared to Nourban. In contrast, both urban land use and AH considerably intensified rainfall and increased its likelihood for shear-line cases in urban areas. A positive correlation was discovered between temperature and precipitation differences for shear-line cases in urban and downstream locations, with a steeper slope for higher AH values, implying that the UHI effect on precipitation is proportional to the underlying urban temperature. Further analysis revealed that the enhanced precipitation during shear-line cases was primarily due to modified circulation and convection induced by the UHI effect, which led to increased wind convergence and water vapor content in urban and some downstream areas. While the presence of urban land surfaces substantially reduced surface wind speed, resulting in more significant vertical wind shear and convection in the GBA mega-city, and also significantly enhancing precipitation in GBA mega-city compared to Nourban. In contrast, for frontal cases, urban land use was found to decrease local water vapor content and slow wind speeds to the north and south of the city, causing wind divergence and significantly reduced frontal rainfall in urban areas. Although the UHI still increased water vapor content and wind convergence, the low-level urban temperature in the AH100 experiment was strongly suppressed due to more robust front intensity and cold advection from the north. The enhanced rainfall resulting from the weakened UHI effect was outweighed by the negative impacts of the urban land surface, such that only the AH300 experiment exhibited significantly increased precipitation intensity and probability compared to Nourban.

5.2 Uncertainties and limitations

The present study has several limitations that warrant further discussion. Firstly, the investigation of urban impacts on rainfall during different seasons and synoptic

backgrounds relied on meteorological parameter differences derived from station observations between urban and rural locations, as well as strong and weak UHI cases. However, these differences may not be solely attributable to urban impact, as they could be influenced by natural climate variability, terrain effects, station geography, land use modifications, and observation equipment, among other factors. Consequently, the precipitation differences between urban and rural areas could be induced by other factors that are not detected by the current methods, potentially compromising the robustness of the results. Moreover, the analysis was limited to observations from 2008 to 2017 due to data constraints, and the relatively small number of extreme cases after classification may introduce uncertainties. Caution should be exercised when comparing meteorological parameters based on these observations. To address these concerns, sensitivity tests using numerical modeling with various experiments were employed to further substantiate the urban impacts on extreme rainfall and understand the underlying mechanisms, with observations providing evidence for the reliability and veracity of model outputs.

Additionally, the definition of extreme rainfall as the 99th percentile of hourly rain rate during each period (TC, winter, and pre-monsoon) may influence the quantification of urbanization impacts on rainfall characteristics (for example, extreme rainfall was also defined as the 95th percentile of wet hourly rainfall in some other studies). Results from alternative indices, such as the 99.99th percentile and annual maximum hourly rainfall (Rmax), demonstrated sensitivity to the chosen extreme index, necessitating caution when quantifying urban influences on extreme rainfall in different periods.

Model uncertainties also pose a significant challenge in this study. The WRF-UCM was

employed to dynamically downscale extreme events selected from station observations in the GBA region. Several measures were taken to reduce model uncertainty, including the use of high-resolution simulations, utilizing spectral nudging of wind, and ensemble members with different starting times. The performance of the model was evaluated based on observations and reanalysis data in each part of this thesis, and the model revealed reasonable and satisfactory outcomes in temperature, wind circulation, TC track and intensity, etc, in the SC area. But there is still bias in precipitation, which is highly sensitive to physical schemes and also forcing data. For example, the pre-monsoon extreme rainfall simulation gave better performance by using ERA5 reanalysis data as the IBCs than by using ERA-Interim (Hoffmann et al., 2019). Future studies could explore the impact of urban-induced aerosol on extreme rainfall formation in the GBA mega-city, as this factor was not considered due to data limitations.

Furthermore, while our study offers insights into urban impacts on precipitation under different seasons, we also recognize certain limitations in our methodology. In particular, due to the lack of comprehensive urban data in GBA, SLUCM was employed in WRF to simulate urban impacts. Whilst the SLUCM provides a feasible solution, it potentially falls short of the complexity offered by the MLUCM, which can better resolve roughness due to buildings and provide a more accurate representation of the urban landscape. Additionally, our simulation approach was somewhat simplified, categorizing all urban grid points within the GBA mega-city as High-Intensity Residence with the same urban parameters for SLUCM. Such representation gives a homogeneous urban landscape that will likely overlook the diverse urban environments in reality. On the other hand, the use of SLUCM and a single type of urban land use has provided a simplified framework for our objectives. We recognize these limitations but

deem them acceptable for the scope of our current analysis, which focuses on the first order sensitivity of precipitation to the mega-city characteristics. Moreover, for section 2 and section 4, experiment with 300W/m^2 diurnal maximum AH in whole GBA urban areas was used for sensitivity investigation, representing an extreme urbanization scenario equivalent to commercial and industrial land use at every urban location. The AH value is extremely high for the whole GBA mega-city in reality, which reflects an extreme urbanization scenario and may underestimate the urban impacts in our analysis. We would like to emphasize that simulation an urban environment as the same as reality is not the main objective of this thesis, WRF experiments were conducted mainly to explore the sensitivity of precipitation in GBA mega-city (to different levels of urban development), so that extreme AH impacts can be inferred. Furthermore, the diurnal profile of AH in our model is heavily influenced by UHI intensity and AH emission habits in summer, which may not be reasonable for pre-monsoon and winter seasons (Quah et al., 2012). The complexity of urban environments, with diverse sources and factors affecting AH, makes direct observation and measurement of AH values challenging. We acknowledge these limitations and propose several strategies for improving AH representation in future studies.

In summary, despite the limitations and uncertainties identified, this study provides valuable insights into the urban impacts on extreme rainfall and the mechanisms involved. Further research could expand upon these findings by considering a more extended time period, incorporating additional factors such as aerosols, and employing more sophisticated and realistic urban land cover representations.

5.3 Innovation and significance

This thesis investigates the urban impacts on extreme rainfall intensity and frequency in the GBA mega-city across different seasons and weather systems. It quantifies the influence of urban land surface and AH on extreme rainfall and elucidates the underlying physical mechanisms.

The innovation and significance of this thesis can be summarized in three main aspects:

(1) Chapter 2 investigates the urban impacts on TC extreme rainfall in GBA mega-city, such a phenomenon was first reported by Zhang et al., 2018, but many details remain unclear yet. To our knowledge, this study is the first to focus on urban impacts on TC extreme rainfall in coastal SC, comparing the effects of UHI and urban surface land use. Furthermore, we first demonstrate that the fractional increase in accumulated rainfall due to urbanization in GBA is proportional to the “storm residence time”, indicating that urban impact on TC rainfall is sensitive to TC speed and size, with stronger exacerbation for slower or larger TCs. These findings provide valuable insights into urban-TC interactions in the GBA, where the region is prone to TC-associated hazards and suffers significant socio-economic losses. The results can inform public understanding and guide policy-making for government and industry stakeholders.

(2) Chapter 3 investigates the potential impacts of urban land surface and the UHI effect on extreme winter rainfall in the GBA using both observational analysis and dynamic downscaling with the WRF model. Few studies have explored extreme winter rainfall in the GBA, with most focusing on long-term accumulated winter precipitation. Our results reveal that although a drier atmosphere induced by lower urban surface evaporation leads to decreased winter precipitation, the UHI effect can significantly enhance winter extreme rainfall intensity and probability in the GBA mega-city. This enhancement is sensitive to synoptic background and is only effective when the UHI effect is not suppressed by front and cold air. These findings address

the knowledge gap in extreme winter precipitation and urban climate in the GBA, demonstrating that urban impacts on extreme rainfall vary with different synoptic backgrounds. These results can also inform future planning and public policy-making in agriculture and transportation.

(3) Chapter 4 shows that the UHI effect can significantly enhance pre-monsoon extreme rainfall in the GBA, with sensitivity to the weather system. Both urban land surface and the UHI effect contribute to the significant increase in extreme rainfall intensity and probability during events induced by shear-line systems. However, urban land use presence significantly decreases rainfall during events induced by the frontal system, even though the UHI effect can enhance frontal extreme rainfall when the temperature in the GBA mega-city is suppressed by strong northerly winds and cold air induced by the front. While previous studies have reported positive urbanization influences on pre-monsoon rainfall (Shou et al., 2019; Su et al., 2019), our findings emphasize the importance of considering synoptic background and weather systems when investigating urban impacts on pre-monsoon extreme rainfall. This study fills a research gap by comparing urban impacts on extreme rainfall under different synoptic systems and further identifying the separate impacts of urban surface and AH.

5.4 Social-economic implications

The findings of this thesis have far-research implications, particularly in the fields of urban planning, policy-making, and climate change adaptation strategies. First of all, the results reveal that urbanization intensifies extreme precipitation in certain scenarios and seasons, which can guide city planners and engineers in designing and implementing resilient urban infrastructure to withstand increased rainfall. For instance, urban drainage systems may need to be improved to

reduce the risk of urban flooding. Green infrastructure such as green roofs, bioswales, and rain gardens could also be strategically integrated into urban landscapes to enhance storm water management. For policy making, this thesis provides crucial insights for policy-makers to formulate climate-adaptive policies. Policies could be designed to control rapid urban sprawl, implement stricter building codes and regulations, promote sustainable urbanization, and encourage the use of low-impact development practices. In addition, this research supports the need for continuous monitoring and research on urban climatology, which can be incorporated into policy frameworks. Finally, Given the escalating impacts of climate change, this study underscores the importance of incorporating urbanization effects into climate change adaptation strategies. The findings can aid in the development of localized climate models, which can further aid in the planning and execution of effective adaptation and mitigation strategies.

5.5 Research outlook

5.5.1 Urban impact on TC rainfall

To further strengthen our findings, we plan to conduct additional WRF simulations of storms, employing a multi-layer urban canopy model (MLUCM) with 10 types of urban land use and more precise urban parameters to better capture urban physics. Moreover, we aim to investigate the influence of detailed TC characteristics, such as the location of TC rain bands, landfall location relative to the city, and the direction of TC movement. Future research will also consider coastal cities in other regions that experience strong TC rainfall, such as the Yangtze River Delta (YRD).

5.5.2 Urban impact on winter extreme rainfall

In future research, we will expand our investigation to other mega-city clusters, such as the YRD and the Beijing-Tianjin-Hebei area. Given the different geographical locations and synoptic backgrounds, there is still much to uncover regarding urban impacts on extreme rainfall under various weather systems during winter. To further support our findings, we plan to simulate additional winter cases and examine whether urban impacts vary under different weather systems. Similar to the TC study, we will employ a multi-layer urban canopy model with 10 types of urban land use to provide more detailed insights into the urban surface and UHI effects on winter rainfall.

5.5.3 Urban impact on pre-monsoon extreme rainfall

For the pre-monsoon period, we will consider extreme rainfall events not only during frontal and shear-line systems but also during warm-sector and vortex systems to better understand urban impacts on extreme rainfall under different weather scenarios. Additionally, we plan to conduct experiments with varying input AH levels in urban areas using the WRF model for frontal cases. This approach will enable us to examine the performance of the UHI effect under different conditions and better understand the sensitivity of the UHI effect to the cooling influence induced by northerly winds and cold air.

5.5.4 Diurnal and seasonal profile of AH

The reliability of AH intensity, diurnal profile, and seasonal profile used in the current study remain to be fully substantiated. Further studies are intended to establish a more accurate AH profile for the GBA mega-city. Generally, the primary sources of AH can be categorized into three domains: traffic, buildings, and human metabolism (Sailor and Lu 2004), building sector can

be further divided into electricity consumption and fuel consumption. To calculate the contribution of each element and determine the intensity and profile of AH in the GBA, a hybrid methodology will be employed, which combines a bottom-up modeling approach for traffic and buildings, and a top-down approach for human metabolism (Sailor et al., 2007; Miao et al., 2009; Sailor 2011; Quah and Roth, 2011). With a more precise and realistic AH profile for different seasons, more detailed understanding of the urban impacts on extreme precipitation events in the GBA mega-city can be unveiled. This refined approach is expected to provide enhanced insights and contribute to a more comprehensive understanding of the environmental dynamics in urban settings.

6. Reference

- Albrecht, B. A. (1989). Aerosols, cloud microphysics, and fractional cloudiness. *Science*, 245(4923), 1227-1230.
- Allen, L., Lindberg, F., & Grimmond, C. S. B. (2011). Global to city scale urban anthropogenic heat flux: model and variability. *International Journal of Climatology*, 31(13), 1990–2005.
- Andreae, M. O., & Rosenfeld, D. (2008). Aerosol–cloud–precipitation interactions. Part 1. The nature and sources of cloud-active aerosols. *Earth-Science Reviews*, 89(1-2), 13-41.
- Ao, X., Yue, C., Yang, X., Deng, L., & Huang, W. (2022). Urbanization Effects on Rainfall Processes Induced by Landfalling Typhoon Lekima (2019) over the Shanghai Metropolitan Area. *Journal of Hydrometeorology*. doi: 10.1175/jhm-d-21-0170.1
- Arnds, D., Böhner, J., & Bechtel, B. (2017). Spatio-temporal variance and meteorological drivers of the urban heat island in a European city. *Theoretical and Applied Climatology*, 128(1-2), 43–61. <https://doi.org/10.1007/s00704-015-1687-4>
- Au-Yeung, A. Y. M., and Chan, J. C. L. (2010), The Effect of a River Delta and Coastal Roughness Variation on a Landfalling Tropical Cyclone, *J. Geophys. Res.*, 115, D19121, doi:10.1029/2009JD013631.

- Bell, B., Hersbach, H., Simmons, A., Berrisford, P., Dahlgren, P., Horányi, A., et al. (2021) The ERA5 global reanalysis: Preliminary extension to 1950. *Q J R Meteorol Soc*, 147(741, 4186–4227. Available from: <https://doi.org/10.1002/qj.4174>
- Benson - Lira, V., Georgescu, M., Kaplan, S., & Vivoni, E. R. (2016). Loss of a lake system in a megacity: The impact of urban expansion on seasonal meteorology in Mexico City. *Journal of Geophysical Research: Atmospheres*, 121(7), 3079-3099
- Berrisford, P., Dee, D., Fielding, K., Fuentes, M., Kållberg, P., et al. (2009). The ERA-Interim Archive. *ERA Rep. Ser.* 1, 1 – 16.
- Blum, A., Ferraro, P., Archfield, S., Ryberg, K. (2020). Causal Effect of Impervious Cover on Annual Flood Magnitude for the United States *Geophysical Research Letters* 47(5).
- Bokwa, A., Wypych, A., & Hajto, M.J. (2018). Role of fog in urban heat island modification in Kraków, Poland. *Aerosol and Air Quality Research*, 18, 178-187.
- Bornstein, R. (1968). Observation of the Urban Heat Island Effect in New York City. *Journal of Applied Meteorology*.
- Bornstein, R., & Lin, Q. (2000). Urban heat islands and summertime convective thunderstorms in Atlanta: three case studies. *Atmospheric Environment* (1994), 34(3), 507 – 516. [https://doi.org/10.1016/S1352-2310\(99\)00374-X](https://doi.org/10.1016/S1352-2310(99)00374-X)
- Burian, S. J., & Shepherd, J. M. (2005). Effect of urbanization on the diurnal rainfall pattern in Houston. *Hydrological Processes*, 19(5), 1089 – 1103. <https://doi.org/10.1002/hyp.5647>
- Cerveny, R. S. (2017). WMO Assessment of Weather and Climate Mortality Extremes: Lightning, Tropical Cyclones, Tornadoes, and Hail. *Weather, Clim. Soc.* 9 (3), 487–497. doi:10.1175/wcas-d-16-0120.1
- Chan, K. T. F., Chan, J. C. L., & Wong, W. K. (2019). Rainfall asymmetries of landfalling tropical cyclones along the South China coast. *Meteorological Applications*, 26(2), 213 – 220. <https://doi.org/10.1002/met.1754>
- Change, I. P. on C. (2014). *Climate Change 2013: The Physical Science Basis*. Cambridge University Press. <https://doi.org/10.1017/cbo9781107415324>
- Chandler, T. J. (Tony J. (1965). The climate of London. Hutchinson.
- Chen, F., and Dudhia, J. (2001). Coupling and advanced land surface-hydrology model with the Penn State-NCAR MM5 modeling system. Part I: Model implementation and sensitivity.

Monthly Weather Review, 129(4), 569-585.

[https://doi.org/10.1175/1520-0493\(2001\)129%3C0569:CAALSH%3E2.0.CO;2](https://doi.org/10.1175/1520-0493(2001)129%3C0569:CAALSH%3E2.0.CO;2)

Chen, J., Tam, C-Y., Cheung, K., Wang, Z., Murakami, H., Lau, N-C., Garner, ST., Xiao, Z., Choy, C-W., and Wang, P. (2021) Changing Impacts of Tropical Cyclones on East and Southeast Asian Inland Regions in the Past and a Globally Warmed Future Climate. *Front. Earth Sci.* 9:769005. doi: 10.3389/feart.2021.769005

Chen, J., Tam, C., Wang, Z., et al. (2022). Future Thermodynamic Impacts of Global Warming on Landfalling Typhoons and Their Induced Storm Surges to the Pearl River Delta Region as Inferred from High-Resolution Regional Models. *Journal of Climate*. 4905 – 4926. 10.1175/JCLI-D-21-0436.1.

Chen, J., Wang, Z., Tam, C.-Y., Lau, N.-C., Lau, D.-S. D., & Mok, H.-Y. (2020). Impacts of climate change on tropical cyclones and induced storm surges in the Pearl River Delta region using pseudo-global-warming method. *Scientific Reports*, 10(1), 1965 – . <https://doi.org/10.1038/s41598-020-58824-8>

Chen, L., Li, Y., and Cheng, Z. (2010). An overview of research and forecasting on rainfall associated with landfalling tropical cyclones. *Adv. Atmos. Sci.*, 27, 967 – 976, <https://doi.org/10.1007/s00376-010-8171-y>.

Chen, L. S., and Xu, Y., (2017). Review of typhoon very heavy rainfall in China. *Meteorological and Environmental Sciences*, 40, 3–10, <https://doi.org/10.16765/j.cnki.1673-7148.2017.01.001>.

Chen, X., Liu, B., Li, Y., Deng, C., Chen, G. (2017). Impact of urbanization on summer precipitation process in Guangzhou. *J. China Hydrol.* 37, 25–32.

Chen, X., Jeong, S., Park, H., Kim, J., & Park, C.-R. (2020). Urbanization has stronger impacts than regional climate change on wind stilling: a lesson from South Korea. *Environmental Research Letters*, 15(5), 54016–. <https://doi.org/10.1088/1748-9326/ab7e51>

Chen, X., Zhang, F., & Zhao, K. (2017). Influence of Monsoonal Wind Speed and Moisture Content on Intensity and Diurnal Variations of the Mei-Yu Season Coastal Rainfall over South China. *Journal of the Atmospheric Sciences*, 74(9), 2835–2856. <https://doi.org/10.1175/JAS-D-17-0081.1>

Cheng, C., and Chan, Johnny. (2012). Impacts of land use changes and synoptic forcing on the

- seasonal climate over the Pearl River Delta of China. *Atmospheric Environment*. 60. 25–36. [10.1016/j.atmosenv.2012.06.019](https://doi.org/10.1016/j.atmosenv.2012.06.019).
- Chung, P., Sui, C., and Li, T. (2011). Interannual relationships between the tropical sea surface temperature and summertime subtropical anticyclone over the western North Pacific. *J. Geophys. Res.* 116, D13111. doi:10.1029/2010JD015554
- CLEUGH, H. A., & OKE, T. R. (1986). Suburban-rural energy balance comparisons in summer for Vancouver, BC. *Boundary-Layer Meteorology*, 36(4), 351–369. <https://doi.org/10.1007/BF00118337>
- Clouthier-López, J et al., (2022) Tropical Cyclone Simulations with WRF Using High Performance Computing. *Comp. y Sist.* vol.26 no.3
- Crutzen, P. J. (2004). New Directions: The growing urban heat and pollution “island” effect—impact on chemistry and climate. *Atmospheric Environment* (1994), 38(21), 3539–3540. <https://doi.org/10.1016/j.atmosenv.2004.03.032>
- Dai, Z., Guldmann, J., Hu, Y. (2019) Thermal impacts of greenery, water, and impervious structures in Beijing’s Olympic area: A spatial regression approach. *Ecol. Indic.* 2019, 97, 77–88.
- Deng, Z., Wang, Z., Wu, X., Lai, C., and Zeng, Z. (2022) Strengthened tropical cyclones and higher flood risk under compound effect of climate change and urbanization across China's Greater Bay Area. *Urban Climate* 44,101224.
- Doan, Q., Dipankar, A., Simón-Moral, A., Sanchez, C., Prasanna, V., Roth, M., & Huang, X. (2021). Urban-induced modifications to the diurnal cycle of rainfall over a tropical city. *Quarterly Journal of the Royal Meteorological Society*, 147(735), 1189–1201. <https://doi.org/10.1002/qj.3966>
- Doan, Q., Kusaka, H., and Ho, B. (2016). Impact of future urbanization on temperature and thermal comfort index in a developing tropical city: Ho Chi Minh City. *Urban Climate*. 17. 20-31. [10.1016/j.uclim.2016.04.003](https://doi.org/10.1016/j.uclim.2016.04.003).
- Dou, J., Wang, Y., Bornstein, R., and Miao, S. (2015). Observed Spatial Characteristics of Beijing Urban Climate Impacts on Summer Thunderstorms. *Journal of Applied Meteorology and Climatology*, 54(1), 94-105.
- Du, J., Wang, K., Jiang, S., Cui, B., Wang, J., Zhao, C., & Li, J. (2019). Urban Dry Island Effect

- Mitigated Urbanization Effect on Observed Warming in China. *Journal of Climate*, 32(18), 5705–5723. <https://doi.org/10.1175/JCLI-D-18-0712.1>
- Dudhia, J. (1989). Numerical study of convection observed during the Winter Monsoon Experiment using a mesoscale two-dimensional model. *J. Atmos. Sci.*, 46, 3077–3107. doi:10.1175/1520-0469(1989)046<3077:NSOCOD>2.0.CO;2
- Eun J., Knutson, T., Lee, T., Ying, M., and Nakagawa, T. (2020). Third assessment on impacts of climate change on tropical cyclones in the Typhoon Committee Region – Part II: Future projections. *Tropical Cyclone Research and Review*, 9(2), 75–86. <https://doi.org/10.1016/j.tctr.2020.04.005>
- Erell E, Pearlmuter D, Williamson T, 2011. Chapter 3: The Urban Heat Island. In: *Urban Microclimate: Designing the Spaces between Buildings*, Earthscan, United Kingdom.
- Fan, C., Ding, M., Wu, P., & Fan, Y. (2018). The Relationship between Precipitation and Aerosol: Evidence from Satellite Observation. <https://doi.org/10.48550/arxiv.1812.02036>
- Fan, Y., Li, Y., & Yin, S. (2018). Interaction of multiple urban heat island circulations under idealised settings. *Building and Environment*, 134, 10-20.
- Fan, J., Zhang, Y., Li, Z., Hu, J., and Rosenfeld, D. (2020). Urbanization-induced land and aerosol impacts on sea-breeze circulation and convective precipitation, *Atmos. Chem. Phys.*, 20, 14163–14182.
- Fu, C., Wang, S., Xiong, Z., Gutowski, W. J., Lee, D.-K., McGregor, J. L., Sato, Y., Kato, H., Kim, J.-W., & Suh, M.-S. (2005). REGIONAL CLIMATE MODEL INTERCOMPARISON PROJECT FOR ASIA. *Bulletin of the American Meteorological Society*, 86(2), 257–266. <https://doi.org/10.1175/BAMS-86-2-257>
- Fung, K.Y., C.-Y. Tam, T.C. Lee and Z. Wang. (2021). Comparing the Anthropogenic Heat and Global Warming Impacts on Extreme Precipitation in urbanized Pearl River Delta area based on Dynamical Downscaling, *Journal of Geophysical Research*, 126, 21.
- Gao, S. (2020). Dynamical downscaling of surface air temperature and precipitation using RegCM4 and WRF over China. *Climate Dynamics*, 55(5-6), 1283–1302. <https://doi.org/10.1007/s00382-020-05326-y>
- Gao, X., Xu, Y., Zhao, Z., Pal, J. S., & Giorgi, F. (2006). On the role of resolution and topography in the simulation of East Asia precipitation. *Theoretical and Applied Climatology*, 86(1-4),

- 173–185. <https://doi.org/10.1007/s00704-005-0214-4>
- Giorgi, F., Jones, G. & Asrar, G. R. (2009). Addressing climate information needs at the regional level: The CORDEX framework. *WMO Bull* 58(3), 175–183 (2009).
- Gómez, B. and Miguez-Macho, G. (2020). Spectral nudging in the Tropics, *Earth Syst. Dynam. Discuss.* [preprint], <https://doi.org/10.5194/esd-2020-71>, 2020.
- Gómez, B. and Miguez-Macho, G. (2017), The impact of wave number selection and spin-up time in spectral nudging. *Q.J.R. Meteorol. Soc.*, 143: 1772-1786. <https://doi.org/10.1002/qj.3032>
- GRAY, W. M. (1968). GLOBAL VIEW OF THE ORIGIN OF TROPICAL DISTURBANCES AND STORMS. *Monthly Weather Review*, 96(10), 669–700. [https://doi.org/10.1175/1520-0493\(1968\)096<0669:GVOTOO>2.0.CO;2](https://doi.org/10.1175/1520-0493(1968)096<0669:GVOTOO>2.0.CO;2)
- Gutowski, W. J., Ullrich, P. A., Hall, A., Leung, L. R., O'Brien, T. A., Patricola, C. M., Arritt, R. W., Bukovsky, M. S., Calvin, K. V., Feng, Z., Jones, A. D., Kooperman, G. J., Monier, E., Pritchard, M. S., Pryor, S. C., Qian, Y., Rhoades, A. M., Roberts, A. F., Sakaguchi, K., ... Zarzycki, C. (2020). The Ongoing Need for High-Resolution Regional Climate Models: Process Understanding and Stakeholder Information. *Bulletin of the American Meteorological Society*, 101(5), E664–E683. <https://doi.org/10.1175/BAMS-D-19-0113.1>
- HALLEGATTE, S., GREEN, C., NICHOLLS, R. J., & CORFEE-MORLOT, J. (2013). Future flood losses in major coastal cities. *Nature Climate Change*, 3(9), 802–806. <https://doi.org/10.1038/NCLIMATE1979>
- Han, J., and Baik, J. (2008). A theoretical and numerical study of urban heat island-induced circulation and convection. *Journal of the Atmospheric Sciences*, 65(6), 1859-1877.
- Han, J., Baik, J., and Lee, H. (2014). Urban impacts on precipitation. *Asia-Pacific Journal of Atmospheric Sciences*, 50(1), 17-30.
- Hand, L. M., & Shepherd, J. M. (2009). An Investigation of Warm-Season Spatial Rainfall Variability in Oklahoma City: Possible Linkages to Urbanization and Prevailing Wind. *Journal of Applied Meteorology and Climatology*, 48(2), 251–269. <https://doi.org/10.1175/2008JAMC2036.1>
- Hao, L., Huang, X., Qin, M., Liu, Y., Li, W., & Sun, G. (2018). Ecohydrological processes explain urban dry island effects in a wet region, southern China. *Water Resources*

- Research, 54, 6757– 6771. <https://doi.org/10.1029/2018WR023002>
- Heaviside, C., Cai, X.-M. and Vardoulakis, S. (2015). The effects of horizontal advection on the urban heat island in Birmingham and the West Midlands, United Kingdom during a heatwave. *Q.J.R. Meteorol. Soc.*, 141: 1429-1441. <https://doi.org/10.1002/qj.2452>
- Hersbach, H, Bell, B, Berrisford, P, et al. (2020). The ERA5 global reanalysis. *Q J R Meteorol Soc.* 146: 1999– 2049. <https://doi.org/10.1002/qj.3803>
- Holst, C., Tam, C., and Chan, J. (2016). Sensitivity of urban rainfall to anthropogenic heat flux: A numerical experiment. *Geophysical Research Letters*, 43(5), 2240-2248. <https://doi.org/10.1002/2015GL067628>
- HONG, S.-Y., NOH, Y., & DUDHIA, J. (2006). A new vertical diffusion package with an explicit treatment of entrainment processes. *Monthly Weather Review*, 134(9), 2318–2341. <https://doi.org/10.1175/MWR3199.1>
- Hou, A., Ni, G., Yang, H., and Lei, Z. (2013). Numerical Analysis on the Contribution of Urbanization to Wind Stilling an Example over the Greater Beijing Metropolitan Area. *Journal of Applied Meteorology and Climatology*, 52(5), 1105-1115. <https://doi.org/10.1175/JAMC-D-12-013.1>
- Hou, H., Liu, K., Li, X., Chen, S., Wang, W., and Rong, K. (2020). Assessing the urban heat island variations and its influencing mechanism in metropolitan areas of Pearl River Delta, South China. *Physics and Chemistry of the Earth, Parts A/B/C.* 120. 102953. 10.1016/j.pce.2020.102953.
- Hu, C., Fung, K., Tam, C-Y., Wang, Z. (2021). Urbanization impacts on Pearl River Delta extreme rainfall – sensitivity to land cover change vs anthropogenic heat. *Earth and Space Science.*
- Huang, S. S. (1986). The heavy rain during the pre-summer period over Southern China (in Chinese) (p. 244). Guangdong Technology Press
- Huang, D., and Gao, S. (2018). Impact of different reanalysis data on WRF dynamical downscaling over China. *Atmospheric Research*, 200, 25-35.
- Huffman, G., Stocker, D., Bolvin, E., and Nelkin. (2014). TRMM 3B42 precipitation data set. NASA Goddard Space Flight Center.
- Iacono, M. J., Delamere, J. S., Mlawer, E. J., Shephard, M. W., Clough, S. A., & Collins, W. D.

- (2008). Radiative forcing by long-lived greenhouse gases: Calculations with the AER radiative transfer models. *Journal of Geophysical Research*, 113(D13), D13103–n/a. <https://doi.org/10.1029/2008JD009944>
- Ivajnšič, D., & Žiberna, I. (2019). The effect of weather patterns on winter small city urban heat islands. *Meteorological Applications*, 26(2), 195–203. <https://doi.org/10.1002/met.1752>
- Jacobs B, Delaney C, (2015). Adapting to Urban Heat: Penrith City Council. Prepared for Penrith City Council by the Institute for Sustainable Futures, University of Technology Sydney.
- Jia, X., and Ge, J. (2017). Interdecadal changes in the relationship between ENSO, EAWM, and the wintertime precipitation over China at the end of the twentieth century. *J. Clim.* 30, 1923–1937. doi:10.1175/JCLI-D-16-0422.1
- Jiang, Z., Zhang, D.-L., Xia, R., & Qian, T. (2017). Diurnal Variations of Presummer Rainfall over Southern China. *Journal of Climate*, 30(2), 755–773. <https://doi.org/10.1175/JCLI-D-15-0666.1>
- JIMENEZ, P. A., DUDHIA, J., GONZALEZ-ROUCO, J. F., NAVARRO, J., MONTAVEZ, J. P., & GARCIA-BUSTAMANTE, E. (2012). A Revised Scheme for the WRF Surface Layer Formulation. *Monthly Weather Review*, 140(3), 898–918. <https://doi.org/10.1175/MWR-D-11-00056.1>
- Jin, K., Wang, F., Chen, D. et al. (2019). A new global gridded anthropogenic heat flux dataset with high spatial resolution and long-term time series. *Sci Data* 6, 139. <https://doi.org/10.1038/s41597-019-0143-1>
- KAYANE, I. (1960). THE DISTRIBUTION AND CLIMATOLOGICAL ANALYSIS OF THE DAILY MINIMUM TEMPERATURE IN AND AROUND THE TOKYO METROPOLITAN AREA. *Geographical Review of Japan*, 33(11), 564–572. <https://doi.org/10.4157/grj.33.564>
- Khouakhi, A., Villarini, G., and Vecchi, G. (2017). Contribution of tropical cyclones to rainfall at the global scale. *J. Climate*, 30, 359–372, <https://doi.org/10.1175/JCLI-D-16-0298.1>.
- Kim, D., Ho, C., Park, D. R., Chan, J. C. L., & Jung, Y. (2018). The Relationship between Tropical Cyclone Rainfall Area and Environmental Conditions over the Subtropical Oceans, *Journal of Climate*, 31(12), 4605–4616. Retrieved
- Khain, A., Rosenfeld, D., & Pokrovsky, A. (2005). Aerosol impact on the dynamics and

microphysics of deep convective clouds. *Quarterly Journal of the Royal Meteorological Society: A journal of the atmospheric sciences, applied meteorology and physical oceanography*, 131(611), 2639-2663.

Knapp, K. R., Kruk, M. C., Levinson, D. H., Diamond, H. J., & Neumann, C. J. (2010). THE INTERNATIONAL BEST TRACK ARCHIVE FOR CLIMATE STEWARDSHIP (IBTrACS): Unifying Tropical Cyclone Data. *Bulletin of the American Meteorological Society*, 91(3), 363–376. <https://doi.org/10.1175/2009BAMS2755.1>

Knapp, K. R., Diamond, H., Kossin, J., Kruk, M., Schreck, C. (2018). International Best Track Archive for Climate Stewardship (IBTrACS) Project, Version 4. [indicate subset used]. NOAA National Centers for Environmental Information. doi:10.25921/82ty-9e16 [access date].

Ko, J., Schlaerth, H., Li, Y., Vahmani, P., Ban-Weiss, G., and Sanders, K. (2022). Investigating the Impacts of Anthropogenic Heat on the Climate of Los Angeles. AGU Fall Meeting 2022. 2022AGUFMGC42P0903K

Kuang, W., Yang, T., Liu, A., Zhang, C., Lu, D., & Chi, W. (2017). An EcoCity model for regulating urban land cover structure and thermal environment: Taking Beijing as an example. *Science China. Earth Sciences*, 60(6), 1098–1109. <https://doi.org/10.1007/s11430-016-9032-9>

Kusaka, H., and Kimura, F. (2004). Thermal Effects of Urban Canyon Structure on the Nocturnal Heat Island: Numerical Experiment Using a Mesoscale Model Coupled with an Urban Canopy Model, *Journal of Applied Meteorology*, 43(12), 1899–1910.

Kusaka, H., Nawata, K., Suzuki-Parker, A., Takane, Y., and Furuhashi, N. (2014). Mechanism of Precipitation Increase with Urbanization in Tokyo as Revealed by Ensemble Climate Simulations. *Journal of Applied Meteorology and Climatology*, 53(4), 824-839. <https://doi.org/10.1175/JAMC-D-13-065.1>

Lan, Z., Yufei, Z., Wenshi, L., Wenfeng, X., Xiaolin, Z., Qi, F. (2015). Numerical simulation of the effect of air pollution on a heavy rain in the Pearl River Delta. *J. Trop. Meteorol.* 264–272.

Li, M., Song, Y., Mao, Z., Liu, M., and Huang, X. (2016). Impacts of thermal circulations induced by urbanization on ozone formation in the Pearl River Delta region, China. *Atmospheric*

- Environment, 127, 382-392.
- Li, S., Li, J., Yang, J., Bao, Q., Liu, Y., & Shen, Z. (2022). Monthly prediction of tropical cyclone activity over the South China Sea using the FGOALS-f2 ensemble prediction system. *Atmospheric and Oceanic Science Letters* = Daqi-He-Haiyang-Kexue-Kuaibao, 15(2), 100116-. <https://doi.org/10.1016/j.aosl.2021.100116>
- Li, Y., Wang, W., Chang, M., and Wang, X. (2021). Impacts of urbanization on extreme precipitation in the Guangdong-Hong Kong-Macau Greater Bay Area. *Urban Climate*. 38. 100904. 10.1016/j.uclim.2021.100904.
- Li, Y., & Zhao, D. (2022). Climatology of Tropical Cyclone Extreme Rainfall over China from 1960 to 2019. *Advances in Atmospheric Sciences*, 39(2), 320–332. <https://doi.org/10.1007/s00376-021-1080-4>
- Li, Z., Luo, Y., Du, Y., & Chan, J. C. L. (2020). Statistical Characteristics of Pre-summer Rainfall over South China and Associated Synoptic Conditions. *Journal of the Meteorological Society of Japan*, 98(1), 213–233. <https://doi.org/10.2151/jmsj.2020-012>
- Liao, J., Wang, X., Li, Y. & Xia, B. (2011). An analysis study of the impacts of urbanization on precipitation in Guangzhou. *J. Meteorol. Sci.* 4.
- Liu, J., Gao, Z., Wang, L., Li, Y., & Gao, C. Y. (2018). The impact of urbanization on wind speed and surface aerodynamic characteristics in Beijing during 1991–2011. *Meteorology and Atmospheric Physics*, 130(3), 311–324. <https://doi.org/10.1007/s00703-017-0519-8>
- Liu, J., Niyogi, D. (2019). Meta-analysis of urbanization impact on rainfall modification *Scientific Reports* 9(1), 7301.
- Liu, J., Schlünzen, KH, Frisia, T., Tian, Z (2021) Effects of urbanization on precipitation in Beijing. *Physics and Chemistry of the Earth, Parts A/B/C*, 122. 103005. ISSN 1474-7065
- Liu, X., Huang, Y., Xu, X., Li, X., Li, X., Ciais, P., Lin, P., Gong, K., Ziegler, A. D., Chen, A., Gong, P., Chen, J., Hu, G., Chen, Y., Wang, S., Wu, Q., Huang, K., Estes, L., & Zeng, Z. (2020). High-spatiotemporal-resolution mapping of global urban change from 1985 to 2015. *Nature Sustainability*, 3(7), 564–570. <https://doi.org/10.1038/s41893-020-0521-x>
- Liu, Y.-F & Yang, L. & Wang, Y. & Liu, J.-P. (2007). Survey study of city humid environment in winter. 39. 701-705.

- Lin, Y., Fan, J., Jeong, J.-H., Zhang, Y., Homeyer, C. R., & Wang, J. (2021). Urbanization-Induced Land and Aerosol Impacts on Storm Propagation and Hail Characteristics. *Journal of the Atmospheric Sciences*, 78(3), 925–947. <https://doi.org/10.1175/JAS-D-20-0106.1>
- Lu, M., Xu, Y., Shan, N., Wang, Q., Yuan, J., & Wang, J. (2019). Effect of urbanisation on extreme precipitation based on nonstationary models in the Yangtze River Delta metropolitan region. *The Science of the Total Environment*, 673, 64–73. <https://doi.org/10.1016/j.scitotenv.2019.03.413>
- Ludwig, F. L., & Dabberdt, W. F. (1973). Effects of urbanization on turbulent diffusion and mixing depth. *International Journal of Biometeorology*, 17(1), 1–11. <https://doi.org/10.1007/BF01553640>
- Luo, M., and Lau, N.-C. (2017). Heat waves in southern China: Synoptic behavior, long-term change and urbanization effects, *Journal of Climate*, vol. 30 (2), 703–720
- Luo, N., Zeng, L., Lin, W., Li, F., Jiang, B., and Li, J. (2017). Simulation of the Impacts of Urbanization on Winter Meteorological Fields over the Pearl River Delta Region. *Advances in Meteorology*. 2017. 1–10. 10.1155/2017/2012401.
- Luo, Y., Xia, R., & Chan, J. C. L. (2020). Characteristics, Physical Mechanisms, and Prediction of Pre-summer Rainfall over South China: Research Progress during 2008–2019. *Journal of the Meteorological Society of Japan*, 98(1), 19–42. <https://doi.org/10.2151/jmsj.2020-002>
- Luo, Z., Liu, J., Zhang, Y., Zhou, Jinjun., Yu, Y., Jia, R. (2021). Spatiotemporal characteristics of urban dry/wet islands in China following rapid urbanization. *Journal of Hydrology*. 601. 126618. 10.1016/j.jhydrol.2021.126618.
- Ma, H., Wang, R., Li, X., Lai, A., Yang, H., and Li, X. (2022). Why was South China extremely wet during January–February 2022 despite La Niña? *Front. Earth Sci.* 10:982225. doi: 10.3389/feart.2022.982225
- Mazrooei, A., Reitz, M., Wang, D., & Sankarasubramanian, A. (2021). Urbanization impacts on evapotranspiration across various spatio-temporal scales. *Earth's Future*, 9, e2021EF002045. <https://doi.org/10.1029/2021EF002045>
- Miao, S., Chen, F., LeMone, M. A., Tewari, M., Li, Q., & Wang, Y. (2009). An Observational and Modeling Study of Characteristics of Urban Heat Island and Boundary Layer Structures in Beijing. *Journal of Applied Meteorology and Climatology*, 48(3), 484–501.

<https://doi.org/10.1175/2008JAMC1909.1>

Miao, S., Chen, F., Li, Q., & Fan, S. (2011). Impacts of Urban Processes and Urbanization on Summer Precipitation: A Case Study of Heavy Rainfall in Beijing on 1 August 2006. *Journal of Applied Meteorology and Climatology*, 50(4), 806–825.
<https://doi.org/10.1175/2010JAMC2513.1>

Miao, Y., Guo, J., Liu, S., Liu, H., Li, Z., Zhang, W., & Zhai, P. (2017). Classification of summertime synoptic patterns in Beijing and their associations with boundary layer structure affecting aerosol pollution. *Atmospheric Chemistry and Physics*, 17(4), 3097–3110. <https://doi.org/10.5194/acp-17-3097-2017>

Ming, Y., Ramaswamy, V., & Persad, G. (2010). Two opposing effects of absorbing aerosols on global-mean precipitation. *Geophysical Research Letters*, 37, L13701. <https://doi.org/10.1029/2010GL042895>

Mohajerani, A., Bakaric, J., and Jeffrey-Bailey, T. (2017). The urban heat island effect, its causes, and mitigation, with reference to the thermal properties of asphalt concrete. *Journal of Environmental Management*, 197, 522-538.

Mote, T. L., Lacke, M. C., & Shepherd, J. M. (2007). Radar signatures of the urban effect on precipitation distribution: A case study for Atlanta, Georgia. *Geophysical Research Letters*, 34(20), L20710–n/a. <https://doi.org/10.1029/2007GL031903>

Neumann, C. (1993). Global overview. In: Holland, G.J. (Ed.), *Global Guide to Tropical Cyclone Forecasting*, WMO/TD-560. World Meteorological Organization, Geneva, pp. 3.1–3.46.

Niu, G.-Y., Yang, Z.-L., Mitchell, K. E., Chen, F., Ek, M. B., Barlage, M., Kumar, A., Manning, K., Niyogi, D., Rosero, E., Tewari, M., & Xia, Y. (2011). The community Noah land surface model with multiparameterization options (Noah-MP); 1, Model description and evaluation with local-scale measurements. *Journal of Geophysical Research*, 116(D12).
<https://doi.org/10.1029/2010JD015139>

NOAA National Centers For Environmental Information, U.S. billion-dollar weather and climate disasters, 1980 – present (NCEI Accession 0209268) (2020). <https://doi.org/10.25921/STKW-7W73%20>(28 January 2021).

Nobre, P., Moura, A. D., & Sun, L. (2001). Dynamical Downscaling of Seasonal Climate Prediction over Nordeste Brazil with ECHAM3 and NCEP's Regional Spectral Models at

- IRI. Bulletin of the American Meteorological Society, 82(12), 2787–2796.
[https://doi.org/10.1175/1520-0477\(2001\)082<2787:DDOSCP>2.3.CO;2](https://doi.org/10.1175/1520-0477(2001)082<2787:DDOSCP>2.3.CO;2)
- Oke, T. (1988). The urban energy balance. *Progress in Physical Geography*, 12(491).
- Oke, TR., Mills, G., Christen, A., Voogt, JA. (2017). Chapter 7: Urban Heat Island. In: *Urban Climates*, Cambridge University Press, United Kingdom.
- Our World in Data, 2020. Urban and rural population projected to 2050, World, 1900 to 2050.
<https://ourworldindata.org/grapher/urban-and-rural-population-2050?time=1900.latest>
- Ouyang, Z., Sciusco, P., Jiao, T., Feron, S., Lei, C., Li, F., John, R., Fan, P., Li, X., Williams, C. A., Chen, G., Wang, C., & Chen, J. (2022). Albedo changes caused by future urbanization contribute to global warming. *Nature Communications*, 13(1), 3800–3800.
<https://doi.org/10.1038/s41467-022-31558-z>
- Pulipati, Y., Balaji, N., and Chakravarthy, B. (2022). Impact of Urbanization on the Extreme Precipitation over a Coastal City: Observational Climatology and Application of Numerical Weather Prediction Model.
- Qiang, X. M., & Yang, X. Q. (2008). Onset and end of the first rainy season in South China. *Chinese Journal of Geophysics*, 51(5), 944–957. <https://doi.org/10.1002/cjg2.1289>
- Quah, A. K. L., & Roth, M. (2012). Diurnal and weekly variation of anthropogenic heat emissions in a tropical city, Singapore. *Atmospheric Environment* (1994), 46, 92–103.
<https://doi.org/10.1016/j.atmosenv.2011.10.015>
- Ramage, C. S. (1952). Variation of rainfall over South China through the wet season. *Bull. Amer. Meteor. Soc.*, 33, 308–311, <https://doi.org/10.1175/1520-0477-33.7.308>.
- Ramanathan, V., Crutzen, P. J., Kiehl, J. T., & Rosenfeld, D. (2001). Aerosols, climate, and the hydrological cycle. *Science*, 294(5549), 2119–2124.
- Ramanathan, V., & Carmichael, G. (2008). Global and regional climate changes due to black carbon. *Nature Geoscience*, 1(4), 221–227. <https://doi.org/10.1038/ngeo156>
- Ramírez-Aguilar, E. A. and L. C. Lucas Souza (2019). "Urban form and population density: Influences on Urban Heat Island intensities in Bogotá, Colombia." *Urban Climate* 29: 100497.
- Rappaport, E. N. (2014). Fatalities in the United States from Atlantic Tropical Cyclones: New Data and Interpretation. *Bulletin of the American Meteorological Society*, 95(3), 341–346.

<https://doi.org/10.1175/BAMS-D-12-00074.1>

- Ren, F. M., Gleason, B., and Easterling, D. (2002). Typhoon impacts on China's precipitation during 1957–1996. *Adv. Atmos. Sci.*, 19(5), 943–952, <https://doi.org/10.1007/s00376-002-0057-1>.
- Ren, Y., Zhang, H., Wei, W., Wu, B., Cai, X., & Song, Y. (2019). Effects of turbulence structure and urbanization on the heavy haze pollution process. *Atmospheric Chemistry and Physics*, 19(2), 1041–1057. <https://doi.org/10.5194/acp-19-1041-2019>
- Rosenfeld, D., & Woodley, W. L. (2000). Deep convective clouds with sustained supercooled liquid water down to -37.5° C. *Nature*, 405(6785), 440–442.
- Sailor DJ, Brooks A, Hart M, Heiple S. American Meteorological Society. (2007). A bottom-up approach for estimating latent and sensible heat emissions from anthropogenic sources. 7th Symposium on the Urban Environment, San Diego.
- Sailor, D. J., & Lu, L. (2004). A top-down methodology for developing diurnal and seasonal anthropogenic heating profiles for urban areas. *Atmospheric Environment* (1994), 38(17), 2737–2748. <https://doi.org/10.1016/j.atmosenv.2004.01.034>
- Sailor, D. J. (2011). A review of methods for estimating anthropogenic heat and moisture emissions in the urban environment. *International Journal of Climatology*, 31(2), 189–199. <https://doi.org/10.1002/joc.2106>
- Sand, M., Samset, B. H., Tsigaridis, K., Bauer, S. E., & Myhre, G. (2020). Black Carbon and Precipitation: an Energetics Perspective. *Journal of Geophysical Research. Atmospheres*, 125(13). <https://doi.org/10.1029/2019JD032239>
- Sajjad, M., and Chan, J. (2020) Tropical Cyclone Impacts on Cities: A Case of Hong Kong. *Front. Built Environ.* 6:575534. doi: 10.3389/fbuil.2020.575534
- Schmid, P. E., & Niyogi, D. (2013). Impact of city size on rainfall-modifying potential. *Geophysical Research Letters*, 40(19), 5263–5267. <https://doi.org/10.1002/grl.50656>
- Schlünzen, K. H., Hoffmann, P., Rosenhagen, G., & Riecke, W. (2010). Long-term changes and regional differences in temperature and precipitation in the metropolitan area of Hamburg. *International Journal of Climatology*, 30(8), 1121–1136. <https://doi.org/10.1002/joc.1968>

- Seinfeld, J. H., & Pandis, S. N. (2016). Atmospheric chemistry and physics: from air pollution to climate change. John Wiley & Sons.
- Shahmohamadi, P., Che-Ani, A. I., Maulud, K. N. A., Tawil, N. M., & Abdullah, N. A. G. (2011). The Impact of Anthropogenic Heat on Formation of Urban Heat Island and Energy Consumption Balance. *Urban Studies Research*, 2011, 1–9.
<https://doi.org/10.1155/2011/497524>
- Shimadera, H., Kondo, A., Shrestha, K., Kitaoka, K., and Inoue, Y. (2015). Numerical Evaluation of the Impact of Urbanization on Summertime Precipitation in Osaka, Japan. *Advances in Meteorology*, 2015(2015), 149-159. <https://doi.org/10.1155/2015/379361>
- Shou, Y., Gao, W., & Lu, F. (2020). A statistical study of pre-summer hourly extreme rainfall over the Pearl River Delta metropolitan region during 2008–2017. *International Journal of Climatology*, 40(9), 4242–4258. <https://doi.org/10.1002/joc.6457>
- Simón-Moral, A., Dipankar, A., Doan, Q., Sanchez, C., Roth, M., Becker, E., & Huang, X. (2021). Urban intensification of convective rainfall over the Singapore – Johor Bahru region. *Quarterly Journal of the Royal Meteorological Society*, 147(740), 3665–3680.
<https://doi.org/10.1002/qj.4147>
- Simpson, R. H., & Starrett, L. G. (1955). Further Studies of Hurricane Structure by Aircraft Reconnaissance. *Bulletin of the American Meteorological Society*, 36(9), 459–468.
<https://doi.org/10.1175/1520-0477-36.9.459>
- Skamarock, W., Klemp, J., Dudhia, J., Gill, D., Barker, D., Duda, M., Huang, X., Wang, W., and Powers, J. (2008). A description of the advanced research WRF version 3 NCAR Tech. Note, NCAR/TN-475+STR.
- Soltani, A., and Sharifi, E. (2017). Daily variation of urban heat island effect and its correlations to urban greenery: A case study of Adelaide. *Frontiers of Architectural Research*, 6(4), 529-538.
- Steensen, B. M., Marelle, L., Hodnebrog, Ø., & Myhre, G. (2022). Future urban heat island influence on precipitation. *Climate Dynamics*, 58(11-12), 3393–3403.
<https://doi.org/10.1007/s00382-021-06105-z>
- Stewart, I. D. (2011). "A systematic review and scientific critique of methodology in modern urban heat island literature." *International Journal of Climatology* 31(2): 200-217

- Su, L., Li, J., Shi, X., & Fung, J. C. H. (2019). Spatiotemporal variation in presummer precipitation over South China from 1979 to 2015 and its relationship with urbanization. *Journal of Geophysical Research: Atmospheres*, 124, 6737– 6749. <https://doi.org/10.1029/2019JD030751>
- Sun, X., Luo, Y., Gao, X., Wu, M., Li, M., Huang, L., Zhang, D.-L., & Xu, H. (2021). On the Localized Extreme Rainfall over the Great Bay Area in South China with Complex Topography and Strong UHI Effects. *Monthly Weather Review*, 149(8), 2777–2801. <https://doi.org/10.1175/MWR-D-21-0004.1>
- TAKAHASHI, M. (1959). RELATION BETWEEN THE AIR TEMPERATURE DISTRIBUTION AND TEH DENSITY OF HOUSES IN SMALL CITIES IN JAPAN. *Geographical Review of Japan*, 32(6), 305–313. <https://doi.org/10.4157/grj.32.305>
- Tan, J., Gu, W. (2015). Research Progress on Urban Induced Rainfall Effect. *Advance Meteorology Technology*. 5(6): 17-22.
- Tewari, M. F., Chen, F., Kusaka, H., and Miao, S. (2008). Coupled WRF/Unified Noah/urban-canopy modeling system, NCAR WRF Documentation, NCAR, Boulder, 1–20.
- Tu, C.-C., Chen, Y.-L., Chen, C.-S., Lin, P.-L., & Lin, P.-H. (2014). A Comparison of Two Heavy Rainfall Events during the Terrain-Influenced Monsoon Rainfall Experiment (TiMREX) 2008. *Monthly Weather Review*, 142(7), 2436–2463. <https://doi.org/10.1175/MWR-D-13-00293.1>
- Twomey, S. (1974). Pollution and the planetary albedo. *Atmospheric Environment* (1967), 8(12), 1251-1256.
- Ueno, M. (1995). A study of the impact of asymmetric components around tropical cyclone center on the accuracy of bogus data and the track forecast. *Meteor. Atmos. Phys.*, 56, 125-134.
- Wai, K. M., Wang, X. M., Lin, T. H., Wong, M. S., Zeng, S. K., He, N., Ng, E., Lau, K., & Wang, D. H. (2017). Observational evidence of a long-term increase in precipitation due to urbanization effects and its implications for sustainable urban living. *The Science of the Total Environment*, 599-600, 647–654. <https://doi.org/10.1016/j.scitotenv.2017.05.014>
- Wang, B., Wu, R., and Fu, X. (2000). Pacific-East Asian teleconnection: How does ENSO affect East Asian climate? *J. Clim.* 13, 1517–1536. doi:10.1175/1520-

0442(2000)013<1517:PEATHD>2.0.CO;2

Wang, D., Jiang, P., Wang, G., and Wang, D. (2015). Urban extent enhances extreme precipitation over the Pearl River Delta, China. *Atmospheric Science Letters*, 16(3), 310-317.

WANG F., ZHOU L., FENG, Y. (2007). Spatial Distribution of Heat Island in Guangzhou in Summer and Winter[J]. 27(3): 198-202.

Wang, J., Chen, Y., Liao, W., He, G., Tett, S. F. B., Yan, Z., Zhai, P., Feng, J., Ma, W., Huang, C., & Hu, Y. (2021). Anthropogenic emissions and urbanization increase risk of compound hot extremes in cities. *Nature Climate Change*, 11(12), 1084–1089.
<https://doi.org/10.1038/s41558-021-01196-2>

Wang, L., Huang, R., Wu, R. (2013). Interdecadal variability in tropical cyclone frequency over the South China Sea and its association with the Indian Ocean sea surface temperature. *Geophys. Res. Lett.* 40 (4), 768–771. doi:10.1002/grl.50171.

Wang, Q., Cai, W., Zeng, L., & Wang, D. (2018). Nonlinear meridional moisture advection and the ENSO-southern China rainfall teleconnection. *Geophysical Research Letters*, 45(9), 4353–4360. <https://doi.org/10.1029/2018GL077446>

Wang, Q., Zhong, W., Yang, S., Wang, J., Zeng, L., Chen, J., & He, Y. (2022). Southern China winter rainfall modulated by South China Sea warming. *Geophysical Research Letters*, 49, e2021GL097181. <https://doi.org/10.1029/2021GL097181>

Wang, X., Liao, J., Zhang, J., Shen, C., Chen, W., Xia, B., & Wang, T. (2014). A Numeric Study of Regional Climate Change Induced by Urban Expansion in the Pearl River Delta, China. *Journal of Applied Meteorology and Climatology*, 53(2), 346–362.
<https://doi.org/10.1175/JAMC-D-13-054.1>

Wang, X., Wang, Z., Qi, Y., & Guo, H. (2009). Effect of urbanization on the winter precipitation distribution in Beijing area. *Science in China. Series D, Earth Sciences*, 52(2), 250–256.
<https://doi.org/10.1007/s11430-009-0019-x>

Wang, Z., Z. Xiao, C.-Y. Tam, W. Pan, J. Chen. C. Hu, C. Ren, W. Wei and S. Yang. (2021). The projected effects of urbanization and climate change on summer thermal environment in Guangdong-Hong Kong-Macao Greater Bay Area of China, *Urban Climate*, 37, 2021, 100866.

Wen, J., Chen, J., Lin, W., Jiang, B., Xu, S., Lan, J. (2020). Impacts of anthropogenic heat flux and

- urban land-use change on frontal rainfall near coastal regions: a case study of a rainstorm over the Pearl River Delta, South China. *J. Appl. Meteorol. Climatol.* 59, 363–379.
- Wong, M., Yang, J., Weng, Q., Menenti, M., and Chan, P. (2015). Modeling of Anthropogenic Heat Flux Using HJ-1B Chinese Small Satellite Image: A Study of Heterogeneous Urbanized Areas in Hong Kong. *IEEE Geoscience and Remote Sensing Letters*, 12(7), 1466-1470. <https://doi.org/10.1109/LGRS.2015.2409111>
- Wu, B., Li, T., and Zhou, T. (2010). Relative contributions of the Indian Ocean and local SST anomalies to the maintenance of the western North Pacific anomalous anticyclone during the El Niño decaying summer. *J. Clim.* 23, 2974–2986. doi:10.1175/2010JCLI3300.1
- Wu, C., & Huang, G. (2016). Projection of climate extremes in the Zhujiang River basin using a regional climate model: PROJECTION OF CLIMATE EXTREMES IN THE ZHUJIANG RIVER BASIN. *International Journal of Climatology*, 36(3), 1184–1196. <https://doi.org/10.1002/joc.4412>
- Wu, M., Luo, Y. (2016). Mesoscale Observational Analysis of Lifting Mechanism of a Warm-Sector Convective System Producing the Maximal Daily Precipitation in China Mainland during Pre-Summer Rainy Season of 2015. *Journal of Meteorological Research*, 30(5), 719–736. <https://doi.org/10.1007/s13351-016-6089-8>
- Wu, M., Luo, Y., Chen, F., & Wong, W. K. (2019). Observed Link of Extreme Hourly Precipitation Changes to Urbanization over Coastal South China. *Journal of Applied Meteorology and Climatology*, 58(8), 1799–1819. <https://doi.org/10.1175/JAMC-D-18-0284.1>
- Xiao, H., Yin, Y., Jin, L., Chen, Q., & Chen, J. (2014). Simulation of aerosol effects on orographic clouds and precipitation using WRF model with a detailed bin microphysics scheme: Simulation of aerosol effects on orographic clouds. *Atmospheric Science Letters*, 15(2), 134–139. <https://doi.org/10.1002/asl2.480>
- Xiao, Q.; Kuo, Y.-H.; Zhang, Y.; Barker, D. M. & Won, D.-J. (2006). A tropical cyclone bogus data assimilation scheme in the MM5 3D-Var system and numerical experiments with Typhoon Rusa (2002) near landfall. *J. Met. Soc. Japan*, 84, 671-689.
- Xiao, Q., Zou, X., and Wang, B. (2000). Initialization and simulation of a landfalling hurricane using a variational bogus data assimilation scheme. *Mon. Wea. Rev.*, 128 , 2252–2269.

- Xiao, Z., Wang, Z., Huang, M., Luo, X., Liang, Y., and Lin, Z. (2020). Urbanization in an underdeveloped city-Nanning, China and its impact on a heavy rainfall event in July. *Earth and Space Science*, 7, e2019EA000991.
- Xiong, Y., Huang, S., Chen, F., Ye, H., Wang, C., & Zhu, C. (2012). The Impacts of Rapid Urbanization on the Thermal Environment: A Remote Sensing Study of Guangzhou, South China. *Remote Sensing* (Basel, Switzerland), 4(7), 2033–2056. <https://doi.org/10.3390/rs4072033>
- Xu, Z., Han, Y., & Yang, Z. (2019). Dynamical downscaling of regional climate: A review of methods and limitations. *Science China. Earth Sciences*, 62(2), 365–375. <https://doi.org/10.1007/s11430-018-9261-5>
- Yan, M., Chan, J. C. L., & Zhao, K. (2020). Impacts of Urbanization on the Precipitation Characteristics in Guangdong Province, China. *Advances in Atmospheric Sciences*, 37(7), 696–706. <https://doi.org/10.1007/s00376-020-9218-3>
- Yang, C., Li, Q., Hu, Z., Chen, J., Shi, T., Ding, K., & Wu, G. (2019). Spatiotemporal evolution of urban agglomerations in four major bay areas of US, China and Japan from 1987 to 2017: Evidence from remote sensing images. *The Science of the Total Environment*, 671, 232–247. <https://doi.org/10.1016/j.scitotenv.2019.03.154>
- Yang, L., Scheffran, J., Qin, H., and You, Q. (2015). Climate-related flood risks and urban responses in the Pearl River Delta, China. *Regional Environmental Change*, 15(2), 379–391. <https://doi.org/10.1007/s10113-014-0651-7>
- Yang, L., Smith, J. A., Baeck, M. L., Bou-Zeid, E., Jessup, S. M., Tian, F., & Hu, H. (2014). Impact of Urbanization on Heavy Convective Precipitation under Strong Large-Scale Forcing: A Case Study over the Milwaukee–Lake Michigan Region. *Journal of Hydrometeorology*, 15(1), 261–278. <https://doi.org/10.1175/JHM-D-13-020.1>
- Yang, S. H., Park, R. J., Lee, S., Jo, D. S., & Kim, M. J. (2023). Impact of changes in refractive indices of secondary organic aerosols on precipitation over China during 1980–2019. *Atmospheric Environment* (1994), 299, 119644–. <https://doi.org/10.1016/j.atmosenv.2023.119644>
- You, C., Fung, J. C.-H., & Tse, W. P. (2019). Response of the Sea Breeze to Urbanization in the Pearl River Delta Region. *Journal of Applied Meteorology and Climatology*, 58(7),

1449–1463. <https://doi.org/10.1175/JAMC-D-18-0081.1>

Yue, C., Tang, Y., Gu, W., Han, Z., & Wang, X. (2019). Study of Urban Barrier Effect on Local Typhoon Precipitation. *Qi xiang*, 11, 1611–.

Zhang, A., Lu, J., Zhang, B., and Liu, S. (1991) The turbulence characteristics in the boundary layer of the rural area and border of urban area of Beijing, *Chinese J. Atmos. Sci.*, 39, 1051–1060, 1991.

Zhang, H., Wu, C., Chen, W., Huang, G. (2019). Effect of Urban Expansion on Summer Rainfall in the Pearl River Delta, South China, 568, pp. 747–757.

Zhang, Q., Zheng, Y., Singh, V. P., Luo, M., & Xie, Z. (2017). Summer extreme precipitation in eastern China: Mechanisms and impacts: Summer Extreme Precipitation in China. *Journal of Geophysical Research. Atmospheres*, 122(5), 2766–2778. <https://doi.org/10.1002/2016JD025913>

Zhang, W., Villarini, G., Vecchi, G. A., & Smith, J. A. (2018). Urbanization exacerbated the rainfall and flooding caused by hurricane Harvey in Houston. *Nature (London)*, 563(7731), 384–388. <https://doi.org/10.1038/s41586-018-0676-z>

Zhang, Y., Miao, S., Dai, Y., and Bornstein, R. (2017). Numerical simulation of urban land surface effects on summer convective rainfall under different UHI intensity in Beijing. *Journal of Geophysical Research: Atmospheres*, 122(15), 7851-7868.

Zhu, X., Li, D., Zhou, W., Ni, G., Cong, Z., & Sun, T. (2017). An idealized LES study of urban modification of moist convection. *Quarterly Journal of the Royal Meteorological Society*, 143(709), 3228–3243. <https://doi.org/10.1002/qj.3176>

